# DESIGN AND FABRICATION OF SOLVENT COMPATIBLE POLYMER MICROFLUIDIC CHIPS AND ITS APPLICATION TO PARTICLE PRODUCTION AND DRUG DELIVERY

by

Reka Geczy

M.S., University of Copenhagen, 2016

A THESIS SUBMITTED IN PARTIAL FULFILLMENT OF

THE REQUIREMENTS FOR THE DEGREE OF

DOCTOR OF PHILOSOPHY

in

THE FACULTY OF GRADUATE AND POSTDOCTORAL STUDIES

(Pharmaceutical Sciences)

THE UNIVERSITY OF BRITISH COLUMBIA

(Vancouver)

October 2020

UNIVERSITY OF COPENHAGEN
DEPARTMENT OF PHARMACY

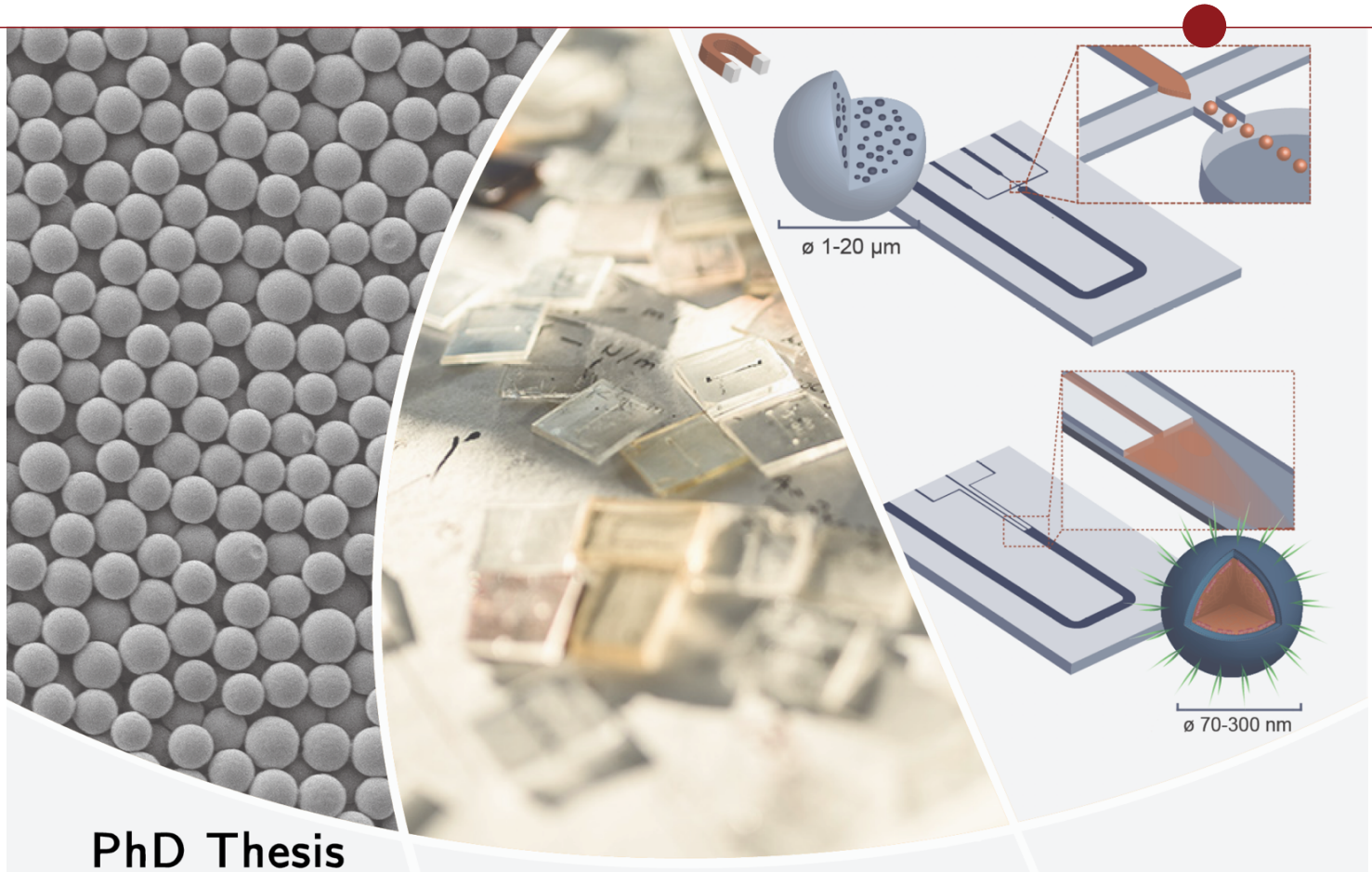


# PhD Thesis

Reka Geczy

# Design and Fabrication of Solvent Compatible Polymer Microfluidic Chips and its Application to Particle Production and Drug Delivery

Supervisor: Urs O. Häfeli

This thesis has been submitted to the Graduate School of Health and Medical Sciences, University of Copenhagen: **March 13th, 2020**

The following individuals certify that they have read, and recommend to the Faculty of Graduate and Postdoctoral Studies for acceptance, the dissertation entitled:

Design and Fabrication of Solvent Compatible Polymer Microfluidic Chips and its Application to Particle Production and Drug Delivery

submitted by Reka Geczy in partial fulfillment of the requirements for

the degree of Doctor of Philosophy

in Pharmaceutical Sciences

**Examining Committee:**

Anan Yaghmur, Department of Pharmacy, University of Copenhagen

University Examiner

Rizhi Wang, Department of Materials Engineering, The University of British Columbia

University Examiner

Winnie E. Svendsen, Technical University of Denmark

External Examiner

**Principal supervisor:**

Urs O. Häfeli
*Professor*
Department of Pharmacy, University of Copenhagen, Copenhagen, Denmark
Faculty of Pharmaceutical Sciences, The University of British Columbia, Vancouver, BC, Canada

**Co-supervisors:**

Jörg P. Kutter
*Professor*
Department of Pharmacy
University of Copenhagen, Copenhagen, Denmark

Camilla Foged
*Professor*
Department of Pharmacy
University of Copenhagen, Copenhagen, Denmark

**Assessment committee:**

Anan Yaghmur
*Associate Professor*
Department of Pharmacy
University of Copenhagen, Copenhagen, Denmark

Winnie E. Svendsen
*Professor*
Department of Biotechnology and Biomedicine
Technical University of Denmark, Kgs. Lyngby, Denmark

Rizhi Wang
*Professor*
Department of Materials Engineering
The University of British Columbia, Vancouver, BC, Canada

# Preface

This dissertation is formatted in accordance with the regulations of the University of Copenhagen and submitted in partial fulfillment of the requirements for a PhD degree awarded jointly by the University of Copenhagen and The University of British Columbia. Versions of this dissertation will exist in the institutional repositories of both institutions.

The experimental work has been carried out at both institutions, at the Department of Pharmacy, Faculty of Health and Medical Sciences, University of Copenhagen, and at the Faculty of Pharmaceutical Sciences, The University of British Columbia.

The work presented has resulted in two internationally peer reviewed publications and one manuscript to be submitted and included in **Chapter 6,** Results and Discussion:

1. Geczy, R., D. Sticker, N. Bovet, U.O. Häfeli, and J.P. Kutter*, Chloroform compatible, thiol-ene based replica molded micro chemical devices as an alternative to glass microfluidic chips, Lab on a Chip, **2019**. 19(5): p. 798-806.
2. Geczy, R., M. Agnoletti, M.F. Hansen, J.P. Kutter, K. Saatchi, and U.O. Häfeli*, *Microfluidic approaches for the production of monodisperse, superparamagnetic microspheres in the low micrometer size range,* Journal of Magnetism and Magnetic Materials, **2019**. 471: p. 286-293.

Additional contributions not considered as part of the thesis include:

3. European Patent 18184178.4-1107 "Methods for the Treatment of Thermoset Polymers"
4. Sticker, D.#, R. Geczy#, U.O. Häfeli, and J.P. Kutter*, *Thiol–Ene Based Polymers as Versatile Materials for Microfluidic Devices for Life Sciences Applications*, ACS Applied Materials & Interfaces, **2020**. 12, 10080-10095. #equal contribution

The project was done in collaboration with other researchers. Their contribution is explained below:

**Chapter 6, Section 2**:
Prof. Urs O. Häfeli conceptualized and Dr. Katayoun Saatchi synthesized the surface modifier enabling favorable wetting modifications of the microfluidic material.

**Chapter 6, Section 3**:
Dr. Mikkel F. Hansen characterized the magnetic response of the magnetic particles. Dr. Monica Agnoletti conducted the viscosity measurements. The results are published in the Journal of Magnetism and Magnetic Materials.

All other experiments in **Chapter 6,** Results and Discussion, were designed, executed, and analyzed by Reka Geczy.

# Acknowledgements

As a PhD student last three years have been filled with challenges and rewards. I would like to express my sincere appreciation to whom both professionally but in many cases, also personally helped and supported me throughout these times.

Firstly, I would like to thank my primary supervisor advisor **Professor Urs Häfeli** for the guidance, help and support during my thesis. I owe a great debt of gratitude to you for accepting and supporting me as a doctoral student in your group and for making my stay in Vancouver, Canada possible. Throughout these years you consistently allowed the research to be my own work, driven by curiosity and not by a forced necessity. This made these investigations fun; however, thanks for steering me in the right direction whenever I needed it.

I would also like to acknowledge my co-supervisor **Professor Jörg Kutter** for his continuous patience and support, not to mention for hosting the vast majority of my research at the Microscale Analytical Systems group. You were involved in my research at every step of the way and kept an eye on my progression to make sure I wasn't getting lost. You have helped me grow as a person, such as how to deal with a bad situation: hint "make the best of it."

Similarly, I would like to extend my gratitude to my co-supervisor **Professor Camilla Foged** for her support and truly insightful scientific input. Moreover, former and current members of her lab have provided me with know-hows and insights, particularly **Abhijeet Lokras**.

I have learned a great deal from many of the **students** and **post docs** here and am truly fortunate to have had the opportunity to work with them. Thank you to all the members of the Professor Häfeli, Kutter, and Foged group, past and present. I appreciate the support. I would like to especially thank my colleagues **Drago Sticker**, **Rasmus Svejdal**, **Alex Jönssön** and **Monica Agnoletti** for their professional and personal support. Particularly thanks for having fruitful discussions about our research and providing me with a cooperative and friendly atmosphere in the lab. Moreover, I would like to extend my gratitude to the Farma workshop, engineers **Lasse Johansson** and **Danny Steffensen**.

On a personal note, I would like to thank **Manish K. Tiwari** for his support, not only through this PhD but also my masters as well. You should really be getting a second doctorate for all the personal and scientific guidance you have provided. Thanks for keeping my spirits high when they were truly low and/or panicked.

Finally, and perhaps most importantly, I would like to express my deepest gratitude to my mother, **Elizabeth**, for providing me with unfailing support when I left the US to study in Denmark and for her continuous encouragement throughout *all* these years of study. This accomplishment would have never been possible without her.

This research was supported by the Lundbeck Foundation grant number 2014-4176 to Urs Häfeli.

Thank you.

# Table of contents

# 1. Abstract

Despite the recent advancements in the field of microfluidics, the potential of rapid development is often limited due to the inherent challenges posed by the materials used for microfluidic device fabrication. For drug delivery applications, there is a need to identify an optimal material that is cost-effective, compatible with 'soft-lithography,' easily replica molded, and resistant to harsh solvents. The family of thiol-ene polymers hold promise as an inexpensive and easy-to-produce alternative. This material shows good chemical compatibility with most organic solvents but falls short for chlorinated solvents which are often used for pharmaceutical applications. Thus, the research presented in this thesis aimed to develop a solvent compatible thiol-ene platform for rapid and cost-effective fabrication of microfluidic chips with a focus on drug delivery applications.

This work initially shows the rendering of thiol-ene polymers chloroform compatible in order to open new prototyping avenues for drug delivery purposes. The approach is simple and effective, resulting in a 50-fold increase in chloroform compatibility, allowing for the operation of microfluidic chips in chloroform for several days without any discernible deformation.

Next, this thesis shows the novel preparation of small (1-2 µm), monodispersed polylactic acid (PLA) microspheres, utilizing chlorinated solvents for their synthesis. This work presents a simple microfluidic chip design achievable in all microfluidic fabrication labs and relies on flow manipulations to shear of droplets well under the often-regarded minimum size limits. The prepared particles show high monodispersity and significant loading with magnetite nanoparticles; hence, hold promise for magnetically targeted drug delivery.

In addition to droplet production, thiol-enes are suited for the bulk precipitation of uniform nanoparticles. The final work presented here focuses on siRNA loading within the lipid-polymer hybrid nanoparticles. This work shows exquisite size control, ranging from 70-300 nm, uniform sizes, and high siRNA encapsulation efficiency.

The results obtained during this study presents a facile method to produce cost-effective and solvent compatible thiol-ene microfluidic chips highly suitable for numerous applications. With extensive experimental evidence, the fabricated thiol-ene microfluidic chips are shown to be very efficient for the production of pharmaceutical delivery vehicles of all sizes, ranging from the nano- to the micro-scale.

## 1.1. Lay Summary

A microfluidic chip is a small device that allows for the movement and manipulation small amounts of liquids within integrated channels that are about the size of a human hair. Microfluidic devices can be used to miniaturize lab processes (lowering costs), but more importantly, the channels can be shaped in such way that all reactions or processes are tailor made to be more effective, consistent, faster or even, include many processes in a single step.

A key consideration of a microfluidic device is the material that it's made out of. Currently most microfluidic chips are made out of plastic, as plastics are easier to shape to have hair-sized channels. Plastics, however, are limited in utility, as they tend to break down when exposed to common laboratory chemicals. Many of these chemicals are essential for the production of pharmaceutical drug carriers, a research area where microfluidic chips are particularly useful to obtain a consistent product. In a controlled reaction, microfluidics can be used to package drugs into a carrier material to yield a stable pharmaceutical that can protect the cargo, target disease sites, modulate drug release, and so on.

To achieve this, the first part of this thesis shows the development of a plastic that can withstand very harsh chemicals (solvents) that are required for the production of both micron- and nanosized drug carriers. This thesis shows that a class of plastics, "thiol-enes," can be modified to be highly solvent compatible, enabling research in pharmaceutical development. The new and improved material can withstand 50x more chloroform exposure than the original.

The utility of this material is then showcased for both micro- and nanoparticles. A novel approach is used to make a particularly challenging size of particles that are 1-2 µm in diameter. These particles were rendered magnetic, such that it holds promise for magnetic targeting to disease sites in a clinical setting. Further, the microfluidic material is used to produce nanoparticles aimed at altering protein levels in cells, which is at present, a highly desirable therapeutic approach.

Combined, this thesis shows both material modifications and pharmaceutical applications, opening new ways of developing drug delivery vehicles in a microfluidic chip. The material can be easily and rapidly molded to make the channels, allowing to produce innovative designs, all while maintaining applicability in harsh chemical environments

# 2. Resumé (på dansk)

Udviklingen af hurtige fremstillingsteknikker til mikrovæskesystemer har fremskyndet deres anvendelse. På trods af de nylige fremskridt er potentialet for mikrovæskesystemers udvikling imidlertid begrænset på grund af de grundlæggende udfordringer, der er ved anvendelsen af forskellige materialer til fremstilling af mikrovæske chips. Det mest anvendelige materiale til udvikling af mikrovæske chips, med henblik på drug delivery er glas, men det er dog både bekosteligt og vanskeligt at fremstille. Der er således behov for at identificere et mere optimalt materiale, der er i) omkostningseffektivt, ii) kompatibelt med standardteknikken "soft-lithography," iii) ubesværet kan blive støbt replika af og iv) som er resistent over for hårde opløsningsmidler, hvilket ofte kræves. Thiol-ene-polymererne er ofte overset, men de har vist sig som et alternativt materiale der både er billigt og enkelt at fremstille. Dette materiale har en god kemisk kompatibilitet med de fleste organiske opløsningsmidler, men ikke med klorerede opløsningsmidler, som regelmæssigt benyttes til lægemiddel sammenhænge. Forskningen der er præsenteret i denne afhandling, blev planlagt og udført med det formål at udvikle en opløsningsmiddelkompatibel thiol-en-platform til hurtig og omkostningseffektiv fremstilling af mikrovæske chips med en potentiel anvendelse i drug delivery.

Arbejdet fokuserede oprindeligt på at gøre thiol-ene-polymererne kloroform-kompatible og muliggøre nye prototypemetoder til at lave mikrovæske chips med anvendelse i drug delivery. Fremgangsmåden er enkel, men ikke desto mindre effektiv og den er baseret på en høj temperaturbehandling af materialet. Behandlingen resulterer i en 50 gange stigning i materialets kloroform-kompatibilitet og muliggør brugen af mikrovæskechips i kloroform i flere dage uden tegn på nedbrydning.

Gennem opnåelsen af opløsningsmiddelkompatibilitet viser dette arbejde dernæst den nye fremstilling af små, monodisperse polymælkesyre (PLA) mikrosfærer. Dette arbejde præsentere et simpelt mikrovæskechipdesign, der kan fremstilles i alle laboratorier som arbejder med mikrovæske systemer og som er afhængig af flowmanipulationer til at skabe dråber med en størrelse betragteligt under typisk ansete minimumsgrænser. De producerede 1-2 µm partikler viser høj monodispersitet og et markant indhold af magnetit-nanopartikler, og det er derfor lovende for udviklingen af en magnetisk målrettet levering af lægemidler.

Thiol-ene er foruden dråbeproduktion især velegnet til masse udfældning af stærkt ensartede nanopartikler. Derfor fokuserer det endelige arbejde, der er præsenteret her, på siRNA-indhold i lipid-polymer-hybrid-nanopartikler. Dette viste fremragende størrelseskontrol, som spænder fra 70-300 nm, med meget ensartede størrelser og høj siRNA indkapslingseffektivitet (70-90%).

Resultaterne som er opnået ved denne undersøgelse, præsenterer en ubesværet metode til at fremstille omkostningseffektive og opløsningsmiddelkompatible thiol-en-mikrovæskechips som er meget velegnet til adskillige anvendelser og viser potentiale som alternativer til glasbaserede chips. Med omfattende eksperimentelle resultater har de fremstillede thiol-ene-mikrovæske chips vist at være meget effektive til fremstilling af farmaceutiske leveringsenheder i alle størrelser, der spænder fra nano- til mikroskala.

# 3. Abbreviations

| | | | |
|---|---|---|---|
| *ACE* | Acetone | *PCL* | Polycaprolactone |
| *ACN* | Acetonitrile | *PDMS* | Polydimethylsiloxane |
| *Bo* | Bond number | *Pe* | Peclét number |
| *Ca* | Capillary number | *PEG* | Polyethylene glycol |
| *CF* | Chloroform | *PETMP* | Pentaerythritol tetrakis(3-mercaptopropionate) |
| *CNC* | Computer numerical control | *PGA* | Poly(glycolic acid) |
| *CNT* | Carbon nanotubes | *PLA* | Poly(D, L-lactide) |
| *COC* | Cyclic olefin copolymer | *PLGA* | Poly(lactic-co-glycolic acid) |
| *CP* | Continuous phase | *PMMA* | Poly(methyl methacrylate) |
| *CV* | Coefficient of variation | *PS* | Polystyrene |
| *DMSO* | Dimethyl sulfoxide | *Re* | Reynolds number |
| *DP* | Dispersed phase | *SEM* | Scanning electron microscopy |
| *EDTA* | Ethane-1,2-diyldinitrilo tetraacetic acid | *siRNA* | Small interfering RNA |
| *GC* | Gas chromatography | *TATATO* | 1,3,5-triallyl-1,3,5-triazine-2,4,6(1H,3H,5H)-trione |
| *HPG* | Hyperbranched polyglycerol | *TE* | Thiol-ene |
| *iTLC* | Instant thin layer chromatography | $T_g$ | Glass transition temperature |
| *LPN* | Lipid polymer nanoparticle | *THF* | Tetrahydranfuran |
| *MMS* | Magnetic microspheres | $T_m$ | Melting temperature |
| *MNP* | Magnetic nanoparticles | *TPO-L* | Trimethylbenzoyldi-phenylphosphinate (photoinitiator) |
| *MS* | Microspheres | *WCA* | Water contact angle |
| *NP* | Nanoparticle | *We* | Weber number |
| *OSTE* | Off-stoichiometric thiol-ene | $\varphi$ | Flow rate ratio |

# 4. Aims and Objectives

For the production and clinical translation of drug delivery systems microfluidic-technologies have emerged as a promising tool to solve major challenges of bulk fabrication approaches. Currently, microfluidics holds high promise to improve the consistency and reproducibility of formulations, increase drug loading and produce a more homogenous size distribution of micro-/ nanosystems.

Traditionally, glass microfluidic devices have been utilized due to the harsh chemical environments often required for particle production (organic solvents such as dichloromethane, chloroform, acetone, etc.). While inherently solvent compatible and inert, the microfabrication of glass is quite cumbersome, costly and requires the use of dangerous etching steps that most fabrication laboratories tend to forgo.

The aim of this thesis is to **(1)** use an alternative microfluidic material, thiol-ene polymers, that while easy to fabricate and offer a long list of advantages, are inherently poorly suited for certain pharmaceutical applications (**Figure 4.1A**). The major shortcomings of the material for drug carrier production include a mildly hydrophobic surface and poor chlorinated solvent compatibility.

The first step of the work includes the **(2)** improvement of thiol-ene polymers (**Figure 4.1B**). Here, a robust super-hydrophilic coating was optimized, and the material rendered chloroform compatible; both improvements critical for micro- and nanocarrier production. Moreover, the research laid a foundation for countless experimental investigations and innovations where hydrophilic surfaces or solvent compatibility are required for optimum performance.

Finally, thiol-ene microfluidic chips were used for a wide variety of **(3)** pharmaceutical applications (**Figure 4.1C**). For this, 70-300 nm siRNA loaded nanoparticles and 1-20 µm magnetic microspheres were produced, showcasing the utility and versatility of the improved material.

In summary, the thesis is built on the hypothesis that "thiol-ene microfluidic chips are the optimum material for all-sized drug carrier production." As an interdisciplinary research field, this thesis ranges from materials chemistry to pharmaceutical formulation development in order to support the hypothesis and showcase the utility of polymeric microfluidic chips in the pharmaceutical sciences.

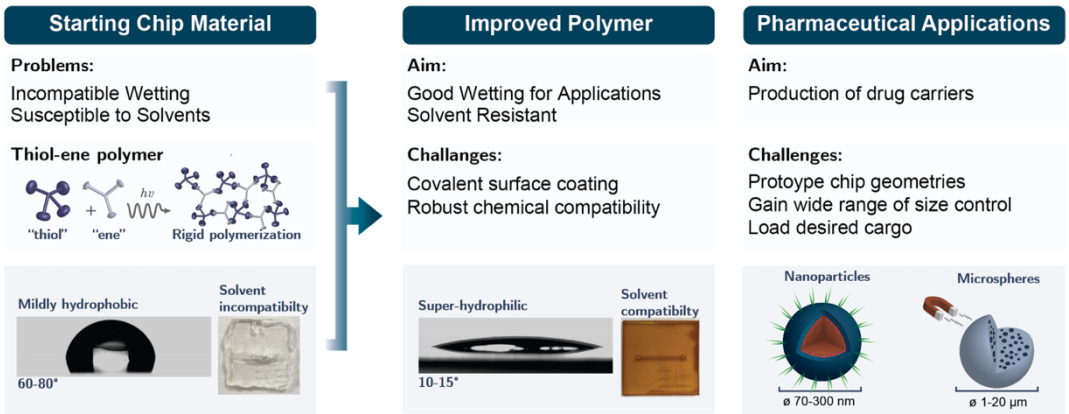


**Figure 4.1. Summary of thesis aim and objectives.** The primary aim is to **A)** take a problematic polymer for pharmaceutical applications with poor wetting and poor solvent compatibility and **B)** solve these challenges and produce an optimum material with a hydrophilic surface and high solvent compatibility. Finally, **C)**, showcase the utility of the material for virtually all-sized drug carrier production from 70 nm to 20+ µm in size.

# 5. Introduction

## 5.1. Drug delivery systems

The efficiency of therapeutics relies both on the effectiveness of the drug as well as the adequacy of the delivery system (carrier). Polymer and/or lipid-based drug delivery systems (both nano- and microparticles) can be used to improve the solubility and chemical stability of the drug, control drug release, increase the local concentration of the drug, reduce dosage intervals, and minimize side effects such as toxicity or immune responses [1, 2].

Drug delivery systems serve an important therapeutic and diagnostic utility in the clinic. Albeit, effective synthetic approaches are necessary to improve their consistency and reliability, but also to further development. For the most part, current approaches have some shortcomings, including batch to batch variation, suboptimal drug loading, as well as a broad size distribution that may poorly impact the release kinetics of the drug [3]. To combat some of the challenges, significant research efforts are placed into advanced materials development and synthetic approaches; the latter of which pertain to the work presented here.

### 5.1.1. Micro- and nanoparticles

Micro- and nano-drug formulations are classified depending on particle size. Microparticles can refer to diameters slightly less than 1 µm and up to 100 µm or more, while nanoparticles are often between 10 and 1000 nm [5]. At all these size ranges, there are various drug delivery systems in place, giving rise to different properties in terms of drug loading, release or even respond to a physiochemical environment (**Figure 5.1**) [4]. For example, micro- or nanocapsules can be formed where the drug is surrounded by a layer of polymer/lipid material such that a drug reservoir system is created. Alternatively, the drug can be dispersed in the polymer/lipid matrix, forming a micro- or nanosphere.

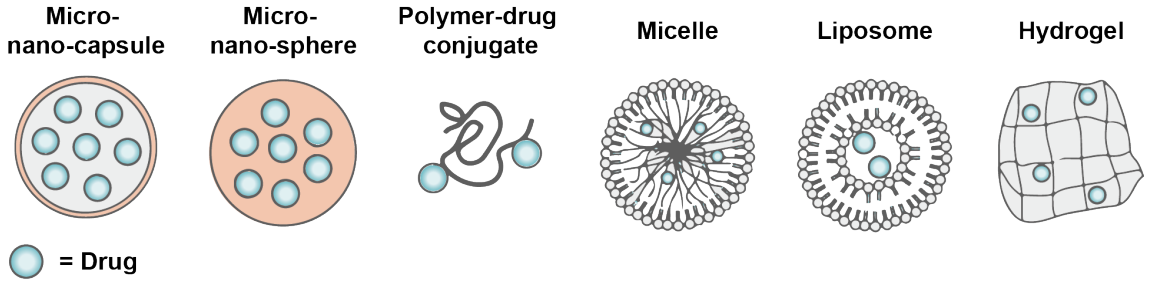


**Figure 5.1. Schematic illustration of various drug delivery sytems' shapes and morphologies.** Each system offers unique benefits such as release properties. Figure adapted, under CC BY 4.0 from [4].

A drug may be covalently linked to a polymer, forming a polymer-drug conjugate. Using a single lipid structure, the drug can be packaged into micelles, or liposomes if a bilayer is used. Finally, hydrogels may be used, which are crosslinked hydrophilic polymers with a high-water content.

The size of the drug delivery system affects its optimal mode of administration and biodistribution properties. A simplified graph of approximate particle diameters, their administration, and target sites are shown in **Figure 5.2**. Clinically, submicron particles are often intravenously (IV) [6]. Here, inorganic colloidal particles of a few tens of nanometers are often used for diagnostic imaging while similar-sized 10 - 50 nm lipid nanoparticles (LNPs) are taken up by the reticuloendothelial system, for example by macrophages in the liver [7]. Slightly larger nanoparticles (NPs), 50 - 200 nm in diameter tend to be long-circulating and particularly appropriate for a tumor or brain delivery of drugs [7]. A few-micron diameter is the cut-off size for effective IV circulation of microspheres; albeit, microspheres are seldom IV injected clinically. Theoretically, by avoiding high local concentrations, any potential lung capillary blockage can be circumvented [8, 9]. Based on *in vivo* intravenous administration of microspheres in beagles, 3-4 µm particles successfully bypass the fine lung capillaries and get cleared through the liver and spleen [6, 10]; therefore, they can have future clinical utility. Currently, larger micron size regimes are mainly limited to intramuscular/subcutaneous administration or inhalation. For intramuscular administration, particle diameters are between 0.5-5 µm, though findings show that 0.5-1 µm yields the lowest level of muscle damage [11] and may be the optimum size. For the inhalation of aerosols, particle diameter determines the deposition site within the respiratory tract. Smaller particles (1-5 µm in diameter) deposit in the bronchi and alveoli, while larger particles (between 8-20 µm) deposit within the upper respiratory tract, often the throat and nasal cavity [12]. Finally, large hundreds of microns or macroscopic drugs are suited for oral or localized delivery [13, 14].

Therapeutic and diagnostic particles of all sizes find importance in the clinic. Some examples of nanoparticles include Abraxane® [15] (albumin-bound paclitaxel formulation for cancer treatment) and Onpattro® [16] (LNP for the treatment of hereditary transthyretin amyloidosis). For microspheres, examples include Optison™ [17] (3-4 µm protein particles used as a contrast agent for ultrasound) and TheraSphere® (yttrium-90 glass microspheres for nonresectable liver tumors) [18].

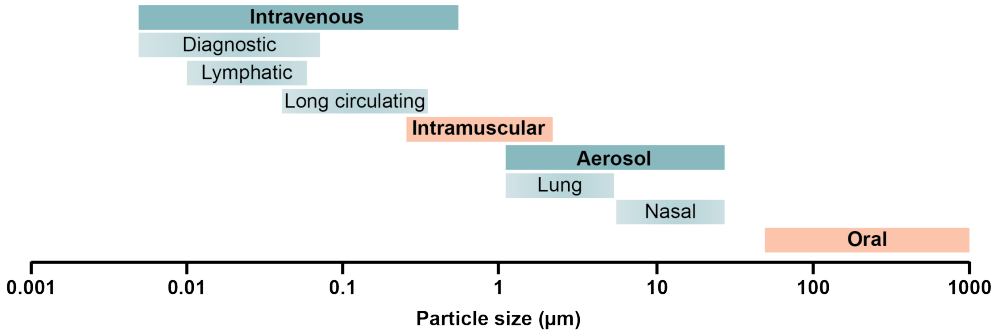


**Figure 5.2. Approximate particle diameters for targeted organ delivery through various administration routes.** Plotted based on information in ref. [19].

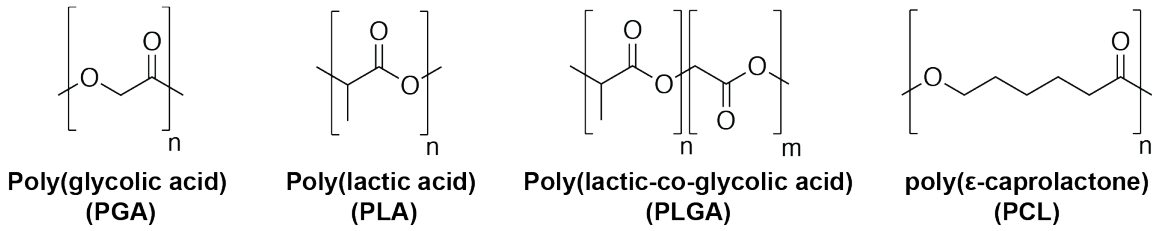


**Figure 5.3. Molecular structures of commonly used biodegradable polyesters:** poly(lactic acid), poly(lactic acid-co-glycolic acid), and poly (ε-caprolactone).

### 5.1.2. Biodegradable polymers for drug delivery

While there are many natural polymer delivery systems, such as protein-based (e.g., collagen) or polysaccharide-based (e.g., chitosan), for this work, the discussion will be limited to biodegradable synthetic polymers. For *in vivo* administration, a critical aspect is biodegradability and biocompatibility of the materials. For polymers, biodegradability means that when broken down to its monomers, the material is non-toxic and can be cleared from the body without side effects. A biocompatible polymer may not necessarily be biodegradable but does not show any negative *in vivo* side effects or inflammatory responses [20].

A very common class of synthetic polymers used in drug delivery are poly(α-esters) that contain an aliphatic ester bond, whose hydrolysis yields polymer degradation, from shorter polymer chains finally yielding $CO_2$ and water. The molecular structures of these polymers are shown in **Figure 5.3** for reference. The first discovered biodegradable polymer for drug delivery applications was poly(glycolic acid) (PGA), a hydrophilic and highly crystalline polymer [21]. However, due to its drawbacks, including relatively rapid hydrolysis into glycolic acid and insolubility in most common solvents, its research use is limited [22].

In lieu, poly(lactic acid) (PLA) is commonly used, as the added methyl group in the backbone makes it more stable and resistant to rapid hydrolysis. Like all poly(α-esters), PLA is degraded through hydrolysis, though here into lactic acid. Moreover, PLA can be easily derived from renewable resources such as corn starch or sugarcane, making it widely accessible. Lactic acid is optically active (i.e., chiral) and can exist as an L or D enantiomer. The fraction of each enantiomer within PLA determines some significant properties for drug delivery purposes. For example, poly (L-lactic acid) (PLLA), containing at least 93% of the L enantiomer, is semi-crystalline, has a higher glass transition temperature ($T_g$), and at equal molecular weight degrades slower than the amorphous poly (D,L-lactic acid) (PDLA) [23]. Therefore, some considerations can be made during the drug delivery system optimization process.

The copolymer of PLA and PGA is poly(lactic-co-glycolic acid) (PLGA), which is often preferred over the homopolymers of its constituents. By using PLGA, a high degree of control can be achieved over the delivery system's properties, particularly by varying the ratio of PLA to PGA

and their molecular weights. The aforementioned parameters can modulate the degradation rate (impacting the drug release kinetics), hydrophobic/hydrophilic balance (which may impact drug loading) and final particle size.

The final commonly used polyester is polycaprolactone (PCL), which is semi-crystalline and has a uniquely low $T_g$ of about -60 °C. This makes the polymer soft at room or body temperature, which does limit its use for drug delivery systems. However, PCL is often synthesized in combination with PLA for example, yielding better mechanical properties, such as a $T_g$ of 170 °C.

In summary, synthetic polyesters have some significant advantages as drug delivery materials. Notably, these include FDA approval and due to their synthetic nature, consistent degradation rates and physicochemical/mechanical properties.

### 5.1.3. Lipids for drug delivery

In addition to polymers, lipids find exceptional utility in drug delivery, particularly for the delivery of nucleic acids. The previously mentioned poly(α-esters) are particularly suited for the delivery of hydrophobic or positively charged molecules, due to their hydrophobic and anionic nature. Hence, their use is limited for applications such as nucleic acid delivery, mostly showing little to no encapsulation. Relevant to this thesis is the production of NPs for the delivery of small interfering RNAs (siRNAs). For this, cationic lipids can be used to fabricate liposomes or lipid nanoparticles

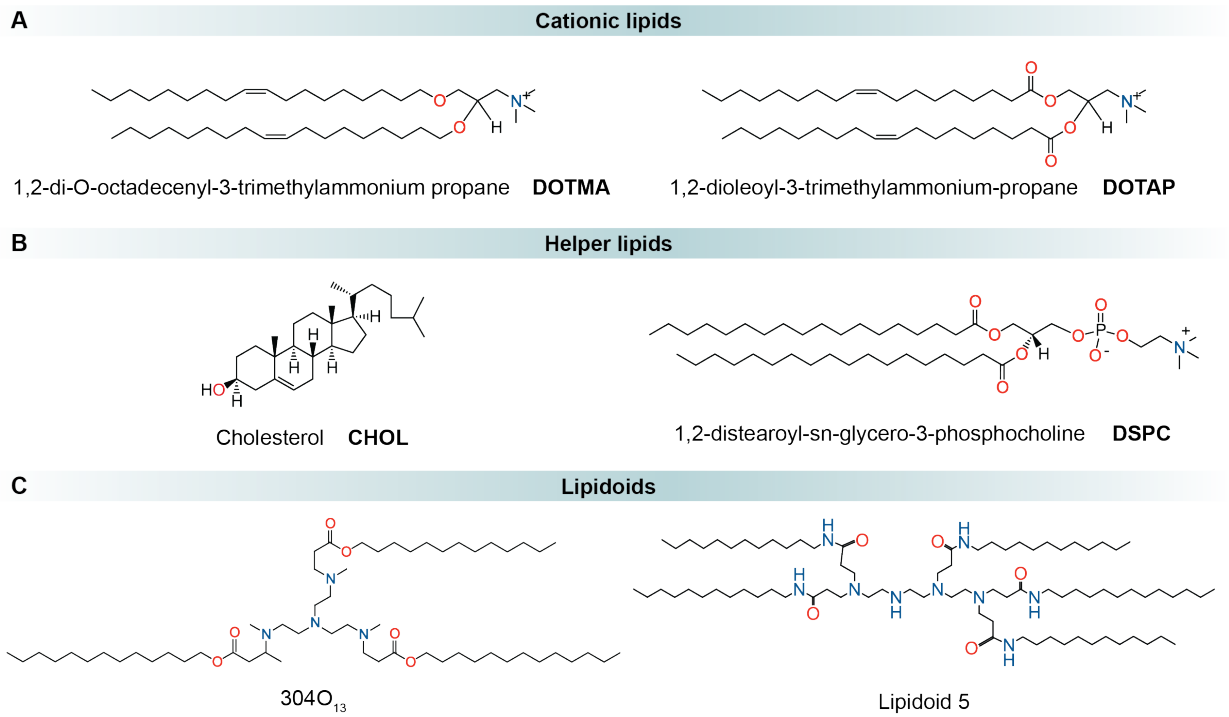


**Figure 5.4. Common commercial lipids and novel lipidoid used for nanoparticle mediated nucleic delivery.** Structure of common **A)** cationic lipids with a permanent positive charge, **B)** helper lipids, and **C)** lipidoids. Lipidoid $304O_{13}$ published in ref. [24] and Lipidoid 5 in ref. [25]. Figure adapted from ref. [26], under CC BY 4.0.

that complex exceptionally well to the negatively charged siRNAs due to electrostatic interactions. A few conventional and commonly used cationic lipids are shown in **Figure 5.4A** and include DOTMA and DOTAP. However, these liposomes often have a highly positive surface charge that yields unwanted interactions with serum proteins and can induce an immune response, both resulting in rapid clearance from the blood [27]. Therefore, to stabilize cationic lipid-based delivery systems, neutral "helper" lipids such as cholesterol or DPSC added (**Figure 5.4B**). The addition of these helper lipids further enhances cellular uptake and aims to reduce some of the negative biological effects and interactions.

A particularly interesting approach to nucleic acid delivery is utilizing both polymers and lipids to mitigate some of the shortcomings of lipid-only delivery systems, especially their biocompatibility. One approach is to decorate the surface of PLGA NPs with conventional cationic lipids, such as DOTAP [28] or a combination of cationic and helper lipids [29]. Here, the PLGA matrix further protects from degradation and provides for the sustained release of the nucleic acids [30]. Such systems are termed lipid-polymer hybrid nanoparticles, or LPNs for short.

Special "lipid-like" molecules (called lipidoids) [31] can further tailor delivery vehicles and increase the efficacy of drug delivery by allowing for the use of custom structural features and functional groups. Screening of lipidoids has been shown to reduce siRNA dose requirements *in vivo* from 1 $mg \cdot kg^{-1}$ to 0.01-0.03 $mg \cdot kg^{-1}$ [32]. For example, features such as more than two amines per molecule can enhance the delivery of siRNA to HeLa cells [31]. Another important feature of lipidoids (as opposed to conventional cationic lipids), is the lower propensity to form micelle-like structures with endogenous anionic lipids that can disrupt cell membranes, often contributing to toxicity. Moreover, without a permanent positive charge (unlike DOTMA and DOTAP), and a lowered pKa, lipidoids are less likely to induce ROS formation both *in vivo* and *in vitro*, resulting in cell apoptosis [33, 34]. Two examples of lipidoids are shown in **Figure 5.4C**; "Lipidoid 5" being a primary component in the formulation used in this thesis.

## 5.2. Bulk and microfluidic fabrication approaches

### 5.2.1. Common fabrication technique: nanoprecipitation

Nanoprecipitation, also known as solvent displacement or interfacial deposition is one of the first approaches developed for loading drugs within polymeric nanoparticles. The first account of nanoprecipitation was published by Fessi *et al.* [35], upon which the method has gained traction as a rapid, efficient and highly reproducible method for nanoparticle production without the use of toxic solvents and without requiring high energy input [36]. The method relies on the rapid mixing of the polymer/drug dissolved in an organic solvent with a non-solvent of the materials (**Figure 5.5**). The two solvents are miscible (e.g., acetone and water), while the solutes (i.e., the polymer/lipid/drug)

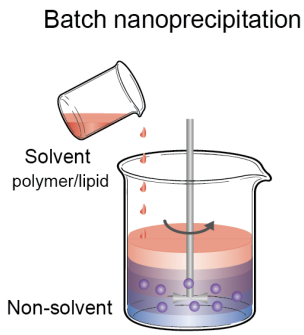


**Figure 5.5. Nanoprecipitation for NP production.** Bulk nanoprecipitation by combining the solvent and anti-solvent under moderate stir speeds.

are freely soluble in the solvent but insoluble in the non-solvent. Commonly for drug delivery purposes, the nonsolvent is water, although surfactants may be used to stabilize the formed particles.

On a molecular level, the process includes three steps, particle nucleation, molecular growth, and aggregation or stabilization, with the rate of each of the steps determining the final particle size distribution (for a theoretical discussion on the mechanism see [37]). As the organic solvent and the aqueous non-solvent mixes through diffusion, the supersaturation of the solutes drives nucleation [38]. Supersaturation occurs when the solution contains more solute than what is capable of being dissolved or a concentration beyond the equilibrium saturation value. Precisely, the mixing between the solvent and the non-solvent decreases the solvent potency to dissolve the solutes, hence placing the system in a supersaturated state. Subsequently, to gain thermodynamic stability, the onset of nucleation occurs [39]. Nucleation stops once the solute concentration is reduced below the critical supersaturation concentration. At this point, the primary nuclei enter the "growth phase," and grow through condensation, that is through the deposition of solute molecules. Additionally, aggregation may occur if sufficient attractive forces are present (such as hydrophobic or Van der Waals interactions). If steric or electrostatic repulsions between the NPs are not sufficient to avoid aggregation, surfactants or other stabilizing molecules may be used to combat the issue and reach a stabilized state.

As opposed to forming an emulsion (see below), nanoprecipitation is a simple one-step preparation method for various NP formation. However, the method shows limitations when the drug and matrix are incompatible for high loading, such when hydrophilic drugs are aimed to be loaded within a hydrophobic matrix. For this, a double-emulsion-solvent-evaporation method is suited.

### 5.2.2. Common fabrication technique: emulsion−solvent evaporation

For the preparation of both micro- and nanoparticles, emulsion−solvent evaporation is one of the most common approaches, though many alternative approaches do exist. Some alternatives for

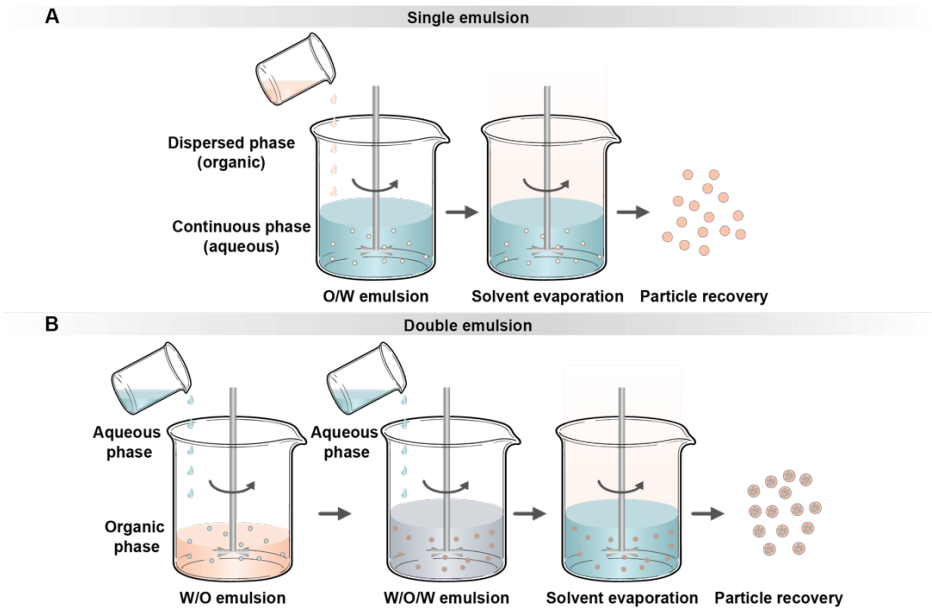


**Figure 5.6. Bulk single and double emulsion micro- nanoparticle fabrication approaches. A)** In a single, two non-miscible liquids, a solute containing organic/dispersed phase and an aqueous continuous phase are stirred or ultrasonicated to yield droplets. Upon solvent evaporation the condensed particles are recovered. **B)** In a double emulsion, first a primary (W/O) single emulsion is formed, by stirring or ultrasonication of an aqueous phase into an oil phase. This phase is then inverted by the addition of larger volume of an aqueous solution, forming a W/O/W solution upon stirring or sonication. Upon solvent evaporation the condensed particles are recovered.

polymeric microparticles include spray drying and phase separation, and for nanoparticles include thin-film hydration (particularly for liposomes). In general, for the emulsion−solvent evaporation method, the polymer/lipid/drug is dissolved in an organic solvent, then solute-rich droplets are generated in an immiscible fluid. After the evaporation of the solvent, the condensed particles can be recovered.

The generation of a single emulsion is rather simple and requires only the mixing of two immiscible phases: a dispersed phase (often an organic solvent such as chloroform or dichloromethane) with a continuous phase (often an aqueous surfactant solution; **Figure 5.6A**). The fundamental methodology to obtain either size regimes is the same; though varying levels of "energy" are placed in the system to yield the appropriate size. More specifically, for micron-sized emulsions, low-energy agitation such as stirring of the two phases is sufficient. However, nanoemulsions require a much greater energy input, which can be achieved by using a probe ultrasonicator. The success of drug encapsulation within the polymer/and or lipid matrix depends largely on the hydrophobicity/hydrophilicity of the drug; although, if applicable special interactions (such as electrostatic interactions) can drastically enhance drug loading. For example, water-insoluble drugs when dissolved with PLA/PLGA can be easily incorporated within the matrix once the solution is added to the water phase. However, for the encapsulation of hydrophilic drugs, an additional emulsification step is required.

Here, using the double-emulsion-solvent-evaporation method, high loading of the hydrophilic drug can be loaded within a hydrophobic matrix (**Figure 5.6B**). The method requires first an emulsion of the hydrophilic drug within a polymer-containing oil phase, generating a primary water-in-oil emulsion (as described before). This emulsion is then either added to a secondary aqueous phase or the secondary aqueous phase is added to it, to form a water-in-oil-in-water emulsion upon agitation or sonication. By using this approach, the drug gets entrapped within the polymeric droplets, often showing high encapsulation efficiencies.

### 5.2.3. Current state-of-the-art approach: microfluidic method

The major challenges in the clinical translation of micro- and nanocarriers are issues with batch to batch consistency and reproducibility, that is, consistently attaining a high drug load and homogeneous size distribution. Current bulk fabrication is performed with sequential steps of the carrier assembly, drug loading, purification, etc. leading to a significant waste of the material, as well as a broad size distribution that negatively impact the release kinetics of the drug [3]. To circumvent the challenges faced in bulk fabrication techniques, recent research has turned towards the microfluidic fabrication of drug nanoparticles. Microfluidics is the interdisciplinary science and engineering of manipulating low volumes of fluids within sub-millimeter channels, often as small as a few tens of microns. On a practical level, the precise control and manipulation of the fluids often occurs within a microfluidic device (microfabricated out of glass or polymers) and may entail miniaturized or fully integrated versions of macroscale technologies (also termed lab-on-a-chip).

Microfluidic emulsion generation was pioneered in the year 2000 [40], and the use of microfluidic mixing for the chemical synthesis of nanoparticles introduced a couple of years later [41]. Since then, the field has opened up for the highly controlled synthesis of organic drug delivery vehicles; either through the formation of emulsion (i.e., droplet) generation or by mixing induced precipitation.

Emulsion generation is often limited to larger (5+ µm) droplets within a microfluidic set-up; as microfluidics often lacks the energy-input required to shear off nanoscale droplets. Albeit, submicron emulsions have been achieved, either through an external energy input (electricity [42]), drastically reduced channel sizes (approaching the range of nanofluidics), or precisely optimized

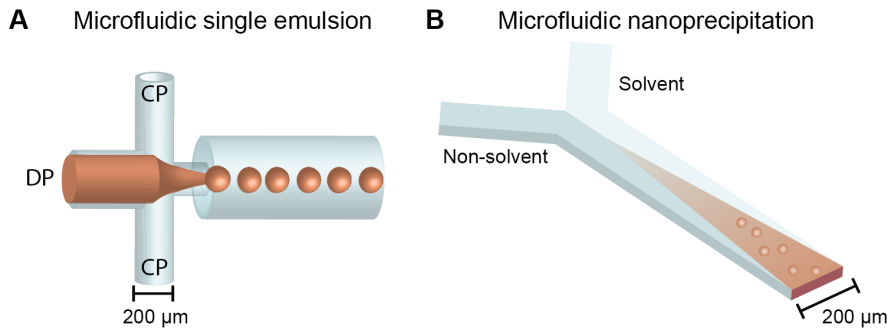


**Figure 5.7. Illustration of microfluidic drug delivery system generators. A)** Flow focusing chip for (micron sized) droplet generation. **B)** Y-junction for nanoparticle synthesis. Scale bars are approximate references of the dimensions.

channel geometries for tip-streaming (discussed below) [43]. In such cases, nevertheless, the emulsion yield is relatively low as each droplet is generated individually as opposed to nanoprecipitation.

Schematic illustrations of two microfluidic drug delivery vehicle generators are shown in **Figure 5.7** and will be discussed in extensive detail further below. **Figure 5.7A** shows a flow-focusing junction for droplet generation, where two immiscible solvents are introduced, meet at a junction and the outer phase shears off uniform droplets of the inner phase. **Figure 5.7B** shows a simple Y-junction that combines two liquids where polymers and lipids precipitate out as NPs when in contact with the non-solvent. These microfluidic devices are often small, smaller than a microscope slide and contain channels on the scale of a human hair to a few human hairs combined. Microfluidics has the potential to produce drug carriers with tunable size characteristics, higher drug encapsulation yield, homogeneous particle production, and the elimination of post-production procedures such as purification, size adjustments. Importantly, microfluidic drug generation is a continuous process, allowing for upscaling and reducing batch to batch variation. For this reason, commercial companies, such as Dolomite Microfluidics and ElveFlow (both primarily focusing on emulsions) or Precision Nanosystems (focusing on nanoprecipitation) are pioneering off-the-shelf devices for drug carrier production.

## 5.3. Basic concepts of microfluidics

The significant decrease in the length scale within microfluidic channels yields unique and often nonintuitive physical phenomena that are not present at the macroscale. In order to fully realize the benefits of microfluidic systems, it is important to understand the unique physics on this scale and how fluid behavior is affected.

### 5.3.1. Fluid flow on a microscale

The flow within a microfluidic channel can be characterized by the dimensionless Reynolds number, $Re$, defined as:

$$Re = \frac{\rho u L}{\eta} \tag{1.}$$

Where $\rho$ is the density of the fluid (kg·m$^{-3}$), $u$ the linear velocity (m·s$^{-1}$), $\eta$ the dynamic shear viscosity (Pa·s) and L (m) the characteristic length scale. The characteristic length scale, also known as the diameter, or hydraulic diameter can be derived for each channel shape. Such that for rectangular channels with side lengths of A and B, relevant to this thesis, L = 2AB/(A+B).

Practically, $Re$ describes the relative strength of inertial forces over the viscous forces. In a microfluidic channel with a small length scale (say 0.1-1 mm) and low fluid flows (0.1-10 mm·s$^{-1}$), $Re$ usually ranges between $10^{-6}$ and 100, though often on the order of 1. This means that the viscous forces dominate. When $Re$ is less than 2300 the fluid flow is considered laminar, while over 2600 it

is considered turbulent. Therefore, one of the most notable features of microfluidics is that fluid flow is always laminar. In laminar flow, the fluid flow lines are parallel and can be thought of as layers sliding along each other. Therefore, mixing between two different fluids occurs through passive molecular diffusion or advection. For both cases, laminar flow reduces the complexity of molecular kinetics and allows for predictable flow behavior of a system.

### 5.3.2. Single-phase flow

Diffusion occurs by the mass transfer of molecules from a region of higher concentration to a lower concentration, which also occurs when a fluid is at rest. The driving force of this process is called Brownian motion, which is the random motion of molecules or suspended particles in a fluid due to collisions with other atoms and molecules, resulting in the mixing of the material. Diffusion can be defined through Fick's law:

$$j = -D\frac{d\varphi}{dx} \tag{2.}$$

Where $\varphi$ is the particle concentration ($kg \cdot m^{-3}$), x is the position of the particle and D is the diffusion coefficient ($m^2 \cdot s^{-1}$). For spherical particles, D can be obtained from the Einstein–Stokes equation:

$$D = \frac{kT}{6\pi\eta R} \tag{3.}$$

where k is Boltzmann's constant, T is the temperature (absolute), R is the radius of the particle (m) and $\eta$ the dynamic shear viscosity (Pa·s) of the solution. Diffusion is nonlinear and the time it takes a species to diffuse scales quadratically with the distance covered. A simple approximation for diffusion time is [44]:

$$t \approx \frac{x^2}{2D} \tag{4.}$$

For a small molecule, the diffusion coefficient is around $10^{-9}$ $m^2 \cdot s^{-1}$ which on the length scale of a microfluidic channel, means that diffusion is significantly faster with the reduced distances. This feature of microfluidics is particularly important, as mixing and reaction times can be quite fast. However often times even shorter mixing times are required. To do this, passive microfluidic mixers are often implemented that can (a) yield parallel lamination to reduce the diffusion distance, or (b) enhancing chaotic advection using special channel geometries. Microfluidic mixers are discussed more in-depth in **Section 5.5.2**; however, in terms of dimensionless numbers they can often be characterized based on the *Re* numbers (discussed previously) or Peclét number, *Pe*, defined as:

$$Pe = \frac{uL}{D} \tag{5.}$$

where u is the velocity of the fluid ($m \cdot s^{-1}$), L is the characteristic length scale (m), D is the diffusion coefficient ($m^2 \cdot s^{-1}$). Pe defines the relative importance of advection (high *Pe*) and diffusion (low *Pe*) in the mass transport associated with the mixing. Advection refers to the mass transfer of a substance due to the bulk motion of the fluid typically in the direction of the fluid flow, (as opposed to diffusion

which occurs at rest). Unlike the *Re* number, there is no characteristic magnitude of *Pe* number in a given microfluidic system. Given channel sizes and flow rates, *Pe* can be anywhere from $10^{-2}$ to 100 or more; therefore, the calculation of *Pe* can be advantageous to define the relative strength of advection to diffusion in the system. Often, however, with the small-length scales in microfluidics, *Pe* number is small, making the kinetics of the system more predictable due to the dominance of diffusion.

### 5.3.3. Two-phase flow – dimensionless numbers

Reynolds and Peclét number are particularly relevant for systems with a single fluid or miscible fluids; however, for non-miscible interfacial flows (relevant to emulsions and droplets), these numbers are rarely used.

At the interface of two immiscible liquids the most important force at play is the interfacial tension (surface energy) which determines the behavior of the interface. There are three dimensionless numbers pertaining to the interfacial tension: the capillary number (*Ca*), Weber number (*We*) and Bond number (*Bo*). However, the most important number to define such systems is the capillary number that takes the relative importance between viscous and interfacial stresses. The *Ca* number is defined by:

$$Ca = \frac{\eta u}{\gamma} \tag{6.}$$

where $\eta$ is the dynamic viscosity (Pa·s), $u$ is the flow rate (m/s), and $\gamma$ is the interfacial tension in (N/m). Depending on the interaction between the viscous and interfacial forces, the multiphase flow can be parallel streams of the two fluids, slugs of one fluid occupying the whole channel, or suspended droplets [45]. As will be evident in the coming sections, the capillary number is critical for defining droplet generation regimes in various microfluidic devices.

The ratio between the inertial and interfacial tension forces is the Weber number, *We*. It can be important for the prediction of the disruption of an interface. *We* is defined by:

$$We = \frac{pu^2 L}{\gamma} \tag{7.}$$

where $p$ the density of the fluid ($kg \cdot m^{-3}$), $u$ is the linear velocity ($m \cdot s^{-1}$), L (m) is the characteristic length scale, and $\gamma$ is the interfacial tension in ($N \cdot m^{-1}$). Due to the low fluid velocities, the Weber number effect in the liquid-liquid system is minimal and can often be ignored. However, the high flow velocities may become important, such as the case of a jet formation [46].

Finally, pertaining to interfacial tension, is the Bond number, *Bo*; although it is seldom used when describing droplet generation systems. This compares the importance of gravitational force (buoyancy) to the interfacial tension, and since most microfluidic droplet generators are horizontal, the effect of the *Bo* number is insignificant and can be ignored.

The critical dimensionless numbers are summarized in **Table 5.1** for reference. The following sections reference these parameters both for mixing and droplet microfluidics.

Table 5.1. Common dimensionless numbers used to describe single and two-phase flow microfluidic systems.

| Symbol | Name | Formula | Physical Meaning |
|---|---|---|---|
| *Re* | Reynolds number | $Re = \frac{\rho u L}{\eta}$ | Inertial force/viscous force |
| *Pe* | Peclet number | $Pe = \frac{uL}{D}$ | Advection/diffusion |
| *Ca* | Capillary number | $Ca = \frac{\eta u}{\gamma}$ | Viscous force/interfacial tension |
| *We* | Weber number | $We = \frac{pu^2 L}{\gamma}$ | Inertial force/interfacial tension |
| *Bo* | Bond number | $Bo = \frac{\Delta p g L^2}{\gamma}$ | Buoyancy/interfacial tension |

## 5.4. Microfluidics for Microsphere Production

Droplet microfluidics manipulates two immiscible fluids in a microfluidic channel to produce a highly controlled and monodisperse emulsion. It has applications stretched from high throughput reaction vessels, to drug delivery vehicle synthesis. Microfluidics is a particularly suited approach for droplet generation as it offers precise control via the prototyping of device geometries and manipulation of the shear stresses exerted on the system to tailor the droplets for the application needs.

### 5.4.1. Droplet generation approaches

Fundamentally, droplet generation involves three steps: two immiscible liquids (continuous phase, CP, and dispersed phase, DP) meet at a junction, where the interface deforms, and droplet breakup occurs. With the confined channel boundaries created in a microfluidic set-up, various channel geometries have been implemented to produce droplets (**Figure 5.8**). The most frequently employed geometries include co-flow, cross flow and flow focusing.

Co-flow is one of the earliest droplet generation approaches, with initially relying on two coaxially aligned capillaries in 3D space to shear off droplet, depicted in **Figure 5.8A** [40]. However, the principle can be translated into 2D channel a microfluidic device for consistency and ease of fabrication through standard soft lithography [47]. Generally, the droplets produced via co-flow are rather large, often larger than the dispersed phase channel diameter, though characterized by high uniformity and monodispersity. Droplet size can be reduced if the system can withstand higher continuous phase flow rates (and associated backpressures). Particularly, jetting [46] and even tip-streaming [48] have been achieved using coaxially aligned capillaries, yielding far smaller droplets, even in the few micron ranges.

A cross-flow geometry is most often implemented as the perpendicular joining of two channels (called a T-junction), where droplets shear-off at the junction (**Figure 5.8B**). Though, other angles (θ) below or beyond 90° would adhere to the method. It is important to note that the variation of

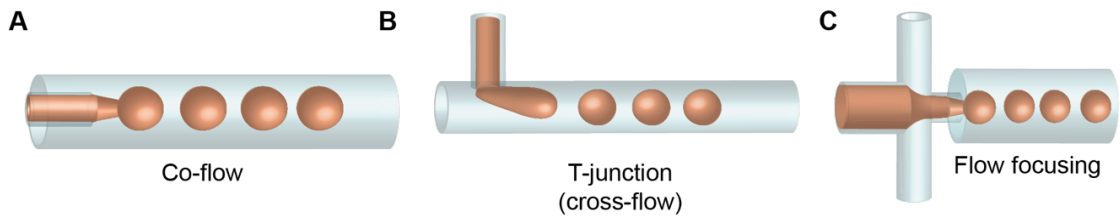


**Figure 5.8. Illustration of droplet generation with different approaches: A)** co-flow **B)** cross flow via a T-junction, and **C)** flow-focusing geometries.

the angle can influence droplet size at a given *Ca* number [49]. The T-junction was first implemented by Thorsen *et al.* in 2001 to produce monodisperse water droplets within an oil continuous phase [50]. Since its introduction, the method gained traction for its simplicity of fabrication through standard soft lithography approaches for monodisperse droplet formation. Due to the simplicity of the system, a 'special feature' of T-junctions is the ease of upscaling by the parallelization of the inlets. In one example, the authors used 128 cross-junction units to produce 0.3 $kg \cdot h^{-1}$ acrylic microspheres with a CV of 1.3%, highlighting the utility of the T-junction approach [51].

Flow-focusing devices are often used for the production of small droplets. Here, the dispersed phase is hydrodynamically focused by the continuous phase (hence the name of the device), where the elongated fluids are passed through a constriction, termed the "orifice" (**Figure 5.8C**). Flow-focusing was first introduced utilizing glass capillaries [52, 53], termed 3D axisymmetric flow-focusing devices. While the axisymmetric devices offer the advantage of the continuous phase fully enclosing the dispersed phase, and avoid wetting problems [54], due to fabrication difficulties their use is limited. The wide-spread utility of flow focusing came about after the introduction of 2D, soft-lithography-based devices by Anna *et al.* 2003 [55].

### 5.4.2. General considerations, solutions and flow rates

As mentioned in the previous section, when dealing with two immiscible liquids in a microfluidic channel, *Ca* is the most important parameter to predict droplet break-off. Above a system dependent (due to unique geometries and solutions) critical capillary number ($Ca_{\mathrm{CRIT}}$), droplet break off occurs.

Additionally, the capillary number is predictive of the droplet size, such that the droplet size inversely proportional with $Ca_{\mathrm{CP}}$. Practically, when producing droplets under constant fluids, *Ca* is influenced by *u*, that is the implemented flow rates. Therefore, the higher the continuous phase flow rate, the smaller the resulting droplets are. This can be illustrated with the following equation [56, 57]:

$$D(T) \propto Ca^{-1} = \left(\frac{\eta_{CP}(T)u_{CP}}{\gamma_{CP}(T)}\right)^{-1} = \left(\frac{\gamma_{CP}(T)}{\eta_{CP}(T)u_{CP}}\right) \quad (8.)$$

where T is the temperature (K), D is droplet diameter, η is the dynamic viscosity (mPa·s), $u_{CP}$ is the flow rate (m/s), and γ is the interfacial tension in (N/m). Here it is important to consider that

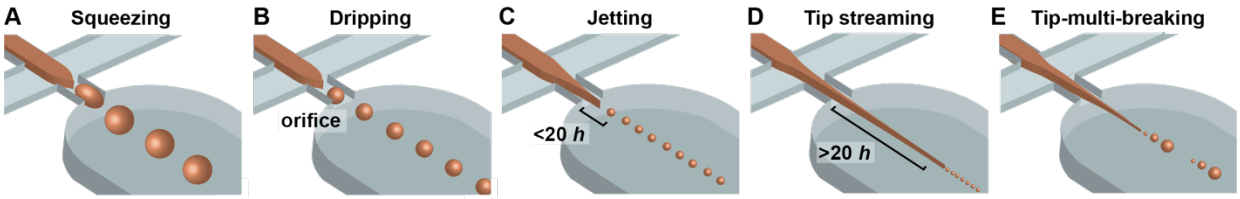


**Figure 5.9. Illustration of droplet generation modes in a 2D flow focusing device.** The regimes include **A)** squeezing, where the dispersed phase fully blocks the junction and is geometry controlled; **B)** dripping, that yields particles smaller than the orifice and is $Ca_{CP}$ controlled; **C)** Jetting; where the droplets break up from an elongated thread due to Rayleigh-Plateau instability; **D)** Tip-streaming; often characterized by a very long and thin thread, from which highly uniform sub-micron to few micron sized droplets shear-off in a Taylor-cone-like configuration; **E)** Tip-multi-breaking, in which droplets with sequentially smaller diameters break off in a geometric pattern.

in addition to the CP flow rate, both viscosity and interfacial tension can become critical. Particularly if temperature changes occur, both the viscosity and the surface tension decrease with increasing temperatures; although at variable rates. Based on the inverse relationship between $Ca_{\mathrm{CP}}$ and droplet size, increasing the viscosity of the CP yields smaller droplets at a given flow rate. This can be explained by a relative increase in the shear force exerted on the DP over the interfacial force [58].

Besides $Ca_{\mathrm{CP}}$, the ratio between the two capillary numbers $Ca_{\mathrm{CP}}/Ca_{\mathrm{DP}}$ is inversely proportional to droplet size. This implies that the larger $Ca_{\mathrm{DP}}$, the larger the particles; therefore increasing the flow rate of the dispersed phase, or increasing its viscosity yields larger droplets. For poly(α-esters) droplets (i.e., PLA or PLGA) in a water phase (O/W emulsion), the polymer solution is a viscoelastic fluid. Here, higher viscosity of the polymer solution can be varied by the polymer concentration and its molecular weight to modulate droplet size. As a side note, the elasticity of the solution may produce elongated filaments at the tailing end of the droplet, resulting in the formation of secondary droplets called satellites. The number and polydispersity of the satellites were found to be dependent on the viscosity ratio between the dispersed and continuous phases [59].

### 5.4.3. Droplet generation regimes

Broadly, there are five droplet generation regimes: squeezing [60], dripping [40], jetting [61], tip-streaming [62], and tip-multi-breaking [63], illustrated in **Figure 5.9.** The first three have been observed in all of the previously discussed droplet generation devices; however, the last two have not been reported in cross-flow T-junctions yet [64]. In general, the droplets formed in squeezing are the largest (larger than the dispersed phase channel diameter) but highly monodisperse. Dripping results in smaller particles, smaller than the DP channel and also highly monodisperse. Jetting is quite polydisperse, though the droplets can be quite small. Tip-streaming results in very small particles, often in the few microns, or even sub-micron range; and tip-multi-breaking results in a polydisperse sample, though the droplets are sequentially smaller during formation. Transitioning between the different modes is achieved by changing the dispersed or continuous phase capillary numbers (albeit,

in the same system the linear velocity would be the only variable changed). By calculating the capillary numbers of each fluid, regime estimations can be made by comparing the *Ca* values to the phase diagram shown in **Figure 5.10**.

Squeezing mode occurs at very low continuous phase capillary numbers ($Ca_{CP} < 0.002$ for T-junctions [65], or $Ca_{CP} < 0.1$ in flow-focusing devices [63]). For all three droplet generation devices, the dispersed phase fluid completely obstructs the junction and halts the continuous phase fluid flow. The obstruction yields pressure build-up in the continuous phase fluid, and when the pressure is larger than the pressure inside the dispersed phase, the droplet is deformed and "squeezed" until break-off. This break-off regime is geometry controlled, as the resulting droplet is confined by the channel walls. In the flow focusing example in **Figure 5.9A**, the droplet is fully constrained by the orifice, yielding an oblong plug initially, rather than a spherical droplet. Due to the low capillary number, the flow rate of the continuous phase does not affect droplet size given the flow rate is higher than that of the dispersed phase. Hence, in this regime, the size of the droplets formed is primarily controlled by the geometry of the channels and the viscosity ratio (λ) of the fluids rather than their flow rate ratio (φ) [66, 67].

When the *Ca* of the continuous phase is increased ($0.1 < Ca_{CP} < 0.3$), the droplet generation regime is transformed from squeezing to dripping [68] (**Figure 5.9B**), where viscous forces that deform the interface overcome the interfacial tension effects that stabilize the droplet from breaking up. Unlike in squeezing, in the dripping regime the emerging droplet no longer blocks the junction/orifice (that yields the alternating pressure build-up and release cycle); therefore, the droplet diameter is controlled by $Ca_{CP}$, such that increasing $Ca_{CP}$ yields smaller particles. Practically, increasing the CP flow rate or increasing the viscosity of the continuous phase yields smaller particles. Here, the droplet diameter is smaller than the channel diameter and is flow rate dependent. In order to predict the droplet size, solving a 3rd order polynomial is required for T-junctions [40] and a 4th order polynomial

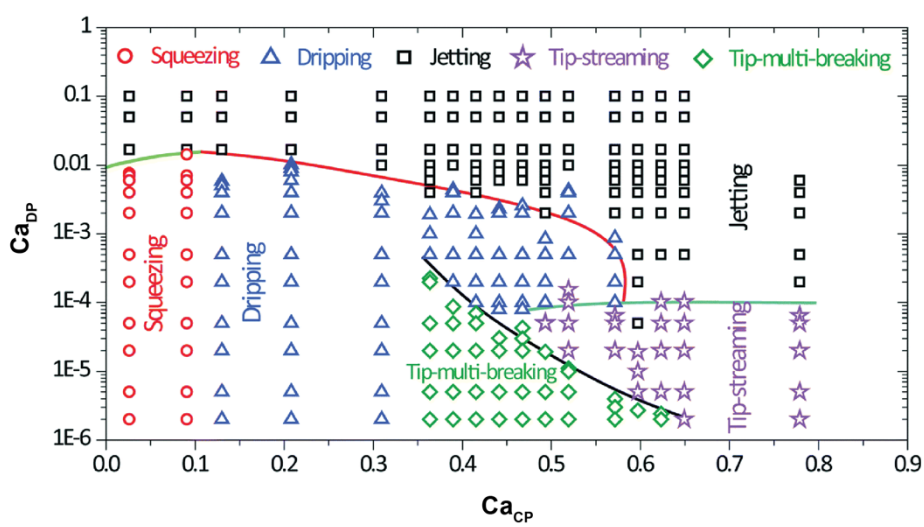


**Figure 5.10. Phase diagram of DP and CP capillary numbers and resulting droplet generation modes.** Data observed in a microcapillary flow-focusing device. Figure reprinted with permissions from ref. [63] Copyright 2015, Springer Nature.

for flow-focusing devices [69]; however, both essentially compare the ratio between the shear stress and surface tension forces (which are analytically determined) to the systems capillary number. Instead of theoretical calculations, droplet size can be experimentally measured at various flow rates and plotted against $Ca_{CP}$ for a better understanding.

Further increasing the capillary number (either $Ca_{DP}$ or $Ca_{CP}$), dripping to jetting transition occurs as shown in **Figure 5.9C**. Here, an extended liquid thread of the dispersed phase appears that breaks into droplets of a broad size distribution due to the Rayleigh-Plateau instability. The extended liquid thread will exhibit perturbations at the interface with unequal pressures depending on the radius of the thread (**Figure 5.11**). Using the Young Laplace equation, we can derive that the pressure is the ratio of the surface tension and radius ($p = \gamma / r$); therefore, the pressure will be higher at the smaller radius regions, resulting in droplet break-off. In terms of dimensionless numbers, jetting can be defined by $Ca_{CP} + We_{DP} \geq 1$ [46]. In a flow-focusing device, jetting can be defined in a couple of ways based on the length of the thread. Either as three or more times longer than the width of the orifice [66]; or shorter than $20h$, the characteristic length scale [70], beyond which another generation mode (tip-streaming) would be appropriate.

Tip-streaming is a particularly interesting generation mode; it has been observed only in co-flow and flow-focusing devices (**Figure 5.9D**). Tip-streaming is a promising approach to forming small droplets (can be smaller than $1/20^{th}$ of the orifice in a flow-focusing geometry) and potentially sub-micron emulsions without employing nanofluidic channels [43]. It was first observed in a planar flow-focusing geometry at very high flow rate ratios (flow rate ratio ($\varphi$) $> 1/300$) and at high surfactant concentrations, where the surfactant concentration is greater than 0.5 of the critical micelle concentration (CMC) [62]. Tip streaming can be characterized by a Taylor cone-like tip that is caused by the accumulation of surfactants near the tip of the structure under the strong shear stress, dropping the local surface tension to near zero. Because of this, surfactant concentration was deemed to be critical until simulation works showed the possibility of surfactant-free tip streaming in a similar Taylor cone-like fashion [71]. Under proper conditions, a long, thin thread can be drawn from the tip of the Taylor cone which then breaks up into droplets less than a few micrometers in diameter [71-73]. Stable tip-streaming is highly geometry dependent; such that iterative geometry prototyping is necessary to achieve stable flow [43, 73]. Other dimensionless number considerations include a low Re number, $Re << 1$ such that creeping flow conditions are in place [74]; though as seen later in

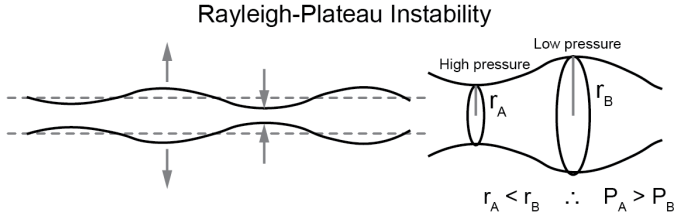


**Figure 5.11. Basic schematic of Rayleigh-plateau instability in jetting.** Left: the liquid thread exhibits perturbations at the interface with unequal pressures in the direction of the convex side. Right: Smaller radii exhibit higher pressure, while larger radii lower pressure, resulting in droplet break-off.

**Section 6.3.2** or **Appendix II**, low $Re$ may not be required. **Figure 5.10** depicts the $Ca$ number considerations in a flow-focusing geometry, such as the $Ca_{\mathrm{CRIT}}$ for the CP is between 0.5 - 0.7, with three to four orders of magnitude smaller $Ca_{\mathrm{DP}}$. However, recent findings show that the viscosity ratio (λ) is a more important determinant of the $Ca_{\mathrm{CRIT}}$, than the flow rate ratio (φ) in tip streaming [48]. Below the observed λ-dependent $Ca_{\mathrm{CRIT}}$ shows unstable threads and polydisperse droplets.

The final droplet generation mode applicable to co-flow and flow-focusing devices is tip-multi-breaking, shown in **Figure 9E**. The generated droplet population is polydisperse, though the sizes of the droplet clusters obey a regular distribution with a common factor for the diameter reduction [63, 75]. $Ca_{\mathrm{CRIT}}$ is shown in the phase diagram as $Ca_{\mathrm{CP}}$ is between 0.35 to 0.63. The polydisperse nature of the droplets is often not applicable for pharmaceuticals, hence this regime is not discussed further.

### 5.4.4. Practical considerations for microfluidic device

With the high surface area to volume ratio in microfluidics, the surface properties need to be closely controlled. For droplet formation, the continuous phase has to preferentially wet the surface, while dispersed phase wetting should be disfavored [76]. This means for an oil-in-water emulsion hydrophilic contact angles, while for a water-in-oil emulsion hydrophobic contact angles are required. For glass and silicon-based chips treatments such as salinization and siliconization can be used to produce hydrophobic surfaces [77, 78], or oxygen plasma can offer a transient hydrophilic surface for the inherently hydrophobic PDMS (and other hydrophobic polymers) [79, 80].

The mechanical properties of the device material can be important for achieving monodispersity. For example, the deformability of PDMS has been shown to adversely affect the efficiency of droplet generation and yields to worse size distributions [81]. The authors found that the deformation-induced changes in the cross-sectional geometry of the channel were the main reason for the increased polydispersity. Along with this note, oscillations in the fluid flow rate primarily caused by the stepper motor in syringe pumps can negatively affect size distributions as well; hence pressure driven pumps are recommended.

A final consideration for the material is its compatibility with the chosen organic solvents or oils used for droplet generation. Most polymeric materials have limited compatibility with harsh solvents, so milder solvent alternatives might be an option. For example, dimethyl carbonate has been used instead of chlorinated solvents for the production of PLGA microspheres in a PDMS microfluidic chip [82].

## 5.5. Microfluidics for Nanoparticle Production

Nanoprecipitation, as discussed previously in **Section 5.2.1**, relies on solvent displacement through rapid mixing to precipitate out the dissolved solutes and form NPs. Performing nanoprecipitation

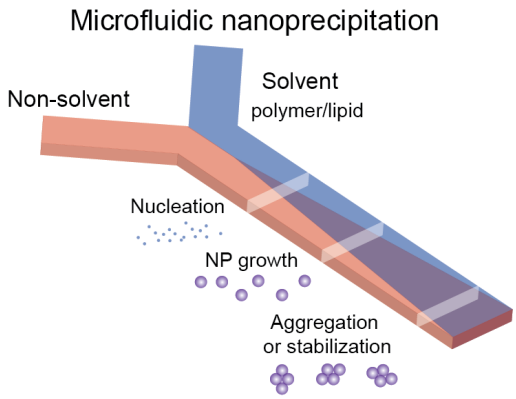


**Figure 5.12. Nanoprecipitation.** Microfluidic nanoprecipitation in a straight channel facilitated by diffusion.

within a microfluidic channel allows for exquisite control of the solvent/solute interaction. A schematic illustration of nanoprecipitation in a simple straight channel is shown in **Figure 5.12**. Here the non-solvent and solute containing solvent phase combine, and through diffusion yield the steps of nanoprecipitation, namely nucleation, growth, and stabilization. The initial concept was first shown in 2008 by the hydrodynamic focusing of PLGA-b-PEG in acetonitrile and water [83], since then a range of microfluidic mixing devices have been implemented in order to provide for a homogenous environment for NP growth. While the mixing rate is critical (with passive mixers discussed later), other formulation parameters particularly relevant to the final nanoparticle size are discussed in this section.

### 5.5.1. Influence of the operating conditions

In order to obtain the desired sized nanoparticles through nanoprecipitation, several parameters should be carefully considered. For this section, the studies referred to generally focus on polymeric nanoparticles; as nanoprecipitation is most well studies in these systems. The most important parameters concerning the particle size are summarized in **Table 5.2**.

It is well understood that the concentration of the dissolved solutes in the solvent phase modulates size by varying the diffusion rate and modulating the diffusion coefficient through the changing viscosity of the solution (applicable to polymers). Consequently, increasing the solute concentration yields higher viscosities and more material to diffuse, which in turn increases the diffusion coefficient and lowers the diffusion rate yielding larger particle sizes. The diffusion rate (Fick's law) and diffusion coefficient (from the Einstein–Stokes equation) was introduced previously in **Section 5.3.2**.

A particularly interesting parameter is the polymer molecular weight. Most studies show that increasing the molecular weight yields larger particles, due to increasing the viscosity of the solution [84-86], for example, in a microfluidic set-up, the obtained sizes of PLGA particles are 25–60 nm for $PLGA_{45K}$ and 50–100 nm for $PLGA_{95K}$. However, in PCL particles the opposite was found; increasing

the molecular weight yielding smaller particles [87]. The authors postulate that the higher molecular weight polymer has a lower solubility in the acetone/water system, hence yielding more rapid precipitation and smaller sizes. Interestingly, polymer molecular weight may influence more than just the size. For example, it was shown that the molecular weight influences particle yield, such that each system may have an "optimum" molecular weight for maximal output [88].

The choice of solvent is critical to consider for particle size modulation, the solubility of the polymer (and or lipid/drug), and even drug loading efficiency. In an aqueous system, increasing the solvent polarity index yields faster diffusion, faster mixing, and consequently smaller NP sizes. On this end, two or more component solvent mixtures may be used to modulate particle size, such by the addition of a highly polar (or apolar) solvent depending on the desired size range. To note, **Figure 6.15A** in the **Results and Discussion** investigates solvent polarity and particle size for the LPN system. A similar investigation for other hybrid systems is shown in ref. [89]. A highly comprehensive study on a large range of solvent for PLGA NP formation was carried out in ref [90], particularly with the aim of loading hydrophilic proteins within the hydrophobic matrix. Here, in addition to the authors showing the effect of polarity on particle size (e.g., the addition of acetone to tetrahydrofuran (THF) yields smaller particles than THF alone); the authors increase protein loading within PLGA by replacing the aqueous non-solvent to alcohols. Similarly, here and also in ref. [91] Dimethyl sulfoxide (DMSO) is shown to be advantageous to load hydrophilic drugs through nanoprecipitation. Overall, it is critical to investigate and determine the most optimum solvent choice for the system as it may influence the solubility of the materials (important for loading considerations) as well as the final size of the NPs through diffusion variation.

Another consideration for size is the ratio of the solvent phase to the organic phase. As before, the ratio influences diffusion time, which is by varying the concentration gradient considered for diffusion. As the volume of the aqueous phase is increased (or the volume of the solvent phase is reduced), the diffusion time for the two phases reduces, yielding smaller NPs.

The final parameter for size modulation is the mixing rate, which in bulk nanoprecipitation is simply varied by changing the magnetic stirring speed and modulating shear mixing, effectively increasing diffusion [92]. In a microfluidic channel, the mixing rate can be efficiently modulated by adding in a mixing element below the junction of the two inlet channels.

**Table 5.2. Influence on operating parameters on NP size.** Table modified from [93]

| Parameter | Increase particle size | Decrease particle size |
|---|---|---|
| Polymer concentration | Increase [polymer] | Decrease [polymer] |
| Polymer molecular weight | Increase polymer MW | Decrease polymer MW |
| Solvent polarity | Decrease polarity (e.g., tetrahydrofuran) | Increase polarity (e.g., alcohols, acetone) |
| Solvent to water phase ratio | Decrease water phase volume | Increase water phase volume |
| Mixing rate | Reduce mixing rate | Increase mixing rate |

### 5.5.2. Microfluidic mixing

On a large scale (i.e., macroscale), mixing occurs by the generation of turbulent fluid flow at high Reynolds numbers ($Re$>2300) or by stirring and creating chaotic advection in the system. As mentioned earlier, with small channel diameters in a microfluidic system, turbulent flow cannot occur; therefore, mixing is facilitated through diffusion. However, countless microscale mixing approaches have been developed to generate rapid mixing, broadly either being passive or active mixers. Passive mixers generally rely on two principles: (a) multi-lamination of the mixing fluids in order to increase the contact area for diffusion or (b) chaotic advection effects, which are complex fluid trajectories (often appearing as turbulent), though highly controlled at laminar flow [94]. Importantly, passive mixers only rely on channel geometry designs creating these effects with mixing times being between 5 – 500 ms. Active mixers, on the other hand, utilize an external energy source to fix fluids, such as acoustic waves, magnetism, electrokinetics, and electrohydrodynamics (see reviews [94, 95]). While active mixers are highly efficient (and particularly efficient at low $Re$ numbers), the fabrication complexities often make their utility limited for most microfabrication laboratories. Therefore, the following section will focus on the utility of passive mixers in the context of nanoparticle production within a microfluidic channel.

The first example of a passive mixer is the butterfly mixer shown in **Figure 5.13A**. It has the element of splitting flows, creating multi-lamination and increasing the fluid contact area for increased diffusion. Additionally, it includes the butterfly-shaped elements that contain abrupt flow path shifts which yield vortex formation (i.e., chaotic advection) to effectively mix the solutions. Similar to the butterfly mixer, it is the standard and well-known Tesla mixer (**Figure 5.13B**), that relies on both splitting the flows and the coanda effect [96]. In the coanda effect fluids tend to stay attached to the curved channel walls. For the Tesla mixer, this means one half of the liquid stream is diverted back into the other stream such that the two fluids collide. In addition, at high $Re$ numbers, the shape of the channel may yield secondary flow vortices, further enhancing mixing. Tesla mixers have been used for lipid-polymer NP production, see ref. [97].

The staggered herringbone mixer (**Figure 5.13C**) is by far the most well-known mixer, originally published by Whiteside's group in 2002 [98]. Since then various iterations of the geometry have been used. It is a 3D mixer, such that the channels have multiple depths, which does increase the complexity of fabrication. Here, the main fluid channel has lowered microgrooves (at various shapes and angles depending on the iteration) but ultimately yields chaotic advection for 5-10 ms mixing time at low Re numbers [99, 100]. It has been used for lipid nanoparticle formation in refs. [101, 102], and the company Precision Nanosystems has based its microfluidic chip products on the design.

Convergence-divergence structures (with constrictions and expansions) cause the formation of expansion vortices that disturb the laminar streamline while increasing the contact area between the

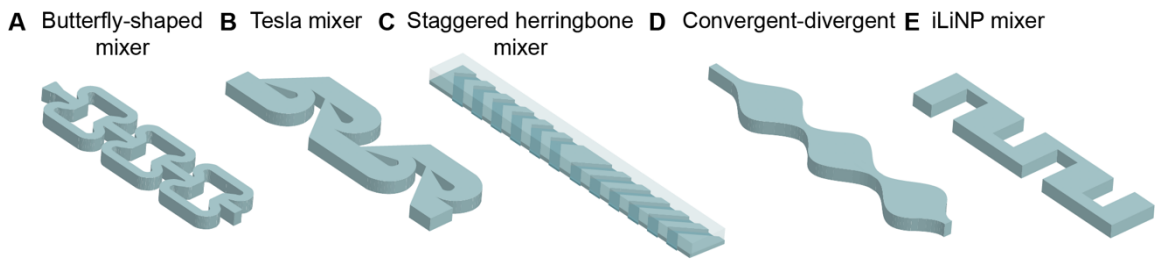


**Figure 5.13. Passive mixers used for nanoparticle fabrication.** Example passive mixers include **A)** the butterfly design, **B)** the Tesla mixer **C)** staggered herringbone **D)** a convergent-divergent sinusoidal mixer, and **E)** iLiNP device.

two fluids [95]. Two examples are shown in **Figure 5.13D, E**, of a sinusoidal wave design [103] and the iLiNP device [104], though various iterations of the principles are available.

Finally, it should be noted that obstacles can represent a way of mixing at high $Re$ >50 flow rates. Obstacles can be presented as pillars, such that vortices tend to form after the obstacle (creating flow recirculation). Similarly, sharp corners, elevation, edges, etc. can all yield secondary flow formation at high $Re$ numbers.

## 5.6. Microfluidic Materials

For each of the aforementioned applications, as well as for countless others, the choice of the microfluidic chip material becomes critical for device success and efficiency. Moreover, the material choice may limit the fabrication approaches, or allow for unique feature integration. The following sections focus on various commonly used device materials with a particular emphasis placed on a unique class of plastics, thiol-enes.

### 5.6.1. Microfluidic materials – a brief introduction

The first account of microfluidic devices fabricated using micromachining technologies originates in the 1970s, with groundbreaking work done developing a gas chromatography (GC) analyzer on a silicon wafer [105], (**Figure 5.14**). The on-chip GC was manufactured through a series of photolithography and etching steps, a process still relevant today. Much of the work done in the nascent stages of microfluidics was conducted on silicon, then due to the relatively lower cost and optical clarity, the early 1990s saw the use of glass devices with innovative work showing an integrated capillary electrophoresis chip [106]. Similar to silicon, glass fabrication was conducted with a series of masking and etching steps.

In addition to silicon and glass, poly(methyl methacrylate) (PMMA) and polystyrene (PS) were among the first materials to be utilized for microfluidics; albeit, polymers only gained popularity following the introduction of the elastomeric material poly(dimethylsiloxane) (PDMS). George

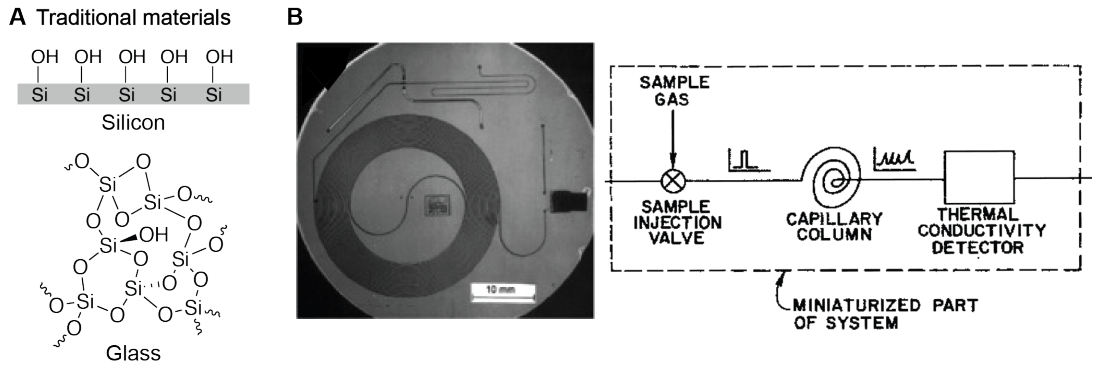


**Figure 5.14. Traditional microfluidic materials. A)** Molecular structure of glass and silicon. **B)** Photograph and device illustration of the GC system described by Terry *et al.* Reprinted with permissions, from [105]. Copyright © 1979, IEEE.

Whitesides and his group at Harvard pioneered the concept of replica molding PDMS [107, 108], by pouring the liquid PDMS monomers over structured silicon wafers and curing the polymer to be used as microfluidic devices. Hot embossing for PMMA structuring was also introduced in the 1990s [109], though a silicon master mold was still utilized for this purpose.

The development of the photosensitive resin, SU-8, by IBM allowed for high aspect ratio channel designs otherwise not achievable using masking and etching steps [110]. SU-8 was used directly as a microfluidic device [111] or used as a mold for PDMS fabrication [112]. Combined, PDMS and SU-8 set in motion the polymer revolution of microfluidics. Currently, there is a myriad of approaches to fabricate polymeric chips, with innovations in materials and fabrication continuously occurring. For example, to produce PMMA devices, techniques such as hot embossing, solvent imprinting, injection molding, and $CO_2$ laser ablation all can be used [113]. With the advent of 3D printing, high resolution, commercial 3D printers are available for the sole purpose of microfluidic device fabrication. One such printer is the "Fluidic Factory 3D Printer" (Dolomite Microfluidics) that utilizes cyclic olefin copolymer (COC) filaments, showing good transparency, biocompatibility and solvent compatibility.

### 5.6.2. Polymers for microfluidic devices

As polymers remain the most widespread material for microfluidic chip fabrication, the following section attempts to briefly summarize some of the properties of relevant polymers. Broadly there are two classes of polymers: thermoplastics and thermosets (including elastomers). Each class of these materials offer unique properties, such as fabrication approaches, mechanical hardness, and solvent compatibility. **Table 5.3** offers a summary of such parameters.

Thermoplastics are not crosslinked, instead, they are made up of linear or branched chains, and can be reshaped after being cured (**Figure 5.15A**). Thermoplastics rapidly soften at their transition temperature ($T_g$), which allows for repeated molding by reheating the material. Thermoplastics can be fully disordered (amorphous) or show local order (semi-crystalline).

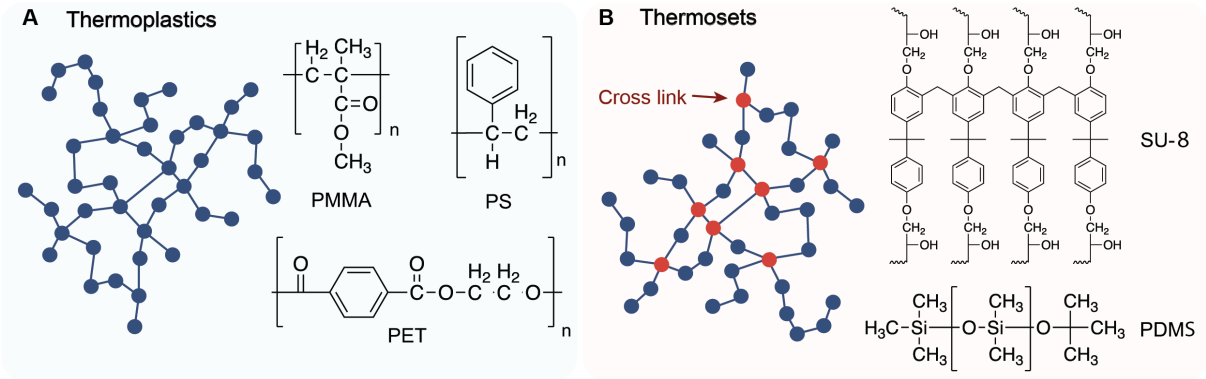


**Figure 5.15. Two broad categories of polymers: thermoplastics and thermosets. A)** Illustration of a thermoplastic structure and example polymers. **B)** Illustration of a thermoset structure (note crosslinking in red) and example polymers.

Amorphous thermoplastics are hard and often brittle below their $T_g$; while at higher temperatures the thermal energy allows for the chains to move, yielding a soft/rubbery material. Amorphous polymers tend to have higher free volume, as opposed to semi-crystalline ones, which does make them more susceptible to solvents. Semi-crystalline thermoplastics have two transition temperatures, a $T_g$ for the amorphous and a $T_m$ for the crystalline regions. Due to the crystalline regions, the free volume of these polymers is lower, allowing for lower water adsorption and better solvent compatibility than a completely amorphous polymer. Common thermoplastics for microchips include PMMA, polycarbonate (PC), polystyrene (PS), and polyethylene terephthalate (PET). These materials show good mechanical strength (high Young's modulus), relatively low water-absorption, and moderate solvent resistivity [114]. For solvent compatibility, alcohols are generally well tolerated, though incompatible with most other organic solvents such as ketones and hydrocarbons [115]. Moreover, with the low oxygen permeability (see **Table 5.3**), prolonged cell studies may be problematic.

Thermosets, when heated or radiated, crosslink to yield a polymer network that cannot be softened and reshaped like thermoplastics (**Figure 5.15B**). Like thermoplastics, thermosets do have a glass transition temperature, at which the material softens, although the crosslinking stays in place. Therefore, reshaping the material is not possible. A special class of thermosets are elastomers, such as PDMS, consisting of lightly crosslinked polymer chains that stretch and compress upon external forces, then return to their original shape when the force is withdrawn. Thermosets show better thermal stability than thermoplastics, show better resistance to solvents (with the exception of elastomers), and are optically transparent.

Commonalties between most widely used polymers are (a) a hydrophobic surface (b) few or no functional groups readily available for modification and (c) often poor solvent compatibility (as opposed to inert materials like glass and silicon). To create functional groups, which is important for both wettability modifications and various molecule attachments (such as for bioassays), a couple of classical approaches can be implemented. Such may be ozone oxidation and oxygen plasma treatment, in order to generate several polar groups (e.g., hydroxyl groups, esters, ketones, and carboxylic acids)

that can be further modified for attachment and simultaneously increases the surface energies (yields hydrophilicity) [116]. For PDMS, these methods are quite transient lasting hours to a few days at most. Plasma/ozone oxidation for PDMS and many other polymers can be particularly problematic, as orders of magnitude increase in background fluorescence can occur, limiting their use for assay development [117]. Another approach is to use highly reactive intermediates, such as free radicals, carbenes, and nitrenes to gain functional groups [118]. For certain polymers, direct covalent modification of the side chain is feasible. As for PMMA, the methyl-ester groups can be reacted with amine groups, yielding amide linkage. However, this process is conducted under highly basic conditions which may not be suitable for all applications and materials [119]. As an overarching theme, there is a clear unmet need for a material whose surface is easily modifiable without the transient nature of the classical approaches, or the often-harsh chemical conditions of covalent modifications.

**Table 5.3. Properties of various microfluidic device materials.** Table adapted from [115]

| Property | Silicon/glass | Elastomer | Thermoset | Thermoplastics |
|---|---|---|---|---|
| Young's modulus (GPa) | 130-180/50-90 | ~0.0005 | 2.0-2.7 | 1.4-4.1 |
| Microfabrication | photolithography | casting | casting, photopolymerization | thermo-molding |
| Smallest channel dimension | <100 nm | <1 µm | <100 nm | ~100 nm |
| Multilayer channels | hard | easy | easy | easy |
| Thermostability | very high | medium | high | medium |
| Solvent compatibility | very high | low | high | moderate |
| Hydrophobicity | hydrophilic | hydrophobic | hydrophobic | hydrophobic |
| Oxygen permeability (barrer[a]) | <0.01 | ~500 | 0.03-1 | 0.05-5 |
| Optical transparency | no/high | high | high | medium to high |

[a]barrer = $3.35 \times 10^{-16}$ (mol · m)/($m^2$ · s · Pa)

### 5.6.3. Thiol-ene polymers

A niche and rather underrepresented material for microfluidic device fabrication are thiol-enes (TEs). Thiol-enes are a large family of thermoset photopolymers that contain two monomers: one with *thiol* groups and a second with allyl (or *ene*) groups. UV-induced radical polymerization of the monomers yields a highly crosslinked material. As a near-perfect "click-reaction," monomer conversion is almost 100% and proceeds very rapidly within seconds. For a TE reaction, high-intensity UV light (or a photoinitiator) causes cleavage of the sulfur-hydrogen bond, yielding a thiyl radicals that can react with any non-sterically hindered allyl groups, more specifically the terminal α-carbon. The reaction between the thiyl radical and the alkene yields a thioether (carbon-sulfur-carbon bond), with the radical being transferred onto the neighboring β-carbon. The intermediate β-carbon radical abstracts

a hydrogen from another thiol, which repeats the cycle in the process of polymerization. While any non-sterically hindered allyl groups can be used, electron-rich monomers result in faster reactions.

### *Monomers and fabrication*

This TE reaction can be implemented using a large variety of monomers in order to prepare TE polymers (a summary of applicable monomers found in ref. [122]). The exact choice of monomers greatly affects the polymer material properties; hence, the focus will remain on the monomers relevant for this work, TATAO and PETMP, shown in **Figure 5.16A**. These liquid monomers can be used to manufacture microscale features using well-established methods such as replica molding or injection molding using PDMS (or other UV-transparent) molds. To produce the PDMS molds, very common approaches of SU-8 based photolithography or micromachining (**Figure 5.16B**) are often implemented. In this work, CNC-milling of PMMA plates is implemented, where the channels are milled to create a positive "master mold" (**Figure 5.16B**, step 1). PDMS is then cast to make a negative mold (step 2), into which the thiol-ene is then replica molded (step 3) and UV cured (step 4) to assemble the final microfluidic device. Assembling the microfluidic device using two halves (channel side and lid) is straightforward. This is mainly due to oxygen inhibition of the radical reaction near the surface of the mold, resulting in a thin, semi-cured monomer layer, allowing for a strong bond between the two chip halves [122, 123]. The simple and highly robust device assembly is rather unique as for many materials complicated techniques are needed, which may yield relatively weak bonding interfaces. For example, bonding glass halves is rather difficult, solvents may be used to bond PMMA halves, or oxygen plasma treatment is used to bond PDMS to glass.

For most applications, using polymers with the highest degree of crosslinking (and hence the highest monomer conversion rates) is desirable to yield a robust material and avoid any potential monomer leeching. To achieve maximal conversion, the number of thiol and ene functional groups should be equal (stoichiometric), for the monomers here, it would require 4 mol TATATO to 3 mol

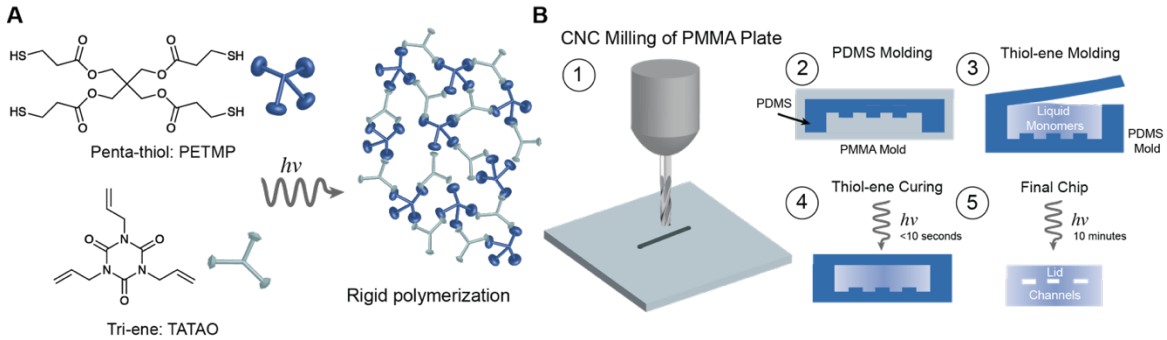


**Figure 5.16. TATAO and PETMP polymerization. A)** Schematic illustration of PETMP and TATAO polymerization. Figure adapted from [120] under CC BY 3.0. **B)** Workflow of thiol-ene chip fabrication. Includes the milling of a master PMMA mold and production of a subsequent PDMS mold, in which the liquid thiol-ene monomers are replica molded and cured. Figure adapted from [121], with permissions. Copyright ©, 2013 IOP Publishing Ltd.

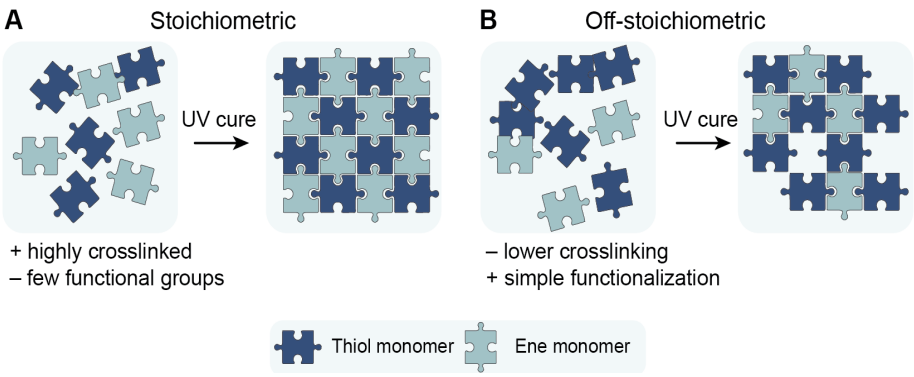


**Figure 5.17. The concept of stoichiometric and off-stoichiometric systems.** Illustration shows both the mixture of monomers before polymerization and the highly simplified final polymer structure.

PETMP (**Figure 5.17A**). However, by adding one of the components in excess, the resulting off-stoichiometric thiol-ene (OSTE) can yield interesting material properties and functionalities [124]. Since in the TE reaction equal amounts of thiols and enes are consumed, any excess functional groups remain in the bulk and surface of the material (**Figure 5.17B**). The remaining functional groups result in a lower degree of crosslinking, which does modify the key properties of the material. Such include the mechanical stiffness, such as that the Youngs modulus can vary from 250 to 1740 MPa, and $T_g$ from 35 to 68 °C [124], or as shown in **Section 6.1**, the solvent compatibility of the material. However, the important aspect of OSTE materials is the ability to easily modify the surface of the polymer using the rapid and mild "click" reaction, which as discussed earlier, can be quite cumbersome for most materials. For TEs, a range of "click-based" surface modifiers are discussed in the next section and experimental data is presented in **Section 6.2**, to highlight the versatility of the material.

As a side note, though not applicable to the work in this thesis, three-component thiol-ene systems (called ternary materials) can offer further unique properties. The third monomer, most commonly an epoxy monomer, can yield a two-step curing reaction for both the thiol-ene and thiol-epoxy [125-132]. Having two steps gives rise to a flexible intermediate material that is easier to bond and has unreacted monomers for surface functionalization. For example, after the first thiol-epoxy cure, the partially cured device can be stored for months, which for a commercialized device can allow for the consumer to custom functionalize the material before the final cure [133].

### *Material properties*

As mentioned previously, a large number of monomers can be used to prepare TE polymers, which can tailor the material properties for virtually all applications. The mechanical properties of TEs can resemble PDMS with a low Youngs modulus and glass transition temperature, yielding an elastomer appropriate for pneumatic valve integrations [120, 124]. For this purpose, a study varied the number of thiol functional groups (di-, tri-, or tetra-thiol) in combination with a di-"ene" monomer to produce elastomeric materials with 1-10 MPa moduli [134]. In addition to varying the monomer composition,

varying the stoichiometric ratio of the monomers yields elastic moduli between 0.1-800 MPa, such that greater thiol monomers result in lower moduli and decreased $T_g$ values [120]. Mostly because thiol monomers in particular often have a high degree of bond rotation, yielding a more flexible material in excess. On the other hand, a stoichiometric ratio of the monomers TATAO and PETMP yields glassy polymers with high glass transition temperatures and Youngs moduli [128, 129, 135, 136]. A hard polymer is particularly useful for high-pressure applications or for the case of droplet microfluidics; as mentioned previously, flexibility in the device material can facilitate polydisperse emulsions [81].

For solvent compatibility, thiol-enes fair significantly better than most commonly used polymers such as PDMS, PMMA, and COCs. However, as before, the monomer composition and the stoichiometry used greatly effects the solvent compatibility of the material [120]. Generally, due to the correlation between $T_g$ and the void volume of the material, more elastic polymers have an increased susceptibility to solvents. Similarly, as storage/Youngs moduli correlate well with the degree of crosslinking, the expected solvent resistance can be gauged from these two parameters. This thesis focuses on great detail of the solvent compatibility of TATAO and PETMP, with an in-depth comparison of TEs with other polymers is shown in **Appendix III, Table 4** [137]. Briefly, thiol-enes can withstand all pharmaceutically relevant organic solvents, except for chloroform and dichloromethane, two solvents particularly relevant for PLA/PLGA microsphere production. Potentially only PTFE (e.g., Teflon) shows such a high degree of solvent compatibility, though lacks optical clarity and the possibility of replica molding (instead requires hot embossing). Therefore, thiol-enes may be a better material for many solvent-based applications. An approach to modify a variety of thiol-ene compositions is to add a filler material, such as carbon nanotubes into the pre-polymer mixture. For the commercial TE, NOA-83H, carbon nanotubes reduce toluene-induced swelling from 18.3% to 1.6% [138]. Though important to keep in mind that the resulting material lacks optical clarity and changes the mechanical properties of the material as well.

A final important consideration for material selection is the water contact angle (WCA), as wetting becomes a critical concern with the high surface-area-to-volume ratio in microfluidics. TEs are mildly hydrophilic with water contact angles between 55-80° depending upon the choice of monomers and stoichiometric ratios [80, 139-143]. Compared to PDMS (which has a WCA of around 120°), aqueous fluid flow occurs rather easily without high resistance stemming from the hydrophobicity. For certain applications, such as droplet microfluidics, or bioassays, OSTE materials with free functional groups can be used to easily photograft various surface modulating molecules. While traditional oxygen plasma treatment is a valid approach [80, 139, 144], a covalent "click" attachment is more desirable for a more permanent modification. Some modifiers include PEG derivates (WCA 35-52° [120, 124]), acrylic acid (WCA 43° [120]) and allyl malonic acid (WCA 25° [145]) for a hydrophilic surface. Similarly, fluorinated acrylates (WCA 102°-140° [120, 140, 146]) and PDMS derivates (WCA 77-97° [124]) have been used for hydrophobic surface. For example, selectively masking off device regions during the photographing of the modifiers can yield both a

hydrophilic and hydrophobic device. Such an approach is particularly useful for producing double-emulsion droplets on a TE chip [147].

In summary, thiol-enes show high promise as an optimal material for pharmaceutical applications. TEs are easy to fabricate, allow for rapid prototyping, are optically clear for visual assessment of the application and can be mechanically glassy/hard to withstand potential high pressures. Some shortcomings of the material include the lack of chlorinated solvent compatibility, a must-solve for PLA/PLGA microsphere production. Additionally, the native wetting property of the material is inadequate for oil in water emulsion; though, the ability to photo-graft molecules shows high promise.

# 6. Results and Discussion

The results presented here are based on two published papers and one manuscript in preparation. Additional unpublished data are presented in this section to further aid the discussion, as well as in the appendices for each of the papers. The core of the project is illustrated in **Figure 6.1**, and can be divided into three main parts:

(1) Microfluidic polymer modification in order to comply the material for pharmaceutical applications. This includes (a) rendering the material solvent resistant and (b) gaining hydrophilic wetting properties.

(2) Application of the improved thiol-ene materials for micro- and nanoparticle production.

The presented results not only open avenues for a myriad of microfluidic applications requiring a robust chip material but also are of relevance for Pharmaceutical Sciences where the utility of microfluidics is still in its nascent stages.

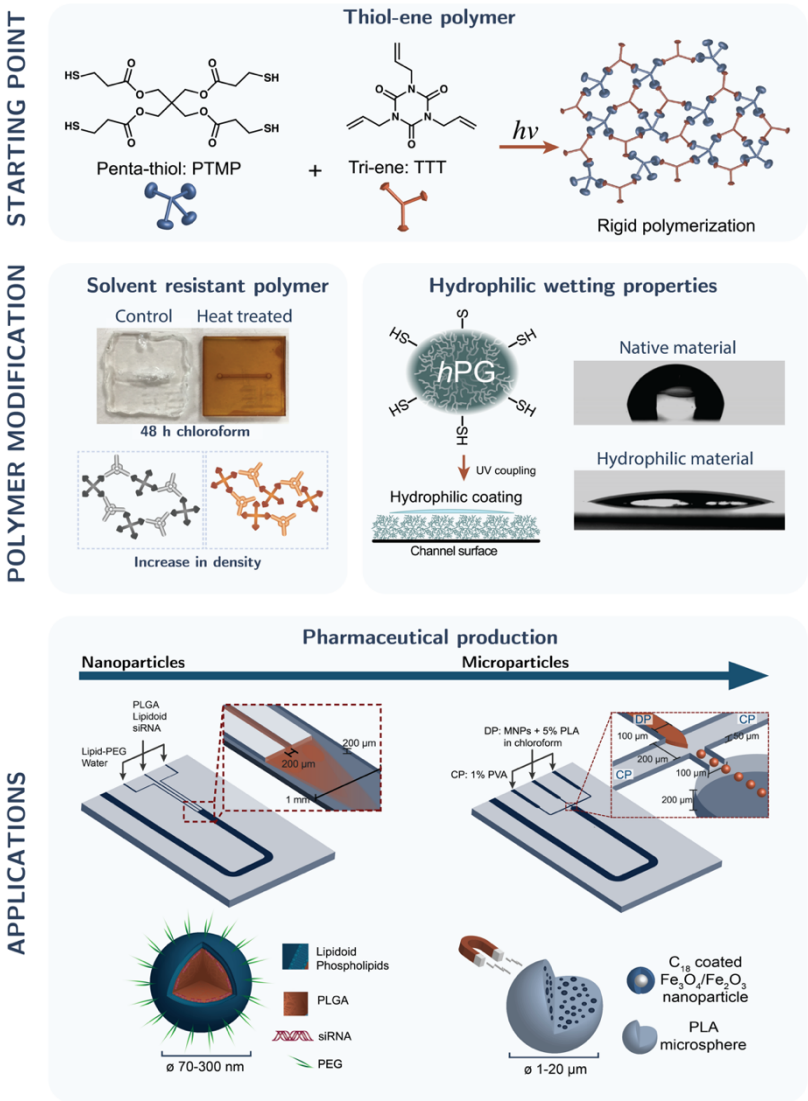


Figure 6.1. Overall summary of research results

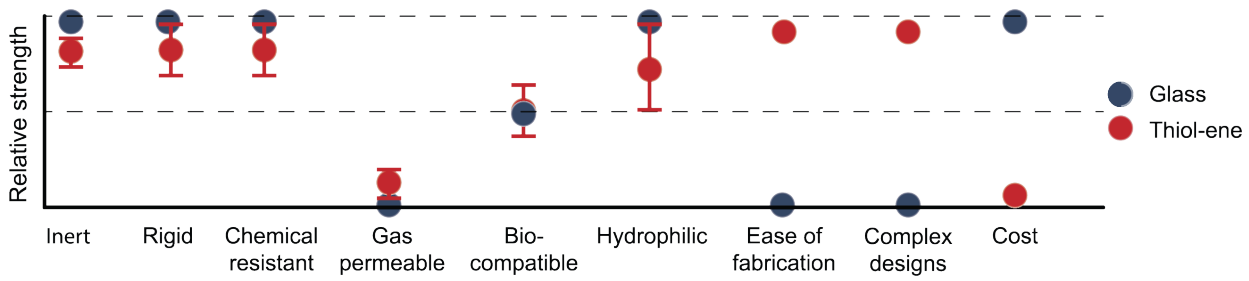


**Figure 6.2.** Qualitative assessment of glass, polymer and thiol-ene microfluidic materials with respect to physico-chemical properties and fabrication possibilities.

Harsh solvents are used in many laboratory-based applications, particularly in pharmaceutical research and development, such as for the production of drug carriers, solvent-based extraction, or purifications and separation. Miniaturization of such processes generally relies on glass microfluidic chips due to the inherent inert properties of glass. The following two sections focus on the material improvements made to thiol-enes and aim to make the case that thiol-enes are a viable alternative material for glass microfluidic chips. As illustrated in **Figure 6.2,** thiol-enes can be on par with glass in terms of being as inert, rigid, chemically resistant, hydrophilic and biocompatible. However, thiol-enes are orders of magnitude easier to fabricate and create complex designs, all-while maintaining a cost-effective price point.

Thiol-enes, like most polymers, show significant deformation to solvents, in particular to chloroform. To assess swelling in response to solvent exposure, microfluidic chips with a single 500 µm wide and 200 µm deep channel were fabricated, through which the solvent of choice was pumped across at 10 µL/min flow rate. As the bulk material swells in response to solvent exposure, the channel narrows which can be monitored using a microscope. The channel width decreases in percent (for simplicity, we will refer to this as "% swelling") can be defined by the following equation:

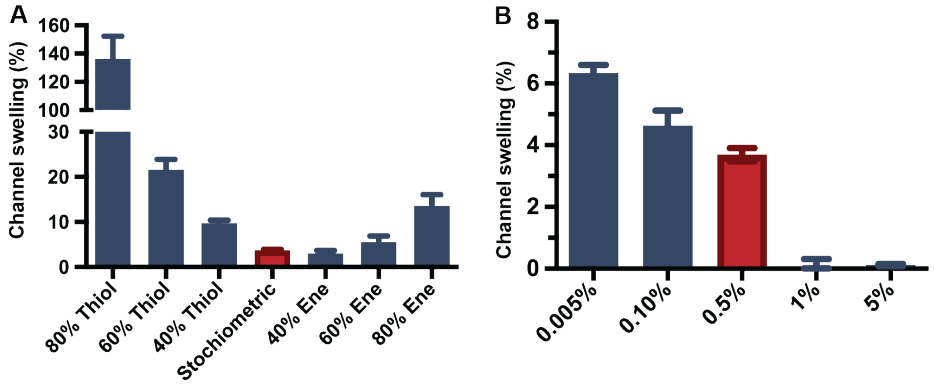


**Figure 6.3. Bulk material composition plays a critical role in chloroform resistance properties. A)** Varying ratio of thiol and ene monomers with 0.5% TPO-L were exposed to 1-h chloroform after 10 min UV exposure at 90 mW/cm$^2$. **B)** Stoichiometric thiol-ene with indicated TPO-L concentrations exposed to chloroform for 1-h after 10 min UV exposure at 90 mW/cm$^2$. All samples conducted in triplicates with the error bars representing the standard deviation.

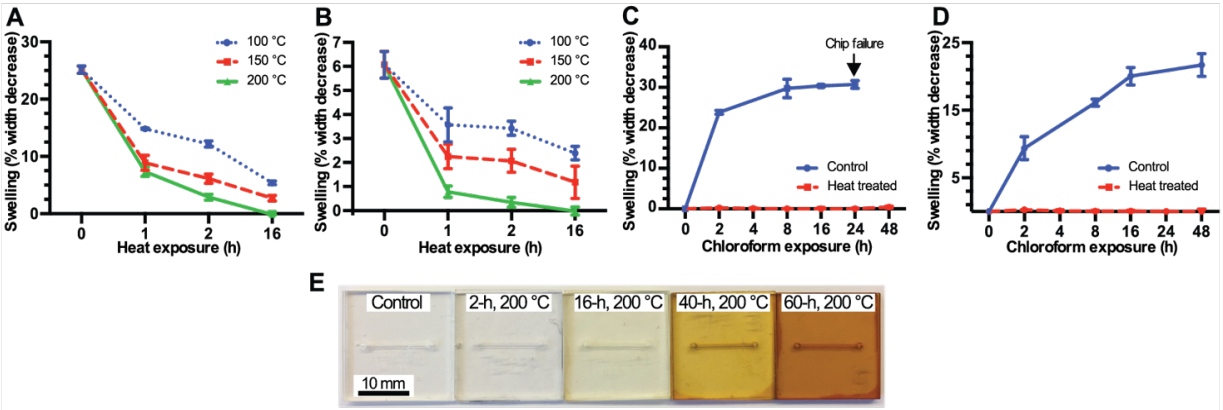


**Figure 6.4. Effect of heat exposure on solvent resistance. A)** 100 °C (blue), 150 °C (red) or 200 °C (green) heat applied to TE chips for 1 to 16 h, as indicated. Chloroform was pumped through the channels at 10 μL min$^{-1}$ for 1 h width decrease measured. **B)** Same as **A)**, but 0.5% TPO-L added to the material. **C)** 200 °C heat applied to TE chips for 60 h (red) or left at RT (blue). Chloroform was pumped through the channels at 10 μL min$^{-1}$ for up to 48 h, with channel width measurements taken at the indicated time points. **D)** Same as **C),** but 0.5% TPO-L added to bulk material. All data points are in triplicates. Error bars represent standard deviation. **E)** Image of thiol-ene chips, control and 200 °C heat treated for the indicated time points.

$$\% \text{ width decrease} = [(\text{initial width} - \text{final width})/\text{initial width}] \cdot 100$$

The level of materials deformation varies greatly with the molar ratios of the monomers (**Figure 6.3A**) such that increasing the "thiol" monomer results in worse performance with solvent compatibility. It has been postulated that this is due to the lower cross-linking density that results from the limiting number of functional groups [148]; moreover, the thiol-monomer has longer side chains as opposed to the more rigid allyl monomer, where the polymer's increasing void volume could contribute to solvent uptake and interaction. Similarly, crosslinking density is affected by the concentration of photoinitiator added to the matrix. In **Figure 6.3B** it is evident that increasing the photoinitiator creates a more robust polymer; however, it is important to note that photoinitiator leaching is of great concern for pharmaceutical and analytical applications due to its toxic nature. For this reason, minimizing its use is common, and even at higher concentrations, long-term solvent compatibility is limited with swelling onset occurring in a few hours. For these reasons, the following sections primarily focus on stoichiometric thiol-ene with 0.5% TPO-L photoinitiator (shown in red in **Figure 6.3**). This is the most commonly used material composition in the field.

In order to mitigate swelling, initially, various surface coatings were investigated, including silicon-based sol-gel coatings[149] and fluorinated coatings such as Teflon AF$^{TM}$ [150] (example results are shown in **Section 9.1**). Surface coatings tend to be non-uniform, can present pinhole defects or cracking, and are often less stable; hence, consistent solvent compatibility was not achieved. Therefore, a modification was conducted on the bulk material to circumvent these problems.

Bulk modification of the polymer using heat exposure is shown in **Figure 6.4.** The influence of temperature and length of exposure is shown in **Figure 6.4A** and **6.4B**, where photoinitiator-free or 0.5% TPO-L containing materials were investigated respectively, in response to 1-hour chloroform

exposure. Both materials show a rapid, temperature and time-dependent response to heat treatment, such that higher temperatures or longer heat exposure times reduce chloroform-induced swelling of the material. Solvent resistance emerges rapidly after just 1 hour of heat exposure with both materials showing virtually no chloroform induced swelling after 16 hours at 200 °C.

Next, instead of short-term heat and chloroform exposure, the chips were heat-treated for 60-hours at 200 °C and exposed to chloroform for 48-hours. Shown in **Figure 6.4C** and **6.4D**, both photoinitiator-free and 0.5% TPO-L containing materials withstood chloroform for the entire test period. This is particularly significant, as the untreated photoinitiator-free material swells to the point of syringe pump failure within 24-h; however, after heat treatment, no detectable swelling is seen (**Figure 6.4C**). Therefore, the addition of the toxic photoinitiator is irrelevant and can be circumvented for most applications. Interestingly, heat treatment yields a characteristic color change, which may affect UV visibility in certain applications, although optical visibility is maintained for most applications (**Figure 6.4E**).

Heat treatment was further tested for various solvents previously reported to be the most damaging to thiol-ene materials [6, 10, 151]. The solvents tetrahydrofuran (THF), dimethylformamide (DMF), acetone (ACE), acetonitrile (ACN) and chloroform (CF) were selected and the material exposed for 96-hours as shown in **Figure 6.5**. Here, for simplicity, the entire microfluidic chip was submerged in the solvent and channel swelling assessed as described previously. All samples contained 0.5% TPO-L for both the control and heat-treated materials. Shown in **Figure 6.5**, heat treatment significantly increases solvent resistance for the solvents tested. THF, DMF, and ACE (**Figures 6.5A-C**) yield a similar degree of swelling in the untreated chips (blue), between 6-12% over the course of 96 hours. Heat treatment (red) significantly reduces swelling, showing little to no solvent-induced deformation, or about 0-1.5%. Acetonitrile, on the other hand, is significantly more damaging for both control and heat-treated samples; albeit heat-treatment significantly improved solvent compatibility (**Figures 6.5D**). Nonetheless, acetonitrile remains damaging and for some applications, this may be beyond acceptable deformation ranges. Lastly, chloroform remains as the most damaging solvent for thiol-enes, resulting in chip failure for the control samples between

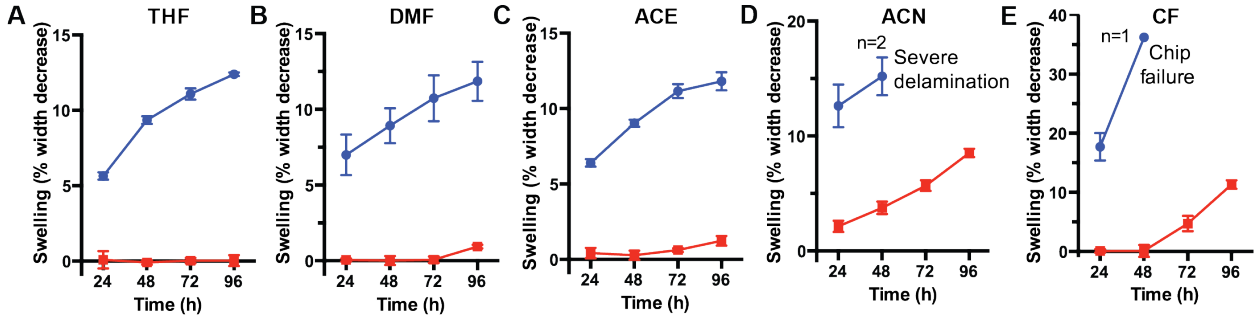


**Figure 6.5. Universal applicability of heat treatment for a range of organic solvents.** TE chips with 0.5% TPO-L photoinitiator were exposed to either **A)** tetrahydrofuran, **B)** dimethylformamide, **C)** acetone, **D)** acetonitrile, **E)** chloroform. Graphs show untreated control (blue) or heat-treated chips at 200 °C for 60 h (red). Samples run in triplicates with channel widths measured every 24 h. Error bars represent standard deviation.

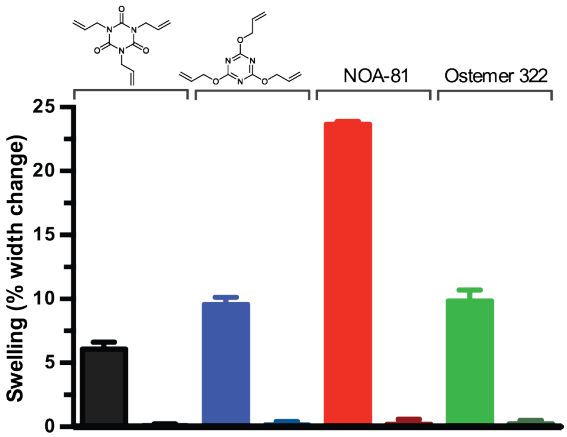


**Figure 6.6. Chloroform compatibility of various thiol-ene formulations**. Left bars are control, RT, materials, right bars are heat treated for 40-h 200 °C. Following formulations were tested: Control TE: TATAO with PETMP (black); triallyloxy-triazine with PETMP (blue); NOA-81 adhesive (red); Ostemer 322 thiol-ene-epoxy (green). The in-house monomers are stoichiometric with regards to the functional groups and contain 0.5% TPO-L photoinitiator. All samples were run in triplicates, error bars represent standard deviation.

24-48 hours (**Figure 6.5E**). As shown previously in **Figure 6.4D**, heat treatment completely prevents material deformation for at least 48 hours. However, solvent resistance begins to wear off by 72 hours, at which point some swelling occurs; still, the channels remained functional for the entire test period of 96 hours. In perspective, the level of swelling of the heat-treated material at 96-hours is equivalent to the swelling at 2-hours for the untreated material; hence, heat treatment results in a 50-fold increase in solvent compatibility. Overall, heat treatment with its easy implementation shows excellent utility for various applications requiring a range of organic solvents.

As thiol-enes are a very diverse class of polymers, heat treatment was investigated for various monomer compositions in order to probe the universal applicability of the method (**Figure 6.6**). Here, the in-house mixed allyl monomers triallyl-triazine-trione (TATAO, control, black), triallyloxy-triazine (blue), and two commercial formulations, NOA-81 (red) and Ostemer 322 (green) were investigated in response to 1-hour chloroform exposure. All untreated materials show significant swelling, with NOA-81 showing the largest degree of deformation. After subjecting the materials to 40-hours of 200 °C heat treatment, all formulations show negligible chloroform induced swelling, between 0-0.2%. Therefore, the results show that heat treatment applies to many different monomer compositions which may open up avenues towards combining novel monomer properties and functionalities with solvent compatibility for a range of microfluidic applications.

Naturally, with such a dramatic increase in solvent compatibility through a simple-to-implement method, significant effort was placed into deconvoluting the underlying mechanism of the method. For brevity, the details of the investigations are shown in the published paper on this subject in **Appendix I** and will be largely omitted from this section. Currently, the working hypothesis is that heat treatment yields a physical change in the polymer, creating a denser material, with a

significantly higher glass transition temperature, and hence a reduced void volume, which mitigates solvent penetration and deformation. However, a few loose ends include the role of oxygen, which was found to be necessary for solvent compatibility, such that oxygen-free heat treatment does not yield gains in solvent compatibility. Similarly, the origin of the characteristic yellow color change is not yet known. A recently published paper seems to elude to the formation of carbon-carbon double bonds that result in a yellow color change in thiol-ene materials, which is allylic hydrogen formation (C=C-H) [152]. This hypothesis was recently tested and shown in **Section 9.1.3**; however, surprising contrary results were found. Though it has become increasing clear that carbon re-arrangements, along with physical property changes are responsible for the solvent compatibility. Albeit the exact understand is currently unclear.

Finally, it is important to note there are other published approaches to gaining solvent compatibility in thiol-enes; albeit, the effects are significantly weaker. Podgorski et al. show that the chemical oxidation of thiol-ene materials results in mechanical property enhancements (such as a significant increase in the glass transition temperature) [153]. Replication of the study with hydrogen peroxide oxidation did result in a lesser degree of chloroform compatibility (data not shown, see **Appendix I, Fig. 5**.). Another approach is the addition of carbon nanotubes into the pre-polymer mixture. The addition of filler materials has also been shown to modify solvent resistance [154]. Here it was shown that toluene-induced swelling could be reduced from 18.3% to 1.6%. For acetone, a more moderate reduction occurred from 9.9% to 4.6%. However, the addition of CNTs renders TEs non-transparent.

In summary, the results of the section presented here were pertinent for the project progression, as for many pharmaceutical applications solvent compatibility is necessary. In particular, for the production of PLA/PLGA microspheres chloroform is used to produce the emulsion, which up to now was limited to the use of glass microfluidic chips. Similarly, for the production of nanoparticles, various harsh solvents may be used, including acetone, acetonitrile, and tetrahydrofuran. For both, having a solvent compatible material opened up possibilities for rapid prototyping of microfluidic chip geometries to accomplish tailor-made drug delivery vehicles.

## 6.2. Establishment of proper wetting properties

With the high surface area to volume ratio in microfluidics, the surface properties need to be carefully considered and tightly controlled. Wettability of a material plays a critical role in determining flow properties, as well as for applications such as droplet microfluidics, while assays involving large molecules depend on reduced non-specific adsorption. Thiol-enes are neither quite hydrophilic nor hydrophobic polymers with a WCA between 60° and 90° depending on the composition and monomer molar ratios [66, 140, 155-158], which can be troublesome for many applications.

Surface wettability is particularly critical for two-phase flow droplet microfluidics, for the production of microspheres. For flow-focusing the continuous phase should exhibit favorable wetting to the channel material; while the dispersed phase wetting should be disfavored [159]. If the wetting properties are not sufficient, then the dispersed phase maintains contact with the channel walls and fails to result in droplet production. The mildly hydrophobic nature of thiol-ene presents a serious challenge for droplet-based microfluidics and is not suited for either water-in-oil or oil-in-water emulsions (the latter used for the production of PLA/PLGA microspheres). In order to overcome this challenge many strategies have been previously implemented, generally taking advantage of free thiol or ene groups in off-stoichiometric thiol-ene (OSTE) chips [160, 161]. Some of these strategies, as mentioned previously, include the conjugation of PEG derivates (WCA 35 - 52° [120, 162]), acrylic acid (WCA 43°[163]) and hydroxyethyl methacrylate (WCA 25 - 43°) [164, 165] to the polymer surface.

In order to solve the wetting properties for droplet microfluidics, replication studies were conducted based on the aforementioned references, along with other surface modifiers such as organosilanes or adsorption approaches (i.e., adsorbed polydopamine or polyvinyl alcohol) as shown in **Figure 6.7A**. The aim of these studies was to attain the wetting properties of borosilicate glass, the gold standard for making polymeric microspheres, which has a WCA of appx. 25°. As seen in **Figure 6.7A**, most approaches yield WCAs far greater than glass and therefore are not sufficient for droplet microfluidics. The replication studies were generally unsuccessful (to achieve the desired outcome) and sufficiently low contact angles were not attained. A classical approach is to oxygen plasma treat the material [121, 139, 144], though the results are often quite transient, yielding favorable surface energies for a couple of days at most. Plasma treatment does, however, provide the

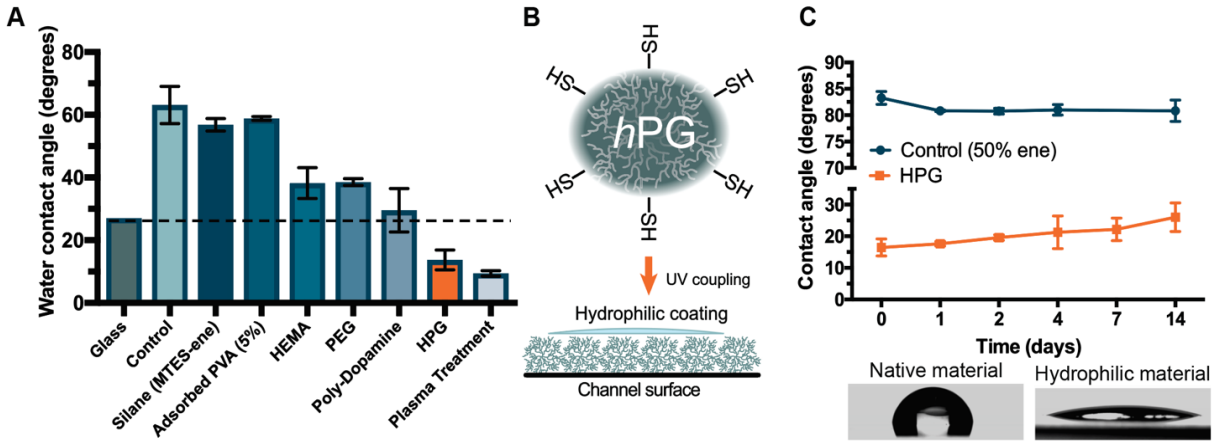


**Figure 6.7. "Click-" or adsorption-based surface modifications. A)** Water contact angle (WCA) of borosilicate glass, stoichiometric TE and thiol-enes coated with: silane (3-methacryloxypropyltrimethoxysilane), PVA (poly-vinyl alcohol), HEMA (hydroxyethyl methacrylate), PEG (mercapto-terminated polyethylene glycol), poly-dopamine, HPG (hyperbranched polyglycerol), or plasma treated TE. All treatments conducted in at least triplicates, with the error bars representing standard deviation. **B)** schematic illustration of HPG UV-grafted onto "ene" excess TE. **C)** HPG coating stability assessed by measuring the WCA of HPG over the course 14 days.

lowest possible water contact angles and is readily achievable in most fabrication labs. The final approach tested was to use a custom synthesized molecule (by Katayoun Saatchi, at UBC), hyperbranched polyglycerol (HPG), which was optimized to yield contact angles between 10-20°. The molecule is approximately 200 kDa in size, contains a large number of hydroxyl groups to provide for excellent wettability with water, and an abundant number of thiol groups, allowing to covalently graft onto "ene" excess thiol-ene materials (**Figure 6.7B**). Importantly, as shown in **Figure 6.7C**, the coating remains in the workable range for up to 10 days, which is at or below the water contact angle of borosilicate glass.

## 6.3. Application for microsphere production

With both solvent compatibility and super hydrophilic contact angles now available in the thiol-ene "toolbox," avenues for flow-focusing applications became available. As mentioned in the introduction, flow-focusing is the most commonly implemented method for the microfluidic production of droplets. Here, two immiscible fluids are forced coaxially through an orifice, where droplets are formed either at the orifice (resulting in larger droplet sizes) or in the downstream "opening," (resulting in smaller particles). In the following sections we will explore the production of PLA microspheres and chromatographic packing material in the size regime of 1 µm – 30 µm.

### 6.3.1.Large 10 µm + PLA microspheres

In order to illustrate the utility of heat treatment, PLA microspheres were produced for 8 hours and size evaluations were conducted. Thiol-ene microfluidic chips are rarely used for oil-in-water droplet production and have not been reported for the production of chloroform-based droplets. Currently, ethyl acetate [80] and toluene [139, 166] droplets have been produced via thiol-ene microfluidic chip materials.

To make the microspheres, two thiol-ene chip halves were heat-treated for 60-h and subsequently plasma treated for one hour to reduce the contact angles (**Figure 6.8A**). The chip was then used for the flow focusing of 5% PLA in chloroform with 1% polyvinyl alcohol (PVA) in water as the continuous phase. Plasma treatment was the chosen method for increasing the surface energy of the channels, as currently, the combination of the HPG coating and heat-treatment is not feasible (See **Section 9.1.2**). However, plasma treatment is quite stable for thiol-enes and yields appropriate contact angles for at least 12-h (**Figure 6.8B**). Implementation of heat treatment is particularly important for the production of uniform microspheres. As shown in **Figure 6.8C**, particle diameter rapidly decreases when using untreated thiol-ene chips. This is likely due to the swelling of the dispersed phase channel (i.e., the channel exposed to chloroform). Consequently, after four hours of

droplet production, the particle size reduces to 80% of the original diameter, and therefore rapidly deteriorating sample monodispersity (**Figure 6.8C**, blue). In contrast, samples produced using the heat-treated material resulted in consistent particle sizes production over the course of four hours (**Figure 6.8C**, red).

Hence to illustrate the utility of heat treatment, microspheres were produced for 8-hours, with samples collected for 10 min, every 2-h. Shown in **Figure 6.8D**, the heat-treated material produces consistent particles of appx. 26 µm in diameter for the course of 8-h. The coefficient of variation of the particles remains low throughout; albeit an increasing onset of satellite particle formation occurs at the 6-hour mark. This may be due to the slight instability of the plasma treatment; therefore, a better approach for attaining hydrophilic contact angles is needed. Nonetheless, as thiol-ene chips are simple to fabricate, are degradable in nature, replacing the microfluidic chip is still a valid alternative to the fabrication of glass microfluidic chips.

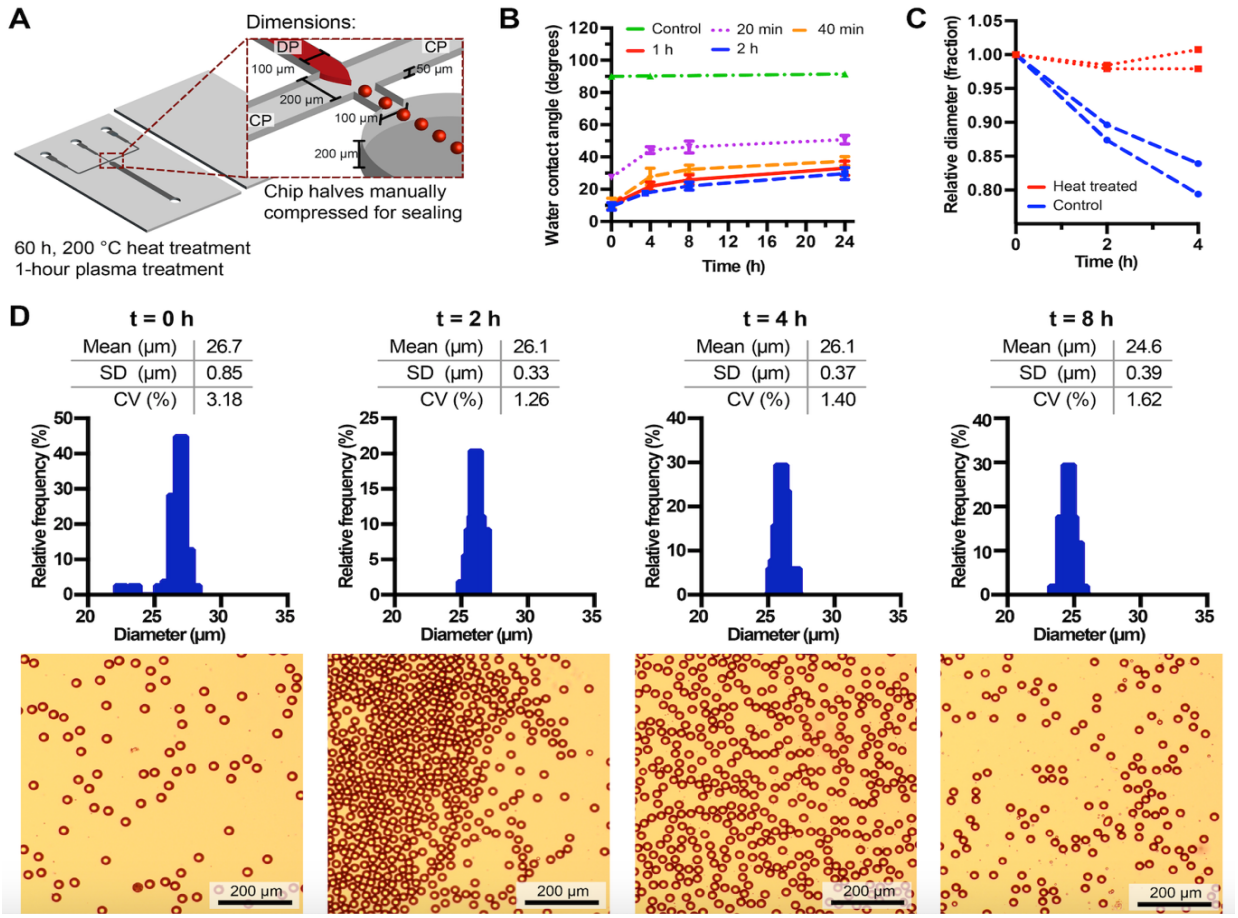


**Figure 6.8. Large PLA microsphere production with solvent compatible TE chips. A)** Schematic illustration of flow focusing chip used for droplet production. **B)** Water contact angle monitored over time for the indicated plasma treatment conditions. **C)** Relative particle diameters over the course of a 4 h production for heat treated (red) and control (blue) TE. **D)** PLA particles were continuously produced for 8 h on heat and plasma treated TE chips. Dispersed phase of 5% PLA in chloroform and continuous phase 1% PVA in water. Distributions and coefficient of variation (CV) of the particles are shown.

### 6.3.2. Small 1-2 µm microspheres

Thus far, relatively large microspheres have been produced using thiol-ene microfluidic chips. However, a special size regime of interest for pharmaceutical applications is in the 1-3 µm diameter range. More specifically, the following section aims to produce magnetic microspheres (MMS) of such sizes (**Figure 6.9A**). This size regime may be appropriate for intravenous administration, as studies show it may bypass lung capillaries [64, 166], and hence avoid unwanted deposition in the lungs. With the addition of magnetite nanoparticles to the PLA/chloroform mixture allows for the formation of responsive particles that can be magnetically manipulated *in vivo* in order to achieve greater therapeutic benefits via localized drug delivery. Therefore, the combination of the 1-3 µm diameter range and the magnetic properties, make the droplets ideal for strong manipulation *in vivo* for effective drug delivery.

Translating such small particle production to a microfluidic set up has been seldom done, generally owing to the high energy input needed for droplet breakup of this size. To achieve such small sizes, our lab previously used batch evaporation/extraction methods, yielding broad size distributions [10]. Other methods have been employed, such as electrospray [11] and commercial flow-focusing nozzles [12]; however, the literature is lacking for the utility of a simple microfluidic chip. Particularly, this may be because in order to use a simple flow-focusing geometry, very small feature sizes are needed; as shear-off of droplets smaller than $1/10^{th}$ of the orifice width is rare [13], making the fabrication costly and labor-intensive. It is important to note that this section focuses on the *direct* production of 1-2 µm microspheres; however, **Section 9.2** and **Appendix II** contains other approaches to purify out this size regime from a more complex size mixture [167]. This is mostly due to the inherent difficulty of achieving these diameters; and hence, the literature commonly employs

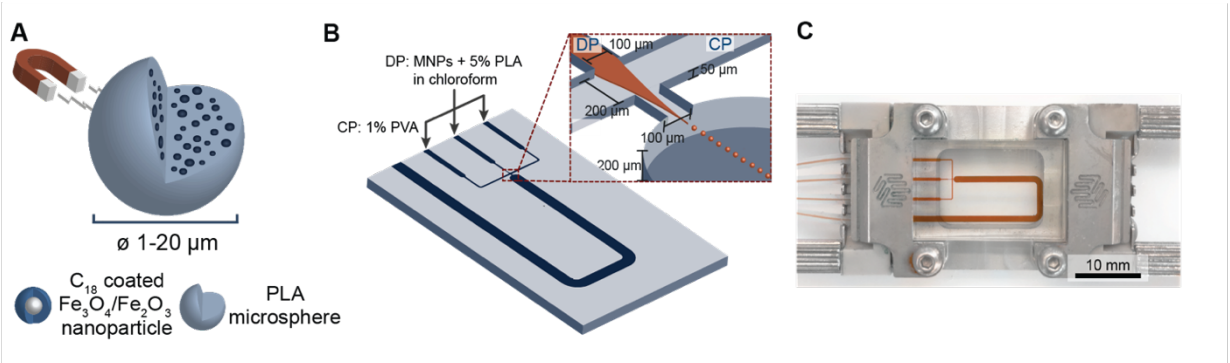


**Figure 6.9. MMS formulation and flow focusing chip. A)** Schematic illustration of magnetic microspheres by loading magnetite/maghemite NPs into PLA particles. **B)** Illustration of the flow focusing chip used for MMS production. Chip dimensions include 50 µm depth, 100 µm wide and long orifice, and a 200 µm deep and 1 mm wide opening. **C)** Image of the thiol-ene chip within the chip interface. Chip dimensions are 22.5 x 15.0 x 4.0 mm.

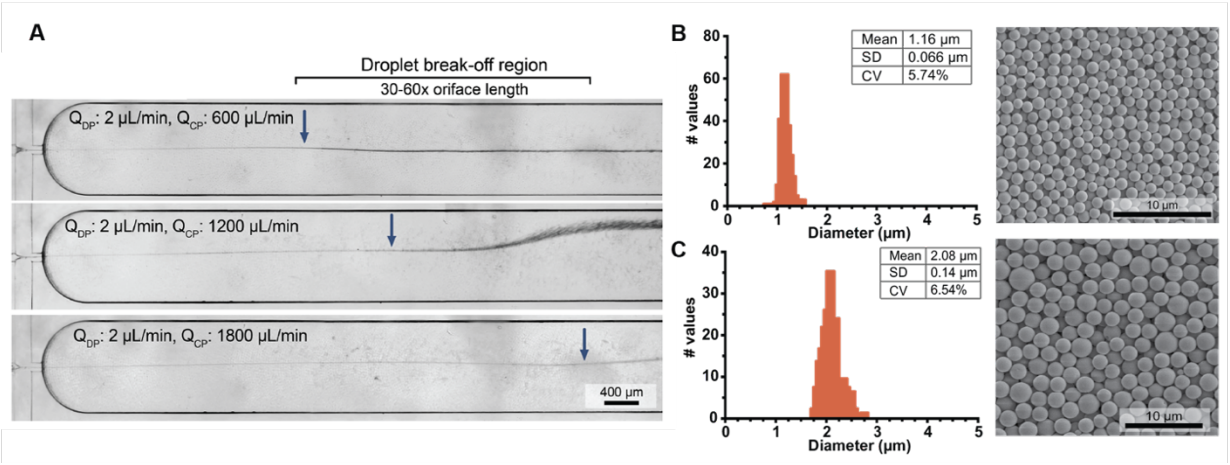


**Figure 6.10. High Re and Ca number production of MMS. A)** Light microscope image of droplet formation at various flow rates and flow rate ratios (as shown on the images). Arrow indicate estimated droplet break-off point. Size distribution and SEM images of **B)** empty PLA particles, **C)** and magnetic NP loaded particles. Empty particles produced at $Q_{DP}$:$Q_{CP}$ of 2:1800 µL min$^{-1}$, while MNP loaded particles at at $Q_{DP}$:$Q_{CP}$ of 2:1000 µL min$^{-1}$.

an *indirect* purification approach. This generally entails the purification of satellite particles (secondary droplets) that arise from the viscoelasticity of polymers [159-161].

The chip dimensions are shown in **Figure 6.9B**, where the orifice, the smallest feature size, is 100 µm in width, making the design simple to produce in most fabrication labs. Upon the orifice, the channel opens up to a 1000 µm wide and 200 µm deep opening, allowing for reduced flow velocities and easy viewing under a microscope. The chip is connected to the solutions using a commercial manifold capable of withstanding chloroform and other harsh solvents (**Figure 6.9C**).

This approach for obtaining small microspheres is rather simple, robust and reliable among replication studies. The basic principle is to increase the continuous phase flow rate to a point where the smallest feature size (i.e., the orifice) no longer plays a governing role in determining the final droplet size. To achieve this, the upper overall flow rate and flow rate ratio limit of the microfluidic set-up was investigated, up until the flow rate induced backpressures were beyond the tolerated range of the syringe pump. Upon increasing the flow rate to such high values, a unique flow profile of the dispersed phase forms, resulting in a long, thin thread extending well into the opening, where jetting (or tip-streaming) of the droplets occurs (**Figure 6.10A**). Shown with blue arrows (in **Figure 6.10A**), the droplet break-off point depends on the flow rate ratio and is directly related to the final droplet size.

The capillary numbers can be calculated using equation (6.) and corresponds to 0.01 for the dispersed phase, and 0.11 – 0.33 for the continuous phase. Comparing these values to a capillary number-based flow map shown in ref. [70], we can estimate the mechanism of droplet formation. Here this system yields a mechanism between jetting and tip-streaming. Published work defines jetting as

droplet break-off within 20$h$, with $h$ being the characteristic length scale (in ref [70], it is the height of the square microfluidic channel being utilized). Tip-streaming is defined as the formation of a stable thread with a length beyond 20$h$, upon which droplet break-off occurs. For our non-square microfluidic channel, h can be defined as the hydraulic diameter corresponding to 2ab/(a+b), yielding a value of 333 µm. The stable thread shown in **Figure 6.10A** has a length of 20$h$, depending on the continuous flow rate used, agreeing both with the capillary number-based estimations as well as the physical descriptions of the regime. This is particularly interesting, as tip-streaming generally relies on A) carefully calculated geometry optimization or B) critical micellar concentrations of the continuous phase surfactant [43, 62, 73], and C) regarded to occur at low $Re$ numbers [74]. In this regime, the droplet diameters are proportional to the diameter of the thread. Practically this means tip-streaming may be easier to achieve than presented in the literature, but also it allows for droplet formation in microfluidic chips with large feature sizes. As droplet diameters no longer rely on the smallest feature size, this effectively makes fabrication requirements much less stringent.

The produced particles are 1-2 µm in diameter, spherical, and highly uniform as seen in **Figure 6.10B, C**. The unloaded PLA particles are smaller, with 1.16 µm diameter and 5.7% CV, **Figure 6.10B**. The particles shown were produced at $Q_{DP}$:$Q_{CP}$ of 2:1800 µL/min. The addition of 0.5% (w/v) magnetite NPs yields larger 2.08 µm average diameter particles, with very similar monodispersity at a 6.5% CV, shown in **Figure 6.10C**. The increase in diameter is largely due to a lower overall flow rate used to make the magnetic samples, as pump failure occurred at the higher flow rates. This is likely due to the viscosity difference of the dispersed phase with the addition of the MNPs; and hence, the particles were produced at a much lower QDP:QCP of 2:1000 µL/min flow rate.

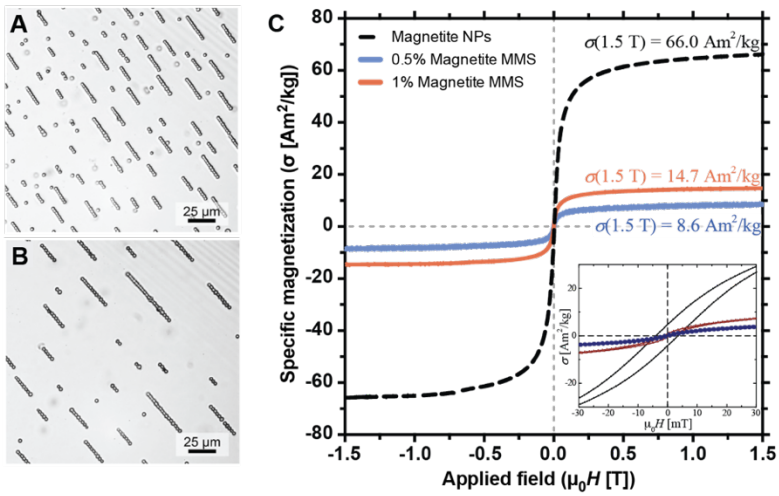


**Figure 6.11. Magnetic response and hysteresis curve.** Light microscope image of **A)** 0.5% or **B)** 1% (w/v) magnetite particle re with a magnet in close proximity. **C)** Hysteresis curve of the starting magnetic nanoparticles (black), 0.5% MNP loaded MMS (blue), and 1% MNP loaded microspheres (red).

**Figure 6.11A, B** shows the self-assembly behavior of the particles in response to a magnet. Magnetization measurement curves were obtained for the starting MNPs (black) and the final MMS (blue and red), as shown in **Figure 6.11C**. The magnetization curves confirm that the starting MNPs display non-negligible hysteresis, whereas the encapsulated MNPs show no detectable hysteresis. The hysteresis in the NP starting material is likely due to magnetic interactions between the particles in the dense sample. The lack of hysteresis in the MMS indicates that they are superparamagnetic at room temperature on a time scale of seconds. The specific magnetization of the 1% (w/v) sample is about 30% that of the starting NPs, while for the 0.5% (w/v) it is roughly 15%, showing good control over the magnetic loading into the PLA particles.

Overall, the results show that the production of 1-3 µm MMS is possible with microfluidic methods, yielding narrow size distributions and without any hysteresis. In order to increase the magnitude of magnetization of the particles, which would be required for effective magnetic targeting *in vivo*, higher magnetic nanoparticle concentrations should be incorporated. Future work can optimize the MNP loading, as well as maximize the magnetite to maghemite content in the MNPs.

### 6.3.3. Applications for thiol-ene bead production

In addition to producing biodegradable microspheres for drug delivery, flow-focusing can open avenues towards making polymeric beads to serve as supports for enzyme immobilization [168], chromatography [169], solid-phase extraction [170] or solid-phase synthesis [171, 172]. For most analytical separations, beads with a diameter of a few microns are preferred [169], with monodispersity and porosity playing an important factor in performance. Crucially, reactive functional groups can be highly advantageous to tailor-make the column properties for effective separations or syntheses.

Due to the ability to surface modify off-stoichiometric thiol-ene, OSTE, this material may serve as an optimum column material. Importantly, size control and monodispersity of the beads can be achieved using flow-focusing. A flow-focusing chip with a 30 µm orifice was fabricated (as opposed to 100 µm previously, **Figure 6.12A,B**. This is to reduce droplet size, mostly as the viscosity of the TE monomers is high, yielding large droplets in the larger feature size chip. Even so, native stoichiometric thiol-ene produces rather large beads, at 33 µm average diameter, albeit with very high monodispersity with a CV or 1.84% (**Figure 6.12C,E**). The addition of 25% (v/w) chloroform can be used to offset both the high viscosity, as well as through solvent evaporation yield an additional 10% size decrease (data not shown). Seen in **Figure 6.12B**, the addition of chloroform changes the droplet formation mechanism (compare **Figure 6.12A**), while yielding smaller sizes at an equivalent flow rate (**Figure 6.12D,F**). The chloroform containing droplets yield beads with a 23 µm average diameter, with an equally high degree monodispersity at a CV of 2.88%. High-resolution surface mapping using SEM shows that beads produced with 50% chloroform are smooth, under 10

µm in diameter and importantly could exhibit porosity as the chloroform evaporates and condenses the beads (**Figure 6.12G**). Previously, thiol-ene beads have been produced in a microfluidic set-up, yielding 200 µm+ particles in size; however, by changing the monomer composition, both macroporous and nonporous beads were produced [173]. In this publication, the authors show that monomer composition very similar to TATAO and PETMP yields nonporous particles, but the beads become porous by adding mercaptoacetic acid into the mixture. Further work can investigate such formulation parameters.

For the desired application of analytical separations, the thus far achieved sizes of 10-30 µm are rather large. In order to reduce the bead size, the previously described jetting/tip-streaming method was implemented. Shown in **Figure 6.13A**, droplet shear-off follows the expected flow profile; albeit, the particles were formed at a jetting mechanism with droplet break-off occurring at $6.6h$. As jetting often yields increasingly polydisperse samples, the resulting particles show a bimodal distribution **Figure 6.13B,C**. The particles are spherical (**Figure 6.13B**), and the sample exhibits a main droplet population with a diameter of 6-7 µm and a satellite population with a diameter is 3 µm (**Figure 6.13C**). Importantly, these results were meant to serve as a proof-of-concept experiment to show that smaller thiol-ene beads are in fact achievable using flow-focusing. Further optimizations

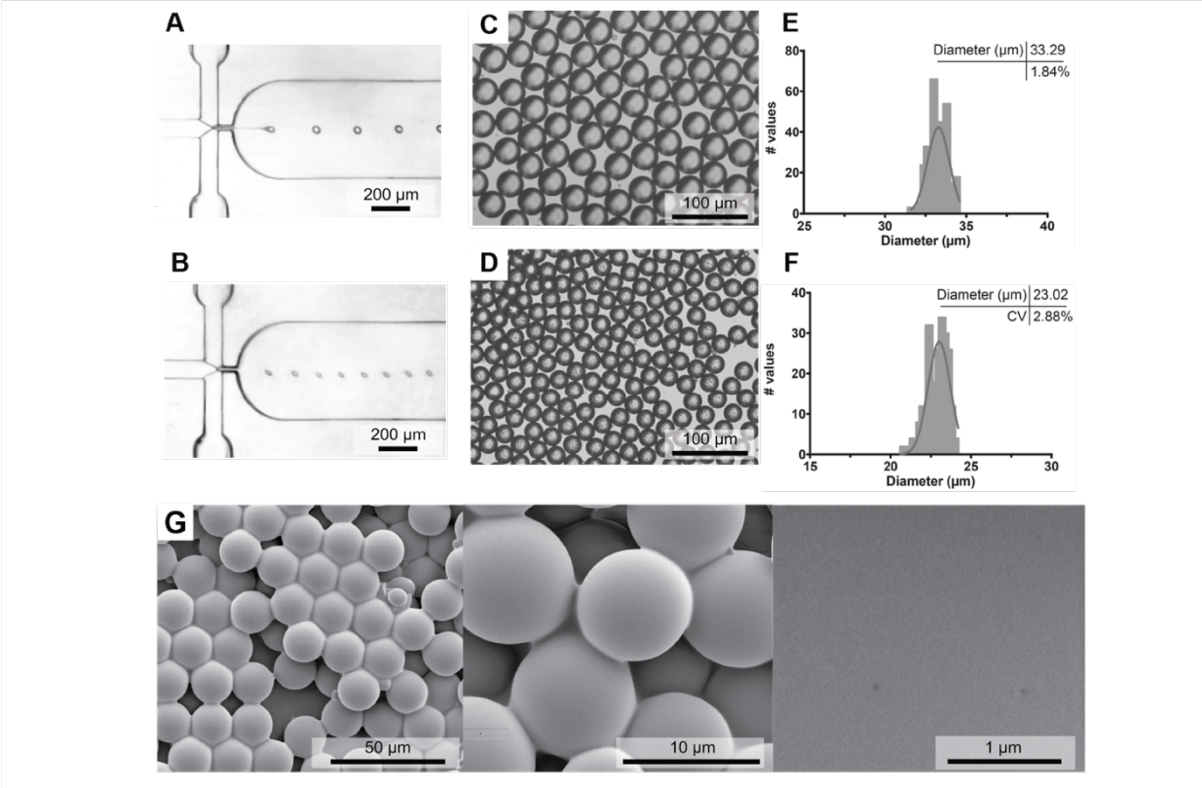


**Figure 6.12. Thiol-ene bead production for chromatography. A)** Light microscope image of thiol-ene beads with 0% or **B)** 25% chloroform concentration (v/v). **C)** Diameters and statistics of obtained beads for 0% or **D)** 25% chloroform concentration. **E)** light microscope image of flow focusing junction for the production of TE beads with 0% or **F)** 25% chloroform concentration (v/v). **F)** SEM images of thiol-ene beads produced with 50% chloroform imaged at 2.0 kV. For all: Stoichiometric thiol-ene with 0.5% TPO-L. Flow rate DP:0.2 µL/min and CP:30 µL/min. Beads were cured at 90 mW/cm$^2$ for 60 seconds prior to microscopy images.

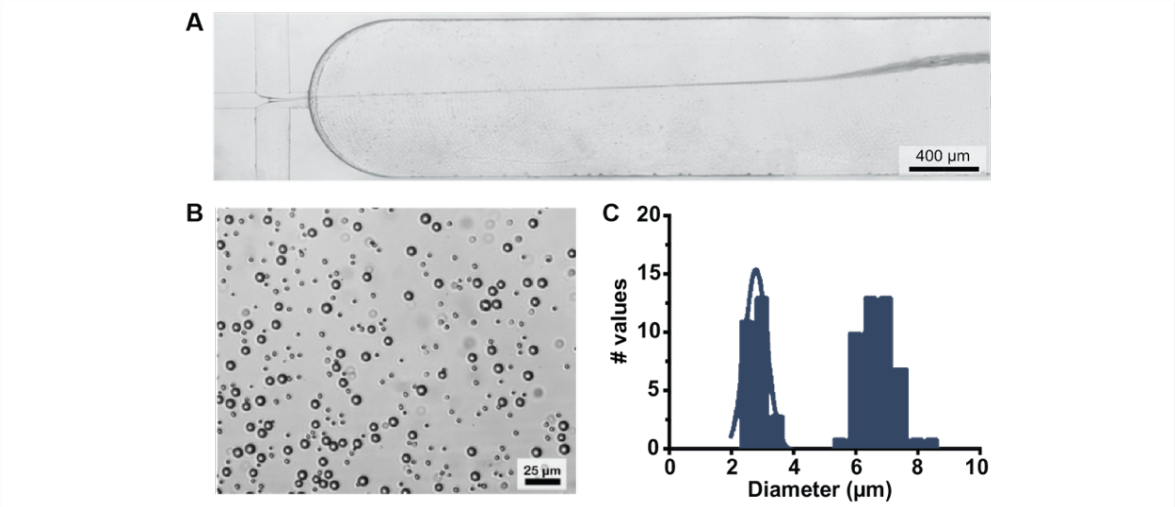


**Figure 6.13. Jetting-mediated thiol-ene bead production. A)** Microscope image of thiol-ene beads (TATAO and PETMP) with 50% (v/w) chloroform being formed at $Q_{DP}$:$Q_{CP}$ of 2.5 : 800 µL/min. **B)** Light microscope image of the thiol-ene beads and **C)** corresponding size distributions.

are needed to stabilize thread and push the formation into a tip-streaming regime to create a more homogenous and smaller sample population.

## 6.4. Application for nanoparticle production

In the following investigation, small interfering RNA (siRNA) loaded lipid-polymer nanoparticles (LPNs) are made using microfluidic nanoprecipitation. This is particularly important as RNA interference (RNAi) based therapeutics can be a powerful tool in disease prevention and reversal. RNAi is mediated by siRNAs in order to provide for a highly specific and potent gene silencing. While siRNAs are potent and efficient, their clinical outcome relies heavily on the delivery system, which can be a major challenge to optimize. For delivery, NPs represent a highly desirable class of drug carriers due to their ability to protect siRNAs from nuclease degradation, modulate biodistribution and importantly, facilitate cellular uptake which is otherwise not feasible for charged macromolecules (such as nucleic acids). An emerging class of nanoparticles, lipid-polymer hybrid systems, combine the advantages and mitigate the adverse properties of lipid- or polymer systems individually [174]. Previously, our group developed a highly effective LPN system for the delivery of siRNAs (**Figure 6.14A**); showing high efficacy and low toxicity for siRNA mediated gene silencing compared to existing formulations[25, 175]; albeit, attained through batch double emulsion approaches. From a formulation standpoint, this system replaces the traditional cationic lipid (e.g., DOTAP) with a custom synthesized lipidoid (i.e., lipid-like molecule) in order to reduce excessive surface charges and lower toxicity of the NP system, (**Figure 6.14B**).

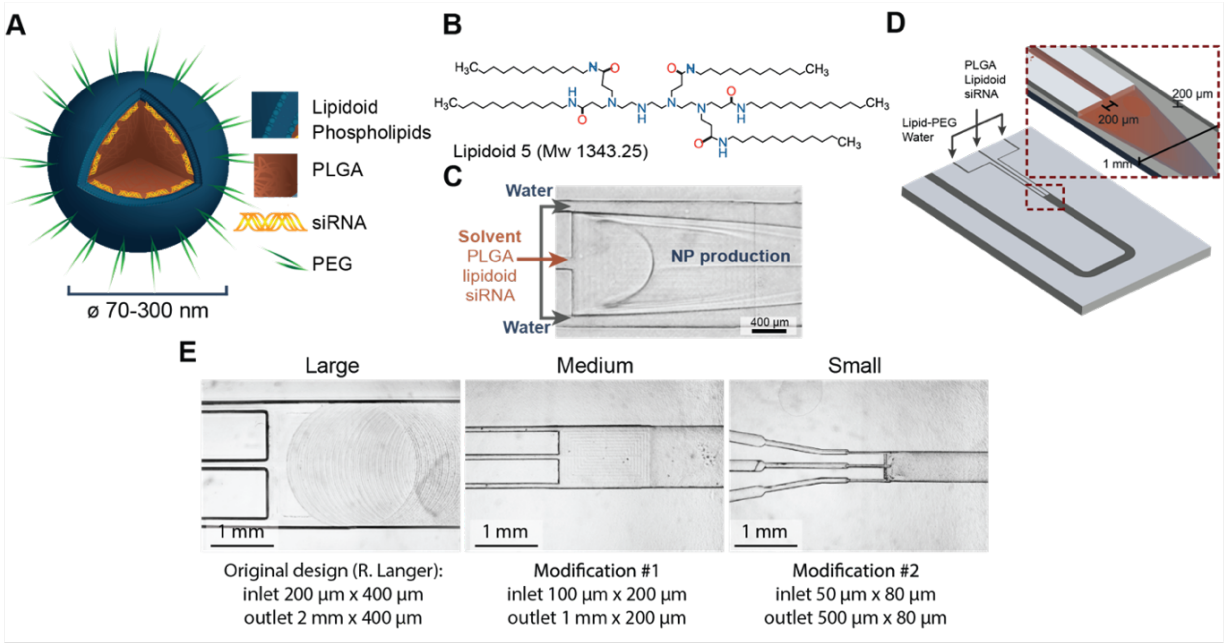


**Figure 6.14. Microfluidic set-up for LPN production. A)** Schematic illustration of the LPNs containing PLGA, PEG-phospholipid, lipidoid and siRNA. **B)** Structure of the lipidoid 5 ($L_5$). **C)** Illustration of the microfluidic chip. **D)** Light microscope image of LPN production. **E)** Various geometry prototypes used for higher flow rates or variable production quantities.

Investigated in this section, is an efficient, alternative method for producing nanoparticles (applicable to both batch and microfluidic approaches) termed nanoprecipitation. As described in **Section 5.2.1.**, nanoprecipitation relies on solvent displacement through rapid mixing to precipitate out the dissolved solutes and form nanoparticles. Nanoprecipitation in a microfluidic channel offers specific advantages such as precise control of fluid flow, exquisite size modulation, low polydispersity and as it is a continuous flow method, batch to batch variation can be eliminated. Through microfluidics, siRNA loaded lipid [101, 176, 177] and unloaded lipid-polymer [178-180] nanoparticles were shown to be as small as 30 nm; though the smallest siRNA containing LPNs were 110-130 nm [181, 182]. However, siRNA loaded LPNs has yet been performed using efficient convective mixers with such large-scale production in a polymeric microfluidic chip.

In order to load siRNA, the lipid, polymer, and siRNA are combined in the solvent phase and mixed with water as the non-solvent (**Figure 6.14C**). The microfluidic chip geometry is based on the microvortex design published by Robert Langer's group [178], albeit with smaller channel sizes (**Figure 6.14D**) in order to downscale the production for optimization purposes. The method is based on the convective, rapid mixing of the fluids; with a variable mixing rate depending upon the total flow velocity of the system (i.e., the *Re* number). Thiol-enes allow for rapid prototyping possibilities, such that the original design and two designs with smaller channels were made to precisely fine-tune the output scale (**Figure 6.14E**). Moreover, this material shows superior solvent compatibility [80, 136] allowing for the utilization of a range of organic solvents for formulation optimization. Commonly used polymers for microfluidic applications include PDMS and PMMA but fall short of

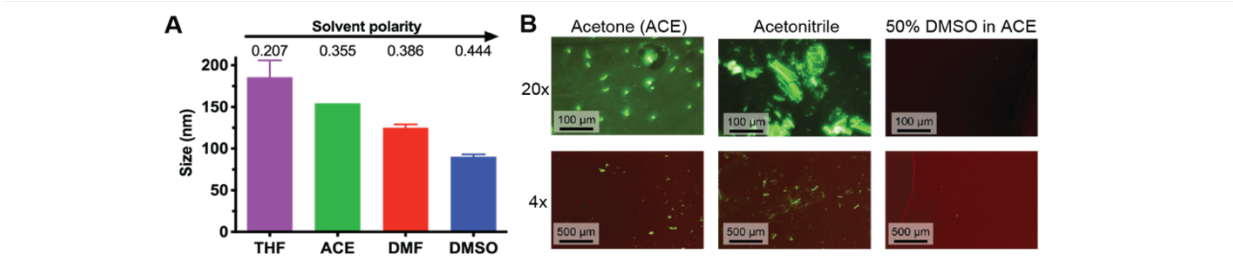


**Figure 6.15. Solvent choice influences size and siRNA solubility. A)** Obtained LPN size shows good correlation with solvent polarity. Average diameters (n=3) shown with indicated solvents. **B)** siRNA alone incubated in 95% of the indicated solvents. Stained with RiboGreen and imaged under a fluorescent microscope to observe microaggregation/precipitation.

solvent compatibility, which is particularly important for lipid and PLGA dissolution. Moreover, as shown below, the solvent choice is an important optimization parameter for LPN production.

Solvent polarity affects the final LNP size, primarily due to diffusion modulation when mixed with the polar non-solvent water. The more polar the solvent is, the faster the diffusion rate in water; hence, yielding smaller LPN sizes (**Figure 6.15A**). The attained siRNA loaded LPN sizes of 70-200 nm are in agreement with batch synthetic approaches, where similar diameters were observed with the indicated solvents [89]. Extremely critical, however, is the siRNA stability in the solvent choice. Previously, 95% of acetone has been used for batch nanoprecipitation of siRNA LPNs, as the authors show excellent siRNA stability in acetone [183]. However, for this system, the opposite applies, as the two most commonly used solvents for siRNA encapsulation, acetone and acetonitrile, are incompatible in this system. Rapid precipitation of the siRNA occurs at 95% acetone and acetonitrile, with the addition of DMSO mitigating precipitation (**Figure 6.15B**, 50% DMSO in ACE shows no siRNA aggregation). Therefore, the final solvent system for LPN production was chosen to be 5% $H_2O$ and 95% acetone/DMSO in a 50/50 (v/v) ratio.

The LPNs exhibit good in-solution stability in an unbuffered aqueous solution without the use of surfactants. However, ultracentrifugation at 50,000g remained challenging, particularly with residual DMSO present in the solution. To combat centrifugation-induced aggregation various approaches were investigated, including the use of PVA, non-ionic surfactants (Pluoronic F68 and F127), dense sugars to dampen the centrifugal forces, and molecular weight cut off filters (data not shown). All the aforementioned approaches yielded little to no effect in preventing pellet collapse and aggregation. Polyethylene glycol (PEG) coating is often used to increase the colloidal stability of NPs, but also to provide charge shieling for effective circulation of intravenously injected particles without clearance from the mononuclear phagocyte system [7, 184]. Ceramide-PEG was chosen to stabilize the LPNs due to its neutral charge, leading to positively charged particles and fast de-PEGylation in the presence of serum albumins [89], both properties desirable for cellular uptake. A dilute solution of ceramide-PEG is added to the water phase, in order to coat the outer layer of the LNPs, providing stability during ultracentrifugation. Shown in **Figure 6.16A**, aggregation, as indicated by large average diameters, subsides upon the addition of 15 mol% cer-PEG with respect to the lipidoid concentration. Similarly, the average PDI values fall as the samples retain uniform

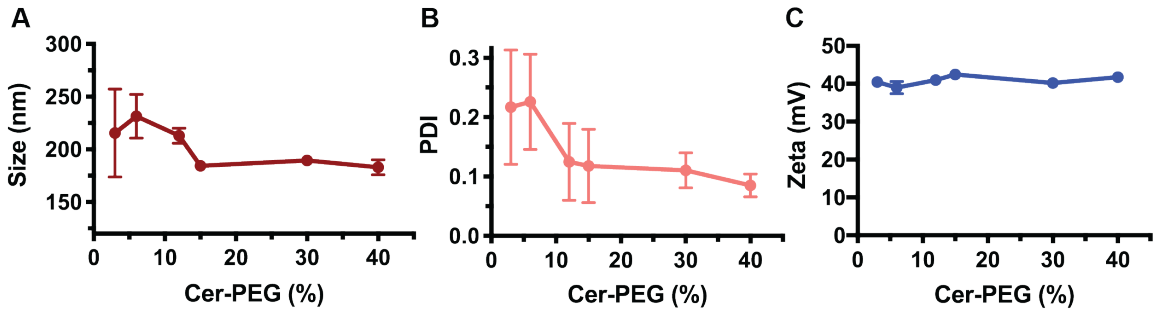


**Figure 6.16. Biophysical characteristics of LPNs with respect to the ceramide-PEG concentration. A)** size (Z-average), **B)** PDI and **C)** zeta potential at the indicated cer-PEG concentrations (molar percent with respect to the lipidoid). All samples conducted in triplicates, with 15% (w/w) lipidoid and 1:200 siRNA moral ratio (siRNA : lipid). 4 mg/mL solute content, produced at Re 75, 1:10 solvent:water flow rate ratio. All samples were purified using an ultracentrifuge prior to measurements.

sizes (**Figure 6.16B**). The particles remain positively charged (**Figure 6.16C**), although, if needed, negatively charged lipid-PEGs (e.g., DSPE-PEG) may be used to reverse the surface charge to -30 mV without any impact on the biophysical characteristics such as encapsulation efficiency (data not shown). The choice of lipid-PEG does have a significant effect on cell uptake; thus, should be carefully considered [89].

With the described formulation, size investigations were carried out in order to obtain a wide range of sizes from 70-250 nm. The parameters investigated include solvent choice, flow rate, flow rate ratio, and solute concentration in the solvent phase, **Figure 6.17A-C**. Shown in **Figure 6.17A** (red), using DMSO, the LPNs are significantly smaller in size (as shown previously in **Figure 6.15A**); ranging from 80 to 145 nm from Reynolds number (Re) 75 to 15, respectively. However, the polydispersity is high; therefore, alternative approaches are needed for sub-100 nm particle synthesis. Acetone and 50% DMSO in acetone samples are similar in size, between 150 nm to 200 nm at the indicated flow rates, with polydispersity remaining low, near 0.1. Size modulation based on flow rates alone is less effective, with variations of 50 nm on average was achieved at a given flow rate ratio (**Figure 6.17B,** compare vertically). Reciprocally, changing the flow rate ratio allows for larger size variation, of approximately 100 nm for a given flow rate (**Figure 6.17B,** compare horizontally). Here, combined, flow velocities were used to produce particles from 98-248 nm, holding all other parameters constant. Finally, size modulation can be achieved by diluting the solute concentration of the solvent phase, for example shown in **Figure 6.17C**, from 4 $mg{\cdot}mL^{-1}$ to 2 $mg{\cdot}mL^{-1}$. Approximately 50 nm size reduction can be achieved at a given lipidoid concentration. Here, the lipid concentration does not statistically significantly affect LPN size, although in a replication study (**Figure 6.19D**) the size differences are significant. An example sample of particles was imaged under the TEM, where the diameters are in agreement with the DLS. Small particles are visible; however, which were not shown as a secondary peak by DLS indicating that the sample preparation caused fragmentation of some of

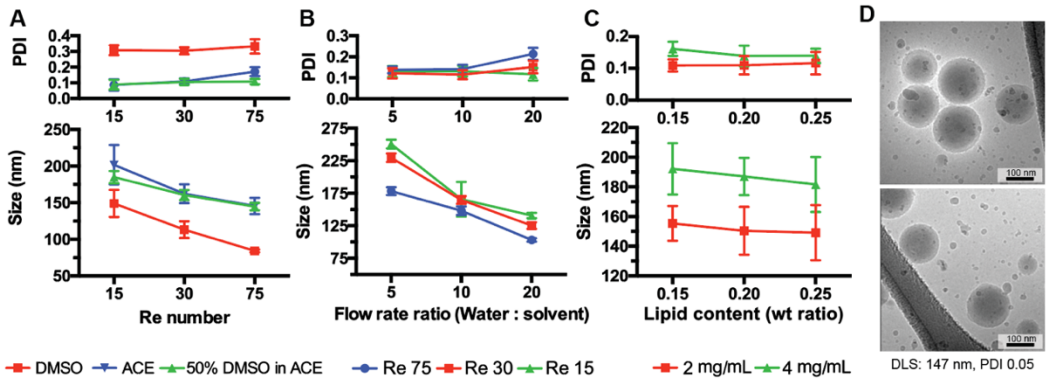


**Figure 6.17. Microfluidic and solvent-based size modulation. A)** Size variation based on solvents choice, **B)** and flow rate ratio. Solvent phase contained 2 mg·mL$^{-1}$ solute concentration, 20 wt% lipidoid and 1 to 150 TNF-α siRNA to lipid mol ratio. **C)** Size modulation based on solute concentration (red: 2 mg·mL$^{-1}$ and green: 4 mg·mL$^{-1}$) and lipid content. **D)** TEM micrograph of 150 nm LPNs.

the particles (**Figure 6.17D**). Overall, these results show a myriad of parameters can be used to modulate nanoparticle diameters in a microfluidic set-up.

A particularly interesting size regime of LPNs for *in vitro* and *in vivo* investigations are in the 60-80 nm range. To achieve this, without modulating the composition (i.e., the organic solvent), the flow rates, flow rate ratios, and solute concentration were varied. As seen previously, the overall flow velocity has the lowest overall impact, which particularly holds for the high flow velocities beyond Re 150 (**Figure 6.18A**). Presumably, beyond $Re = 150$ the microvortex flow profile may not vary extensively, resulting in similar convective mixing rates. Conversely, the flow rate ratio significantly affects the diameters, with a size range of 86-162 nm at Re 150. Therefore, in this system, the best approach to achieve small LPN diameters is to reduce the solute concentration, increase the flow

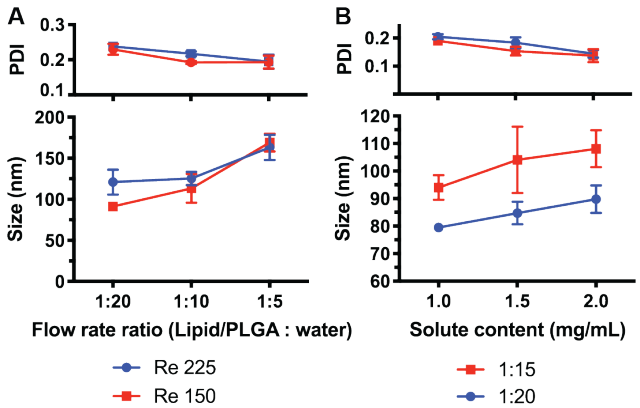


**Figure 6.18. Small-sized LPN production. A)** High flow rate LPN production, Re 225 (blue) and Re 150 (red). At high flow rates size variation is dependent on the flow rate ratio over the total system flow rate. 1.5 mg·mL$^{-1}$ solute concentration in the solvent phase. B) Re 125 LPN production at varying flow rate ratio (1:15 and 1:20 solvent:water) at indicated solute concentration in the solvent phase. For both: 20 wt% lipidoid and 1:200 mol ratio of siRNA in the formulation, with 50% DMSO in ACE as the solvent phase.

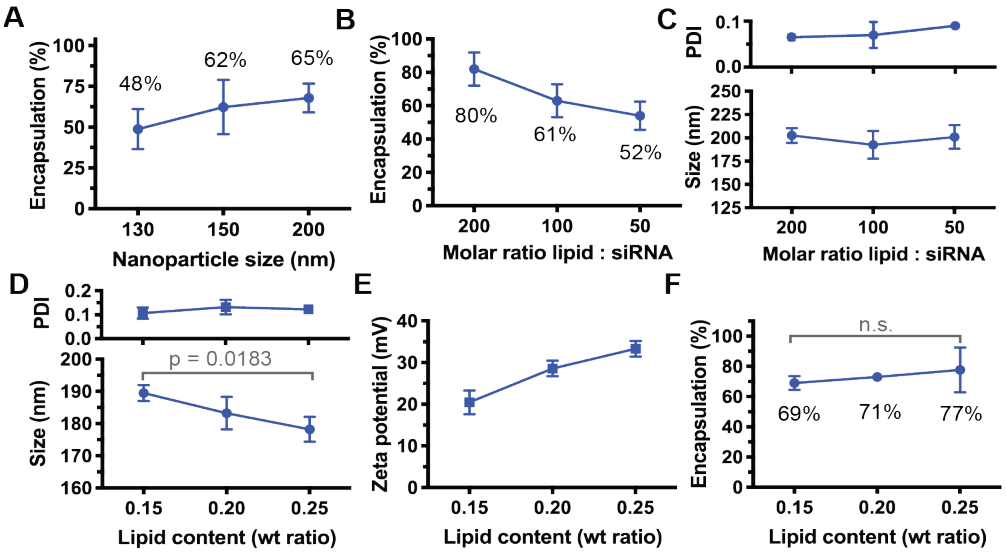


**Figure 6.19. siRNA encapsulation. A)** Average encapsulation of siRNA at the indicated LPN size. **B)** Size and PDI, **C)** encapsulation efficiency of LPNs produced with 16 wt% lipidoid, but increasing $L_5$ to siRNA mol-ratio as indicated. **D)** Size and PDI, **E)** encapsulation efficiency and **F)** zeta potential of LPNs produced increasing wt% lipidoid content but constant siRNA to $L_5$ mol-ratio of 150. Welch's t-test used to analyze significance where indicated.

rate ratio, while maintaining moderately high flow velocities. At $Re = 125$ with a high flow rate ratio of 1:20 between the solvent and the water phase, particle size ranges between 79.5 ± 1.2 nm to 89.8 ± 5.0 nm when changing the solute concertation from 1 mg·mL$^{-1}$ to 2 mg·mL$^{-1}$ (**Figure 6.18B**). For the latter size, this allows for the production of particles as small as 90 nm and as large as 250 nm (see **Figure 6.18B**) with the same solute concentration, 2 mg·mL$^{-1}$, by only changing the flow rates and ratios. Further reduction in size may be possible by increasing the temperature of the microfluidic system, which would facilitate the diffusion rate. With the high $T_g$ of thiol-ene polymers, the system could remain under high pressure with the flow velocities and withstand temperatures of up to 117 °C if heat treatment is applied to the material [136].

Next, TNF-α siRNA loading efficiency was investigated for the purposes of inflammation reduction [185]. Shown in **Figure 6.19A**, siRNA encapsulation decreases with decreasing size. Smaller 130 nm particles show 48% encapsulation (7.1 µg·mg$^{-1}$), while larger 200 nm particles show 65% encapsulation (11 µg·mg$^{-1}$) on average. The optimum molar ratio of lipid to siRNA is 200 to 1 (**Figure 6.19B**), with no statistically significant increase in loading observed at 300 to 1 (data not shown). The molar ratio of 200 to 1 has been previously validated by our group to be the optimal ratio when produced via batch double emulsion solvent evaporation methods [25]. While theoretically appx. 10 lipids are needed to neutralize each of the siRNA duplex charges, encapsulation efficiency rapidly falls when approaching this ratio. Presumably, some of the $L_5$ lipidoids are interacting with the negatively charged PLGA in order to make the energetically stable hybrid particles. While the siRNA to lipid ratio does not seem to affect size (**Figure 6.19C**), the lipid content may have a statistically significant effect as seen in **Figure 6.19D**). This, however, is not reproducible, as seen earlier in **Figure**

6.17C, though in both cases increasing the lipid content reduces the average diameter. It is important to keep in mind any potential size deviation that may arise with a formulation change. As expected, the zeta potential of the particles rises with increasing cationic lipid content (**Figure 6.19E**), from 20 to 35 mV. This increase in positive charges does not yield a statistically significant loading increase, though average encapsulation does increase with increasing $L_5$ content (**Figure 6.19F**). Therefore, if high positive charges are not of concern, increasing the lipidoid content within the formulation, can effectively increase encapsulation.

Finally, single-step chelator attachment is possible within the microfluidic set up for *in vivo* pharmacokinetic/ biodistribution purposes. The commercially available phosphoethanolamine-DTPA, PE-DTPA (**Figure 6.20A**) was added to the solvent phase at 2.5-10 mol% $L_5$ concentration in order to incorporate the chelator for radiolabeling with the gamma emitter $^{111}$In ($^{111}$indium) ($T_{1/2}$ = 2.8 d; E$\gamma$ = 171 and 245 keV) (**Figure 6.20B**). The addition of PE-DTPA shows no effect on the biophysical characterization of the particles (**Figure 6.20C**) with average diameters remaining similar to the control. Rapid 1-hour radiolabeling was conducted after centrifugation of the particles in order to remove any excess chelator. In order to verify radiolabeling, both instant thin layer chromatography (iTLC) and centrifugation were conducted, where the starting sample and the pellet was measured for radioactivity using a dose calibrator. Both the iTLC and centrifugation confirm high indium uptake, with approximately 18.5 MBq added to each of the samples. The results show no added benefit to increasing the DTPA concentration to 10 mol%, with the 5 mol% sample showing

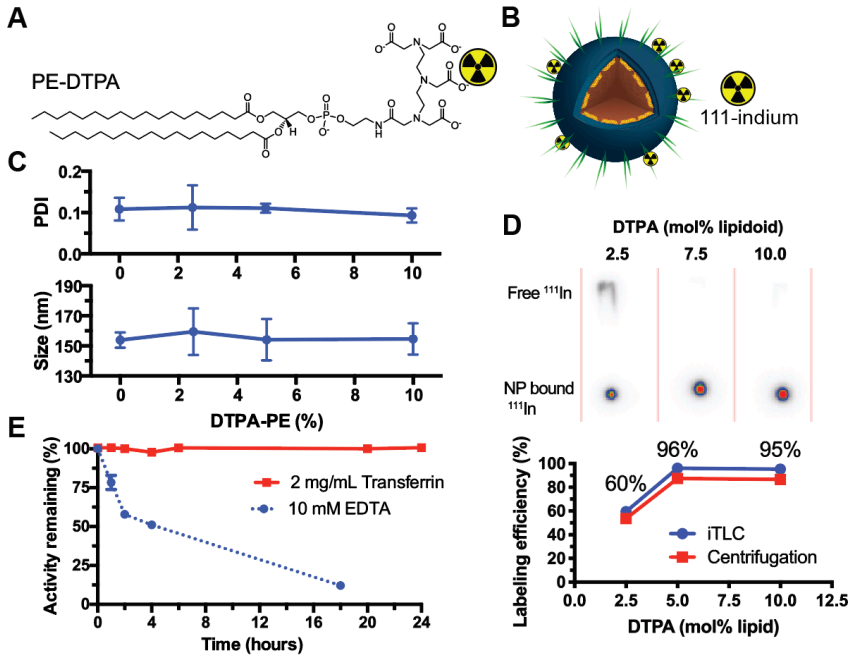


**Figure 6.20. $^{111}$Indium radiolabeling, particle characterization and challenge tests. A)** structure of PE-DTPA used for indium chelation and **B)** resulting particle illustration. **C)** Size and PDI of particles at indicated PE-DTPA concentrations, n=3. **D)** Raw iTLC image of indium labelled LPNs and quantification of bound and free indium using both the iTLC and centrifugation of the LPNs with the activity in the pellet measured in a dose calibrator. **E)** iTLC based quantification of free and bound indium in the presence of 10 mM EDTA (blue) or 2 mg/mL transferrin incubated at 37 °C, shaking 600 rpm.

equivalent 95%+ radiolabeling efficiency (**Figure 6.20D**). The particles remain $^{111}$In labelled when challenged against transferrin, which is an iron-transporting blood protein that also can chelate other metals (**Figure 6.20E**). Therefore, the challenge test was conducted under physiological conditions for 72 hours, using the physiological concentration of serum transferrin. No loss of activity from the LPNs is observed. Interestingly, the rapid loss of activity occurs with 10 mM EDTA, which is at a minimum in over 5000-fold excess over DTPA and can result in Nonetheless, the results show a simple and effective radiolabeling of the LPNs for *in vivo* biodistribution studies using a commercially available lipid-chelator system.

In summary, the preceding section aimed to highlight the utility of thiol-ene microfluidic chips for size-controlled nanoparticle production. Microfluidic size modulation is shown with diameters as low as 70 nm and large as 250 nm. In addition to size investigation, a one-step on-chip radiolabeling method was presented for easy biodistribution studies, with near-complete $^{111}$In labeling.

# 7. Concluding Remarks

The primary aim of this thesis has been to show the utility of a relatively uncommon polymeric microfluidic device material, thiol-enes, for the production of pharmaceutical delivery vehicles of all sizes, ranging from the nano- to the micro-scale.

As thiol-ene polymers are not inherently suitable for these pharmaceutical applications, significant emphasis was placed on optimizing the material for these purposes. Initially, the work focused on rendering the material chloroform compatible with the production of biodegradable microspheres. As surface coatings were minimally effective against chloroform-induced material deformation, a bulk modification approach was found successful against a large range of solvents. Here, the simple, yet effective approach of high-temperature treatment (100–200 °C for up to 60 hours) yields a 50-fold increase in chloroform compatibility. The material withstands chloroform, among many solvents, for several days without any discernable deformation. Such a degree of chemical compatibility is exceptional amongst polymers.

In addition to rendering the material solvent compatible, an in-house synthesized super-hydrophilic surface was developed and the coating optimized. The coating was covalently attached to the material, resulting in robust surface modification. The coating allows for the production of oil-in-water droplets in a flow-focusing geometry, where the outer aqueous phase is needed to preferentially wet the surface of the channels. To show utility, various droplets were produced, including PLA microspheres and thiol-ene beads.

Once TEs were optimized for pharmaceutical applications, this thesis showed a novel method for the production of 1-2 µm, monodispersed magnetic microspheres. The production of this regime has been consistently challenging due to the high energy input needed for droplet break-off. This work shows a simple microfluidic chip design with large channel dimensions achievable in all microfluidic fabrication labs. The prepared 1-2 µm particles show good loading with magnetite nanoparticles and show promise for the magnetically targeted delivery of drugs.

Finally, thiol-enes were shown suitable for the bulk precipitation of uniform nanoparticles. For this purpose, a range of solvents can be explored which allow for size modulation based on solvent polarity; or with rapid prototyping, various chip geometries can be investigated in order to maximize drug encapsulation or further modulate the particle sizes. The final work presented here focuses on siRNA loading within lipid-polymer hybrid nanoparticles. This work shows exquisite size control, ranging from 70-300 nm, highly uniform sizes, and high siRNA encapsulation efficiency (70-90%).

In summary, the presented thesis would like to show the utility of thiol-ene microfluidic chips for the production of pharmaceutical delivery vehicles of all sizes, ranging from nanoparticle to the microparticle scale. Moreover, the rapid prototyping and solvent compatibility of the material makes it promising for a range of applications well beyond the scope of this work.

# 8. Future Perspectives

*(1) Material and microfluidic devices*

For prototyping, PDMS is often the preferred material due to its ease of fabrication, although its commercial implementation is limited due to its volatile surface chemistry and inability to upscale production with its (relatively) lengthy polymerization times [124]. UV-curable thiol-enes can be an optimum material for both rapid prototyping and viable commercial translation, bridging the gap that often exists when translating PDMS prototypes to alternative materials. For the designs presented in this thesis, injection molding, sub-second curing, and automated assembly are possible for mass production. Moreover, solvent compatibility can be gained through high-temperature treatment on already assembled devices; hence, large numbers of mass-produced chips can be treated simultaneously.

There are still some bottlenecks with the material, namely the inability to modify the surface after heat treatment or maintain surface modification post-heat treatment (**Section 9.1.2**). As discussed below in **Section 9.1.3**, heat-induced carbon rearrangements could be a reason for solvent compatibility [152]. Using IR in **Section 9.1.3**, a loss of 'enes' were found; meaning carbon rearrangements could be a reason. Because of this, the covalently attached superhydrophilic coating (HPG) is no longer a viable surface treatment for PLGA/chloroform droplet microfluidics, limiting its use as a commercial system. To solve the limited surface functional groups post-heat treatment, wet oxidation may be an avenue to produce hydroxyl groups that are well characterized for modifications such as silanization to increase hydrophilicity. Nonetheless, thiol-enes still offer a route for rapid prototyping prior to translating the geometries to glass devices. Given large enough device numbers, the etching and bonding of glass can be viable (relatively low cost per device) for both an academic and commercial settings.

*(2) Droplets and emulsions*

The presented flow-focusing chip, with its large feature sizes and dual depth to reduce back pressures, has been quite successful at producing microspheres from 1 µm to 20 µm in size (though larger sizes are possible but were not of interest for the group). Various droplets were produced, PLGA/chloroform, thiol-ene/chloroform and albumin/water (data not shown) highlighting its versatility for a range of applications. However, the system can be translated to all single emulsion needs, by changing the matrix composition or loaded drug.

A particularly valuable area of research and one where thiol-enes have an edge, are double-emulsion droplet generators. This thesis has not explored the production of a double emulsion flow focusing chip, though masking off each junction for a UV-induced hydrophobic then hydrophilic

surface modification has been achieved using the material [147]. Future work with double emulsions can involve high throughput cell analysis [186], microsensing [187] and material synthesis [188].

Based on the thesis presented here, two other applications can be further pursued. In the section below (**Section 9.2.3**), macro-porous thiol-ene structures were implemented to break up larger PLGA droplets into a smaller emulsion. While the resulting particles are far from perfect (and appear to be quite polydisperse), the proof of concept experiment shows that this frit-like structure could be a way to mass-produce small droplets for applications such as chromatography. Mass-production of small droplets can also be implemented using the parallelization of the flow-focusing junction on a single device, yielding mL/hour dispersed phase output [189, 190]. With the rapid prototyping of thiol-ene devices, studies on parallel production would open avenues for pre-clinical studies of the small microspheres.

*(3) Nanoprecipitation and single-phase mixing*

Similar to the droplet microfluidic chip, the nanoparticle producing system is easy to implement further for other targets, certainly as it was developed for siRNA encapsulation. For this, the siRNA sequence can be rather easily changed to encompass a range of diseases where protein downregulation is a therapeutic approach.

For the current TNF-α siRNA loaded LPNs, a long-range of interesting experiments can be performed; generally, comparison studies between the traditional double emulsion solvent evaporation synthetic method and the here presented microfluidic nanoprecipitation. These include siRNA release studies, *in vitro* RAW 264.7 murine macrophage knockdowns, or even small-angle X-ray scattering for structural information. The limiting factor for these has been poor lipidoid solubility in DMSO, generally yielding inconsistent lipid precipitation in the stock solution. Therefore, a pertinent first set of experiments would be the re-formulation of the solvent system, finding a water-miscible solvent that fully dissolves the lipidoid, while maintaining a favorable environment for the siRNA. Unfortunately, with the time-limited PhD, this was not performed.

In addition to LPN production, microfluidic mixing can be used for a range of applications. For example, an area of research is metal-nanocluster-based biosensors. My master's thesis focused on the structural investigation of DNA templated silver nanoclusters for miRNA sensing [191, 192]. Their preparation involves the in-solution reduction of metal ions onto a stabilizing scaffold (such as proteins and nucleic acids). Interestingly, microfluidic mixing is seldom implemented, with to my knowledge, only a gold-palladium cluster system was synthesized using a microfluidic mixer [193]. This research area is open for new studies, with the mixing rate potentially modifying the metal cluster emission wavelength or simply allowing for the production of highly uniform species for enhanced detection or uniformity for structural studies.

# 9. Unpublished Investigations

This chapter aims to provide some insights and know-hows (primarily relevant to the research labs in which this dissertation was conducted in), along with additional findings, or experiments that were not fully successful yet.

## 9.1. Surfaces and material

### 9.1.1. Surface coatings for solvent compatibility

Initially, to try to mitigate the chloroform induced polymer deformation, various covalent and adsorptive coatings were investigated. However, surface coatings are often difficult to execute consistently, without pinhole defects or microscopic cracks. **Figure 9.1** shows both channel deformation (A, C) and solvent-induced mass increase (B, D) with various surface treatments. As most of the coatings were unsuccessful, only two will be described in detail, silanization, and adsorptive FluroPel$^{TM}$ coating.

*Silanization*

Organosilanes are by far the most commonly used coatings, often referred to as giving rise to "glass-like" properties. They have shown great success in increasing the chemical resistance of PDMS [194]. Based on previous optimizations (not included), the combination of the thiol terminated silane ("MTES-thiol") and the allyl terminated silane ("TEOS-ene") seemed most promising in providing a barrier against chlorinated solvents (**Figure 9.2A**). Both silane monomers were combined in ethanol

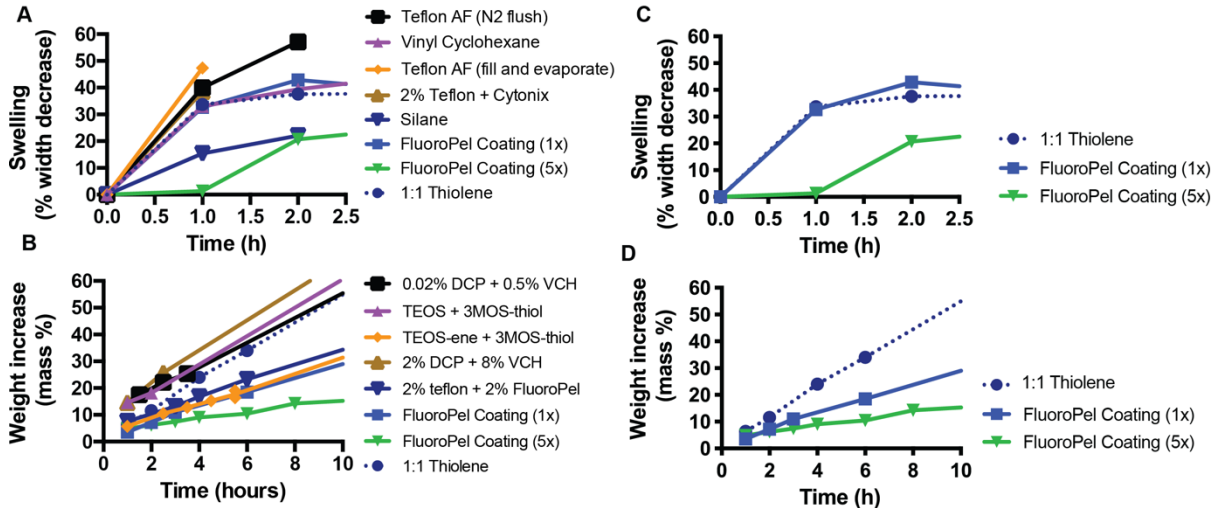


**Figure 9.1. Swelling measurements with various surface coatings. A)** solvent induced channel width decrease or **B)** weight increase at indicated time points of native thiol-ene (dashed), PTFE-based, vinyl cyclohexane polymerized, and silantated materials. **C)** solvent induced channel width decrease or **D)** weight increase at indicated time points of native thiol-ene (blue, dashed), 1x or 5x coated thiol-ene with FluoroPel$^{TM}$.

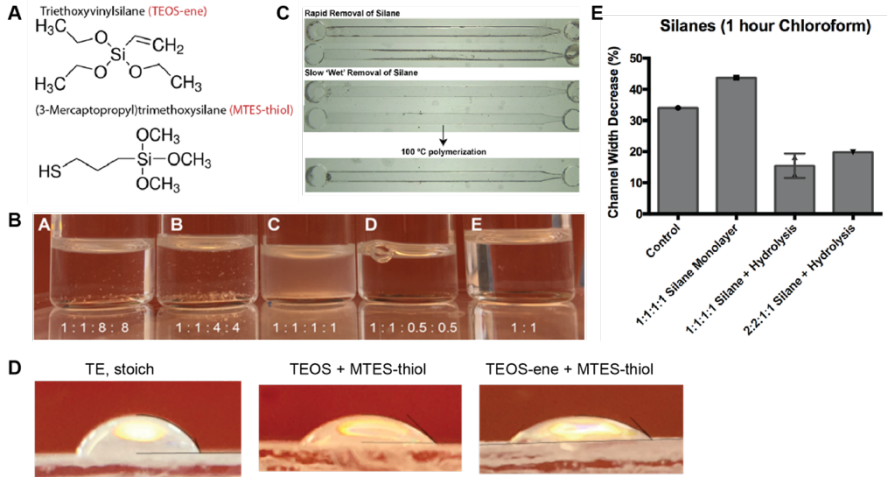


**Figure 9.2. Thiol-ene silanation. A)** Monomers used for silanizations. **B)** Prepolymerization of TEOS-ene + MTES-thiol at indicated ratios (monomer : monomer : EtOH : MQ at pH 4.5). Preconversion seen in the 1:1:1:1 ratio. **C)** channels coated with silanes. Top: $N_2$ removal of UV cured silane results in thick, uneven deposits. Middle: Water/EtOH (wet) removal allows for an even, thin layer formation. Heat polymerization of wet removal results in a dense, yet even coating. **D)** Water contact angles show increased hydrophilicity, consistent with expected results. **E)** Concentration of silanes is less critical than hydrolysis and subsequent polymerization of the oligomer silanes. Silane coated channels were subjected to chloroform for one hour at 20 µL/min flow rate.

and pH 4.5 $H_2O$ (HCl) in a 1:1:1:1 ratio, resulting in a final pH of 5.1. The solutions were let to pre-oligomerize for 24 hours at RT. The solutions were not miscible unless briefly stirred under heating; therefore, initially they were heated at 200 ˚C, until the solution became miscible, opaque and marginally more viscous (**Figure 9.2B,** formulation C).

The final protocol used is as follows: TE chip is first filled with 96% ethanol (as EtOH wets the surface better than water), then without introducing air, the channel is filled with a solution of 50% EtOH in $H_2O$. Again, without introducing air, the channel is flushed 5 times with the pre-oligomerized silane solution containing 5% of the photoinitiator 2,4,6-trimethylbenzoyl-diphenyl-phosphineoxide (TPO). The chip is placed under UV light for 10 seconds (90 mW/cm$^2$, it does not seem to matter if the exposure is split to 5 seconds each side), then rapidly flushed with the original pre-oligomerized silane solution, quickly followed by 50% EtOH, and 96% EtOH to remove the excess material. Finally, $N_2$ is used to dry the channel.

Next the chip is placed on a heat-plate set at 100 °C and let the temperature equilibrate. The wells are filled with non-photoinitiator containing silane, at which point solvent evaporation occurs within seconds. To prolong polymerization, the channel is maintained filled for over 10 seconds, visually resulting in a coating (**Figure 9.2C**). The WCA of silane treated materials decrease, though exact measurements were not taken, see **Figure 9.2D**. One-hour chloroform exposure to the channels shows a marginal, albeit likely significant increase in solvent resistance for the pre-oligomerized TEOS-ene + MTES-thiol modified channels (**Figure 9.2E**), whose protocol was described. In hindsight, the thiol-ene bulk material should have been off-stoichiometric, ideally "ene excess," and only the thiol-terminated silane should have been used with a standard triethoxysilane (TEOS).

*Teflon AF™ and FluroPel™ coating*

Both Teflon AF™ (601S1-100-6, DuPont, 6% solution in FC-75, DuPont) and perfluoroalkyl copolymer (FluoroPel™ PFC-602A, Cytonix) were tested to provide an adsorptive barrier coating against chloroform. While both are fluorinated hydrocarbons, an important difference between Teflon AF™ and FluroPel™ is the temperature at which the solution is heated. FluoroPel™ requires 100 °C for 10 minutes, while Teflon AF™ requires 180 °C+ for 15 minutes +. In fact, for better adhesion, DuPont recommends a 330 °C final bake after solvent evaporation. Coating efficiency was confirmed by contact angle measurements (not shown), producing highly hydrophobic surfaces for both.

Of the conditions tested, FluoroPel™ performed consistently better than Teflon AF™. **Figure 9.1 C, D** shows the swelling data of both disks and channels using FluoroPel™, with a sequential 5x coating showing the highest promise. Importantly for both fluorinated polymers, the hydrophobic contact angles are incompatible with oil-in-water droplet microfluidics, hence the avenue of such coatings was not pursued furhter. However, for an opposite emulsion the method may be applicable, especially if harsh solvents are not required, at which point a single thin layer of FluoroPel™ would be sufficient for a hydrophobic surface.

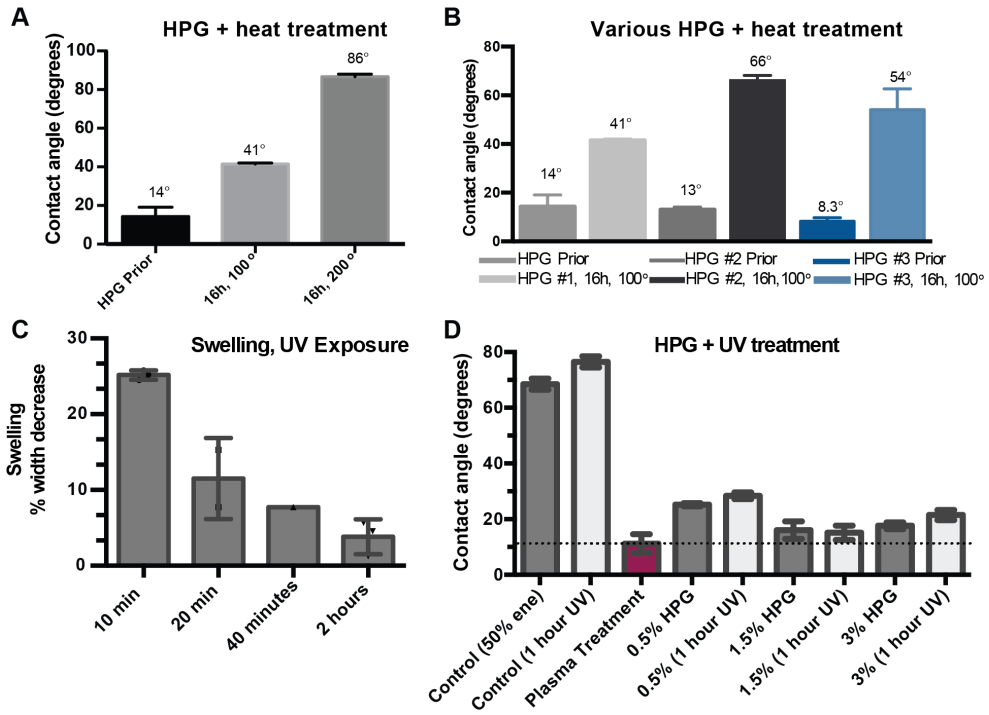


**Figure 9.3. HPG coating and heat incompatibility. A)** Water contact angle of HPG coated discs exposed to 16 h 100 °C or 200 °C heat. **B)** Water contact angle of 200-SH-HPG (#1, light grey), 50-SH-HPG (#2, dark grey), or C-N bond HPG (blue) TE discs exposed to 16 h 100 °C heat treatment. **C)** 1 h chloroform induced channel swelling of 10 min – 2 h UV treated thiol-ene. No photoinitiator added, stoichiometric. **D)** Water contact angle of control TE, plasma treated TE, and various concentrations of HPG used for coating TE discs. Each material was exposed to UV for 1 h, and contact angles measured prior to and after UV exposure. UV refers to 90 mW/cm2 measured at 365 nm.

### 9.1.2. HPG coating and heat compatibility

As discussed previously (in **Section 6.2**), hyper-branched polyglycerol (HPG) was used to modify TEs to yield glass-like contact angles. However, a major pitfall of the material is the inability to heat-treat the coating and retain low contact angles. This limits the use of the materials as true glass alternative, as only plasma treatment can be implemented for both solvent compatibility and high hydrophilicity. Seen in **Figure 9.3A**, a rapid rise in water contact angles occurs upon 16 h 100 °C or 200 °C heat treatment. To solve this, an alternative HPG was synthesized by Katayoun Saatchi, (named here HPG #3 in **Figure 9.3B**) that couples the polyglycerol arms through a C-N bond, as opposed to the previously utilized peptide bond. Theoretically, the elimination of the peptide bond should yield a more resilient coating, both to heat and hydrolysis, though the results show no difference between the two synthetic approaches. It is important to note that significant gains in solvent compatibility can be achieved simply by prolonged UV-treatment of the material (**Figure 9.3C**). Here, of course, substantial heat is generated (up to 120 °C after two hours of 90 mW/cm$^2$ UV, measured with an IR thermometer). Nonetheless, the traditional peptide bond containing HPG

withstands 1 hour of high-intensity UV exposure (**Figure 9.3D**), which generates sufficient solvent compatibility for more mild solvents, or shorter chloroform exposure times.

### 9.1.3. Plausible explaination for solvent compatibility

The fundamental reasoning for the solvent compatibility yielding from heat treatment was not properly investigated nor explained. Based on density measurements (see next section for know-hows), the heated chips have a higher density; hence, we presumed a reduced void volume that yields solvent compatibility. This might as well be the case; however, interesting scattering and a fluorescence property are seen in the heat-treated material. Shown in **Figure 9.4A**, under 365 nm light the heated material (right) is scattering or fluorescing. To investigate further, a mold was fabricated that yields slabs of thiol-ene which snuggly fit into a 10 mm Hellma Quartz fluorescence cuvette. The slabs of material were put into a fluorescence spectrophotometer (Jasco FP-6300, 5 nm excitation and emission slit, medium response and sensitivity, 1 nm data pitch, and 200 nm/min scanning speed) with the emission scanned when excited at 365 nm (the wavelength of the UV light shown before). Shown in **Figure 9.4B** for the ene-excess heat-treated chip, we see emission with a maximum at 450 nm when excited at 365 nm. Therefore, next the origin of the emission was investigated. To do this, the excitation wavelength was varied 10 nm and emission scanned at longer wavelengths. This is in order to differentiate between scattering and a true fluorescent cluster: with

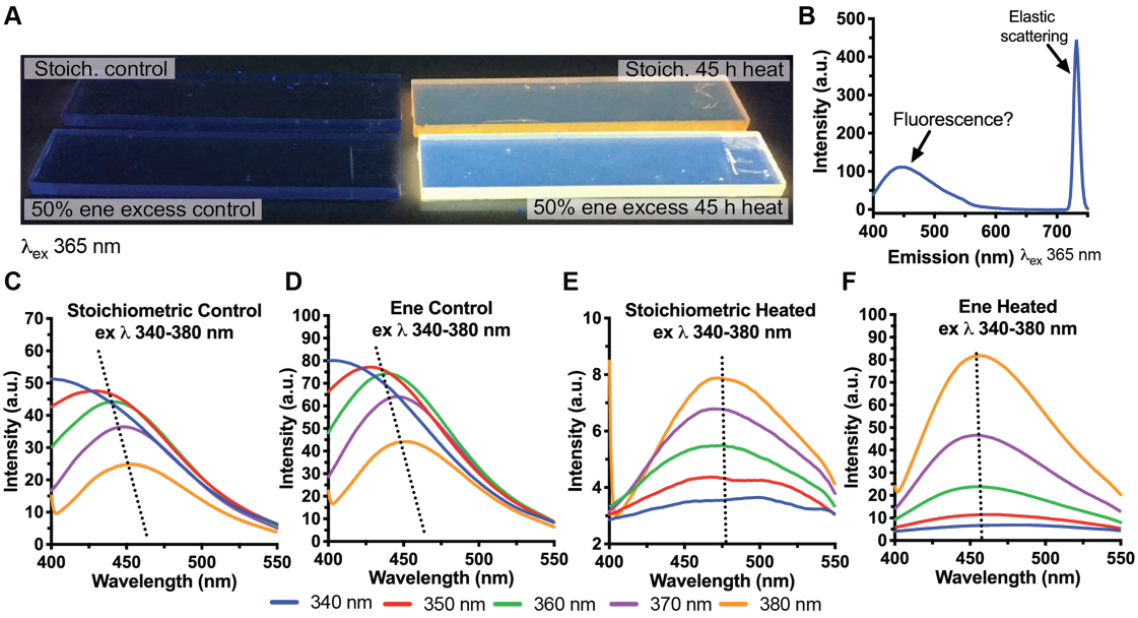


**Figure 9.4. Scattering and fluorescent behavior of heat treated thiol-enes. A)** Slabs of thiol-ene under a handheld 365 nm UV light source. Material either untreated (left), or 60 h heat treated (right), at stoichiometric (top) or 50% ene excess (bottom) formulations. **B)** Fluorescent emission scan of thiol-ene slabs when excited with 365 nm light. Emission scan of **C)** stoichiometric control, **D)** 50%-ene excess control, **E)** stoichiometric heat treated, or **F)** 50% ene-excess heat treated at 340-380 nm excitation wavelengths as indicated.

scattering the emission maxima are progressively increasing with an increasing excitation wavelength, while in fluorescence the emission maxima should stay the same. We see in **Figure 9.4C, D**, the untreated material is scattering near the 365 nm wavelength, such that the maxima are right field shifting with the changing input light. However, for both heat-treated materials, we have a steady fluorescent center at $\lambda_{em}$ 475 nm for the stochiometric (albeit very low intensity) and high-intensity fluorescence center at $\lambda_{em}$ 460 nm for the ene-excess material (**Figure 9.4E, F**). The elastic scattering regions (0.5x, 1x, 2x $\lambda_{ex}$) were not investigated.

The results of forming a fluorescent center hints at the possibility of a chemical (conjugated system) change in the material upon heat treatment. More so, as the 50% ene-excess material exhibits an order of magnitude higher fluorescence, this chemical change may be attributed to the allyl groups. A recent paper by Bowman shows the characteristic orange/yellow hue in his material, which using near-infrared measurements was attributed to vinyl conversion [152]. More specifically, the yellow-colored material shows peaks centered at 6132 $cm^{-1}$, which is characteristic of allylic hydrogen stretches (C=C-H). Therefore, it is entirely possible that under heat treatment the material undergoes a chemical structural rearrangement, forming allylic hydrogen stretches, which then yield a denser material, with a reduced void volume, but also cause the fluorescent centers.

Near-IR study of our material shows the opposite effect (**Figure 9.5**). Duplicates of RT control (green), a 16 h 200 °C (orange), and duplicate 48 h (blue) treated materials were measured. The water content of the material (5250 $cm^{-1}$) decreases with heat exposure, as expected, as it evaporates under the temperatures. Interestingly, the allylic hydrogen stretches (6132 $cm^{-1}$) disappear over the course of heat exposure, contrary to the expected outcome. This can be explained by a potential increase in crosslinking density, such that any free allyl groups are consumed. However, further investigations are needed to confirm the source of the color change and solvent compatibility.

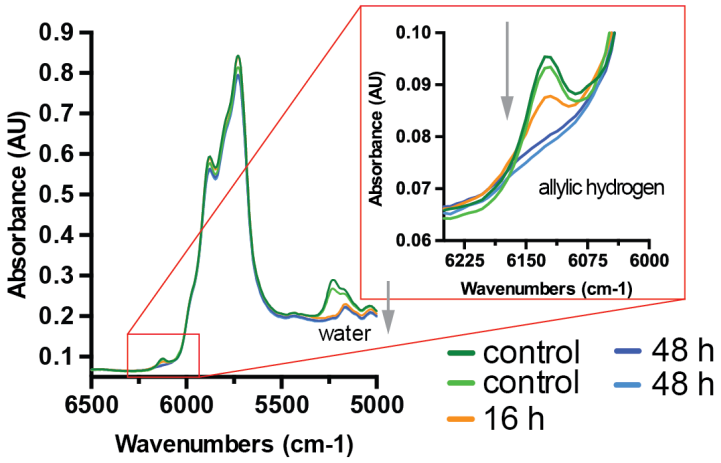


**Figure 9.5. Near-IR absorbance of heated and control TE.** RT control (green), a 16 h 200 °C (orange), and 48 h (blue) treated materials were measured on Shimadzu UV-3600, UV-VIS-NIR Spectrophotometer. Slabs of TE that fit into a 10 mm Hellma Quartz were generated. Absorbance taken from 1000-2000 nm, scan speed fast, data pitch 2 nm, slit width 2 nm.

### 9.1.4. Density measurement of solids (know-how)

A know-how worth mentioning is the simple determination of the density of irregular shaped solids, which was used in the paper in **Appendix I**. The principle is straightforward: prepare a solution of calcium nitrate that is concentrated enough to suspend the solid, then with water additions, dilute the solution until the solid sinks (**Figure 9.6A**). By noting down the amount of extra water added, the final concentration of calcium nitrate can be determined. Then we can use the equation in **Figure 9.6B** to solve for the final density of the solution (which equates to the density of the solid). The equations should be set equal to each other (choose the appropriate one based on the temperature) and solve for "d." Personally, for this MatLab or a CAS equipped calculator can be used for convenience. It is important that once a "rough" density is obtained, the measurement should be repeated with the addition of very small amounts of water increments (say 200 μL for a 100 mL solution), which will allow for a very precise density determination.

**A**

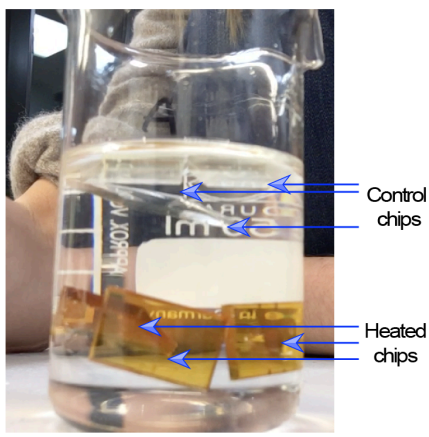


**B**

$$\phi = \frac{1}{d}\left[M_2 - \frac{1000}{m}\frac{(d - d_1)}{d_1}\right] \qquad (1)$$

$$\phi_{25^\circ} = 40.164 + 6.3098m^{1/2} + 0.6472m - 0.1903m^{3/2}$$
$$\phi_{30^\circ} = 42.415 + 4.8587m^{1/2} + 1.0061m - 0.22081m^{3/2}$$
$$\phi_{35^\circ} = 43.200 + 4.9135m^{1/2} + 0.8987m - 0.20738m^{3/2}$$
$$\phi_{40^\circ} = 44.454 + 4.0641m^{1/2} + 1.1143m - 0.22415m^{3/2}$$
$$\phi_{50^\circ} = 46.580 + 3.0556m^{1/2} + 1.3055m - 0.23637m^{3/2}$$
$$\phi_{60^\circ} = 48.001 + 2.5945m^{1/2} + 1.3363m - 0.23274m^{3/2}$$

d= density of $Ca(NO_3)_2 \cdot 4H_2O$
$M_2$= MW of $Ca(NO_3)_2$
m= molarity based on $Ca(NO_3)_2 \cdot 4H_2O$ MW
$d_1$=density of water at given temperature

**Figure 9.6. Density measurement experimental set-up and analysis. A)** set up includes a solution of calcium nitrate suspending various thiol-ene slabs. Water is added until the slabs sunk. **B)** Equations from ref [5] were used to calculate the densities.

A

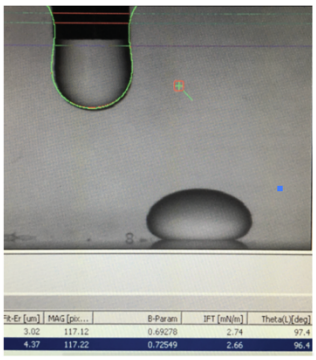


B

| Interfacial Tension (mN/m) | |
|---|---|
| 3.1 | 2.52 |
| 2.5 | 3.18 |
| 3.12 | 2.64 |
| 2.78 | 3.13 |
| 2.39 | 2.84 |
| 3.27 | 2.93 |
| 3.11 | 2.87 |
| 3.05 | 2.74 |
| 2.67 | 2.46 |
| 2.58 | 2.82 |
| 2.9 | 3.61 |
| 2.91 | |
| Average (mN/m) | 2.865 |

**Figure 9.7 Interfacial tension measurement. A)** Example of a measurement on KRUSS DSA100. **B)** Interfacial tension between PLA and PVA.

## 9.2. Emulsions and separations

### 9.2.1. Interfacial tension determination (know-how)

Interfacial tension can be determined in order to calculate the capillary number. For the work shown in **Appendix II**, interfacial tension was determined using the pendant drop method, where 5% PLA in chloroform is suspended in a solution of 1% PVA. Measurements were carried out on the KRUSS DSA100 drop shape analyzer (KRUSS GmbH, Hamburg, Germany). The PLA solution was slowly drop-by-drop injected into a quartz container filled with PVA using a 500 µL Hamilton syringe and an 18-gauge flat tip needle **Figure 9.7A**. Droplet shape and pinch-off was recorded on the camera and interfacial tension determined using the DSA100 software.

The results for the interfacial tension measurements between 5% PLA (10-18 kDa) and 1% PVA (30-70 kDa) are shown in **Figure 9.7B**. Trials were conducted according to the DSA100 Manual, followed word by word. Measurements were repeated 23 times and the average yielded 2.9 ± 0.3 mN/m.

### 9.2.2. Particle sorting: Dean flow and pinched flow fractionation

If the aim is to produce small droplets using microfluidic techniques, then the collection of satellite droplets may be an avenue towards obtaining the desired sized population. Satellite particles form owing to the elasticity of polymer solutions during the retraction of the DP in droplet formation. Often 2-3 sequentially smaller droplets (termed primary, secondary, tertiary satellites) are formed and represent approximately 1% in volume of the parent droplet. Satellite droplets can be particularly useful as the production of small droplets is difficult to achieve owing to the high energy input

needed, though as shown in the **Results and Discussion**, and **Appendix II**, the direct production of small droplets can be achieved.

However, prior to discovering a way to directly produce small droplets, suitable particle sorting methods were investigated in order to isolate satellite droplets. Active particle sorting involves some sort of an external field (acoustic pressure, optical force, magnetic and electric fields etc.). Active sorting is generally more efficient; however, more difficult in terms of fabrication and implementation. Passive sorting manipulates droplets based on channel dimensions and flow fields making implementation easier. It is important to note that the flow rate (or more specifically the flow velocity) can play a critical factor in passive separation efficiency. Therefore, when coupled in-line with a droplet generator chip, an appropriate separation geometry should be chosen. The two passive separators discussed here are pinched for fractionation and Dean flow-based spiral microfluidics.

*Pinched-flow fractionation*

On approach to particle sorting is called pinched flow fractionation (PFF). The design has the critical geometry features shown in [195] (**Figure 9.8A**). Here a continuous phase and a polydisperse emulsion/droplets are introduced into the chip. The continuous phase focuses the droplets on one side of the wall where there is a slight difference in positioning based on the size of the droplets. The droplets then enter a broadening, amplifying the differences in position (that is each droplet is picked up by a laminar flow streamline based on their center of mass), and the particles can be separated through the various outlet channels based on said streamlines. The authors in [195] show the separation of 3.8 ± 1.5, 28.8 ± 7.4, and 47.7 ± 7.4 µm oil droplets using the chip.

To make this chip with 8 inlets/outlets, a commercial chip holder was used (Dolomite Microfluidics) and each outlet channel was made identical in length and depth to avoid differences in backpressures that would skew the separation. The dimensions of the chip are 50 µm overall depth, 100 µm wide inlets converging to 50 µm wide and 100 µm long constriction, followed by a broadening that is formed by the intersection of 6x 200 µm channels. Because of the flow rate limitations (5

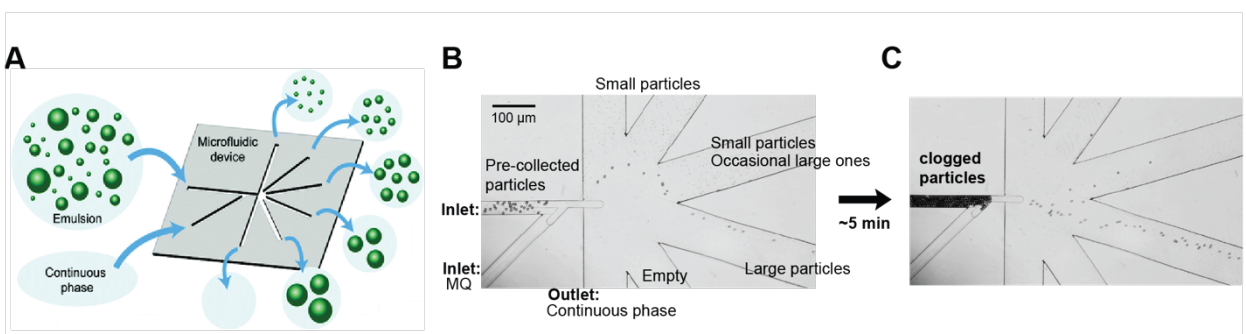


**Figure 9.8. Pinched flow fractionation (PFF)-based separation of satellite particles. A)** Schematic of the pinched flow fractionation chip. Figure reprinted with permissions from ref. [195]. Copyright © 2008 American Chemical Society. **B)** Separation of small and large PLGA particles. **C)** Constant and rapid onset clogging occurs due to the unstable loading of the particles.

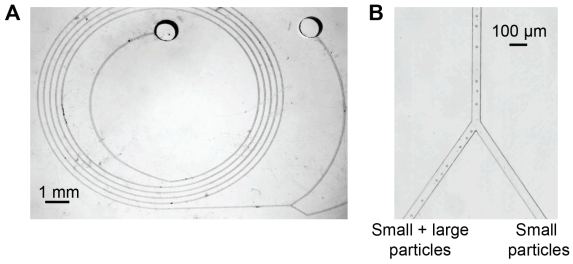


**Figure 9.9. Inertial focusing of satellite particles. A)** Overall image of the spiral chip: 4 mm radius of the first rotation, 5 rotations and 200 µm pitch. **B)** Light microscope image of the separation of 3 µm and 11 µm particles.

µL/min for the particles and 45 µL/min for the continuous phase) already condensed particles were loaded, as flow-focusing droplet formation is often done at 100+ µL/min.

We see in **Figure 9.8B**, all the small particles enter exit channels 1, 2 and 3, with channel 3 occasionally taking in a larger one. Most of the larger parent particles exit channel 4. None of the particles do not enter channel 5 and or the primary exit channel, here only the continuous flow flows there. The primary limitation of this approach is the settling of the pre-formed particles within the syringe and the resulting inconsistent rush of particles within the PFF chip (**Figure 9.8C**). This rush of particles results in the clogging of the constriction, disrupting the flow and hindering with particle collection. The clog can be removed with solvents, but does hinder the utility of the method.

*Dean flow – spiral microfluidic separation*

The initial spiral chip was designed based on Lisa Sprenger's suggestion of the geometry [196]. The spiral has a radius of 4 mm, pitch of 200 µm and 5 rotations with the splitting at the end being even and a final depth of 43 µm (**Figure 9.9A**). In addition to the chip, a new chip holder was printed in PLA. The chip was tested with HPG coating to minimize the interaction between the PLGA particles and the channel walls.

The chip was designed in dimensions to separate already condensed particles -- as opposed to continuous in-line separation. When connecting the flow focusing chip in-line to this spiral chip, the droplets appeared too large, approaching the dimensions of the channel, resulting in strong interaction between the droplet and the channel walls and failing to separate properly. Here the primary droplets at the end of the flow focusing chip are around 44 µm, while the satellite droplets are 10 µm.

Instead, already produced and washed particles in sizes of 3 µm and 11 µm were loaded into the chip. This is a particularly tedious task as the particles end up settling in syringe within seconds or settling in the tubing resulting in a clog. Separation only briefly occurred, with the output of the particle being too low for size analysis. When observed by eye, equal distribution of small particles were evident on both sides of the channel (**Figure 9.9B**). While none of the big particles entered the right exit, a large fraction of the satellites did exit with the primary particles.

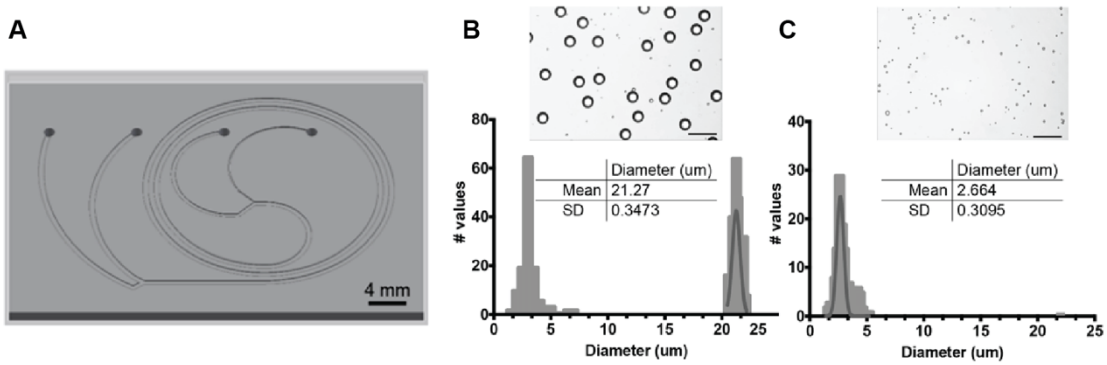


**Figure 9.10. Larger dean flow design. A)** Schematic of spiral microfluidic channels used for dean's flow fractionation. **B)** Histogram of particle distribution for the inner wall channel in Dean's flow chip, **C)** Histogram of particle distribution collected for the outer wall channel. Both: Gaussian fit was approximated to the histogram and mean diameter and standard deviation. Light microscope images taken shown with a 50 µm scale bar.

A larger dean flow chip was designed with an added continuous phase channel and larger channel dimensions in order to separate uncondensed droplets. The channel dimension, radius and pitch is based on ref. [197], with a 500 µm wide and 155 µm deep channel (**Figure 9.10A**). Here, the particles were directly in-line introduced into the spiral chip, with a 1:9 ratio of the droplet sample to continuous flow rate. The starting sample characteristics are shown in **Figure 9.10B**, with an average parent droplet diameter of 20 µm and 3 µm for the satellite particles. Separation of the particles had a much higher output than the previous version and yielded enough particles for quantification. Droplet formation was not impaired with the in-line connected spiral chip. The results show significant clean-up of the small particles, albeit some of the parent particles did contaminate the sample (**Figure 9.10C**).

### 9.2.3. Monoliths to break-up droplets

Thiol-ene monoliths are a collection of thiol-ene beads of approximately 1 µm in diameter, cured within a channel, providing for a macro-porous structure. In order to get small PLGA particles (perhaps even nanoparticles), thiol-ene monolith was used to break up larger droplets (see schematic in **Figure 9.11A**). The monolith length was increased to 7 mm to try to further break up the particles (**Figure 9.11B**), as previously (not shown here) 2.5 mm was not sufficient to break up all the droplets.

Using this chip design, six identical monolith chips were made. Of the six chips, only 1 resulted in ideal droplet breakup properties, the rest resulted in larger microspheres. For the working monolith, in consequence of its length, there was tremendous back pressure prohibiting the proper flow focusing of droplets. Instead intermittent PLGA droplets entered the monolith with some continuous phase (at very low flow rates of under 10 µL/min total flow rate due to the backpressure).

Nonetheless, the exiting droplets were mostly very small, with only seldom getting large droplets (**Figure 9.11C**).

The resulting PLGA droplets were analyzed both with DLS and manually measured by hand through a light microscope image. DLS shows very high PDI's of ~0.3 depending on the specific measurement. The average sizes were 750-800 nm (**Figure 9.11D**). Interestingly, the light microscope shows an average size of 2.4 µm (**Figure 9.11E**) and these particles did not show up on the DLS. Potentially, the particles settled at the bottom of the cuvette, or (most likely) they represent a far smaller fraction than the nanoparticles that are not visible under the light microscope. It is evident that the monolith method is still very much a work in progress, albeit holds promise for the breakup of droplets if monodispersity is not critical.

*Methods for the thiol-ene monolith*: Chip was milled at 50 µm depth with a 100 µm orifice and small indentations on the opening channel to physically hold the monolith in place. The outlet channel is 200 µm in-depth in order to minimize surface interactions between the channel walls and the thiol-ene emulsion. Various monolith conditions were tested in different chip geometries. The best condition as follows: A deeper outlet geometry is better such as 50 µm deep/500 µm wide, or 200 µm deep/600 µm wide all worked far better than 45 µm deep/1000 µm wide. Thiol-ene emulsion is 20% thiol-ene monomers (40% ene excess), and 80% methanol. It is stirred for 5 minutes (2000 rpm), then 10% TPO-L dissolved in EtOH is added to make up 0.1% TPO-L final concentration in the solution (15 µL to 1500 µL). The solution is stirred for an additional 5 minutes, then quickly loaded into the channels. Pre-hydrophilic coated chip is masked off such that 4-7 mm of the outlet channel is exposed to the UV light. It is exposed to 15 mW/cm$^2$ for 60 seconds, then flushed with $N_2$. It is re-exposed for 60 seconds, then washed with MeOH. Then a standard hydrophilic coating is applied to the monolith.

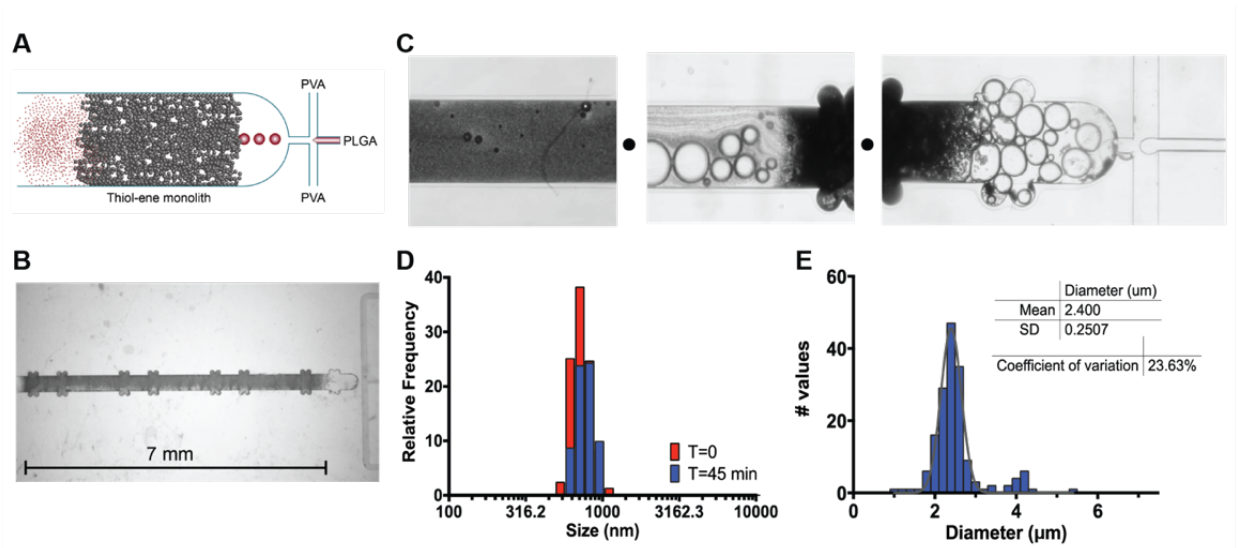


**Figure 9.11. Monolith-based small particle production. A)** Illustration of the thiol-ene monolith in the opening of a flow focusing chip in order to break up the PLGA emulsion. **B)** Example image of a monolith. Denser (or longer) monoliths create too much back pressure. **D)** Dynamic light scattering of the broken-up emulsion at t = 0 and t = 45 min into the production as indicated. **E)** Manually sized particles (t = 0) based on a light microscope image.

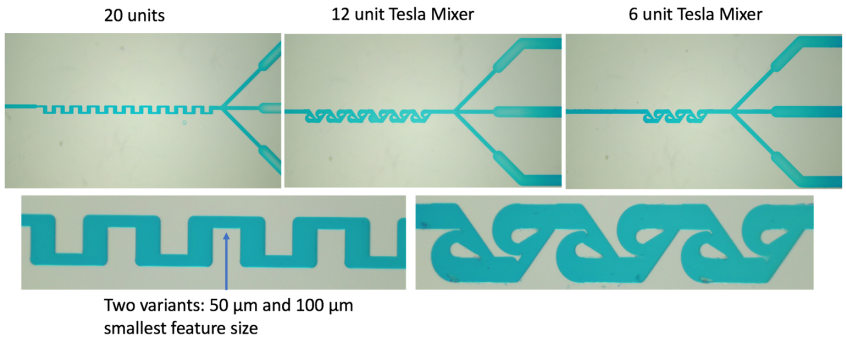


**Figure 9.12. Milled designs.** Two types of designs were milled, a turbulence-based (left) and split and re-combined/turbulence based Tesla mixer (right).

## 9.3. Microfluidic nanoparticle synthesis

Prior to utilizing the microvortex chip for nanoparticle synthesis, a few standard mixing geometries were investigated. The results below show the performance of the Tesla mixer, iLiNP device and the staggered herringbone mixer.

### 9.3.1. Tesla mixer and iLiNP designs

The two alternative chip designs are shown **Figure 9.12**. For the first design, namely the iLiNP chip, the authors show 10 nm size modulation based on the flow rates [104]. The chip design was discussed in **Section 5.5.2**, with the maxing basis relying on convergence and divergence. The second design (the Tesla mixer) is well known and frequently used for NPs -- as an example see the highly cited Valencia *et al.* in *ACS Nano* [97]. Here, different repeats were fabricated, 6 or 12, as varying the repeat amounts modulated may modulate the size range. For the iLiNP design, the on-chip aggregation is immediately apparent, **Figure 9.13A**. The resulting NPs were highly aggregated and hence polydisperse, with the DLS revealing secondary or tertiary peaks, with the average size between 300-500 nm (data not shown). Varying the flow rate (100 µL/min vs. 500 µL/min) does not appear to

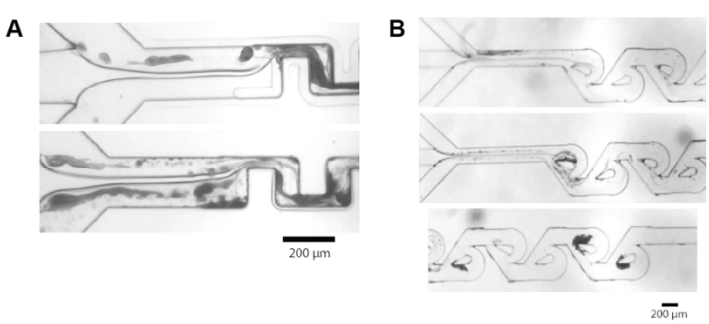


**Figure 9.13. Rapid onset of aggregation with the Tesla and iLiNP design. A)** iLiNP chip and **B)** Tesla mixer. Microscope image taken shortly after starting the NP production under a light microscope. All solutions were mixed from a lipid (10 mg/mL, EtOH) and a PLGA (50 mg/mL, THF) stock solution. siRNA was dissolved in MQ at 1 mg/mL concentration. **A** 4 mg/mL solution (200 **µ**L) at a ratio of 1+4, 2.7 **µ**L of **siRNA** stock added to a tube (2.7 **µ**g), in this 7.3 **µ**L of extra water, then 163 **µ**L of THF, 13 **µ**L of the lipid stock (0.13 mg), finally 13 **µ**L of the PLGA (0.67 mg) added.

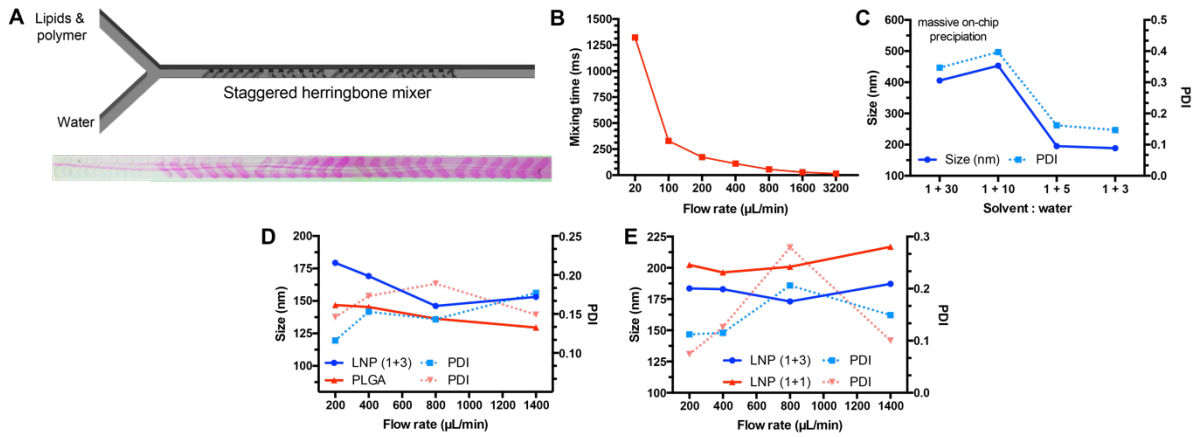


**Figure 9.14. A)** Top: SHM mixer, 300 µm wide, 100 µm deep with extra 70 µm downward grooves that are 100 µm wide. Bottom: microscope image of mixing performance at 20 µL/min. **B)** Mixing performance in milliseconds at indicated flow rates determined using phenolphthalein. **C)** Average NP size and PDI at indicated flow rate ratios. Overall flow rate of 800 µL/min, lipid to PLGA 1 + 2, with a 5 mg/mL overall concentration. **D)** Comparison of the average size and PDI of LNPs (blue) and PLGA only particles (red), at the indicated flow rates. Flow rate ratio of 1 + 3, solvent to water. Overall concentration PLGA or Lipid/PLGA 5 mg/mL. Lipid to PLGA ratio of 1 part to 3 parts. **E)** Size and PDI comparison of increased lipid concentration. One to one lipid to PLGA (red) or one part to three parts lipid to PLGA. Flow rate ratio of 1 + 3, solvent to water at 5 mg/mL concentration. For all samples **C-E**), solvent is acetone with 1.5% ethanol, anti-solvent is MilliQ water. Centrifuged at 15,000g for 5 min at 4 °C, resuspended in MilliQ and DLS obtained.

modulate the size, nor can concrete conclusions be drawn from the flow rate ratio (1:5 or 1:10). Similar results were produced using the Tesla mixer. Rapid onset of aggregation was apparent, **Figure 9.13B**, and the resulting samples all exhibited bi-tri-modal distribution.

The primary reason for the aggregation likely stems from surface interaction between the lipid-PLGA mixture and the thiol-ene chip. Unlike the microvortex chip with 1000 µm x 200 µm channels, both chips here have small feature sizes. In addition, aggregation appears rapidly near the junction of the flow focusing region; therefore, low mixing performance in this diffusion-dominated region may be a strongly contributing factor for aggregation.

### 9.3.2. Staggered-herringbone design for NP production

In order to achieve more rapid mixing, the well-understood staggered herringbone micromixer was tested (**Figure 9.14A** [99, 100]). The results show that the SHM allows for rapid mixing on a ms time scale, that is consistent with previously published data [101], (**Figure 9.14B**). Further tests were run to investigate the ratio of lipid/PLGA to the water phase for size modulation. The results show that a low ratio is required, at least one-part solvent to five parts water, in order to avoid significant on-chip precipitation, even with a hydrophilic surface coating (**Figure 9.14C**). When comparing PLGA (red) and lipid/polymer (blue) nanoparticles, the addition of the lipid increases the mean size of the particles by ~20 nm (**Figure 9.14D**). Both formulations show some degree of size control via the flow

rate; however, the polydispersity of the samples is relatively high. Additional investigation of the lipid concentration was conducted in **Figure 9.14E**, which compares equal concentration of lipid to PLGA (red) and one-part lipid to three-parts PLGA (blue). Here, it is evident that further increasing the lipid concentration increases the mean size of the NPs. As seen before, the PDIs are relatively high as well. Moreover, the mean size with relation to the flow rate is inconsistent, resulting in larger particles at higher flow rates. Overall, these results shed doubt on the effectiveness of the SHM, in particular with regards to consistency and monodispersity. Further investigation of the SHM mixer was not conducted.

# 10. References


1. Haag, R. and F. Kratz, *Polymer therapeutics: concepts and applications,* Angewandte Chemie International Edition, **2006**. 45(8): p. 1198-215.
2. Li, C., J. Wang, Y. Wang, H. Gao, G. Wei, Y. Huang, H. Yu, Y. Gan, Y. Wang, L. Mei, H. Chen, H. Hu, Z. Zhang, and Y. Jin, *Recent progress in drug delivery,* Acta Pharm Sin B, **2019**. 9(6): p. 1145-1162.
3. Dietzel, A., *Microsystems for pharmatechnology: Manipulation of Fluids, Particles, Droplets, and Cells.* Vol. 1. **2016**: Springer.
4. Janssen, M., G. Mihov, T. Welting, J. Thies, and P. Emans, *Drugs and Polymers for Delivery Systems in OA Joints: Clinical Needs and Opportunities,* Polymers, **2014**. 6(3).
5. Stefánsson, E. and T. Loftsson, *CHAPTER 13 - Microspheres and nanotechnology for drug delivery*, in *Retinal Pharmacotherapy*, Q.D. Nguyen, et al., Editors. **2010**, W.B. Saunders: Edinburgh. p. 86-90.
6. Slack, J.D., M. Kanke, G.H. Simmons, and P.P. Deluca, *Acute hemodynamic effects and blood pool kinetics of polystyrene microspheres following intravenous administration,* Journal of Pharmaceutical Sciences, **1981**. 70(6): p. 660-664.
7. Ernsting, M.J., M. Murakami, A. Roy, and S.D. Li, *Factors controlling the pharmacokinetics, biodistribution and intratumoral penetration of nanoparticles,* Journal of Controlled Release, **2013**. 172(3): p. 782-94.
8. Kakar, S., D. Batra, R. Singh, and U. Nautiyal, *Magnetic microspheres as magical novel drug delivery system: A review,* Journal of Acute Disease, **2013**. 2(1): p. 1-12.
9. Müller, K., D.A. Fedosov, and G. Gompper, *Margination of micro- and nano-particles in blood flow and its effect on drug delivery,* Scientific Reports, **2014**. 4: p. 4871.
10. Kanke, M., G.H. Simmons, D.L. Weiss, B.A. Bivins, and P.P. Deluca, *Clearance of 141Ce-labeled microspheres from blood and distribution in specific organs following intravenous and intraarterial administration in beagle dogs,* Journal of Pharmaceutical Sciences, **1980**. 69(7): p. 755-762.
11. Brazeau, G., S.L. Sauberan, L. Gatlin, P. Wisniecki, and J. Shah, *Effect of particle size of parenteral suspensions on in vitro muscle damage,* Pharmaceutical Development and Technology, **2011**. 16(6): p. 591-598.
12. Labiris, N.R. and M.B. Dolovich, *Pulmonary drug delivery. Part I: Physiological factors affecting therapeutic effectiveness of aerosolized medications,* British Journal of Clinical Pharmacology, **2003**. 56(6): p. 588-599.
13. Cooper, R.C. and H. Yang, *Hydrogel-based ocular drug delivery systems: Emerging fabrication strategies, applications, and bench-to-bedside manufacturing considerations,* Journal of Controlled Release, **2019**. 306: p. 29-39.
14. Luppi, B., F. Bigucci, T. Cerchiara, and V. Zecchi, *Chitosan-based hydrogels for nasal drug delivery: from inserts to nanoparticles,* Expert Opinion on Drug Delivery, **2010**. 7(7): p. 811-828.
15. Miele, E., G.P. Spinelli, E. Miele, F. Tomao, and S. Tomao, *Albumin-bound formulation of paclitaxel (Abraxane (R) ABI-007) in the treatment of breast cancer,* International Journal of Nanomedicine, **2009**. 4(1): p. 99-105.
16. Adams, D., A. Gonzalez-Duarte, W.D. O'Riordan, C.C. Yang, M. Ueda, A.V. Kristen, I. Tournev, H.H. Schmidt, T. Coelho, J.L. Berk, K.P. Lin, G. Vita, S. Attarian, V. Plante-Bordeneuve, M.M. Mezei, J.M. Campistol, J. Buades, T.H. Brannagan, B.J. Kim, J. Oh, Y. Parman, Y. Sekijima, P.N. Hawkins, S.D. Solomon, M. Polydefkis, P.J. Dyck, P.J. Gandhi, S. Goyal, J. Chen, A.L. Strahs, S.V. Nochur, M.T. Sweetser, P.P. Garg, A.K. Vaishnaw, J.A. Gollob, and O.B. Suhr, *Patisiran, an RNAi Therapeutic, for Hereditary Transthyretin Amyloidosis,* New England Journal of Medicine, **2018**. 379(1): p. 11-21.

17. Cohen, J.L., J. Cheirif, D.S. Segar, L.D. Gillam, J.S. Gottdiener, E. Hausnerova, and D.E. Bruns, *Improved left ventricular endocardial border delineation and opacification with OPTISON (FS069), a new echocardiographic contrast agent - Results of a phase III multicenter trial,* Journal of the American College of Cardiology, **1998**. 32(3): p. 746-752.
18. Salem, R. and R.D. Hunter, *Yttrium-90 microspheres for the treatment of hepatocellular carcinoma: A review,* International Journal of Radiation Oncology Biology Physics, **2006**. 66(2): p. S83-S88.
19. Danaei, M., M. Dehghankhold, S. Ataei, F. Hasanzadeh Davarani, R. Javanmard, A. Dokhani, S. Khorasani, and M.R. Mozafari, *Impact of Particle Size and Polydispersity Index on the Clinical Applications of Lipidic Nanocarrier Systems,* Pharmaceutics, **2018**. 10(2).
20. Li, M., O. Rouaud, and D. Poncelet, *Microencapsulation by solvent evaporation: state of the art for process engineering approaches,* Int J Pharm, **2008**. 363(1-2): p. 26-39.
21. Gentile, P., V. Chiono, I. Carmagnola, and P.V. Hatton, *An Overview of Poly(lactic-co-glycolic) Acid (PLGA)-Based Biomaterials for Bone Tissue Engineering,* International Journal of Molecular Sciences, **2014**. 15(3): p. 3640-3659.
22. Prajapati, S.K., A. Jain, A. Jain, and S. Jain, *Biodegradable polymers and constructs: A novel approach in drug delivery,* European Polymer Journal, **2019**. 120.
23. Auras, R., B. Harte, and S. Selke, *An overview of polylactides as packaging materials,* Macromolecular Bioscience, **2004**. 4(9): p. 835-864.
24. Whitehead, K.A., J.R. Dorkin, A.J. Vegas, P.H. Chang, O. Veiseh, J. Matthews, O.S. Fenton, Y.L. Zhang, K.T. Olejnik, V. Yesilyurt, D.L. Chen, S. Barros, B. Klebanov, T. Novobrantseva, R. Langer, and D.G. Anderson, *Degradable lipid nanoparticles with predictable in vivo siRNA delivery activity,* Nature Communications, **2014**. 5.
25. Thanki, K., X. Zeng, S. Justesen, S. Tejlmann, E. Falkenberg, E. Van Driessche, H. Morck Nielsen, H. Franzyk, and C. Foged, *Engineering of small interfering RNA-loaded lipidoid-poly(DL-lactic-co-glycolic acid) hybrid nanoparticles for highly efficient and safe gene silencing: A quality by design-based approach,* European Journal of Pharmaceutics and Biopharmaceutics, **2017**. 120: p. 22-33.
26. Barba, A.A., S. Bochicchio, A. Dalmoro, and G. Lamberti, *Lipid Delivery Systems for Nucleic-Acid-Based-Drugs: From Production to Clinical Applications,* Pharmaceutics, **2019**. 11(8).
27. Lin, Q.Y., J. Chen, Z.H. Zhang, and G. Zheng, *Lipid-based nanoparticles in the systemic delivery of siRNA,* Nanomedicine, **2014**. 9(1): p. 105-120.
28. Jensen, D.K., L.B. Jensen, S. Koocheki, L. Bengtson, D.M. Cun, H.M. Nielsen, and C. Foged, *Design of an inhalable dry powder formulation of DOTAP-modified PLGA nanoparticles loaded with siRNA,* Journal of Controlled Release, **2012**. 157(1): p. 141-148.
29. Hasan, W., K. Chu, A. Gullapalli, S.S. Dunn, E.M. Enlow, J.C. Luft, S.M. Tian, M.E. Napier, P.D. Pohlhaus, J.P. Rolland, and J.M. DeSimone, *Delivery of Multiple siRNAs Using Lipid-Coated PLGA Nanoparticles for Treatment of Prostate Cancer,* Nano Letters, **2012**. 12(1): p. 287-292.
30. Cun, D.M., D.K. Jensen, M.J. Maltesen, M. Bunker, P. Whiteside, D. Scurr, C. Foged, and H.M. Nielsen, *High loading efficiency and sustained release of siRNA encapsulated in PLGA nanoparticles: Quality by design optimization and characterization,* European Journal of Pharmaceutics and Biopharmaceutics, **2011**. 77(1): p. 26-35.
31. Akinc, A., A. Zumbuehl, M. Goldberg, E.S. Leshchiner, V. Busini, N. Hossain, S.A. Bacallado, D.N. Nguyen, J. Fuller, R. Alvarez, A. Borodovsky, T. Borland, R. Constien, A. de Fougerolles, J.R. Dorkin, K.N. Jayaprakash, M. Jayaraman, M. John, V. Koteliansky, M. Manoharan, L. Nechev, J. Qin, T. Racie, D. Raitcheva, K.G. Rajeev, D.W.Y. Sah, J. Soutschek, I. Toudjarska, H.P. Vornlocher, T.S. Zimmermann, R. Langer, and D.G. Anderson, *A combinatorial library of lipid-like materials for delivery of RNAi therapeutics,* Nature Biotechnology, **2008**. 26(5): p. 561-569.
32. Love, K.T., K.P. Mahon, C.G. Levins, K.A. Whitehead, W. Querbes, J.R. Dorkin, J. Qin, W. Cantley, L.L. Qin, T. Racie, M. Frank-Kamenetsky, K.N. Yip, R. Alvarez, D.W.Y. Sah, A. de Fougerolles, K. Fitzgerald, V. Koteliansky, A. Akinc, R. Langer, and D.G. Anderson, *Lipid-like materials for low-dose,*

*in vivo gene silencing,* Proceedings of the National Academy of Sciences of the United States of America, **2010**. 107(5): p. 1864-1869.

33. Yan, W.L., W.S. Chen, and L. Huang, *Reactive oxygen species play a central role in the activity of cationic liposome based cancer vaccine,* Journal of Controlled Release, **2008**. 130(1): p. 22-28.
34. Aramaki, Y., S. Takano, and S. Tsuchiya, *Induction of apoptosis in macrophages by cationic liposomes,* Febs Letters, **1999**. 460(3): p. 472-476.
35. Fessi, H., F. Puisieux, J.P. Devissaguet, N. Ammoury, and S. Benita, *Nanocapsule formation by interfacial polymer deposition following solvent displacement,* International Journal of Pharmaceutics, **1989**. 55(1): p. R1-R4.
36. Lassalle, V. and M.L. Ferreira, *PLA nano- and microparticles for drug delivery: an overview of the methods of preparation,* Macromolecular Bioscience, **2007**. 7(6): p. 767-83.
37. Horn, D. and J. Rieger, *Organic Nanoparticles in the Aqueous Phase—Theory, Experiment, and Use,* Angewandte Chemie International Edition, **2001**. 40(23): p. 4330-4361.
38. Lince, F., D.L. Marchisio, and A.A. Barresi, *Strategies to control the particle size distribution of poly-epsilon-caprolactone nanoparticles for pharmaceutical applications,* J Colloid Interface Sci, **2008**. 322(2): p. 505-15.
39. Martinez Rivas, C.J., M. Tarhini, W. Badri, K. Miladi, H. Greige-Gerges, Q.A. Nazari, S.A. Galindo Rodriguez, R.A. Roman, H. Fessi, and A. Elaissari, *Nanoprecipitation process: From encapsulation to drug delivery,* International Journal of Pharmaceutics, **2017**. 532(1): p. 66-81.
40. Umbanhowar, P.B., V. Prasad, and D.A. Weitz, *Monodisperse Emulsion Generation via Drop Break Off in a Coflowing Stream,* Langmuir, **2000**. 16(2): p. 347-351.
41. Edel, J.B., R. Fortt, J.C. deMello, and A.J. deMello, *Microfluidic routes to the controlled production of nanoparticles,* Chemical Communications, **2002**(10): p. 1136-1137.
42. Li, X., S.S. Wei, L.C. Chen, G. Qu, H.S. Zhang, Z. Liu, L.Q. Wang, T.T. Kong, and T.F. Wang, *Pulsation of electrified jet in capillary microfluidics,* Scientific Reports, **2017**. 7.
43. Jeong, W.C., J.M. Lim, J.H. Choi, J.H. Kim, Y.J. Lee, S.H. Kim, G. Lee, J.D. Kim, G.R. Yi, and S.M. Yang, *Controlled generation of submicron emulsion droplets via highly stable tip-streaming mode in microfluidic devices,* Lab on a Chip, **2012**. 12(8): p. 1446-1453.
44. Tabeling, P., *Introduction to microfluidics*. 2005: OUP Oxford.
45. Lin, B., *Microfluidics: technologies and applications*. Vol. 304. **2011**: Springer.
46. Utada, A.S., A. Fernandez-Nieves, H.A. Stone, and D.A. Weitz, *Dripping to jetting transitions in coflowing liquid streams,* Physical Review Letters, **2007**. 99(9): p. 094502.
47. Anna, S.L., *Droplets and Bubbles in Microfluidic Devices,* Annual Review of Fluid Mechanics, **2016**. 48(1): p. 285-309.
48. Gordillo, J.M., A. Sevilla, and F. Campo-Cortés, *Global stability of stretched jets: conditions for the generation of monodisperse micro-emulsions using coflows,* Journal of Fluid Mechanics, **2014**. 738: p. 335-357.
49. Abate, A.R., A. Poitzsch, Y. Hwang, J. Lee, J. Czerwinska, and D.A. Weitz, *Impact of inlet channel geometry on microfluidic drop formation,* Physical Review E, **2009**. 80(2 Pt 2): p. 026310.
50. Thorsen, T., R.W. Roberts, F.H. Arnold, and S.R. Quake, *Dynamic pattern formation in a vesicle-generating microfluidic device,* Phys Rev Lett, **2001**. 86(18): p. 4163-6.
51. Nisisako, T. and T. Torii, *Microfluidic large-scale integration on a chip for mass production of monodisperse droplets and particles,* Lab on a Chip, **2008**. 8(2): p. 287-93.
52. Ganan-Calvo, A.M. and J.M. Gordillo, *Perfectly monodisperse microbubbling by capillary flow focusing,* Phys Rev Lett, **2001**. 87(27 Pt 1): p. 274501.
53. Ganan-Calvo, A.M., *Perfectly monodisperse microbubbling by capillary flow focusing: an alternate physical description and universal scaling,* Physical Review E, **2004**. 69(2 Pt 2): p. 027301.
54. Takeuchi, S., P. Garstecki, D.B. Weibel, and G.M. Whitesides, *An Axisymmetric Flow-Focusing Microfluidic Device,* Advanced Materials, **2005**. 17(8): p. 1067-1072.

55. Anna, S.L., N. Bontoux, and H.A. Stone, *Formation of dispersions using "flow focusing" in microchannels,* Applied Physics Letters, **2003**. 82(3): p. 364-366.
56. Gonzalez-Estefan, J.H., M. Gonidec, T.T. Vu, N. Daro, and G. Chastanet, *In Situ Fine-Tuning of Microfluidic Chips by Swelling and Its Application to Droplet Microfluidics,* Advanced Materials Technologies, **2019**. 4(8).
57. Stan, C.A., S.K.Y. Tang, and G.M. Whitesides, *Independent Control of Drop Size and Velocity in Microfluidic Flow-Focusing Generators Using Variable Temperature and Flow Rate,* Analytical Chemistry, **2009**. 81(6): p. 2399-2402.
58. Serra, C., N. Berton, M. Bouquey, L. Prat, and G. Hadziioannou, *A predictive approach of the influence of the operating parameters on the size of polymer particles synthesized in a simplified microfluidic system,* Langmuir, **2007**. 23(14): p. 7745-7750.
59. Husny, J. and J.J. Cooper-White, *The effect of elasticity on drop creation in T-shaped microchannels,* Journal of Non-Newtonian Fluid Mechanics, **2006**. 137(1-3): p. 121-136.
60. Garstecki, P., I. Gitlin, W. DiLuzio, G.M. Whitesides, E. Kumacheva, and H.A. Stone, *Formation of monodisperse bubbles in a microfluidic flow-focusing device,* Applied Physics Letters, **2004**. 85(13): p. 2649-2651.
61. Cramer, C., P. Fischer, and E.J. Windhab, *Drop formation in a co-flowing ambient fluid,* Chemical Engineering Science, **2004**. 59(15): p. 3045-3058.
62. Anna, S.L. and H.C. Mayer, *Microscale tipstreaming in a microfluidic flow focusing device,* Physics of Fluids, **2006**. 18(12): p. 121512.
63. Zhu, P., T. Kong, Z. Kang, X. Tian, and L. Wang, *Tip-multi-breaking in Capillary Microfluidic Devices,* Sci Rep, **2015**. 5: p. 11102.
64. Zhu, P. and L. Wang, *Passive and active droplet generation with microfluidics: a review,* Lab on a Chip, **2017**. 17(1): p. 34-75.
65. Tice, J.D., A.D. Lyon, and R.F. Ismagilov, *Effects of viscosity on droplet formation and mixing in microfluidic channels,* Analytica Chimica Acta, **2004**. 507(1): p. 73-77.
66. Christopher, G.F. and S.L. Anna, *Microfluidic methods for generating continuous droplet streams,* Journal of Physics D: Applied Physics, **2007**. 40(19): p. R319.
67. Baroud, C.N., F. Gallaire, and R. Dangla, *Dynamics of microfluidic droplets,* Lab on a Chip, **2010**. 10(16): p. 2032-45.
68. Christopher, G.F., N.N. Noharuddin, J.A. Taylor, and S.L. Anna, *Experimental observations of the squeezing-to-dripping transition in T-shaped microfluidic junctions,* Phys Rev E Stat Nonlin Soft Matter Phys, **2008**. 78(3 Pt 2): p. 036317.
69. Erb, R.M., D. Obrist, P.W. Chen, J. Studer, and A.R. Studart, *Predicting sizes of droplets made by microfluidic flow-induced dripping,* Soft Matter, **2011**. 7(19): p. 8757-8761.
70. Cubaud, T. and T.G. Mason, *Capillary threads and viscous droplets in square microchannels,* Physics of Fluids, **2008**. 20(5): p. 053302.
71. Suryo, R. and O.A. Basaran, *Tip streaming from a liquid drop forming from a tube in a co-flowing outer fluid,* Physics of Fluids, **2006**. 18(8).
72. Ward, T., M. Faivre, and H.A. Stone, *Drop Production and Tip-Streaming Phenomenon in a Microfluidic Flow-Focusing Device via an Interfacial Chemical Reaction,* Langmuir, **2010**. 26(12): p. 9233-9239.
73. Lee, W., L.M. Walker, and S.L. Anna, *Role of geometry and fluid properties in droplet and thread formation processes in planar flow focusing,* Physics of Fluids, **2009**. 21(3).
74. Tseng, Y.H. and A. Prosperetti, *Local interfacial stability near a zero vorticity point,* Journal of Fluid Mechanics, **2015**. 776: p. 5-36.
75. Zhu, P.G., T.T. Kong, L.Y. Lei, X.W. Tian, Z.X. Kang, and L.Q. Wang, *Droplet Breakup in Expansion-contraction Microchannels,* Scientific Reports, **2016**. 6.

76. Gu, H., M.H.G. Duits, and F. Mugele, *Droplets Formation and Merging in Two-Phase Flow Microfluidics,* International Journal of Molecular Sciences, **2011**. 12(4): p. 2572-2597.
77. Belder, D. and M. Ludwig, *Surface modification in microchip electrophoresis,* Electrophoresis, **2003**. 24(21): p. 3595-606.
78. Handique, K., D.T. Burke, C.H. Mastrangelo, and M.A. Burns, *Nanoliter liquid metering in microchannels using hydrophobic patterns,* Analytical Chemistry, **2000**. 72(17): p. 4100-4109.
79. Xia, Y.N. and G.M. Whitesides, *Soft lithography,* Angewandte Chemie-International Edition, **1998**. 37(5): p. 550-575.
80. Wägli, P., A. Homsy, and N.F. de Rooij, *Norland optical adhesive (NOA81) microchannels with adjustable wetting behavior and high chemical resistance against a range of mid-infrared-transparent organic solvents,* Sensors and Actuators B: Chemical, **2011**. 156(2): p. 994-1001.
81. Sollier, E., C. Murray, P. Maoddi, and D. Di Carlo, *Rapid prototyping polymers for microfluidic devices and high pressure injections,* Lab on a Chip, **2011**. 11(22): p. 3752-65.
82. Chung, C.H.Y., B.B. Cui, R.Y. Song, X. Liu, X.N. Xu, and S.H. Yao, *Scalable Production of Monodisperse Functional Microspheres by Multilayer Parallelization of High Aspect Ratio Microfluidic Channels,* Micromachines, **2019**. 10(9).
83. Karnik, R., F. Gu, P. Basto, C. Cannizzaro, L. Dean, W. Kyei-Manu, R. Langer, and O.C. Farokhzad, *Microfluidic platform for controlled synthesis of polymeric nanoparticles,* Nano Letters, **2008**. 8(9): p. 2906-12.
84. Limayem Blouza, I., C. Charcosset, S. Sfar, and H. Fessi, *Preparation and characterization of spironolactone-loaded nanocapsules for paediatric use,* International Journal of Pharmaceutics, **2006**. 325(1): p. 124-131.
85. Martin-Banderas, L., J. Alvarez-Fuentes, M. Duran-Lobato, J. Prados, C. Melguizo, M. Fernandez-Arevalo, and M.A. Holgado, *Cannabinoid derivate-loaded PLGA nanocarriers for oral administration: formulation, characterization, and cytotoxicity studies,* Int J Nanomedicine, **2012**. 7: p. 5793-806.
86. Lim, J.-M., A. Swami, L.M. Gilson, S. Chopra, S. Choi, J. Wu, R. Langer, R. Karnik, and O.C. Farokhzad, *Ultra-High Throughput Synthesis of Nanoparticles with Homogeneous Size Distribution Using a Coaxial Turbulent Jet Mixer,* ACS Nano, **2014**. 8(6): p. 6056-6065.
87. Seremeta, K.P., D.A. Chiappetta, and A. Sosnik, *Poly(ε-caprolactone), Eudragit® RS 100 and poly(ε-caprolactone)/Eudragit® RS 100 blend submicron particles for the sustained release of the antiretroviral efavirenz,* Colloids and Surfaces B: Biointerfaces, **2013**. 102: p. 441-449.
88. Legrand, P., S. Lesieur, A. Bochot, R. Gref, W. Raatjes, G. Barratt, and C. Vauthier, *Influence of polymer behaviour in organic solution on the production of polylactide nanoparticles by nanoprecipitation,* Int J Pharm, **2007**. 344(1-2): p. 33-43.
89. Zhu, X., W. Tao, D. Liu, J. Wu, Z. Guo, X. Ji, Z. Bharwani, L. Zhao, X. Zhao, O.C. Farokhzad, and J. Shi, *Surface De-PEGylation Controls Nanoparticle-Mediated siRNA Delivery In Vitro and In Vivo,* Theranostics, **2017**. 7(7): p. 1990-2002.
90. Bilati, U., E. Allémann, and E. Doelker, *Development of a nanoprecipitation method intended for the entrapment of hydrophilic drugs into nanoparticles,* European Journal of Pharmaceutical Sciences, **2005**. 24(1): p. 67-75.
91. Yoo, H.S., H.K. Choi, and T.G. Park, *Protein–fatty acid complex for enhanced loading and stability within biodegradable nanoparticles,* Journal of Pharmaceutical Sciences, **2001**. 90(2): p. 194-201.
92. Asadi, H., K. Rostamizadeh, D. Salari, and M. Hamidi, *Preparation of biodegradable nanoparticles of tri-block PLA–PEG–PLA copolymer and determination of factors controlling the particle size using artificial neural network,* Journal of Microencapsulation, **2011**. 28(5): p. 406-416.
93. Budhian, A., S.J. Siegel, and K.I. Winey, *Haloperidol-loaded PLGA nanoparticles: systematic study of particle size and drug content,* Int J Pharm, **2007**. 336(2): p. 367-75.
94. Lee, C.Y., C.L. Chang, Y.N. Wang, and L.M. Fu, *Microfluidic mixing: a review,* International Journal of Molecular Sciences, **2011**. 12(5): p. 3263-87.

95. Cai, G., L. Xue, H. Zhang, and J. Lin, *A Review on Micromixers,* Micromachines (Basel), **2017**. 8(9).
96. Hong, C.C., J.W. Choi, and C.H. Ahn, *A novel in-plane passive microfluidic mixer with modified Tesla structures,* Lab on a Chip, **2004**. 4(2): p. 109-113.
97. Valencia, P.M., P.A. Basto, L.F. Zhang, M. Rhee, R. Langer, O.C. Farokhzad, and R. Karnik, *Single-Step Assembly of Homogenous Lipid - Polymeric and Lipid - Quantum Dot Nanoparticles Enabled by Microfluidic Rapid Mixing,* ACS Nano, **2010**. 4(3): p. 1671-1679.
98. Stroock, A.D., S.K.W. Dertinger, A. Ajdari, I. Mezic, H.A. Stone, and G.M. Whitesides, *Chaotic mixer for microchannels,* Science, **2002**. 295(5555): p. 647-651.
99. Feng, Q., J. Sun, and X. Jiang, *Microfluidics-mediated assembly of functional nanoparticles for cancer-related pharmaceutical applications,* Nanoscale, **2016**. 8(25): p. 12430-43.
100. Jiang, X.Y., J.M.K. Ng, A.D. Stroock, S.K.W. Dertinger, and G.M. Whitesides, *A miniaturized, parallel, serially diluted immunoassay for analyzing multiple antigens,* Journal of the American Chemical Society, **2003**. 125(18): p. 5294-5295.
101. Belliveau, N.M., J. Huft, P.J.C. Lin, S. Chen, A.K.K. Leung, T.J. Leaver, A.W. Wild, J.B. Lee, R.J. Taylor, Y.K. Tam, C.L. Hansen, and P.R. Cullis, *Microfluidic Synthesis of Highly Potent Limit-size Lipid Nanoparticles for In Vivo Delivery of siRNA,* Molecular Therapy-Nucleic Acids, **2012**. 1.
102. Rungta, R.L., H.B. Choi, P.J.C. Lin, R.W.Y. Ko, D. Ashby, J. Nair, M. Manoharan, P.R. Cullis, and B.A. MacVicar, *Lipid Nanoparticle Delivery of siRNA to Silence Neuronal Gene Expression in the Brain,* Molecular Therapy-Nucleic Acids, **2013**. 2.
103. Afzal, A. and K.Y. Kim, *Convergent-divergent micromixer coupled with pulsatile flow,* Sensors and Actuators B-Chemical, **2015**. 211: p. 198-205.
104. Kimura, N., M. Maeki, Y. Sato, Y. Note, A. Ishida, H. Tani, H. Harashima, and M. Tokeshi, *Development of the iLiNP Device: Fine Tuning the Lipid Nanoparticle Size within 10 nm for Drug Delivery,* Acs Omega, **2018**. 3(5): p. 5044-5051.
105. Terry, S.C., J.H. Jerman, and J.B. Angell, *A gas chromatographic air analyzer fabricated on a silicon wafer,* IEEE Transactions on Electron Devices, **1979**. 26(12): p. 1880-1886.
106. Harrison, D.J., A. Manz, Z. Fan, H. Luedi, and H.M. Widmer, *Capillary electrophoresis and sample injection systems integrated on a planar glass chip,* Analytical Chemistry, **1992**. 64(17): p. 1926-1932.
107. Kim, E., Y. Xia, and G.M. Whitesides, *Polymer microstructures formed by moulding in capillaries,* Nature, **1995**. 376(6541): p. 581-584.
108. Zhao, X.M., Y.N. Xia, and G.M. Whitesides, *Fabrication of three-dimensional micro-structures: Microtransfer molding,* Advanced Materials, **1996**. 8(10): p. 837-&.
109. Martynova, L., L.E. Locascio, M. Gaitan, G.W. Kramer, R.G. Christensen, and W.A. MacCrehan, *Fabrication of plastic microfluid channels by imprinting methods,* Analytical Chemistry, **1997**. 69(23): p. 4783-4789.
110. Lorenz, H., M. Despont, N. Fahrni, J. Brugger, P. Vettiger, and P. Renaud, *High-aspect-ratio, ultrathick, negative-tone near-UV photoresist and its applications for MEMS,* Sensors and Actuators a-Physical, **1998**. 64(1): p. 33-39.
111. Guerin, L.J., M. Bossel, M. Demierre, S. Calmes, and P. Renaud. *Simple and low cost fabrication of embedded micro-channels by using a new thick-film photoplastic.* in *Proceedings of International Solid State Sensors and Actuators Conference (Transducers '97)*. 1997.
112. Jo, B.H., L.M. Van Lerberghe, K.M. Motsegood, and D.J. Beebe, *Three-dimensional micro-channel fabrication in polydimethylsiloxane (PDMS) elastomer,* Journal of Microelectromechanical Systems, **2000**. 9(1): p. 76-81.
113. Chen, Y., L.Y. Zhang, and G. Chen, *Fabrication, modification, and application of department of analytical poly(methyl methacrylate) microfluidic chips,* Electrophoresis, **2008**. 29(9): p. 1801-1814.
114. Tsao, C.W., *Polymer Microfluidics: Simple, Low-Cost Fabrication Process Bridging Academic Lab Research to Commercialized Production,* Micromachines, **2016**. 7(12).

115. Ren, K.N., J.H. Zhou, and H.K. Wu, *Materials for Microfluidic Chip Fabrication,* Accounts of Chemical Research, **2013**. 46(11): p. 2396-2406.
116. Davidson, M.R., S.A. Mitchell, and R.H. Bradley, *Surface studies of low molecular weight photolysis products from UV-ozone oxidised polystyrene,* Surface Science, **2005**. 581(2): p. 169-177.
117. Diaz-Quijada, G.A., R. Peytavi, A. Nantel, E. Roy, M.G. Bergeron, M.M. Dumoulin, and T. Veres, *Surface modification of thermoplastics—towards the plastic biochip for high throughput screening devices,* Lab on a Chip, **2007**. 7(7): p. 856-862.
118. Mathieu, H.J., Y. Chevolot, L. Ruiz-Taylor, and D. Léonard, *Engineering and Characterization of Polymer Surfaces for Biomedical Applications*, in *Radiation Effects on Polymers for Biological Use*, H. Kausch, et al., Editors. 2003, Springer Berlin Heidelberg: Berlin, Heidelberg. p. 1-34.
119. Fixe, F., M. Dufva, P. Telleman, and C.B. Christensen, *One-step immobilization of aminated and thiolated DNA onto poly(methylmethacrylate) (PMMA) substrates,* Lab on a Chip, **2004**. 4(3): p. 191-5.
120. Mongkhontreerat, S., K. Oberg, L. Erixon, P. Lowenhielm, A. Hult, and M. Malkoch, *UV initiated thiol-ene chemistry: a facile and modular synthetic methodology for the construction of functional 3D networks with tunable properties,* Journal of Materials Chemistry A, **2013**. 1(44): p. 13732-13737.
121. Sikanen, T.M., J.P. Lafleur, M.-E. Moilanen, G. Zhuang, T.G. Jensen, and J.P. Kutter, *Fabrication and bonding of thiol-ene-based microfluidic devices,* Journal of Micromechanics and Microengineering, **2013**. 23(3): p. 037002.
122. Hoyle, C.E., T.Y. Lee, and T. Roper, *Thiol–enes: Chemistry of the past with promise for the future,* Journal of Polymer Science Part A: Polymer Chemistry, **2004**. 42(21): p. 5301-5338.
123. Bartolo, D., G. Degre, P. Nghe, and V. Studer, *Microfluidic stickers,* Lab on a Chip, **2008**. 8(2): p. 274-279.
124. Carlborg, C.F., T. Haraldsson, K. Oberg, M. Malkoch, and W. van der Wijngaart, *Beyond PDMS: off-stoichiometry thiol-ene (OSTE) based soft lithography for rapid prototyping of microfluidic devices,* Lab on a Chip, **2011**. 11(18): p. 3136-3147.
125. Marco, S., C. Monica, C. Giovanna, R. Ignazio, and A.O. Ricardo, *Preparation and characterization of hybrid thiol-ene/epoxy UV–thermal dual-cured systems,* Polymer International, **2010**. 59(8): p. 1046-1051.
126. Flores, M., A.M. Tomuta, X. Fernández-Francos, X. Ramis, M. Sangermano, and A. Serra, *A new two-stage curing system: Thiol-ene/epoxy homopolymerization using an allyl terminated hyperbranched polyester as reactive modifier,* Polymer, **2013**. 54(21): p. 5473-5481.
127. Jian, Y., Y. He, Y. Sun, H. Yang, W. Yang, and J. Nie, *Thiol–epoxy/thiol–acrylate hybrid materials synthesized by photopolymerization,* Journal of Materials Chemistry C, **2013**. 1(29): p. 4481-4489.
128. Carlborg, C.F., A. Vastesson, Y. Liu, W. van der Wijngaart, M. Johansson, and T. Haraldsson, *Functional off-stoichiometry thiol-ene-epoxy thermosets featuring temporally controlled curing stages via an UV/UV dual cure process,* Journal of Polymer Science Part A: Polymer Chemistry, **2014**. 52(18): p. 2604-2615.
129. Guzman, D., X. Ramis, X. Fernandez-Francos, and A. Serra, *Preparation of click thiol-ene/thiol-epoxy thermosets by controlled photo/thermal dual curing sequence,* RSC Advances, **2015**. 5(123): p. 101623-101633.
130. Acebo, C., X. Fernandez-Francos, X. Ramis, and A. Serra, *Multifunctional allyl-terminated hyperbranched poly(ethyleneimine) as component of new thiol-ene/thiol-epoxy materials,* Reactive & Functional Polymers, **2016**. 99: p. 17-25.
131. Guzmán, D., X. Ramis, X. Fernández-Francos, S. De la Flor, and A. Serra, *New bio-based materials obtained by thiol-ene/thiol-epoxy dual curing click procedures from eugenol derivates,* European Polymer Journal, **2017**. 93: p. 530-544.

132. Mishra, V., J. Desai, and K.I. Patel, *High-performance waterborne UV-curable polyurethane dispersion based on thiol-acrylate/thiol-epoxy hybrid networks,* Journal of Coatings Technology and Research, **2017**. 14(5): p. 1069-1081.
133. Zhou, X.C., R. Sjoberg, A. Druet, J.M. Schwenk, W. van der Wijngaart, T. Haraldsson, and C.F. Carlborg, *Thiol-ene-epoxy thermoset for low-temperature bonding to biofunctionalized microarray surfaces,* Lab on a Chip, **2017**. 17(21): p. 3672-3681.
134. Good, B.T., S. Reddy, R.H. Davis, and C.N. Bowman, *Tailorable low modulus, reversibly deformable elastomeric thiol-ene materials for microfluidic applications,* Sensors and Actuators B-Chemical, **2007**. 120(2): p. 473-480.
135. Mays, R.L., P. Pourhossein, D. Savithri, J. Genzer, R.C. Chiechi, and M.D. Dickey, *Thiol-containing polymeric embedding materials for nanoskiving,* Journal of Materials Chemistry C, **2013**. 1(1): p. 121-130.
136. Geczy, R., D. Sticker, N. Bovet, U.O. Häfeli, and J.P. Kutter, *Chloroform compatible, thiol-ene based replica molded micro chemical devices as an alternative to glass microfluidic chips,* Lab on a Chip, **2019**. 19(5): p. 798-806.
137. Sticker, D., R. Geczy, U.O. Häfeli, and J.P. Kutter, *Thiol–Ene Based Polymers as Versatile Materials for Microfluidic Devices for Life Sciences Applications,* ACS Applied Materials & Interfaces, **2020**.
138. Prichard, T.D., S.S. Singh, N. Chawla, and B.D. Vogt, *Flocculated carbon nanotube composites for solvent resistant soft templated microfeatures,* Polymer, **2013**. 54(3): p. 1130-1135.
139. Hung, L.-H., R. Lin, and A.P. Lee, *Rapid microfabrication of solvent-resistant biocompatible microfluidic devices,* Lab on a Chip, **2008**. 8(6): p. 983-987.
140. Pardon, G., F. Saharil, J.M. Karlsson, O. Supekar, C.F. Carlborg, W. van der Wijngaart, and T. Haraldsson, *Rapid mold-free manufacturing of microfluidic devices with robust and spatially directed surface modifications,* Microfluidics and Nanofluidics, **2014**. 17(4): p. 773-779.
141. Silvestrini, S., D. Ferraro, T. Toth, M. Pierno, T. Carofiglio, G. Mistura, and M. Maggini, *Tailoring the wetting properties of thiolene microfluidic materials,* Lab on a Chip, **2012**. 12(20): p. 4041-3.
142. Gu, H., M.H.G. Duits, and F. Mugele, *A hybrid microfluidic chip with electrowetting functionality using ultraviolet (UV)-curable polymer,* Lab on a Chip, **2010**. 10(12): p. 1550-1556.
143. Levache, B., A. Azioune, M. Bourrel, V. Studer, and D. Bartolo, *Engineering the surface properties of microfluidic stickers,* Lab on a Chip, **2012**. 12(17): p. 3028-3031.
144. Tähkä, S.M., A. Bonabi, M.-E. Nordberg, M. Kanerva, V.P. Jokinen, and T.M. Sikanen, *Thiol-ene microfluidic devices for microchip electrophoresis: Effects of curing conditions and monomer composition on surface properties,* Journal of Chromatography A, **2015**. 1426: p. 233-240.
145. Hoffmann, C., M. Pinelo, J.M. Woodley, and A.E. Daugaard, *Development of a thiol-ene based screening platform for enzyme immobilization demonstrated using horseradish peroxidase,* Biotechnol Prog, **2017**. 33(5): p. 1267-1277.
146. Çakmakçi, E., B. Yuce-Dursun, and S. Demir, *Maleic anhydride functionalization of OSTE based coatings via thiol-ene "Click" reaction for the covalent immobilization of xylanase,* Reactive and Functional Polymers, **2017**. 111: p. 38-43.
147. Mazurek, P., A.E. Daugaard, M. Skolimowski, S. Hvilsted, and A.L. Skov, *Preparing mono-dispersed liquid core PDMS microcapsules from thiol-ene-epoxy-tailored flow-focusing microfluidic devices,* RSC Advances, **2015**. 5(20): p. 15379-15386.
148. Krishnan, K.M., *Biomedical nanomagnetics: a spin through possibilities in imaging, diagnostics, and therapy,* IEEE transactions on magnetics, **2010**. 46(7): p. 2523-2558.
149. Sarwar, A., A. Nemirovski, and B. Shapiro, *Optimal Halbach permanent magnet designs for maximally pulling and pushing nanoparticles,* Journal of Magnetism and Magnetic Materials, **2012**. 324(5): p. 742-754.
150. Paulus, J.-M., *Platelet size in man,* Blood, **1975**. 46(3): p. 321-336.

151. Ross, D.W., L.H. Ayscue, J. Watson, and S.A. Bentley, *Stability of hematologic parameters in healthy subjects: Intraindividual versus interindividual variation,* American journal of clinical pathology, **1988**. 90(3): p. 262-267.
152. Sinha, J., B.D. Fairbanks, H.B. Song, and C.N. Bowman, *Phosphate-Based Cross-Linked Polymers from Iodo–ene Photopolymerization: Tuning Surface Wettability through Thiol–ene Chemistry,* ACS Macro Letters, **2019**. 8(2): p. 213-217.
153. Namdee, K., A.J. Thompson, P. Charoenphol, and O. Eniola-Adefeso, *Margination Propensity of Vascular-Targeted Spheres from Blood Flow in a Microfluidic Model of Human Microvessels,* Langmuir, **2013**. 29(8): p. 2530-2535.
154. Häfeli, U.O., K. Saatchi, P. Elischer, R. Misri, M. Bokharaei, N.R. Labiris, and B. Stoeber, *Lung perfusion imaging with monosized biodegradable microspheres,* Biomacromolecules, **2010**. 11(3): p. 561-567.
155. Nosrati, Z., N. Li, F.o. Michaud, S. Ranamukhaarachchi, S. Karagiozov, G. Soulez, S. Martel, K. Saatchi, and U.O. Häfeli, *Development of a Coflowing Device for the Size-Controlled Preparation of Magnetic-Polymeric Microspheres as Embolization Agents in Magnetic Resonance Navigation Technology,* ACS Biomaterials Science & Engineering, **2018**. 4(3): p. 1092-1102.
156. Zhao, H., K. Saatchi, and U.O. Häfeli, *Preparation of biodegradable magnetic microspheres with poly (lactic acid)-coated magnetite,* Journal of Magnetism and Magnetic Materials, **2009**. 321(10): p. 1356-1363.
157. Gun, S., M. Edirisinghe, and E. Stride, *Encapsulation of superparamagnetic iron oxide nanoparticles in poly-(lactide-co-glycolic acid) microspheres for biomedical applications,* Materials Science and Engineering: C, **2013**. 33(6): p. 3129-3137.
158. Martín-Banderas, L., R. González-Prieto, A. Rodríguez-Gil, M. Fernández-Arévalo, M. Flores-Mosquera, S. Chávez, and A.M. Gañán-Calvo, *Application of flow focusing to the break-up of a magnetite suspension jet for the production of paramagnetic microparticles,* Journal of Nanomaterials, **2011**. 2011: p. 4.
159. Tottori, N. and T. Nisisako, *High-throughput production of satellite-free droplets through a parallelized microfluidic deterministic lateral displacement device,* Sensors and Actuators B: Chemical, **2018**. 260: p. 918-926.
160. Tan, Y.-C. and A.P. Lee, *Microfluidic separation of satellite droplets as the basis of a monodispersed micron and submicron emulsification system,* Lab on a Chip, **2005**. 5(10): p. 1178-1183.
161. Yamada, M., M. Nakashima, and M. Seki, *Pinched Flow Fractionation: Continuous Size Separation of Particles Utilizing a Laminar Flow Profile in a Pinched Microchannel,* Analytical Chemistry, **2004**. 76(18): p. 5465-5471.
162. Zhang, X., *Dynamics of drop formation in viscous flows,* Chemical Engineering Science, **1999**. 54(12): p. 1759-1774.
163. Tjahjadi, M., H.A. Stone, and J.M. Ottino, *Satellite and subsatellite formation in capillary breakup,* Journal of Fluid Mechanics, **1992**. 243: p. 297-317.
164. Carrier, O., E. Dervin, D. Funfschilling, and H.-Z. Li, *Formation of satellite droplets in flow-focusing junctions: volume and neck rupture,* Microsystem Technologies, **2015**. 21(3): p. 499-507.
165. Hoyle, C.E. and C.N. Bowman, *Thiol–ene click chemistry,* Angewandte Chemie International Edition, **2010**. 49(9): p. 1540-1573.
166. Cygan, Z.T., J.T. Cabral, K.L. Beers, and E.J. Amis, *Microfluidic platform for the generation of organic-phase microreactors,* Langmuir, **2005**. 21(8): p. 3629-3634.
167. Geczy, R., M. Agnoletti, M.F. Hansen, J.P. Kutter, K. Saatchi, and U.O. Häfeli, *Microfluidic approaches for the production of monodisperse, superparamagnetic microspheres in the low micrometer size range,* Journal of Magnetism and Magnetic Materials, **2019**. 471: p. 286-293.

168. Miletić, N., Z. Vuković, A. Nastasović, and K. Loos, *Macroporous poly(glycidyl methacrylate-co-ethylene glycol dimethacrylate) resins—Versatile immobilization supports for biocatalysts,* Journal of Molecular Catalysis B: Enzymatic, **2009**. 56(4): p. 196-201.
169. Slater, M., M. Snauko, F. Svec, and J.M. Frechet, *"Click chemistry" in the preparation of porous polymer-based particulate stationary phases for mu-HPLC separation of peptides and proteins,* Analytical Chemistry, **2006**. 78(14): p. 4969-75.
170. Fontanals, N., R.M. Marcé, P.A.G. Cormack, D.C. Sherrington, and F. Borrull, *Monodisperse, hypercrosslinked polymer microspheres as tailor-made sorbents for highly efficient solid-phase extractions of polar pollutants from water samples,* Journal of Chromatography A, **2008**. 1191(1-2): p. 118-124.
171. Vaino, A.R. and K.D. Janda, *Solid-phase organic synthesis: a critical understanding of the resin,* J Comb Chem, **2000**. 2(6): p. 579-96.
172. Orzaez, M., P. Mora, L. Mondragon, E. Perez-Paya, and M.J. Vicent, *Solid-phase chemistry: a useful tool to discover modulators of protein interactions,* International Journal of Peptide Research and Therapeutics, **2007**. 13(1-2): p. 281-293.
173. Prasath, R.A., M.T. Gokmen, P. Espeel, and F.E. Du Prez, *Thiol-ene and thiol-yne chemistry in microfluidics: a straightforward method towards macroporous and nonporous functional polymer beads,* Polymer Chemistry, **2010**. 1(5): p. 685-692.
174. Zhang, L., J.M. Chan, F.X. Gu, J.-W. Rhee, A.Z. Wang, A.F. Radovic-Moreno, F. Alexis, R. Langer, and O.C. Farokhzad, *Self-Assembled Lipid−Polymer Hybrid Nanoparticles: A Robust Drug Delivery Platform,* ACS Nano, **2008**. 2(8): p. 1696-1702.
175. Thanki, K., X. Zeng, and C. Foged, *Preparation, Characterization, and In Vitro Evaluation of Lipidoid–Polymer Hybrid Nanoparticles for siRNA Delivery to the Cytosol*, in *Nanotechnology for Nucleic Acid Delivery: Methods and Protocols*, M. Ogris and H. Sami, Editors. 2019, Springer New York: New York, NY. p. 141-152.
176. Sato, Y., Y. Note, M. Maeki, N. Kaji, Y. Baba, M. Tokeshi, and H. Harashima, *Elucidation of the physicochemical properties and potency of siRNA-loaded small-sized lipid nanoparticles for siRNA delivery,* Journal of Controlled Release, **2016**. 229: p. 48-57.
177. Li, Y.J., R.J. Lee, X.Q. Huang, Y.H. Li, B.C. Lv, T.P. Wang, Y.H. Qi, F. Hao, J.H. Lu, Q.F. Meng, L.R. Teng, Y.L. Zhou, J. Xie, and L.S. Teng, *Single-step microfluidic synthesis of transferrin-conjugated lipid nanoparticles for siRNA delivery,* Nanomedicine-Nanotechnology Biology and Medicine, **2017**. 13(2): p. 371-381.
178. Kim, Y., B. Lee Chung, M. Ma, W.J. Mulder, Z.A. Fayad, O.C. Farokhzad, and R. Langer, *Mass production and size control of lipid-polymer hybrid nanoparticles through controlled microvortices,* Nano Letters, **2012**. 12(7): p. 3587-91.
179. Feng, Q., L. Zhang, C. Liu, X.Y. Li, G.Q. Hu, J.S. Sun, and X.Y. Jiang, *Microfluidic based high throughput synthesis of lipid-polymer hybrid nanoparticles with tunable diameters,* Biomicrofluidics, **2015**. 9(5).
180. Bokare, A., A. Takami, J.H. Kim, A. Dong, A. Chen, R. Valerio, S. Gunn, and F. Erogbogbo, *Herringbone-Patterned 3D-Printed Devices as Alternatives to Microfluidics for Reproducible Production of Lipid Polymer Hybrid Nanoparticles,* Acs Omega, **2019**. 4(3): p. 4650-4657.
181. Zhang, L., Q. Feng, J. Wang, J. Sun, X. Shi, and X. Jiang, *Microfluidic synthesis of rigid nanovesicles for hydrophilic reagents delivery,* Angew Chem Int Ed Engl, **2015**. 54(13): p. 3952-6.
182. Li, Y., X. Huang, R.J. Lee, Y. Qi, K. Wang, F. Hao, Y. Zhang, J. Lu, Q. Meng, S. Li, J. Xie, and L. Teng, *Synthesis of Polymer-Lipid Nanoparticles by Microfluidic Focusing for siRNA Delivery,* Molecules, **2016**. 21(10).
183. Zhu, X., Y. Xu, L.M. Solis, W. Tao, L. Wang, C. Behrens, X. Xu, L. Zhao, D. Liu, J. Wu, N. Zhang, Wistuba, II, O.C. Farokhzad, B.R. Zetter, and J. Shi, *Long-circulating siRNA nanoparticles for*

*validating Prohibitin1-targeted non-small cell lung cancer treatment,* Proc Natl Acad Sci U S A, **2015**. 112(25): p. 7779-84.

184. Koide, H., A. Okamoto, H. Tsuchida, H. Ando, S. Ariizumi, C. Kiyokawa, M. Hashimoto, T. Asai, T. Dewa, and N. Oku, *One-step encapsulation of siRNA between lipid-layers of multi-layer polycation liposomes by lipoplex freeze-thawing,* Journal of Controlled Release, **2016**. 228: p. 1-8.
185. Jansen, M.A.A., L.H. Klausen, K. Thanki, J. Lyngso, J.S. Pedersen, H. Franzyk, H.M. Nielsen, W. van Eden, M.D. Dong, F. Broere, C. Foged, and X.H. Zeng, *Lipidoid-polymer hybrid nanoparticles loaded with TNF siRNA suppress inflammation after intra-articular administration in a murine experimental arthritis model,* European Journal of Pharmaceutics and Biopharmaceutics, **2019**. 142: p. 38-48.
186. Macosko, E.Z., A. Basu, R. Satija, J. Nemesh, K. Shekhar, M. Goldman, I. Tirosh, A.R. Bialas, N. Kamitaki, E.M. Martersteck, J.J. Trombetta, D.A. Weitz, J.R. Sanes, A.K. Shalek, A. Regev, and S.A. McCarroll, *Highly Parallel Genome-wide Expression Profiling of Individual Cells Using Nanoliter Droplets,* Cell, **2015**. 161(5): p. 1202-1214.
187. Wu, B. and H.Q. Gong, *Formation of fully closed microcapsules as microsensors by microfluidic double emulsion,* Microfluidics and Nanofluidics, **2013**. 14(3-4): p. 637-644.
188. Kim, S.H., J.W. Kim, J.C. Cho, and D.A. Weitz, *Double-emulsion drops with ultra-thin shells for capsule templates,* Lab on a Chip, **2011**. 11(18): p. 3162-3166.
189. Conchouso, D., D. Castro, S.A. Khan, and I.G. Foulds, *Three-dimensional parallelization of microfluidic droplet generators for a litre per hour volume production of single emulsions,* Lab on a Chip, **2014**. 14(16): p. 3011-3020.
190. Amstad, E., M. Chemama, M. Eggersdorfer, L.R. Arriaga, M.P. Brenner, and D.A. Weitz, *Robust scalable high throughput production of monodisperse drops,* Lab on a Chip, **2016**. 16(21): p. 4163-4172.
191. Yang, S.W. and T. Vosch, *Rapid Detection of MicroRNA by a Silver Nanocluster DNA Probe,* Analytical Chemistry, **2011**. 83(18): p. 6935-6939.
192. Shah, P., S.W. Choi, R. Nagda, R. Geczy, S.K. Cho, Y.J. Bhang, T.H. Kim, T.Y. Song, P.H. Lee, J.H. Kang, P.W. Thulstrup, M.J. Bjerrum, I.L. Jung, and S.W. Yang, *The structural shift of a DNA template between a hairpin and a dimer tunes the emission color of DNA-templated AgNCs,* Nanoscale, **2018**. 10(44): p. 20717-20722.
193. Hayashi, N., Y. Sakai, H. Tsunoyama, and A. Nakajima, *Development of Ultrafine Multichannel Microfluidic Mixer for Synthesis of Bimetallic Nanoclusters: Catalytic Application of Highly Monodisperse AuPd Nanoclusters Stabilized by Poly(N-vinylpyrrolidone),* Langmuir, **2014**. 30(34): p. 10539-10547.
194. Abate, A.R., D. Lee, T. Do, C. Holtze, and D.A. Weitz, *Glass coating for PDMS microfluidic channels by sol-gel methods,* Lab on a Chip, **2008**. 8(4): p. 516-518.
195. Maenaka, H., M. Yamada, M. Yasuda, and M. Seki, *Continuous and size-dependent sorting of emulsion droplets using hydrodynamics in pinched microchannels,* Langmuir, **2008**. 24(8): p. 4405-4410.
196. Sprenger, L., S. Dutz, T. Schneider, S. Odenbach, and U.O. Hafeli, *Simulation and experimental determination of the online separation of blood components with the help of microfluidic cascading spirals,* Biomicrofluidics, **2015**. 9(4).
197. Hou, H.W., M.E. Warkiani, B.L. Khoo, Z.R. Li, R.A. Soo, D.S.W. Tan, W.T. Lim, J. Han, A.A.S. Bhagat, and C.T. Lim, *Isolation and retrieval of circulating tumor cells using centrifugal forces,* Scientific Reports, **2013**. 3.

# Appendices

**Appendix I:** Geczy, R., D. Sticker, N. Bovet, U.O. Häfeli, and J.P. Kutter*, Chloroform compatible, thiol-ene based replica molded micro chemical devices as an alternative to glass microfluidic chips, Lab on a Chip, **2019**. 19(5): p. 798-806.

Including.: European Patent 18184178.4-1107 "Methods for the Treatment of Thermoset Polymers"

**Appendix II:** Geczy, R., M. Agnoletti, M.F. Hansen, J.P. Kutter, K. Saatchi, and U.O. Häfeli*, *Microfluidic approaches for the production of monodisperse, superparamagnetic microspheres in the low micrometer size range,* Journal of Magnetism and Magnetic Materials, **2019**. 471: p. 286-293.

Additional contribution not considered for as part of the thesis:

**Appendix III:** Sticker, D.#, R. Geczy#, U.O. Häfeli, and J.P. Kutter*, *Thiol–Ene Based Polymers as Versatile Materials for Microfluidic Devices for Life Sciences Applications*, ACS Applied Materials & Interfaces, **2020**. In press. *equal contribution

# 11. Appendix I

**Publication 1: Lab on a Chip**

---

Geczy, R., D. Sticker, N. Bovet, U.O. Häfeli, and J.P. Kutter, Chloroform compatible, thiol-ene based replica molded micro chemical devices as an alternative to glass microfluidic chips, Lab on a Chip, **2019**. 19(5): p. 798-806.

Lab on a Chip

PAPER

View Article Online
View Journal | View Issue



Cite this: *Lab Chip*, 2019, **19**, 798

# Chloroform compatible, thiol-ene based replica molded micro chemical devices as an alternative to glass microfluidic chips

Reka Geczy,[ab] Drago Sticker,[a] Nicolas Bovet,[c] Urs O. Häfeli[ab] and Jörg P. Kutter*[a]

Received 16th November 2018,
Accepted 22nd January 2019

DOI: 10.1039/c8lc01260a

rsc.li/loc

Polymeric microfluidic chips offer a number of benefits compared to their glass equivalents, including lower material costs and ease and flexibility of fabrication. However, the main drawback of polymeric materials is often their limited resistance to (organic) solvents. Previously, thiol-ene materials were shown to be more solvent resistant than most other commonly used polymers; however, they still fall short in "harsh" chemical environments, such as when chlorinated solvents are present. Here, we show that a simple yet effective treatment of thiol-ene materials results in exceptional solvent compatibility, even for very challenging chemical environments. Our approach, based on a temperature treatment, results in a 50-fold increase in the chloroform compatibility of thiol-enes (in terms of longevity). We show that prolonged heat exposure allows for the operation of the microfluidic chips in chloroform for several days with no discernable deformation or solvent-induced swelling. The method is applicable to many different thiol-ene-based materials, including commercially available formulations, and also when using other commonly considered "harsh" solvents. To demonstrate the utility of the solvent compatible thiol-enes for applications where chloroform is frequently employed, we show the continuous and uniform production of polymeric microspheres for drug delivery purposes over a period of 8 hours. The material thus holds great promise as an alternative choice for microfluidic applications requiring harsh chemical environments, a domain so far mainly restricted to glass chips.



## Introduction

Organic solvents generally considered "harsh," including chloroform, find numerous laboratory, pharmaceutical and industrial applications, such as for solvent-based extraction and purification and dye production. These processes are commonly carried out in glass apparatus due to the chemical resistance and optical clarity of glass. Large, mass-produced glass is easy and relatively inexpensive to manufacture; however, costs rise significantly when the size or production numbers of the devices are smaller. This is particularly relevant for glass microfluidic devices, which are labor intensive and costly to produce, severely limiting prototyping of the microfluidic chips to, for example, optimize channel geometries. As very few polymers are compatible with chlorinated solvents, glass microfluidic chips are still commonly employed under harsh chemical conditions. Glass chips are, for example, used for solvent extraction and purification,[1] droplet and nanoparticle fabrication,[2] and on-chip HPLC.[3]

To mitigate the production cost and challenges of fabricating microfluidic chips, polymeric alternatives have been widely employed. Polydimethylsiloxane (PDMS) is currently the most widely used material for microfluidic devices in academia, offering straightforward and low cost fabrication, optical clarity, and oxygen permeability (important for cell cultures);[4] however, it is lacking solvent resistance, resulting in swelling in a broad range of mild and harsh solvents.[5] Therefore, recent trends are towards the development and use of alternative polymers for microfluidic purposes, specifically aiming to combine solvent resistance and ease of fabrication when compared to glass. Proposed alternative materials include fluorinated polymers,[6,7] fluoroelastomers,[8–10] polyimides,[11] as well as various coatings on conventional chip materials, such as sol–gel salinations[12] and polyelectrolyte coatings.[13] The proposed materials, while extremely solvent resistant, still present other drawbacks, which may include cumbersome fabrication steps, highly hydrophobic surfaces, incompatible mechanical characteristics, or unfavorable optical properties. Coatings, on the other hand, are more difficult

[a] *Department of Pharmacy, Faculty of Health and Medical Sciences, University of Copenhagen, 2100 Copenhagen, Denmark. E-mail: jorg.kutter@sund.ku.dk*
[b] *Faculty of Pharmaceutical Sciences, University of British Columbia, Vancouver, British Columbia V6T 1Z3, Canada*
[c] *Nano-Science Center, Department of Chemistry, University of Copenhagen, 2100 Copenhagen, Denmark*

to consistently prepare at a uniform thickness without any pinhole defects, are subject to cracking, and are often less stable (*e.g.*, due to potential degradation).

A fairly new thermoset polymer class, which is based on the thiol-ene crosslinking reaction, is gaining attention for microchip fabrication.[14–17] These thiol-ene polymers are excellent for rapid prototyping due to their compatibility with standard 'soft-lithography' techniques in combination with properties such as optical clarity, applicability to replica molding, and good chemical resistance to a range of mild solvents. Thiol-ene based polymers have already been shown to be more solvent resistant than other commonly used polymers, *e.g.*, PDMS and cyclic olefin co-polymers (COC). Solvent resistance has previously in particular been investigated for the commercially available Norland Optical Adhesive (NOA-81), showing good compatibility with most organic solvents.[18–20] However, this was not the case for chlorinated solvents, showing greater than 30% swelling for chloroform.[19] Therefore, for microfluidic applications relying on chloroform as the main solvent, *e.g.*, for the production of drug delivery vehicles, pristine (untreated) thiol-ene falls short in solvent resistance resulting in rapid material deformation.

Previous attempts to modify thiol-enes for gaining solvent resistance are few and show limitations. The addition of 1 wt% carbon nanotubes to the material has been shown to reduce toluene and acetone-induced swelling, though harsher solvents were not tested.[21] Importantly, single walled carbon nanotubes are optically opaque, costly and difficult to nanofabricate. An alternative approach is through the use of ester-free thiol monomers, as esters are quickly hydrolyzed in acidic and basic environments.[22] These monomers, while yielding polymers with acid/base resistance, are not commercially available, which limits their relevance for most research facilities.

Here, we present a method for treating thiol-ene polymers to overcome the susceptibility to, especially, chloroform. We show that a simple and effective treatment, heat exposure beyond the glass transition temperature, results in a significant increase in solvent resistance. Upon heat treatment for 60 hours at 200 °C, the polymer shows no apparent sign of chloroform-induced degradation or deformation even after 48 hours of continuous exposure to the solvent. In comparison, under the same conditions, untreated chips are rendered unfunctional due to material deformation within a matter of hours. For the proof-of-concept, we show the utility of the modified material for the prolonged production of microspheres using droplet microfluidics, where chloroform in water emulsions are frequently employed.

## Results and discussion

In order to improve the resistance of thiol-ene materials to chloroform, two approaches have been investigated - surface coating and bulk modification. Initially, various previously described surface coatings were investigated, such as silicon-based sol–gel coatings[23] and Teflon AF[24] (data not included). Results showed that the employed surface coatings offer marginal resistance against solvents, are not stable, and are difficult to achieve in a consistent manner. Therefore, modification of the bulk material was investigated as an alternative strategy. For bulk material modification, it was found that heat treatment under ambient air conditions results in a dose and exposure dependent response in solvent resistance.

### Chloroform compatibility of heat-treated thiol-ene polymer

Solvent resistance of thiol-ene polymers when exposed to chloroform (and similar "harsh" solvents) was investigated by evaluating the induced channel swelling,[5] where the starting and final channel widths are measured using light microscopy. As the bulk material swells in response to solvent exposure, the channel width becomes smaller. We can define the channel width decrease in percent (for simplicity, we will refer to this as "% swelling" in the discussion) using the following equation,

$$\%\ \text{width decrease} = \frac{(\text{Initial width} - \text{Final width})}{\text{Initial width}} \times 100\% \quad (1)$$

Here, 100% swelling corresponds to an infinitesimal final channel width. The percent ratio of final and starting channel dimensions were plotted after chloroform exposure at 10 μL min$^{-1}$ flow rate across an initially 500 μm wide straight channel. The influence of exposure temperature and exposure time is shown in Fig. 1A and B, where the swelling of both photoinitiator-free and 0.5% TPO-L containing thiol-ene polymers were investigated after a 1-hour chloroform exposure. The addition of photoinitiator greatly reduces the baseline swelling of the material from 25% swelling (Fig. 1A) to 6% swelling (Fig. 1B) after 1-hour chloroform exposure. Notably, both photoinitiator-free and photoinitiator containing thiol-ene chips show a temperature and time dependent response to the heat treatment, where increasing temperatures or longer exposure times reduce the swelling of the material. A rapid gain in solvent resistance is seen after just 1 hour of heat exposure, leveling off with further increased exposure times. Both materials show virtually no swelling after 16 hours at 200 °C heat exposure.

Next, instead of short term chloroform exposure, chips were exposed to chloroform at a 10 μL min$^{-1}$ flow rate for up to 48 hours and channel widths were measured at regular intervals during the exposure period. Triplicates of photoinitiator free and 0.5% TPO-L thiol-ene were heat treated for 60 hours at 200 °C, while appropriate control chips were maintained at room temperature for 60 hours. Here, we see that both initiator-free and photoinitiator containing control samples exhibit significant swelling in response to chloroform exposure over the course of 48 hours (Fig. 1C and D, blue lines). Moreover, the photoinitiator-free thiol-ene chips swell to a significant level after 24 hours such that the syringe pump malfunctions due to the swelling-induced narrowing of the channel diameter. After heat



 

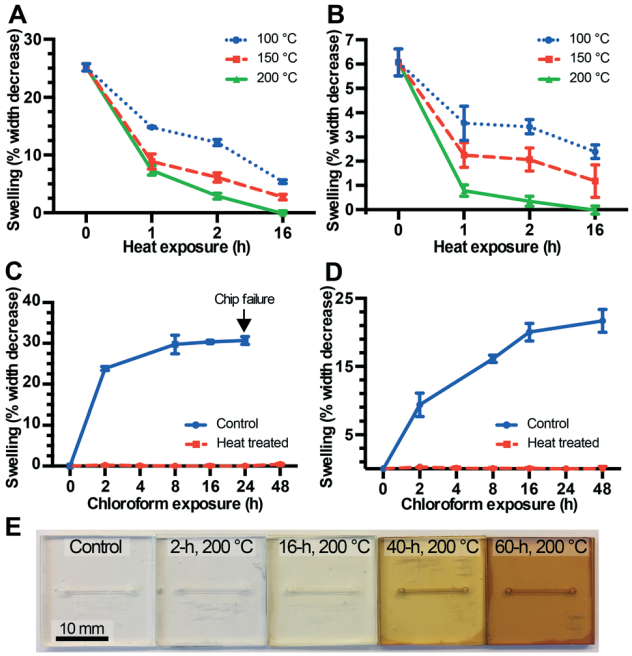


Fig. 1 Effect of heat exposure on solvent resistance. (A) 100 °C (blue), 150 °C (red) or 200 °C (green) heat applied to chips for indicated time points. Chips were then exposed to chloroform for one hour and the channel width was measured. (B) Same as (A), except 0.5% photoinitiator (TPO-L) added to bulk material. (C) 200 °C heat applied to chips for 60 hours (red), or RT control (blue). Chips were exposed to chloroform for the times indicated, after which the channel width was measured. (D) Same as (C), except 0.5% photoinitiator (TPO-L) added to bulk material. All chips were cured for 10 minutes at 90 mW $cm^{-2}$ under 365 nm light. All data points were run in triplicates. Error bars represent standard deviation among replicates. (E) Image of thiol-ene chips, control and 200 °C heat treated at indicated time points. Chips were imaged simultaneously under identical lighting conditions.

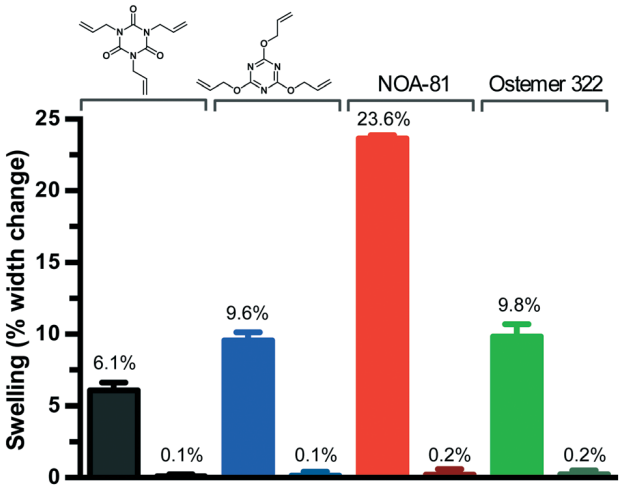


Fig. 2 1-hour chloroform exposure of various thiol-ene formulations, before and after 40-hour 200 °C heat treatment. Control: TTT with PETMP, black; triallyloxy-triazine with PETMP, blue; NOA-81 commercial adhesive, red; Ostemer 322 commercial thiol-ene-epoxy, green. The in-house mixtures are stoichiometric with regards to the allyl and thiol functional groups and contain 0.5% TPO-L photoinitiator. All chips were cured under 90 mW $cm^{-2}$ for 10 minutes after assembly. Both Ostemer 322 samples were heated for 1 hour at 110 °C as suggested by the manufacturer. All samples were run in triplicates, error bars represent standard deviation (for abbreviations, see Experimental).

treatment, however, no detectable swelling is seen (Fig. 1C and D, red line) for the course of 48 hours. No significant difference in swelling is seen between the initiator-free and TPO-L chips, which is particularly important if initiator leaching is of concern for the application in mind.

Interestingly, a characteristic color change occurs after prolonged heat exposure, where the material changes from clear (Fig. 1E) to a yellow-orange hue, potentially hinting to the onset of complex carbonization processes in the material. The color change is important to keep in mind for certain optical applications, as the material now exhibits strong absorbance in the blue-violet region between 400–500 nm. Heat treatment does not affect the absorbance properties in the UV-A region and above 500 nm.

### Chloroform compatibility of heat-treated thiol-ene derivatives

In order to investigate the universal applicability of heat treatment for other formulations and monomer combinations, additional thiol-ene based formulations were tested. In the first set of experiments, the allyl monomer was varied from the previously investigated triallyl-triazine-trione (Fig. 2, black) to the triallyloxy-triazine (blue). In addition, the commercially available NOA-81 (red) and Ostemer 322 (green) formulations were investigated as well. All untreated thiol-ene materials show significant swelling in response to one-hour chloroform exposure, with NOA-81 being the most affected. All samples were heat treated for 40 hours at 200 °C. After heat exposure, all samples displayed basically negligible chloroform induced swelling, within the range of 0–0.2%. Therefore, the results clearly emphasize the excellent applicability of the heat treatment for a variety of thiol-ene materials, both in-house mixed and commercial formulations.

### Compatibility with various 'harsh' solvents

Universal applicability was further tested for various mild and harsh solvents previously investigated in connection with thiol-ene polymers.[19,20,25] For the mild solvents (water, ethanol, isopropanol, hexane and toluene), both the control and heat-treated materials show negligible swelling, under 0.5% after a 24 h exposure period (data not shown). Therefore, long-term exposure studies were focused on the solvents most damaging to thiol-ene: tetrahydrofuran (THF), dimethylformamide (DMF), acetone (ACE), acetonitrile (ACN), chloroform (CF) and dichloromethane (DCM). Here, 4-day long solvent exposure experiments were conducted, where single channel chips were fully submerged in the solvent and the channel width decrease was assessed according to eqn (1). The bulk material contained 0.5% TPO-L photoinitiator for both the control and 200 °C, 60-hour heat treated chips. The results show that heat treatment increases solvent resistance

 

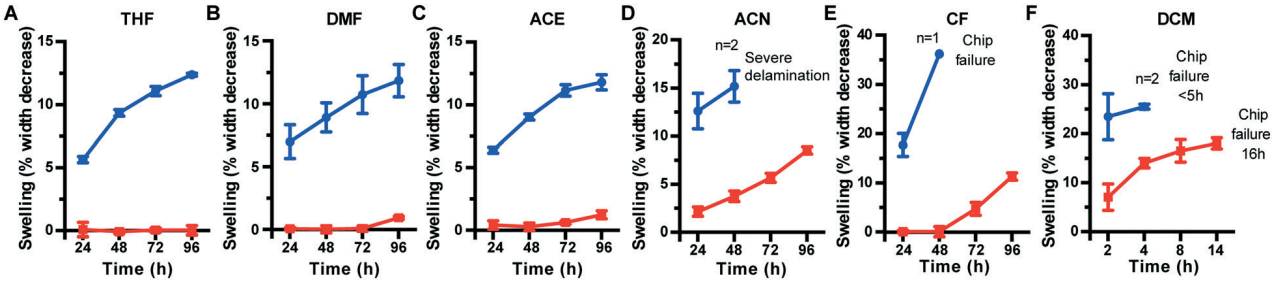


Fig. 3 Applicability of heat treatment for various harsh solvents. Thiol-ene chips with 0.5% TPO-L photoinitiator were exposed to (A) tetrahydrofuran, (B) dimethylformamide, (C) acetone, (D) acetonitrile, (E) chloroform, (F) dichloromethane. Blue lines show untreated and red lines show heat treated chips at 200 °C for 60 h. Channel widths measured every 24 hours in triplicates. Error bars represent standard deviation.



for all tested solvents (Fig. 3), albeit to various extents. THF, DMF and ACE (Fig. 3A–C) resulted in similar degrees of swelling in the untreated controls (blue), from 6–12% over the course of 96 hours. Heat treatment (red) mitigated swelling, and all samples show little to no swelling, 0–1.5%. Acetonitrile affected both the control and heat treated samples; however, the heat treated samples faired significantly better (Fig. 3D). Even so, exposure to acetonitrile over extended time periods is ultimately damaging both treated and untreated materials. Increasingly damaging, chloroform resulted in chip failure for the control samples between 24–48 hours, Fig. 3E. As already shown above (Fig. 1D), heat treatment completely prevents swelling for the first 48 hours. Interestingly, solvent resistance wears off by 72 hours, upon which swelling occurs; still, the channels maintain functionality up to the 96 hours mark. The level of swelling at 96 hours appears already after 2 hours in the untreated material, thus yielding a 50-fold increase in solvent compatibility (in terms of longevity) as a result of heat treatment. Finally, the most damaging solvent is dichloromethane, Fig. 3F, where both the control and heat treated materials are significantly affected. The control material is rendered non-functional within 4–5 hours, while heat treatment prolongs the time to channel failure to 16 hours. In general, heat treatment shows excellent utility for various applications requiring a range of organic solvents.

### Investigation of heat treated thiol-ene polymer

In order to investigate the underlying mechanism of the thiol-ene heat treatment, several additional experiments were performed. Given that the samples are heated in the presence of oxygen, we hypothesized that oxidation of the thiol groups to sulfoxides and sulfones may be contributing to the increased solvent resistance. Based on the work of Podgórski *et al.*, chemical oxidation of thiolether materials results in mechanical property enhancements (such as a significant increase in the glass transition temperature).[26] It was hypothesized that oxidation of the thioethers improves the compatibility to solvents. To investigate whether the presence or absence of oxygen is required, thiol-ene chips were heated under argon or nitrogen in a sealed aluminum vessel. Controls at room temperature, and the samples heated in ambient air, argon, or nitrogen were conducted using 0.5% TPO-L containing thiol-ene. The materials were heated for 60 hours at 200 °C or remained at room temperature. What is immediately apparent is the stark color difference between the three groups, with the characteristic orange color only apparent in the 200 °C air samples (Fig. 4A). A slight discoloration of the argon and nitrogen samples is presumably due to an incomplete replacement of ambient air. Subsequent exposure to chloroform for 16 hours highlights the necessity of air (oxygen) during the heat treatment. The results show that heating under argon or nitrogen is not sufficient to achieve chloroform resistance (Fig. 4B), showing a nonsignificant difference in swelling between chips treated under argon or nitrogen and the controls. Only when heated in air are the desired effects observed.

In order to investigate whether the oxidation of sulfur atoms directly increases the solvent compatibility, thiol-ene chips were oxidized using hydrogen peroxide. Similar to the heat treated samples, chemical oxidation of the thiol-ene chips resulted in significant gains in solvent resistance

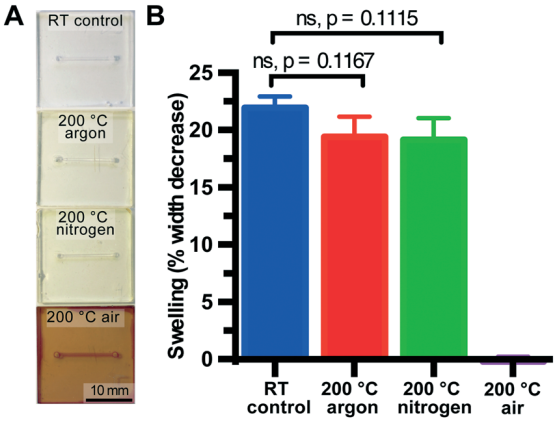


Fig. 4 Heat treatment in air or argon. (A) Image of the control, 200 °C air heated, 200 °C argon, 200 °C nitrogen heated chips. (B) Chips were heated at 200 °C for 60 hours in the presence of ambient air (purple), argon (red) or nitrogen (green). Control chips remained at room temperature for 60 hours (blue). Chips were subsequently exposed to chloroform for 16 hours, and channel swelling was measured. All chips contain 0.5% TPO-L photoinitiator. Error bars represent standard deviation, $n = 3$. Unpaired $t$-test was conducted assuming unequal standard deviations.

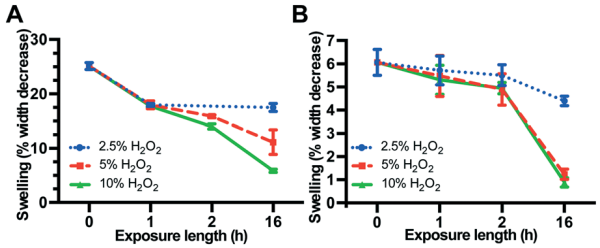


Fig. 5 Effect of oxidation on solvent resistance. (A) Chips immersed in 2.5% (blue), 5% (red) or 10% $H_2O_2$ (green) for indicated time points. Chips were subsequently exposed to chloroform for one hour and the channel size was measured. (B) Same as (A), except 0.5% photoinitiator (TPO-L) added to the bulk material. All chips were cured for 10 minutes at 90 mW $cm^{-2}$ and 365 nm. All data points were run in triplicates. Error bars represent standard deviation among replicates.

(Fig. 5A and B). After 16 hours of 10% $H_2O_2$ treatment, both photoinitiator free and 0.5% TPO-L containing polymers achieve low levels of swelling after chloroform exposure, at 5.5% and 0.8%, respectively (Fig. 5A and B, green). Still, chemical oxidation was not able to achieve the same degree of solvent compatibility as heat treatment. Increasing the concentration of $H_2O_2$ results in chemical burns of the photoinitiator-free material, leading to delamination and deformation. Therefore, we found that 16 hours of exposure to 10% $H_2O_2$ yields the maximum achievable oxidation without material damage. Since the results clearly demonstrate that chemical oxidation of the material significantly improves the swelling behavior, the heat treated materials were further investigated on the oxidation state of the sulfur.

To probe the oxidation state of the heated samples, X-ray photoelectron spectroscopy (XPS) measurements were performed. XPS is the ideal method for investigating surface oxidation, because the addition of oxygen to the sulfur results in large peak shifts in electron binding energy in the spectrum. For the measurements, 60 h at RT control, 16 h in 30% hydrogen peroxide and 60 h at 200 °C heat treated disks of thiol-ene were analyzed and the sulfur binding energies (S2p doublet) are shown in Fig. 6A. The results show that the control sample is mildly oxidized to sulfoxides, with 76.7% unmodified thiols and 23.3% sulfoxide formation, Fig. 6A, red. Here, we see mostly unmodified thiols with the $S2p_{3/2}$ at 163.3 eV as well as the minor fraction of sulfoxides, where the addition of a single oxygen shifts the $S2p_{3/2}$ peak to 165.6 eV. The $H_2O_2$ treated sample is (as expected) almost fully oxidized to sulfones, showing 81% sulfones (167.8 eV), 12.6% sulfoxides (165.9 eV), and 6.6% unmodified thiols (163.3 eV), Fig. 6A, blue. Finally, the heated sample shows no oxidation at the sulfur atom, Fig. 6A, green. The heated sample shows 100% unmodified thiols (163.3 eV) and hence this data strongly suggests that oxidation of the thioether is not the underlying mechanism for the increased solvent compatibility.

XPS spectra for other species than sulfur were also investigated. Both nitrogen and oxygen spectra showed no discernable difference between the heated and unheated samples (data not shown). Interestingly, only the carbon spectra revealed a change. The carbon peak of the heated sample displays increased broadening of around 25% with prolonged heat treatment, which is indicative of a more disordered chemical environment. Curve fitting of the carbon spectra of the unheated (Fig. 6B) and heated (Fig. 6C) samples shows a 0.3 eV difference of the full width at half maximum (FWHM). This points to the possibility that heat is changing the structural arrangement of the thiol-ene material.

In order to investigate whether heat treatment changes the mechanical properties of the thiol-ene polymer, dynamic mechanical analysis (DMA) was performed on 200 °C heat treated (16 and 60 h) and pristine (RT control) thiol-ene slabs. The storage modulus is shown in Fig. 7A, where no significant difference is apparent in both the glassy and rubbery state for the control and heat treated samples. The glass transition temperature ($T_g$) of the pristine samples was determined to be 64 °C, while the heat treatment increased the $T_g$ to 87 °C and 117 °C, for 16 h and 60 h treatments, respectively (Fig. 7B). Since an increase of $T_g$ is directly related to a decrease in free volume inside the polymer, the result supports the hypothesis of a volumetric change in the polymer

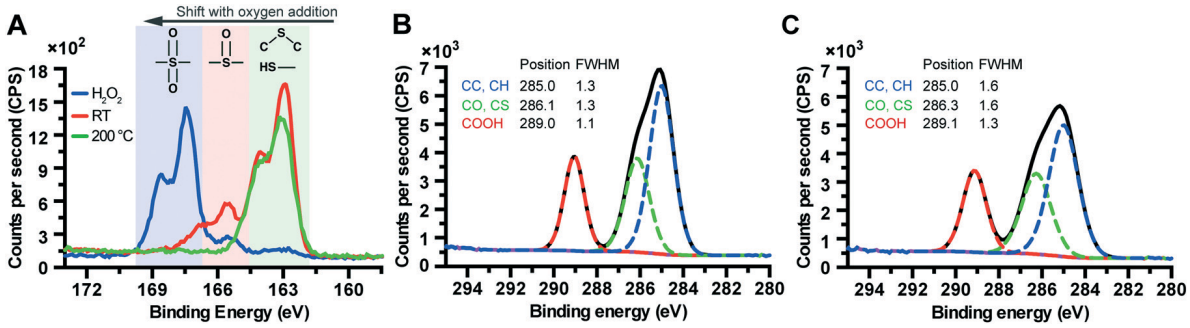


Fig. 6 Sulfur and carbon XPS spectra. (A) Combined sulfur XPS spectra of control (red, 60 h at RT), heat treated (green, 60 h at 200 °C), or $H_2O_2$ oxidized (blue, 16 h in 30% $H_2O_2$) materials. Spectra show the S2p binding energy region. Control sample shows both unmodified thiols and sulfoxides. 60 h at 200 °C heat treated samples show no oxygen modification of the thiols. $H_2O_2$ oxidized sample shows all three sulfur species present – sulfones, sulfoxides and unmodified thiols. (B) Carbon 1s binding energy region for control (60 h at RT) sample. (C) Carbon 1s binding energy region for heat treated (60 h at 200 °C) sample.



 

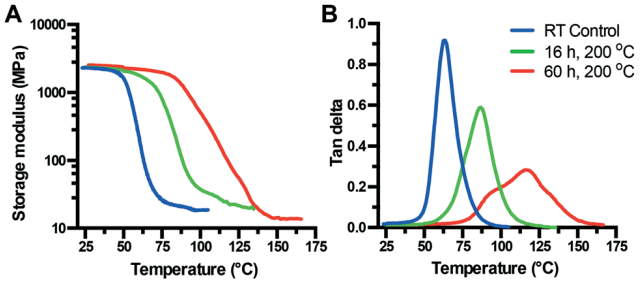


Fig. 7 Dynamic mechanical properties of heat treated thiol-ene materials. (A) Storage modulus and (B) tan delta measurements of the pristine (blue), 16 h (green) 200 °C and 60 h 200 °C (red) heat treated samples. All data points were run in triplicates.

due to the heat treatment.[27] A decrease in free volume is known to be directly related to a decreased penetration of solvents into the polymer and would hence result in decreased swelling.[28] To further confirm a volumetric change, density and mass measurements were conducted showing 0.18 ± 0.03% increase in density and a 0.58 ± 0.02% decrease in weight. The combined effect of the two changes yields a decrease of approximately 0.75% in polymer volume. Additional analysis of the DMA data shows that the full-width-at-half-maximum (FWHM) values for the glass transition of the pristine and the 16 h and 60 h heat treated samples are 15 °C, 21 °C and 45 °C, respectively (Fig. 7B). While the pristine polymer exhibits a sharp single peak, an additional shoulder appears for the 60 h heat treated samples. This indicates an increase of the structural heterogeneities of the heat treated network compared to the pristine network. The structural heterogeneity seen in the mechanical data is perfectly in line with the XPS carbon spectra, where a more disordered environment was detected. The results from these additional experiments seem to support the hypothesis that a reduction of the void volume of the material upon heating, and hence the

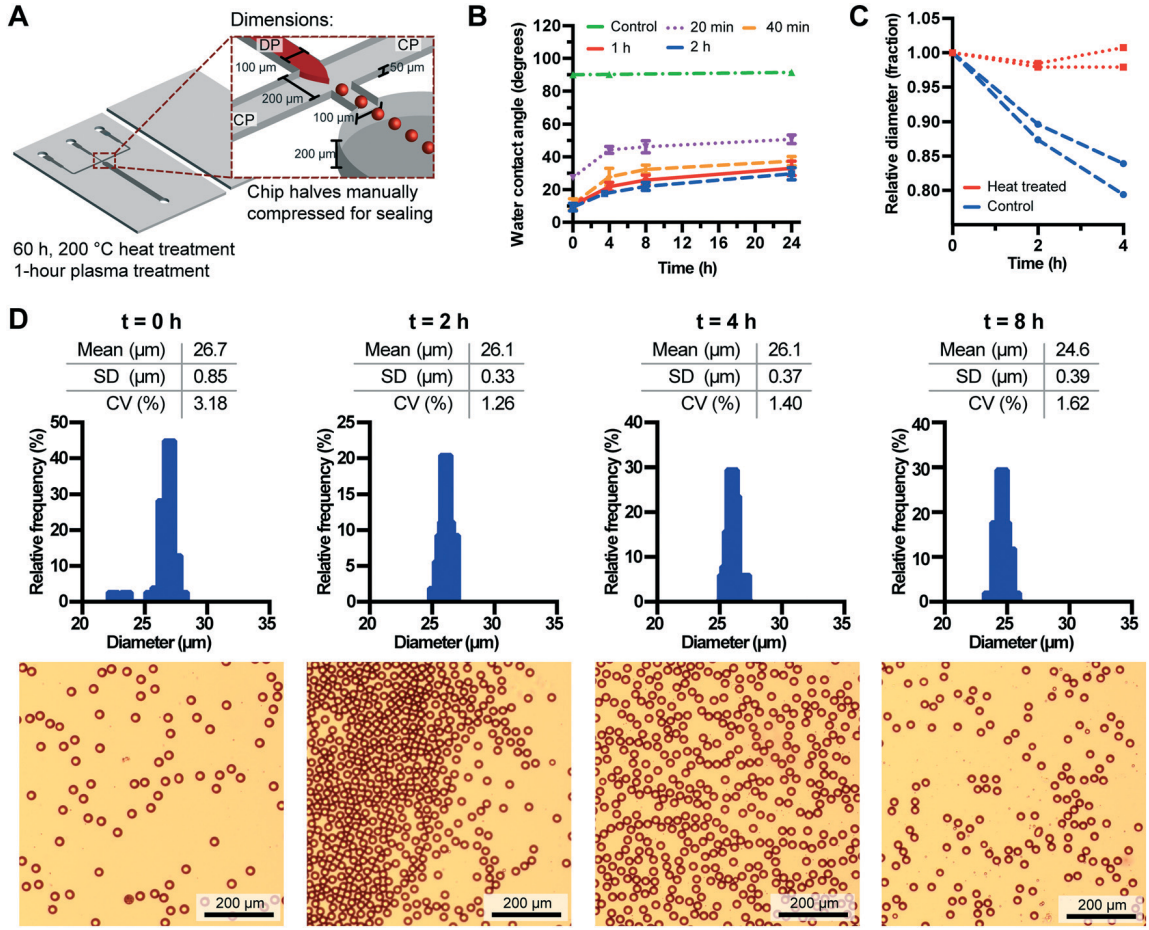


Fig. 8 Pharmaceutical application of solvent resistant thiol-ene chips. (A) Schematic illustration of flow focusing chip used for microsphere production. Chip dimensions include 50 µm overall depth, 100 µm wide orifice and a 1 mm wide opening with 200 µm depth. (B) Water contact angle development over time of heat-treated thiol-ene and subsequent plasma treatment for 20 minutes (purple), 40 minutes (orange), 1 hour (red), 2 hours (blue) and control (green). Contact angles were followed for 24 hours. Error bars represent standard deviation among triplicates. (C) Relative size of particles over the course of production. Sizes were normalized to hour 0 average diameters, for both heat treated chips (red) and untreated chips (blue). Heat treated chips contain 0.5% TPO-L and untreated chips contain 1% TPO-L. (D) 60 h 200 °C heat treated chips were plasma treated for 1 hour. PLA particles were continuously produced for 8 hours. Dispersed phase was 5% PLA in chloroform, and continuous phase 1% PVA in water. Upon washing, particles were sized and Gaussian distributions plotted, from which coefficient of variations (CV) were derived. Results at the beginning of production, and after 2, 4, and 8 hours are shown. The numbers of particles seen in the microphotographs are not correlated to chip performance.



 

decreased ability of the solvents to penetrate into the material, is mainly responsible for the improved solvent compatibility. Still, the presence and role of oxygen during heating, and how this contributes to the overall solvent compatibility, is still not conclusively elucidated. More detailed experiments are therefore still necessary; however, we deem this to be well outside the scope of the work described here.

### Chloroform resistant chip for microparticle production

Finally, we show the applicability of the solvent resistant thiol-ene material in the context of pharmaceutical microparticle production, where the usage of glass microfluidic chips is the gold standard. Here, we use a conventional flow focusing geometry for the production of chloroform/PLA droplets in water. The chip geometry is shown in Fig. 8A, featuring a 100 μm wide and 50 μm deep orifice, and a 1 mm wide and 200 μm deep opening. For droplet formation in two-phase flow microfluidics, surface wettability becomes a critical concern. Ultimately, the continuous phase should exhibit favorable surface wetting, contrary to the dispersed phase, where surface wetting should be minimized.[29] Therefore, for PLA microsphere production, which is based on an oil-in-water emulsion, hydrophilic channels are required. Pristine thiol-ene has a water contact angle (WCA) of 60–70° (depending on composition), which can present a serious challenge for droplet-based microfluidics. Some strategies have been previously implemented to modify the channel surface, generally taking advantage of free thiol groups in off-stoichiometric thiol-ene (OSTE) chips.[30,31] These "click" modifications include PEG (WCA = 52°), acrylic acid (WCA = 43°), and hydroxyethyl methacrylate (WCA = 43°). Importantly, high excess of thiol groups results in only "loosely" polymerized chips causing a 3-fold increase in solvent susceptibility, as shown through acetone induced swelling studies.[30] For the case of chloroform, we found an over 37-fold increase in swelling in 90% thiol-excess chips when compared to the stoichiometric control (data not shown). PEG addition to allyl excess thiol-ene has been shown to yield a 35° WCA;[14] however, we were only able to achieve a 40.5 ° WCA, which is not hydrophilic enough for droplet microfluidics. Therefore, to achieve favorable wettability while maintaining solvent resistance, plasma treatment was used to increase the hydrophilicity of the channel surfaces. Fig. 8B shows that the heat-treated thiol-ene surface has a contact angle of 90°, while with prolonged plasma treatment it decreases down to 9.2° (for 2 h treatment). The data shows that no significant gains in contact angle are made after 40 min of plasma treatment. Moreover, plasma treatment wears off with time, which is suboptimal, as changes in the surface wettability can interfere with consistent microsphere production. Lastly, as plasma treatment of the inner surface renders chip bonding impossible, the chip halves have to be manually compressed together for sealing.

For the production of microspheres, the thiol-ene chip halves were heat treated for 60 hours and subsequently plasma treated for one hour. The chip was then used for the flow focusing of 5% (w/v) PLA in chloroform with 1% (w/v) polyvinyl alcohol (PVA) in water as the continuous phase. Initially, it is important to note that the particle diameter rapidly decreases in untreated thiol-ene chips due to heavy swelling of the dispersed phase channel (*i.e.*, the channel exposed to chloroform). As a consequence, within four hours, the particle diameter is only 80% of the value at the beginning, resulting in a polydisperse sample (Fig. 8C, blue). In comparison, in the heat and plasma treated chips the particles maintain a similar diameter over the course of 4 hours (red).

Additionally, microspheres were collected for 10 minutes every 2 hours for a total of 8 hours of continuous operation using heat treated chips. The results show that the heat treated thiol-ene is capable of producing consistent particles for the duration of 8 hours (Fig. 8D). The coefficient of variation (CV) of the main droplets remain low throughout; however, increasing amounts of satellite particles are formed after 6 hours. This is likely due to the plasma treatment wearing off as shown in Fig. 8B; therefore, better approaches for providing sufficient and long-term stable surface hydrophilicity are needed. Nonetheless, given that thiol-ene chips are simple to fabricate and disposable, chip replacement upon the degradation of favorable wetting properties is an easy and valid alternative.

## Conclusions

In summary, we present a simple yet effective method for gaining solvent compatible polymeric microfluidic chips. We show that heat treatment of thiol-ene materials at 100–200 °C for up to 60 hours results in a significant increase in chloroform compatibility allowing for the operation of the microfluidic chip for several days. Using XPS and DMA analysis we show that the heat treatment significantly reduces the void volume inside the polymer. Based on these findings, we postulate that the solvent compatibility increases due to the decreased ability of solvents to penetrate into the thiol-ene network. However, a complete understanding of the underlying mechanism is yet to be established and beyond the scope of this paper. In addition, we show a successful proof-of-concept application of the material in a pharmaceutical setting. PLA microspheres were synthesized for 8 continuous hours with consistent main particle sizes. The presented solvent compatible thiol-ene shows promise to replace glass as a low-cost alternative to many microfluidic applications. Moreover, due to the ease of fabrication and replica molding of thiol-ene chips, the method opens avenues towards the miniaturization of countless applications utilizing harsh chemical environments where extensive geometry prototyping poses a challenge in the development stage.

## Experimental

### Materials

The monomers (pentaerythritol tetrakis(3-mercaptopropionate), (PETMP), 1,3,5-triallyl-1,3,5-triazine-2,4,6(1*H*,3*H*,5*H*)-trione,

 

(TTT) and 2,4,6-triallyloxy-1,3,5-triazine are all from Sigma Aldrich, Schnelldorf, Germany. Commercial formulations are NOA-81 (Norland Products Inc., Cranbury, NJ, USA) and 322 Ostemer Crystal Clear (Mercene Labs, Stockholm, Sweden). Positive molds were fabricated on poly(methyl methacrylate) (PMMA, Nordisk Plast A/S, Randers, Denmark) and negative molding used polydimethylsiloxane (PDMS, Sylgard® 184, Dow Corning, Wiesbaden, Germany). As indicated, self-mixed formulations incorporated Lucirin® TPO-L (BASF, Ludwigshafen, Germany). Chemical oxidation was done using hydrogen peroxide (30%, Emsure ISO, Merck KGaA, Darmstadt, Germany). The following solvents were used: chloroform, dichloromethane, tetrahydrofuran, and toluene, (all ACS reag., Merck KGaA, Darmstadt, Germany); acetonitrile (HPLC LC-MS grade, VWR, Fontenay-sous-Bois, France); dimethylformamide, (ReagentPlus, Sigma Aldrich, Schnelldorf, Germany). For microsphere production, poly(D,L-lactide) (PLA, 10–18 kDa, Resomer® R 202 H) and poly(vinyl alcohol) (PVA, MW 30–70 kDa, 87–90% hydrolyzed), both from Sigma Aldrich, Schnelldorf, Germany were used.

### Chip fabrication

Unless otherwise indicated, thiol-ene microfluidic chips were fabricated from the monomers PETMP and TTT based on previous descriptions in ref. 32. Channel geometries were designed using Autodesk® Inventor® Professional (Autodesk Inc., San Rafael, CA, USA) and InventorCAM (SolidCAM Inc., Newtown, PA, USA). PMMA plates were computer numerical controlled (CNC) milled (MiniMill, Minitech Machinery, Norcross, GA, USA), serving as the positive master mold. Spacers and lids were laser cut using Epilog Laser Mini 18 (Golden, CO, USA). The master mold, spacer and lid were combined and PDMS casted (10 : 1 ratio of base: curing agent), then heated for 2 h at 80 °C. Stoichiometric PETMP and TTT with or without 0.5% (w/w) TPO-L were subsequently molded in the PDMS negatives and exposed to UV light. For bulk material sans photoinitiator, both sides of the mold were exposed to 12 seconds of 90 mW $cm^{-2}$ intensity UV light (at 365 nm), (Dymax 5000-EC Series UV curing flood lamp, Dymax Corp., Torrington, CT, USA). When 0.5% TPO-L was added, the non-bonding side of the mold was exposed to 1.8 seconds of 12 mW $cm^{-2}$ intensity UV light (at 365 nm), (LS-100-3C2 near UV light source, Bachur & Associates, Santa Clara, CA, USA). After UV exposure, the chips were assembled by manually aligning and pressing together the top and bottom pieces. Each side of the chip was cured for 5 minutes at 90 mW $cm^{-2}$ intensity.

### Heat exposure and $H_2O_2$ oxidation

Stoichiometric thiol-ene chips, with and without 0.5% TPO-L, were exposed to $H_2O_2$ of various strength (0.1–10%) and duration (1–16 hours), then desiccated under a vacuum to remove residual $H_2O_2$. The chip channels were filled with $H_2O_2$ and the whole chip submerged at RT, away from light. Similarly, for heat treatment, 10-minute UV cured, stoichiometric thiol-ene chips, with and without 0.5% TPO-L were heated under ambient air within an oven (UNB 100, Memmert GmbH + Co. KG, Schwabach, Germany) at various temperatures (100–200 °C) and duration (1–60 hours).

### Swelling determination

A simple, single channel chip design was manufactured ($W$: 500 μm × $D$: 250 μm, 2 mm thick chip) and solvents were pumped through the channels at a flow rate of 10 μL $min^{-1}$. Flow was maintained for the indicated time points or until solvent-induced narrowing of the channel resulted in high back-pressures that stalled the syringe pump. Alternatively, (as indicated) for the four-day solvent exposure experiment, the channels were filled with the solvent and the material fully submerged for the duration of the exposure times. Microscope images at high magnification were taken prior to solvent exposure and at each time point. Channel widths were determined using ImageJ. For statistics, unpaired $t$-test was calculated in GraphPad Prism, assuming non-equal standard deviations.

### X-ray photoelectron spectroscopy (XPS)

XPS is a surface sensitive technique that gives chemical information of the top 10 nm at the surface. The instrument was a Kratos Axis Ultra$^{DLD}$ equipped with a charge neutralizer. The X-ray source was Al Kα (1486.6 eV, power at 150 W). No noticeable beam damage was observed. The data were analyzed using the software CasaXPS and using the aliphatic C1s line for calibration at 285 eV. The sulfur 2p line consists of a doublet with separation of 1.18 eV which was fixed during fitting. Accuracy of reported binding energies is ±0.1 eV.

### Dynamic mechanical analysis

Thiol-ene slabs were prepared with the addition of 0.5% (w/w) TPO-L with a thickness of 0.5 mm. Mechanical properties were measured on a Q800 dynamic mechanical analyzer (TA Instruments, New Castle, USA) with an oscillation of 1 Hz, an amplitude of 15 μm and a heating rate of 3 °C $min^{-1}$. Glass transition values were determined by peak maximum of tan delta signal.

### Density measurements

Densities were measured based on a previous investigation of thiol-enes.[33] A known concentration of calcium nitrate was prepared with a density higher than the thiol-ene substrates, suspending the material. With subsequent addition of water, and thus dilution of the calcium nitrate solution, the thiol-ene slabs transitioned from being suspended to sinking in the solution. Based on the concentration of calcium nitrate, its density was calculated using the equations previously reported.[34] The measurements were repeated with smaller volume additions until densities were determined to 3 significant digits and then repeated three times.



 

### Microsphere production

Microspheres were produced as previously described in ref. 35. Briefly, the flow focusing microfluidic chip had an orifice 50 μm deep, 100 μm wide and 100 μm deep, and a post-orifice opening 200 μm deep and 1 mm wide. The chip is 4 mm thick and connected to the syringe pump using the Linear 4-way Connector and 4-way Top Interface (both Dolomite Microfluidics, Blacktrace Holdings Ltd., Royston, UK). Each chip half was plasma treated with air for 1 hour at maximum power using the Atto Plasma Laboratory Unit (Diener electronic GmbH, Ebhausen, Germany). Clamping of the chip halves was achieved using laser-cut 5 mm PMMA pieces screwed together. The dispersed phase (DP) consisted of 5% (w/v) PLA, dissolved in chloroform. The continuous phase (CP) consisted of an aqueous solution of 1% (w/v) PVA. Flow control was achieved by a neMESYS low-pressure syringe pump (CETONI GmbH, Germany) at DP flow rate of 1 μL $min^{-1}$ and CP flow rate of 20 μL $min^{-1}$. Droplets were collected for 10 minutes, spun at 2000 rcf and resuspended with 100× vol MilliQ to facilitate solvent evaporation to result in dense microspheres. Microspheres were imaged on an Olympus IX71 inverted microscope. At least 200 diameters were measured in ImageJ and plotted as a histogram in GraphPad prism where coefficient of variation was calculated.

## Conflicts of interest

There are no conflicts to declare.

## Acknowledgements

This study was made possible by a grant from the Lundbeck Foundation, Denmark (grant number 2014-4176, the UBC-SUND Lundbeck Foundation professorship to UOH).

## References

1 K. K. R. Tetala, J. W. Swarts, B. Chen, A. E. M. Janssen and T. A. van Beek, *Lab Chip*, 2009, **9**, 2085–2092.
2 M. Bokharaei, T. Schneider, S. Dutz, R. C. Stone, O. T. Mefford and U. O. Häfeli, *Microfluid. Nanofluid.*, 2016, **20**, 6.
3 R. F. Gerhardt, A. J. Peretzki, S. K. Piendl and D. Belder, *Anal. Chem.*, 2017, **89**, 13030–13037.
4 K. Ren, J. Zhou and H. Wu, *Acc. Chem. Res.*, 2013, **46**, 2396–2406.
5 J. N. Lee, C. Park and G. M. Whitesides, *Anal. Chem.*, 2003, **75**, 6544–6554.
6 K. Ren, W. Dai, J. Zhou, J. Su and H. Wu, *Proc. Natl. Acad. Sci. U. S. A.*, 2011, **108**, 8162–8166.
7 S. Begolo, G. Colas, J.-L. Viovy and L. Malaquin, *Lab Chip*, 2011, **11**, 508–512.
8 J. P. Rolland, R. M. Van Dam, D. A. Schorzman, S. R. Quake and J. M. DeSimone, *J. Am. Chem. Soc.*, 2004, **126**, 2322–2323.
9 N. S. G. K. Devaraju and M. A. Unger, *Lab Chip*, 2011, **11**, 1962–1967.
10 T. J. A. Renckens, D. Janeliunas, H. van Vliet, J. H. van Esch, G. Mul and M. T. Kreutzer, *Lab Chip*, 2011, **11**, 2035–2038.
11 K.-I. Min, T.-H. Lee, C. P. Park, Z.-Y. Wu, H. H. Girault, I. Ryu, T. Fukuyama, Y. Mukai and D.-P. Kim, *Angew. Chem., Int. Ed.*, 2010, **49**, 7063–7067.
12 J. Thiele, A. R. Abate, H. C. Shum, S. Bachtler, S. Förster and D. A. Weitz, *Small*, 2010, **6**, 1723–1727.
13 P. Kumlangdudsana, A. Tuantranont, S. T. Dubas and L. Dubas, *Mater. Lett.*, 2011, **65**, 3629–3632.
14 C. F. Carlborg, T. Haraldsson, K. Oberg, M. Malkoch and W. van der Wijngaart, *Lab Chip*, 2011, **11**, 3136–3147.
15 J. F. Ashley, N. B. Cramer, R. H. Davis and C. N. Bowman, *Lab Chip*, 2011, **11**, 2772–2778.
16 J. P. Lafleur, R. Kwapiszewski, T. G. Jensen and J. P. Kutter, *Analyst*, 2013, **138**, 845–849.
17 S. Senkbeil, J. Aho, L. Yde, L. R. Lindvold, J. F. Stensborg, J. Rantanen, J. P. Lafleur and J. P. Kutter, *J. Micromech. Microeng.*, 2016, **26**, 075014.
18 L.-H. Hung, R. Lin and A. P. Lee, *Lab Chip*, 2008, **8**, 983–987.
19 G. Sheppard, T. Oseki, A. Baba, D. Patton, F. Kaneko, L. Mao and J. Locklin, *Biomicrofluidics*, 2011, **5**, 26501.
20 P. Wägli, A. Homsy and N. F. de Rooij, *Sens. Actuators, B*, 2011, **156**, 994–1001.
21 T. D. Prichard, S. S. Singh, N. Chawla and B. D. Vogt, *Polymer*, 2013, **54**, 1130–1135.
22 M. Podgórski, E. Becka, S. Chatani, M. Claudino and C. N. Bowman, *Polym. Chem.*, 2015, **6**, 2234–2240.
23 A. R. Abate, D. Lee, T. Do, C. Holtze and D. A. Weitz, *Lab Chip*, 2008, **8**, 516–518.
24 V. Arima, M. Bianco, A. Zacheo, A. Zizzari, E. Perrone, L. Marra and R. Rinaldi, *Thin Solid Films*, 2012, **520**, 2293–2300.
25 S. M. Tähkä, A. Bonabi, V. P. Jokinen and T. M. Sikanen, *J. Chromatogr. A*, 2017, **1496**, 150–156.
26 M. Podgórski, C. Wang, Y. Yuan, D. Konetski, I. Smalyukh and C. N. Bowman, *Chem. Mater.*, 2016, **28**, 5102–5109.
27 K. P. Menard and N. R. Menard, in *Encyclopedia of Polymer Science and Technology*, Wiley, USA, 2015, DOI: 10.1002/0471440264.pst102.pub2.
28 J. S. Vrentas, J. L. Duda and W. J. Huang, *Macromolecules*, 1986, **19**, 1718–1724.
29 H. Gu, M. H. Duits and F. Mugele, *Int. J. Mol. Sci.*, 2011, **12**, 2572–2597.
30 S. Mongkhontreerat, K. Öberg, L. Erixon, P. Löwenhielm, A. Hult and M. Malkoch, *J. Mater. Chem. A*, 2013, **1**, 13732–13737.
31 G. Pardon, F. Saharil, J. M. Karlsson, O. Supekar, C. F. Carlborg, W. van der Wijngaart and T. Haraldsson, *Microfluid. Nanofluid.*, 2014, **17**, 773–779.
32 T. M. Sikanen, J. P. Lafleur, M.-E. Moilanen, G. Zhuang, T. G. Jensen and J. P. Kutter, *J. Micromech. Microeng.*, 2013, **23**, 037002.
33 G. Yang, S. L. Kristufek, L. A. Link, K. L. Wooley and M. L. Robertson, *Macromolecules*, 2016, **49**, 7737–7748.
34 W. W. Ewing and R. J. Mikovsky, *J. Am. Chem. Soc.*, 1950, **72**, 1390–1393.
35 R. Geczy, M. Agnoletti, M. F. Hansen, J. P. Kutter, K. Saatchi and U. O. Häfeli, *J. Magn. Magn. Mater.*, 2019, **471**, 286–293.

Europäisches Patentamt
European Patent Office
Office européen des brevets

European Patent Office
80298 MUNICH
GERMANY

**Questions about this communication ?**
Contact Customer Services at www.epo.org/contact

Géczy, Réka
Københavns Universitet
Nørregade 10
1165 København K
DANEMARK

| Date |
|---|
| 10.09.18 |

| Reference | Application No./Patent No. |
|---|---|
| | 18184178.4 - 1107 |
| Applicant/Proprietor | |
| Københavns Universitet | |

**Designation as inventor - communication under Rule 19(3) EPC**

You have been designated as inventor in the above-mentioned European patent application. Below you will find the data contained in the designation of inventor and further data mentioned in Rule 143(1) EPC:

DATE OF FILING : 18.07.18

PRIORITY : / /

TITLE : METHODS FOR THE TREATMENT OF THERMOSET POLYMERS

DESIGNATED STATES : AL AT BE BG CH CY CZ DE DK EE ES FI FR GB GR HR HU IE IS IT LI LT LU LV MC MK MT NL NO PL PT RO RS SE SI SK SM TR

INVENTOR (PUBLISHED = 1, NOT PUBLISHED = 0):

1/Sticker, Drago/Københavns Universitet Nørregade 10/1165 København K/DK
1/Géczy, Réka/Københavns Universitet Nørregade 10/1165 København K/DK
1/Kutter, Jörg P./Københavns Universitet Nørregade 10/1165 København K/DK
1/Häfeli, Urs Otto/Københavns Universitet Nørregade 10/1165 København K/DK

DECLARATION UNDER ARTICLE 81 EPC:
The applicant(s) has (have) acquired the right to the European patent as employer(s).

**Receiving Section**

Europäisches Patentamt • European Patent Office • Office européen des brevets

# 12. Appendix II

**Publication 2: Journal of Magnetism and Magnetic Materials**

---

Geczy, R., M. Agnoletti, M.F. Hansen, J.P. Kutter, K. Saatchi, and U.O. Häfeli, *Microfluidic approaches for the production of monodisperse, superparamagnetic microspheres in the low micrometer size range,* Journal of Magnetism and Magnetic Materials, **2019**. 471: p. 286-293.

Journal of Magnetism and Magnetic Materials 471 (2019) 286–293

Contents lists available at ScienceDirect

Journal of Magnetism and Magnetic Materials

journal homepage: www.elsevier.com/locate/jmmm

Research articles

# Microfluidic approaches for the production of monodisperse, superparamagnetic microspheres in the low micrometer size range

Reka Geczy[a,b], Monica Agnoletti[a,b], Mikkel F. Hansen[c], Jörg P. Kutter[a], Katayoun Saatchi[b], Urs O. Häfeli[a,b,*]

[a] Department of Pharmacy, Faculty of Health and Medical Sciences, University of Copenhagen, 2100 Copenhagen, Denmark
[b] Faculty of Pharmaceutical Sciences, University of British Columbia, Vancouver, British Columbia V6T 1Z3, Canada
[c] Department of Micro- and Nanotechnology, Technical University of Denmark, 2800 Kongens Lyngby, Denmark

ABSTRACT

The preparation of small, monodispersed magnetic microparticles through microfluidic approaches has been consistently challenging due to the high energy input needed for droplet break-off at such small diameters. In this work, we show the microfluidic production of 1–3 µm magnetic nanoparticle-loaded poly(D, L-lactide) (PLA) microspheres. We describe the use of two approaches, using a conventional flow-focusing microfluidic geometry. The first approach is the separation of target size satellite particles from the main droplets; the second approach is the direct production using high flow rate jetting regimes. The particles were produced using a polymeric thiol-ene microfluidic chip platform, which affords the straightforward production of multiple chip copies for single-time use, due to large feature sizes and replica molding approaches. Through the encapsulation of magnetite/maghemite nanoparticles, and their characterization with scanning electron microscopy (SEM) and vibrating sample magnetometry (VSM) measurements, we show that the resulting particles are monosized, highly spherical and exhibit superparamagnetic properties. The particle size regime and their magnetic response show potential for in vivo intravenous applications of magnetic targeting with maximum magnetic response, but without blocking an organ's capillaries.

## 1. Introduction

There are many potential *in vivo* applications for magnetic nanoparticles (MNPs) including therapeutic applications such as drug delivery (with the drug being encapsulated or bound to the MNPs) and magnetic hyperthermia (where the entire MNP heats up under the influence of an alternating magnetic field). Furthermore, diagnostic applications such as the imaging of receptor expression and cell types by magnetic particle imaging, MRI contrast and biosensing for diseases detection also benefit from MNPs [1]. For magnetic targeting under the influence of an external magnetic field, the typically used 20–100 nm sized particles are not ideal, as the magnetic force acting on a single particle is too small to overcome the blood stream's inertial and shear forces. Therefore, accumulation in the target tissues (e.g., a tumor) or a target organ (e.g., the pancreas) requires high magnetic fields and field gradients [2]. The easiest solution to overcoming these challenges in magnetic drug targeting is to increase the particle size, i.e., moving from nanoparticles to microparticles.

For *in vivo* intravenous administration, the magnetic microspheres (MMS) must be smaller than red blood cells, which have an average size of 6.5 µm, and should be spherical, monodisperse and superparamagnetic. Any capillary blockage can thus be avoided, both with and without an applied magnetic field, and allow for efficient and predictable magnetic targeting. An optimal targeting particle size might be one based on nature, namely the size of thrombocytes (blood platelets), which have a maximum size of between 2 and 3 µm [3], and typically circulate in the blood stream for 8–9 days [4]. This size regime effectively bypasses lung capillaries [5,6], while showing greater localization to the endothelium than the sub-micron counterparts [7]. Our lab favors the use of biodegradable monodisperse MMS, as they combine the defined magnetic targetability, the capability of encapsulation and controlled release of drugs with low toxicity, FDA-approval, and biodegradability once the MMS have done their job. Up to now, our lab made monodisperse MMS with a microfluidic glass chip at sizes between 8 and 50 µm [8], and later with a co-flow method to yield sizes up to 700 µm [9]. Smaller MMS had to be prepared by a solvent evaporation/extraction batch method, which yielded very broad size distributions between 1 and 2 µm [10].

The aim of the present study was to explore the production of small monodisperse MMS, which could be used in the bloodstream, would not clog the capillaries, and would be able to react to an external magnetic force. To ensure monodispersity and the continuous production of particles, microfluidic methods were utilized for the MMS production. We decided on investigating both direct and indirect microfluidic

* Corresponding author.
*E-mail address:* urs.hafeli@ubc.ca (U.O. Häfeli).

https://doi.org/10.1016/j.jmmm.2018.09.091
Received 29 June 2018; Received in revised form 23 September 2018; Accepted 23 September 2018
Available online 25 September 2018
0304-8853/ 

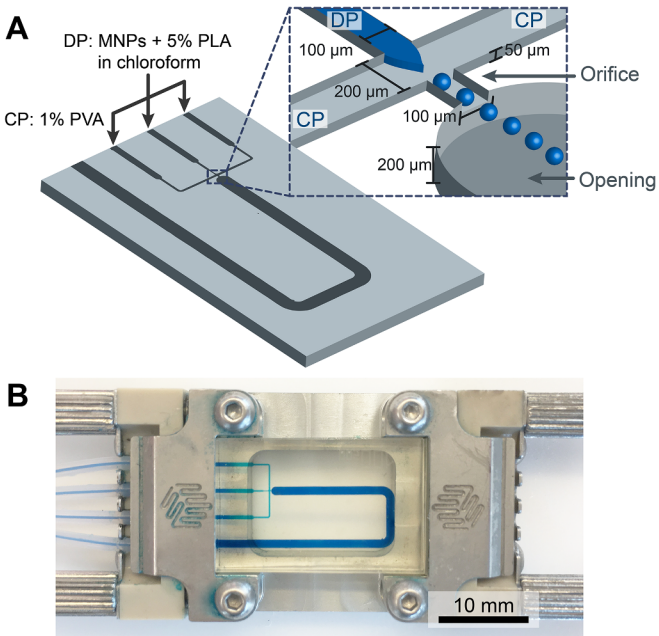


**Fig. 1.** Microfluidic chip and dimensions. A) Schematic illustration of flow focusing chip used for microsphere production. Chip dimensions include a 50 µm overall channel depth, a 100 µm wide and long orifice, and a 200 µm deep and 1 mm wide outlet opening. DP: dispersed phase, CP: continuous phase. B) Image of the thiol-ene chip within the chip holder. Chip dimensions are 22.5 × 15.0 × 4.0 mm.

methods to produce MMS sized in the low micrometer range (1–3 µm). The direct method utilizes flow focusing, where an inner non-miscible solvent stream breaks up into monosized droplets after passing through an orifice, as shown in Fig. 1. The indirect method refers to the collection of satellite particles that arise commonly in the just described microfluidic droplet generator in conjunction with the primary droplets.

Direct production of MMS of the size regime investigated here (~2 µm) has been realized by bulk methods [10], electrospray [11], and commercial flow focusing nozzles [12]. However, to our knowledge, a simple microfluidic chip has not yet been employed. This is partly because microfluidic production of small droplets is extremely difficult to achieve owing to the high energy input needed for droplet breakup. This generally requires small feature sizes as the production of droplets smaller than one-tenth of the orifice is rare [13], making the microfluidic chip fabrication costly and labor intensive. Indirect production of small MS through the collection of satellite droplets has been demonstrated [14–16], albeit for non-magnetic particles. Satellite particles are formed through the surface instabilities of the dispersed phase [17–19], and are generally considered problematic as the primary droplet polydispersity rapidly increases resulting in lower quality sample yield. However, if the aim is to produce small droplets using straightforward microfluidic techniques not requiring expensive fabrication approaches, then collection of satellite droplets may open an avenue towards obtaining the desired sized population.

In this study, we demonstrate the production and separation of satellite particles, as well as the direct production of 1 µm unloaded and 2 µm magnetite nanoparticle loaded PLA microspheres. Both methods were carried out using a simple-to-fabricate, polymeric microfluidic chip utilizing thiol-ene chemistry [20]. The microfluidic chip incorporates a flow focusing geometry with large feature sizes obtainable in most microfluidic laboratories without the use of a clean room. Our results show that the obtained MMS are narrow in size distribution, highly spherical, and superparamagnetic.

## 2. Materials and methods

### 2.1. Chip fabrication

Thiol-ene chips were fabricated as described previously in [21]. Chips were designed using a combination of Autodesk® Inventor® Professional (Autodesk Inc., San Rafael, CA, USA) and InventorCAM (SolidCAM Inc., Newtown, PA, USA). Computer numerical controlled (CNC) milling of the positive master mold (poly(methyl methacrylate) (PMMA) plates, Nordisk Plast A/S, Randers, Denmark) was executed by MiniMill (Minitech Machinery, Norcross, GA, USA), while the spacers and lids were $CO_2$ laser cut using an Epilog Laser Mini 18 (Golden, CO, USA). Combining the master mold, spacer, and lid, polydimethylsiloxane (PDMS, Sylgard® 184, Dow Corning, USA) negatives were molded and cured for 2 h at 80 °C, as recommended by the manufacturer. The following parameters for chip fabrication were obtained in a pilot experiment. Monomers were mixed 50% allyl excess with 1% Lucirin® TPO-L (BASF, Ludwigshafen, Germany) and molded within the PDMS negatives, using the thiol monomer (pentaerythritol tetrakis(3-mercaptopropionate) and tri-allyl monomer (1,3,5-triallyl-1,3,5-triazine-2,4,6(1H,3H,5H)-trione (both from Sigma Aldrich, Schnelldorf, Germany). Non-bonding sides of the molds were exposed to 1.6 s of UV light, 12 mW/cm$^2$ at 365 nm (LS-100-3C2 near UV light source, Bachur & Associates, Santa Clara, CA, USA), the cured halves were removed from the molds, and the chip was assembled by pressing together the two halves. Upon fabrication, the chips were washed and coated with an in-house synthesized, thiolated, hydroxyl-rich compound in order to reduce the contact angle from 70° to < 15°. The solution was prepared at 1.5% concentration with equal percentage of Irgacure 184 photoinitiator. Upon loading within the channels the chip was exposed to 12 mW/cm$^2$ (365 nm) UV light for 90 s. The coating procedure was repeated a total of 3 times. The final chip was cured for 10 min at 90 mW/cm$^2$ at 365 nm (Dymax 5000-EC Series UV curing flood lamp, Dymax Corp., Torrington, CT, USA).

### 2.2. Microsphere production

The dispersed phase (DP) consisted of poly(D, L-lactide) (PLA, 10–18 kDa, Resomer® R 202H, Sigma Aldrich, Schnelldorf, Germany) dissolved in chloroform at 2.5–5% (w/v) concentration (or 5% PLA and MNP's at 0.5–1% (w/v) mix). The continuous phase (CP) consisted of an aqueous solution of 1% (w/v) poly(vinyl alcohol) (PVA) (MW 30,000–70,000, 87–90% hydrolyzed, Sigma Alrich, Schnelldorf, Germany), 0.45 µm PTFE filtered prior to use. All solutions were prepared fresh prior to flow focusing. The flow focusing chip had an orifice of 50 µm deep, 100 µm wide and 100 µm long. The post-orifice opening was 1 mm wide and 200 µm deep to reduce potential interaction between the PLA droplets and channel walls (Fig. 1A). For satellite particle production, the microspheres were produced at $Q_{DP}$ of 2 µL/min and $Q_{CP}$ of 80 µL/min. For the continuous production of 1–3 µm microspheres, the flow rate was 1–2 µL/min for the DP while the CP was run at 600–2000 µL/min as indicated in the figures or figurelegends. Flow control was achieved by a neMESYS low-pressure syringe pump (CETONI GmbH, Korbußen, Germany) and glass syringes to minimize flow fluctuations often seen in traditional syringe pumps and plastic syringes. The chip was connected to the syringe pump using the Interface H and 4 Linear Connector 4-way system (Dolomite, Roystone, UK). After collection, the particles were spun at 2000 rcf (5 min, at 4 °C) and resuspended in 100x volume of MilliQ water to facilitate solvent extraction.

### 2.3. Viscosity of and interfacial tension between the DP and CP solutions

To characterize and explain the mechanism of droplet formation, the dynamic viscosity of the DP (i.e., 5% PLA in chloroform) and the CP (i.e., 1% PVA in water) at the tested flow rates, and their interfacial

tension were measured. The dynamic viscosity was determined with an AR G2 Rheometer (TA Instrument, West Sussex, England) equipped with cone-plate measuring system (cone radius 40 mm, cone angle 1 degree) at 25 °C. All sample measurements were repeated 6 times. A rotational test was used to determine the shear solution viscosity (η, Pa·s) as a function of shear rate ($\gamma$, $s^{-1}$) from 0.1 to 1000 $s^{-1}$ for the DP, and from 0.1 to 3000 $s^{-1}$ for the CP. The viscosity values where taken at specific shear rates for both the DP and CP, which correspond to the shear rate ($\gamma$) values of the solutions in the opening chamber (the site of droplet break-off) at specific flow rates, according to the following equation:

$$\gamma = \frac{4 \cdot Q}{\pi \cdot r^3} \tag{1}$$

where Q is the flow rate (mL/s) and r is the radius of the opening (cm). The radius was estimated to match the cross-sectional area of the rectangular channels.

Interfacial tension was determined using the pendant drop method, where 5% PLA in chloroform was suspended in a solution of 1% PVA. Measurements were carried out on the KRUSS DSA100 drop shape analyzer (KRUSS GmbH, Hamburg, Germany). The PLA solution was slowly, drop-by-drop injected into a quartz container filled with PVA using a 500 µL glass syringe and an 18 gauge flat tip needle. Droplet shape and pinch-off was recorded on the camera and interfacial tension determined using the DSA100 software. Measurements were repeated > 20 times in order to understand the reproducibility of the measurements.

### 2.4. $Fe_3O_4$ nanoparticle synthesis

Magnetic iron oxide nanoparticles (MNP) were synthesized using the co-precipitation of Fe(II) and Fe(III) and coated with $C_{12}$-bisphosphonate as described previously by our group [9].

### 2.5. Imaging and size distribution

The samples were washed post-separation with 15 mL MilliQ water through centrifugation (2000 rcf, 5 min, at 4 °C) and resuspension. Light microscope images were taken on an Olympus IX71 inverted microscope. High-resolution surface mapping was done on a FEI Quanta 3D FEG scanning electron microscope at 2.0 kV acceleration voltage. Average diameters, standard deviation, and coefficient of variation were calculated by measuring at least 200 microspheres per sample using ImageJ. Gaussian fit for obtaining the histogram of distribution, and statistics were performed using GraphPad Prism.

### 2.6. Magnetization measurements

Vibrating sample magnetometry (VSM) measurements were carried out at room temperature in a LakeShore 7407 VSM. Each sample was prepared for measurements by (1) weighing a thin-walled 200 µL plastic tube, (2) adding the sample suspension and letting the liquid evaporate such that a sample pellet was formed at the bottom, (3) weighing the tube with the sample pellet, and (4) fixing the sample pellet using transparent nail polish. Measurements were performed using a custom-built sample mount in which the tube with the sample was mounted upside down. No corrections for background contributions were made. Results are reported as the specific magnetization (magnetic moment per sample mass), s, measured in units of $Am^2/kg$.

## 3. Results and discussion

### 3.1. Microfluidic material and design

For droplet generation, a polymeric microfluidic chip material was chosen due to its low cost and ease of production, while maintaining comparable results to glass. Naturally, due to the harsh chemical environment of chlorinated solvents used here, the polymer chips are not expected to last very long, but that is compensated for by the ease of replicate production when needed. The replicates are autoclavable, disposable, and eliminate the nuisances associated with clogging. Thiol-ene chips were used and were fabricated as we previously described [21], using CNC milling of PMMA plates, PDMS negative molding, and click-polymerization of thiol-ene monomers under UV light. The thiol-ene monomers were mixed in an off-stoichiometric ratio to gain allyl surface functional groups that are click-modifiable with thiol-containing compounds, e.g., to vary the surface properties to gain glass-like contact angles necessary for oil in water droplet formation [13]. To our knowledge, thiol-ene microfluidic chips are seldom used for oil in water

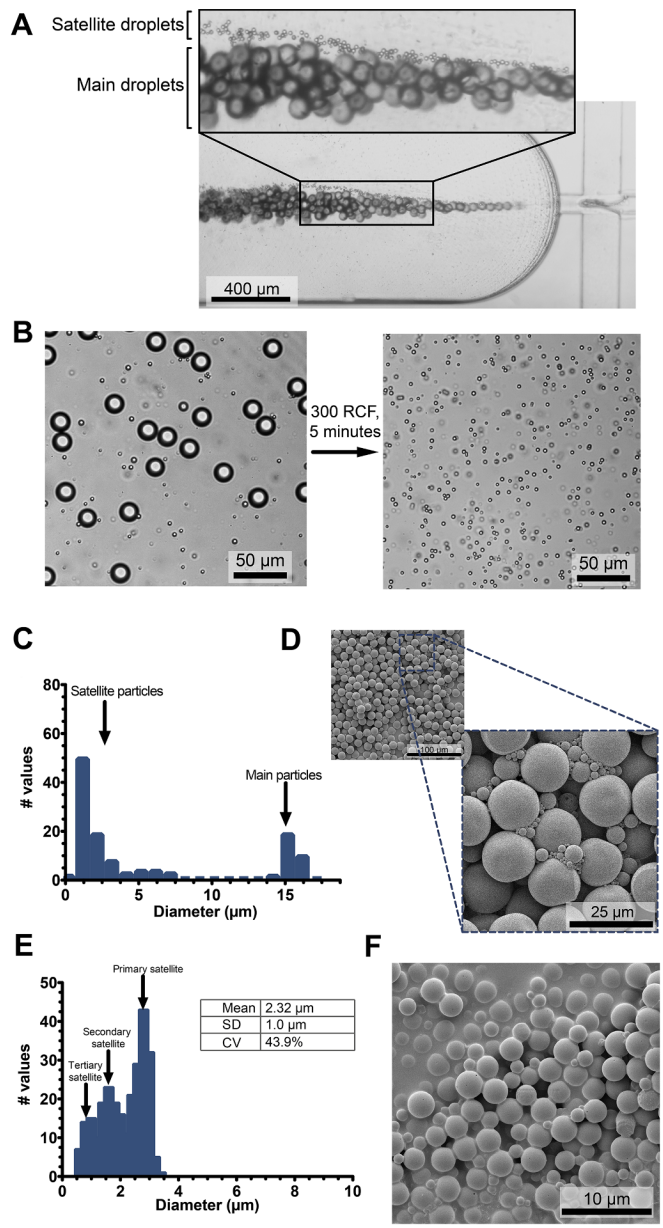


**Fig. 2.** Preparation, separation and characterization of satellite particles. A) Optical microscope image of the main and satellite droplets formed with 2 µL/min $Q_{DP}$ and 80 µL/min $Q_{CP}$. Dispersed phase is 5% PLA in chloroform and continuous phase is 1% PVA. B) Light microscope image of PLA particles before (left) and after (right) centrifugation at 300 rcf for 5 min. C) Size distribution of particles based on the SEM images. D) SEM image of starting material showing the satellite particles. E) Size distribution of satellite particles based on the SEM images F) SEM image of satellite particles.

droplet production and have not been reported for the production of chloroform droplets for polymeric particle production. Thus far, only the production of ethylacetate [22] and toluene [23,24] droplets in water have been shown with these chip materials.

The chip geometry consisted of a flow focusing design where the dispersed phase (DP) flows perpendicularly to the continuous phase (CP), resulting in droplet break-off. The geometry includes a 100 µm wide and 50 µm deep orifice and a 1 mm wide and 200 µm deep outlet opening to minimize surface interaction between the channel walls and the PLA droplets (Fig. 1A). The final chip is optically transparent (Fig. 1B) and allows for continuous production of droplets for a few hours before severe swelling is induced by the chloroform exposure. As shown in the supplementary video files, the optical transparency also allows for observing the droplet formation directly on a microscope. This is particularly helpful to find stable production conditions (which generally take place within a couple of minutes).

### 3.2. Satellite particle approach

Droplet formation in a flow focusing system starts with the dispersed and continuous phase entering the junction/orifice and forming an interface where the continuous phase deforms the dispersed phase, creating an unstable thread that finally spontaneously breaks forming droplets [25]. During the production of the main droplets, additional breakup sequences of the thinned thread often results in the formation of satellite droplets [18]. The satellite droplets are generally very small, typically 1% in volume of the parent droplet [17], and thus present as an opportunity for small particle synthesis by separation and collection of the small satellites.

To achieve satellite formation, the flow rates and flow rate ratios in the so-called dripping regime were optimized to $Q_{DP}$:$Q_{CP}$ of 2:80 µL/min (Fig. 2A, Supplementary Video 1). The video shows the formation of the satellite droplets in conjunction with the main droplet, where a small, single population is evident. The whole sample was collected, spun at 300 rcf in a centrifuge for 5 min, and the supernatant was retained. Here, the large PLA particles pelleted and the small particles remained in suspension; albeit, 40 ± 8% of the satellites were lost to the pellet. The supernatant contained only the small particles, allowing for rapid size-based separation of the sample Fig. 2B. Both the starting material and collected supernatant were further characterized using SEM. In Fig. 2C, the size distribution shows main particles of 15 µm diameter and a range of sub-7.5 µm satellite particles. The distribution was based on the SEM image shown in Fig. 2D, where both the main and satellite particles are clearly visible. After size separation, the remaining satellite particles are highly polydisperse, with primary, secondary and tertiary populations being evident, Fig. 2E. By light microscopy, such as in Supplementary Video 1, the large fraction of submicron particles are not visible. The clear distribution of secondary and tertiary satellites can only be observed using SEM, as seen in Fig. 2F. Nonetheless, the small particles are highly spherical in spite of a large range of diameters.

Our results of multiple satellite populations is consistent with previous studies [15,26]. Given the polydispersity, more focus needs to be directed towards the separation of each satellite species through both in-line and post-processing steps. Deterministic lateral displacement offers the finest resolution for size-based separation [14,26,27]; however, other methods such as Dean flow [28–30] and pinched flow fractionation [16] have also been employed. For the case of magnetic microspheres, active sorting through magnetic fields may offer a more efficient avenue for separation [31]. Furthermore, it is important to note that a single monodisperse population of satellite droplets has been reported through the modification of the flow focusing geometry, where droplet break-off is focused to a single point [32]. Finally, it may be worthy to consider the careful optimization of flow rates and ratios, as well as investigating the influence of the viscosity ratio between the two phases [33], the interfacial tension [34] and interfacial elasticity [35].

### 3.3. Jetting mediated synthesis of microspheres

A second approach for small particle formation is by increasing the continuous phase flow rate to the point where the feature sizes of the microfluidic chip (more specifically, around the orifice) no longer play a critical role in the resulting droplet size. Here, we investigated the upper flow rate and flow rate ratio limits of our microfluidic set-up in order to minimize the droplet size. The CP flow rate was systematically increased until the backpressure prevented any further increase and led to, e.g., mechanical issues with the syringe pump. Example flow profiles are shown in Fig. 3 and Supplementary Video 2, where a long, thin thread of the dispersed phase is visible, at the end of which jetting of the droplets occurs. The point of droplet break-off is dependent upon the CP flow rate and the flow rate ratio of the two phases. A significant increase in the outer phase flow rate, as tested here, changes the droplet formation regime, which can be characterized by the dimensionless capillary number (Ca), relating the influence of viscous *vs.* interfacial forces. The capillary number is often used in droplet microfluidics as a defining parameter for the regime of droplet formation. It is defined where η is the dynamic viscosity (Pa·s), U is the flow rate (m/s), and σ is the interfacial tension in (N/m). The Ca was calculated for both phases at the flow velocities corresponding to flow rates of 2 and 1800 µL/min in a 200 µm × 1000 µm opening by using our measured values of $\eta_{DP} = 2 \times 10^{-1}$ Pa·s for the DP, $\eta_{CP} = 6.3 \times 10^{-3}$ Pa·s for the CP and σ = 3 mN/m for the interfacial tension between the two phases.

The system can be defined by a Ca number of $1 \times 10^{-2}$ for the DP and 0.11–0.33 for the CP. Comparing to a capillary number-based flow map shown in [36], the capillary numbers correspond to a regime that falls between jetting and threading. In this article, the authors define the threading regime as providing a stable thread with a length of 20*h*, with *h* being a characteristic length scale, namely the height of the square microfluidic channel in their experiments. In the jetting regime, on the other hand, droplets break off within the length of 20*h*. In our system, the length of the stable thread before droplet break-off was observed to be 10–20*h* depending on the $Ca_{CP}$ or the flow rate of the CP. Here, *h* is defined as the hydraulic diameter, which is calculated from the side lengths of the rectangular channel cross section according to 2ab/(a + b), yielding a value of 333 µm. In this regime, droplet size is proportional to the diameter of the thread, where the end of the thread breaks off due to the amplifying Rayleigh-Plateau instability [25]. This means that the droplet diameter no longer relies on the microfluidic chip feature sizes but instead the flow rates, making the fabrication requirements much less stringent.

### 3.4. Empty PLA microsphere production

Initially, empty PLA particles were produced using the narrow jet regime. Stable jetting was observed from $Q_{DP}$:$Q_{CP}$ of 2:600 µL/min up

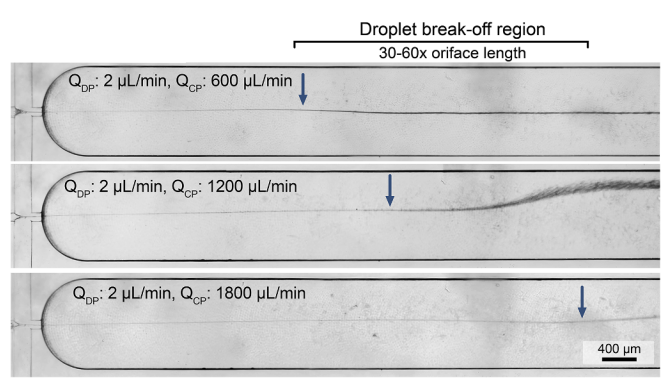


**Fig. 3.** High flow rate production of PLA droplets. Light microscope image of droplet formation at various flow rates and flow rate ratios (as indicated). Arrow shows approximate droplet break-off point.

to $Q_{DP}$:$Q_{CP}$ of 2:1800 μL/min. For all flow rates investigated in this regime, the final PLA particle diameters remained under 2 μm with a narrow size distribution, having a coefficient of variation between 5 and 8%. At these flow rates, 150 mg of PLA microspheres are produced per day using a single chip; however, parallel production is a possibility for production upscaling. Size distribution and SEM images of the PLA particles produced at $Q_{DP}$:$Q_{CP}$ of 2:1800 μL/min are shown in Fig. 4. For 2.5% PLA in chloroform, the average size is 1.16 μm with a coefficient of variation of 5.74%, as shown in Fig. 4A. The particles are highly uniform and spherical as seen in the SEM images (Fig. 4B and C). Increasing the PLA concentration to 5% resulted in slightly larger particles at 1.36 μm average in diameter, with a slightly better CV of 5.46% (Fig. 4D). Similarly, the SEM images show highly spherical and uniform particles (Fig. 4E and F).

### 3.5. Magnetic microsphere production

We previously showed the preparation of MNPs with a mixed magnetite/maghemite core and $C_{12}$-bisphosphonate coating having an average diameter of 12 ± 3.6 nm [9]. Approximately 0.5% or 1% (w/v) of homogeneously dispersed MNPs were added to the DP with 5% PLA in chloroform. Due to a different DP composition, the viscosity and interfacial tension changed which required the reoptimization of the flow rates for small MMS synthesis. In general, higher Reynolds numbers, but a smaller difference between the DP and CP flow rate ratios are required for effective MMS production. The final flow rates used were $Q_{DP}$:$Q_{CP}$ of 2:1000 μL/min.

SEM shows a narrow size distribution for MMS with 0.5% or 1% (w/v) MNPs, albeit larger than the empty PLA microspheres. The larger size may be due to a combination of the modified flow rate condition as well as the effect of the MNP encapsulation. The 0.5% particles have a mean size of 2.08 ± 0.14 μm and a CV of 6.54% (Fig. 5A) with a smooth surface and spherical shape (Fig. 5B and C). The 1% particles are slightly larger at 2.31 ± 0.18 μm with a CV of 7.61% (Fig. 5D) and exhibit a more irregular and rougher surface (Fig. 5E and F). Such effects have been seen especially at higher concentrations, where dimples and sometimes even holes form, which are explained by jammed MNPs on the surface of the MMS. For a discussion of this effect, see [37].

Fig. 6A and B shows the assembly behavior of the particles in response to a magnet. Magnetization measurements were obtained for the starting MNPs (black) and the final MMS (blue and red), as shown in Fig. 6C. The magnetization curves confirm that the starting MNPs display non-negligible hysteresis, whereas the encapsulated MNPs show no detectable hysteresis. The hysteresis in the NP starting material is likely due to magnetic interactions between the particles in the dense sample. The lack of hysteresis in the MMS indicates that they are superparamagnetic at room temperature on a time scale of seconds. The specific magnetization of the 1% (w/v) sample is about 30% that of the starting NPs, while for the 0.5% (w/v) it is roughly 15%, showing good control over the magnetic loading into the PLA particles.

We demonstrated here that the production of 1–3 μm MMS is possible with microfluidic methods, at very narrow size distributions and without any hysteresis. To make these MMS appropriate for magnetic drug targeting, ideally higher MNP concentrations need to be incorporated. For large MMS, above 5 μm, we were in previous work able to incorporate up to about 50–60 wt% of magnetite [9,37]. Future work will optimize the MNP concentration, as well as maximize the magnetite to maghemite content in the MNPs, such as through the reduction of the coating thickness. The coating thickness of the MNPs with $C_{12}$-bisphosphonate is already thinner and more stable than a $C_{18}$ oleic acid coating used by other authors [38]. We have previously attempted to further minimize its thickness to $C_8$, but the MNP behavior was not favorable, e.g. exhibiting unfavorable physiochemical properties, such as poor solubility in chloroform (results not shown).

## 4. Conclusion

In this work, we present two simple microfluidic methods for the production of 1–3 μm superparamagnetic particles. Both methods rely on easy-to-fabricate and cost-effective polymeric microfluidic chips with large feature sizes. Both of the methods presented here produce microspheres up to 6 mg/h. To increase throughput of microfluidic droplet generators, numerous studies have reported effective parallelization of the flow focusing junction on a single microfluidic chip, up to 512 identical junctions [39–41], resulting in mL/hour dispersed phase flow rates. Application of such parallelization, even if only 10-fold, could then result in more than 1 g microspheres per day, making it attractive for preclinical studies.

The microfluidic chip material, a thiol-ene polymer, offers the advantages of rapid production through replica molding and swift UV curing. Furthermore, the surface is click-modifiable, relatively heat resistant (allowing for sterilization), and disposable (for medical applications or in the event of clogging). Here, we demonstrate the utility of a material that is not normally compatible with chlorinated solvents being used for several hours of oil-in-water emulsion production. Thiol-ene chips have not been used before under such conditions for the production of polymeric particles. This opens an avenue for the rapid prototyping of channel geometries not easily achievable with glass due to time, effort and costs.

Initially, we show the production of small polymeric particles through the collection and separation of satellite particles. Even though our method yielded a broad range of satellite populations, starting from sub-micron to 2 μm in size, further strategies to minimize the number of satellites need to be investigated. Such include the modification of the outlet channel shape (Fig. 1A) from semi-circular to triangular, creating maximal velocity at a single point near the orifice resulting in more precise droplet generation [32]. Additionally, increasing the DP viscosity (through a higher concentration or molecular weight) should further aid in satellite population reduction [33]. Naturally, microfluidic size-based or magnetic separation is an alternative to achieving a single population of satellites [14,16,31]. All of these options are beyond the scope of this study, but utilizing the power of rapid prototyping through thiol-ene chips greatly facilitates the investigations of the channel geometries for both the production and separation of satellite particles.

Finally, we show the direct production of 1–3 μm polymeric particles without the need for particle separations. Importantly, this method allows for obtaining larger quantities of small microspheres, as opposed to the collection of satellites that only make up roughly 1% in volume of the sample [17]. Moreover, circumventing the use of satellites eliminates heavy losses of the starting material.

Using the direct production approach, we showed that the empty PLA particles are 1 μm in size, monodisperse, smooth and spherical. The MMS are 2 μm in size, similarly monodisperse, spherical and loaded with up to 30% MNPs, resulting in superparamagnetic properties. Here, the CP flow rate was increased to maximum velocities in order to form a long, thin thread, at the end of which jetting of the droplets occurs. In this droplet generation regime, the droplet size is proportional to the diameter of the thread, instead of the actual channel sizes. This results in extremely small droplet formation in a microfluidic chip with large feature sizes, circumventing the need for advanced clean room fabrication. While the particle size is mostly independent of the channel geometry in this regime, additional design changes may reveal further ways to reduce the particle diameters, such as, e.g., through the elongation of the orifice [42].

Overall, this work has exemplified the utility of polymeric chips for MMS production in harsh chemical environments. To the best of our knowledge, this is the first report to show production of MMS in this size regime and with well-defined distributions using a simple microfluidic set-up, thus clearly offering an alternative to more traditional fabrication approaches.

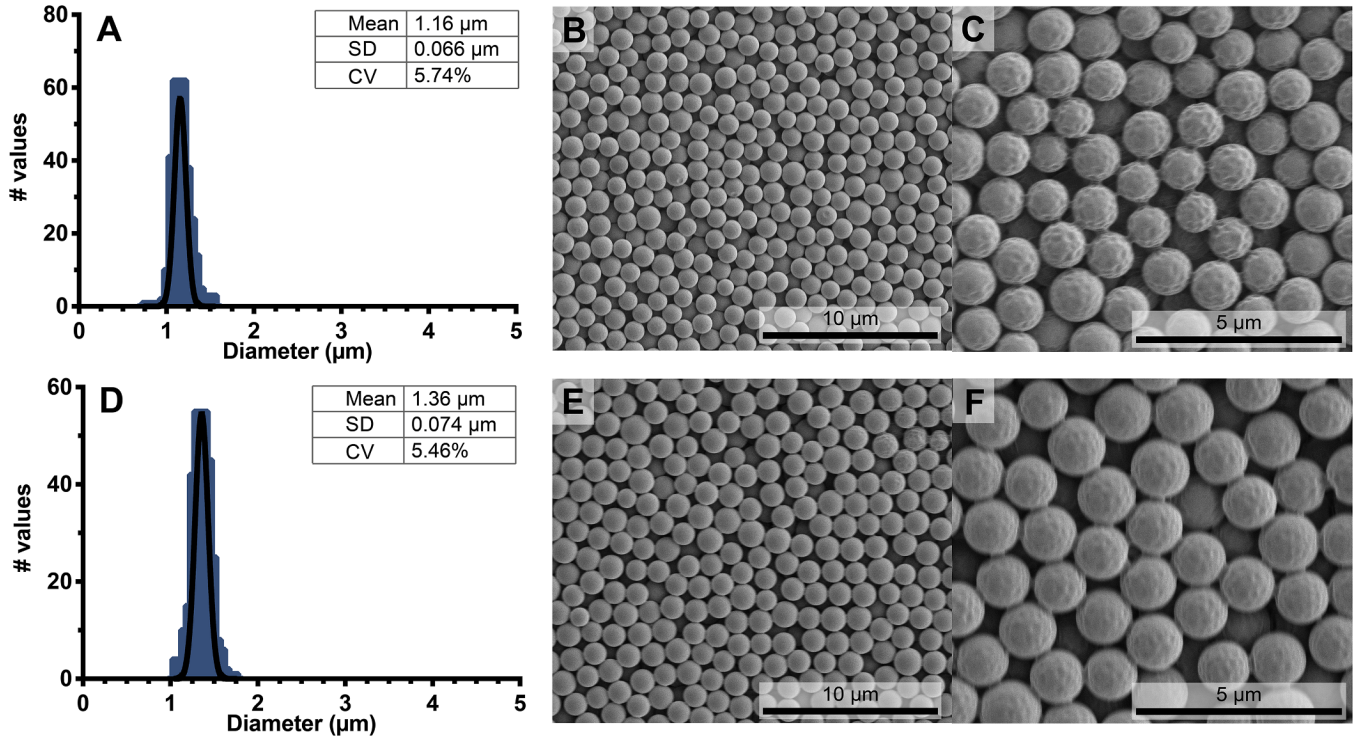


**Fig. 4.** Size distribution and surface mapping of empty PLA particles. A) Size distribution and statistics of MS made with 2.5% PLA in chloroform and shown in B) 15,000× magnification (SEM) and C) 50,000× magnification (SEM). D) Size distribution and statistics of MS made with 5% PLA in chloroform and shown in E) 15,000x magnification (SEM) and F) 50,000× magnification (SEM). Both samples produced at $Q_{DP}$:$Q_{CP}$ of 2:1800 µL/min, diameters measured of > 200 particles for the histograms.

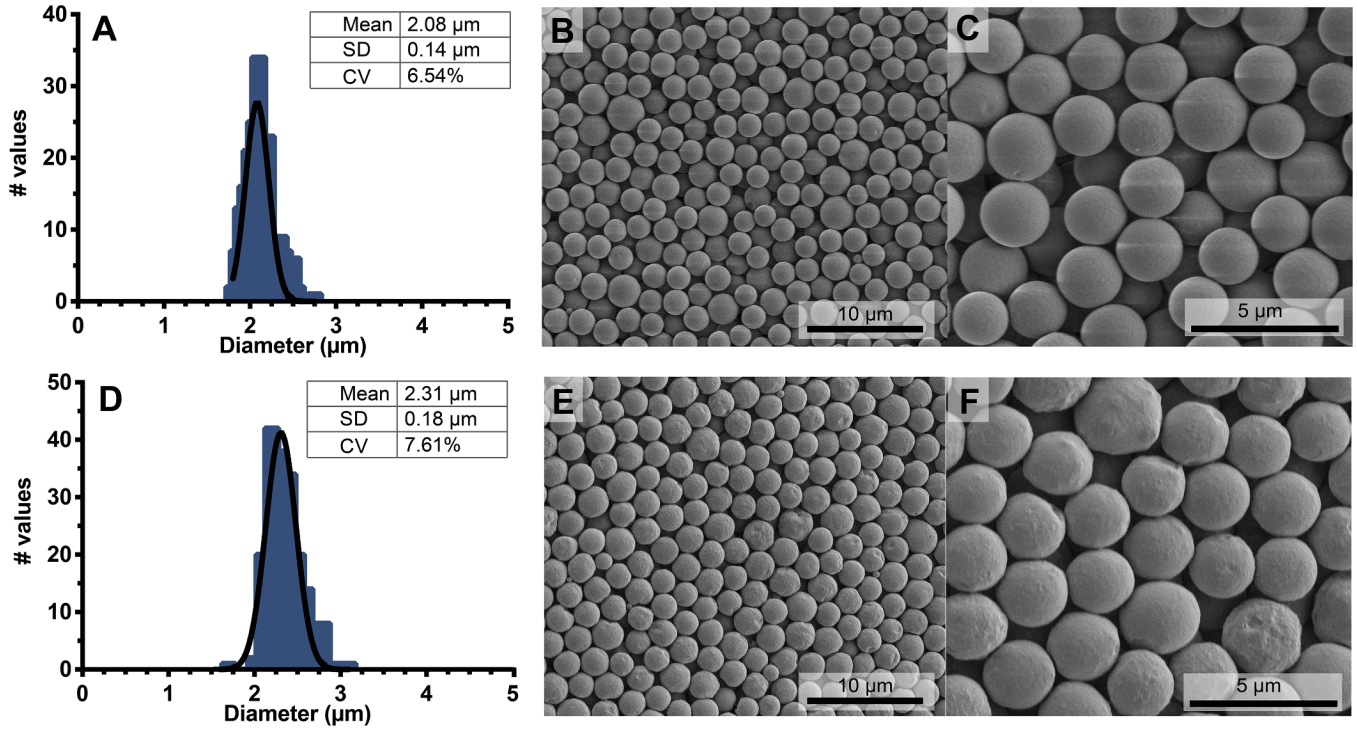


**Fig. 5.** Size distribution and surface mapping of MNP-loaded PLA particles. A) Size distribution and statistics of MMS made with 0.5% (w/v) magnetite and 5% PLA in chloroform and shown in B) at 15,000x magnification (SEM) and C) at 50,000x magnification. D) Size distribution and statistics of MMS made with 1% (w/v) magnetite and 5% PLA in chloroform and shown in E) at 15,000× magnification (SEM) and F) at 50,000x magnification. Both samples produced at $Q_{DP}$:$Q_{CP}$ of 2:1000 µL/min, diameters of > 200 particles measured for the histograms.

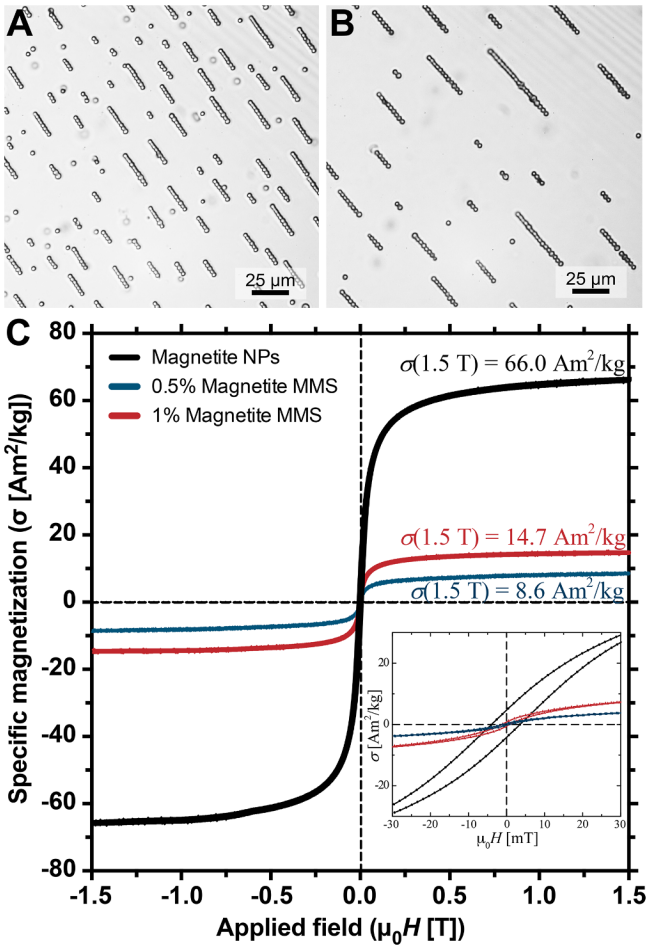


**Fig. 6.** Magnetic response and hysteresis curve. A) 0.5% or B) 1% (w/v) magnetite particles responding to a magnet imaged through light microscopy. C) Magnetization curve of starting MNPs (black), 0.5% MNP loaded MMS (blue), and 1% MNP loaded MMS (red). (For interpretation of the references to colour in this figure legend, the reader is referred to the web version of this article.)

## Acknowledgments

We thank Cordula Grüttner and micromod Partikeltechnologie GmbH for providing the PLA. We acknowledge the Core Facility for Integrated Microscopy, Faculty of Health and Medical Sciences, University of Copenhagen for the SEM images. This study was supported by the Lundbeck Foundation, Denmark (grant number 2014-4176, the UBC-SUND Lundbeck Foundation professorship to UOH).

## Appendix A. Supplementary data

Supplementary data associated with this article can be found, in the online version, at https://doi.org/10.1016/j.ijpharm.2018.05.006.

## References

[1] K.M. Krishnan, Biomedical nanomagnetics: a spin through possibilities in imaging, diagnostics, and therapy, IEEE Trans. Magn. 46 (2010) 2523.
[2] A. Sarwar, A. Nemirovski, B. Shapiro, Optimal Halbach permanent magnet designs for maximally pulling and pushing nanoparticles, J. Magn. Magn. Mater. 324 (2012) 742.
[3] J.-M. Paulus, Platelet size in man, Blood 46 (1975) 321.
[4] D.W. Ross, L.H. Ayscue, J. Watson, S.A. Bentley, Stability of hematologic parameters in healthy subjects: intraindividual versus interindividual variation, Am. J. Clin. Pathol. 90 (1988) 262.
[5] J.D. Slack, M. Kanke, G.H. Simmons, P.P. Deluca, Acute hemodynamic effects and blood pool kinetics of polystyrene microspheres following intravenous administration, J. Pharm. Sci. 70 (1981) 660.
[6] M. Kanke, G.H. Simmons, D.L. Weiss, B.A. Bivins, P.P. Deluca, Clearance of 141Ce-labeled microspheres from blood and distribution in specific organs following intravenous and intraarterial administration in beagle dogs, J. Pharm. Sci. 69 (1980) 755.
[7] K. Namdee, A.J. Thompson, P. Charoenphol, O. Eniola-Adefeso, Margination propensity of vascular-targeted spheres from blood flow in a microfluidic model of human microvessels, Langmuir 29 (2013) 2530.
[8] U.O. Häfeli, K. Saatchi, P. Elischer, R. Misri, M. Bokharaei, N.R. Labiris, B. Stoeber, Lung perfusion imaging with monosized biodegradable microspheres, Biomacromolecules 11 (2010) 561.
[9] Z. Nosrati, N. Li, F.O. Michaud, S. Ranamukhaarachchi, S. Karagiozov, G. Soulez, S. Martel, K. Saatchi, U.O. Häfeli, Development of a coflowing device for the size-controlled preparation of magnetic-polymeric microspheres as embolization agents in magnetic resonance navigation technology, ACS Biomater. Sci. Eng. 4 (2018) 1092.
[10] H. Zhao, K. Saatchi, U.O. Häfeli, Preparation of biodegradable magnetic microspheres with poly (lactic acid)-coated magnetite, J. Magn. Magn. Mater. 321 (2009) 1356.
[11] S. Gun, M. Edirisinghe, E. Stride, Encapsulation of superparamagnetic iron oxide nanoparticles in poly-(lactide-co-glycolic acid) microspheres for biomedical applications, Mater. Sci. Eng. C 33 (2013) 3129.
[12] L. Martín-Banderas, R. González-Prieto, A. Rodríguez-Gil, M. Fernández-Arévalo, M. Flores-Mosquera, S. Chávez, A.M. Gañán-Calvo, Application of flow focusing to the break-up of a magnetite suspension jet for the production of paramagnetic microparticles, J. Nanomater. 2011 (2011) 4.
[13] G.F. Christopher, S.L. Anna, Microfluidic methods for generating continuous droplet streams, J. Phys. D Appl. Phys. 40 (2007) R319.
[14] N. Tottori, T. Nisisako, High-throughput production of satellite-free droplets through a parallelized microfluidic deterministic lateral displacement device, Sens. Actuators B 260 (2018) 918.
[15] Y.-C. Tan, A.P. Lee, Microfluidic separation of satellite droplets as the basis of a monodispersed micron and submicron emulsification system, Lab Chip 5 (2005) 1178.
[16] M. Yamada, M. Nakashima, M. Seki, Pinched flow fractionation: continuous size separation of particles utilizing a laminar flow profile in a pinched microchannel, Anal. Chem. 76 (2004) 5465.
[17] X. Zhang, Dynamics of drop formation in viscous flows, Chem. Eng. Sci. 54 (1999) 1759.
[18] M. Tjahjadi, H.A. Stone, J.M. Ottino, Satellite and subsatellite formation in capillary breakup, J. Fluid Mech. 243 (1992) 297.
[19] O. Carrier, E. Dervin, D. Funfschilling, H.-Z. Li, Formation of satellite droplets in flow-focusing junctions: volume and neck rupture, Microsyst. Technol. 21 (2015) 499.
[20] C.E. Hoyle, C.N. Bowman, Thiol–ene click chemistry, Angew. Chem. Int. Ed. 49 (2010) 1540.
[21] T.M. Sikanen, J.P. Lafleur, M.-E. Moilanen, G. Zhuang, T.G. Jensen, J.P. Kutter, Fabrication and bonding of thiol-ene-based microfluidic devices, J. Micromech. Microeng. 23 (2013) 037002.
[22] P. Wägli, A. Homsy, N.F. de Rooij, Norland optical adhesive (NOA81) microchannels with adjustable wetting behavior and high chemical resistance against a range of mid-infrared-transparent organic solvents, Sens. Actuators B 156 (2011) 994.
[23] L.-H. Hung, R. Lin, A.P. Lee, Rapid microfabrication of solvent-resistant biocompatible microfluidic devices, Lab Chip 8 (2008) 983.
[24] Z.T. Cygan, J.T. Cabral, K.L. Beers, E.J. Amis, Microfluidic platform for the generation of organic-phase microreactors, Langmuir 21 (2005) 3629.
[25] P. Zhu, L. Wang, Passive and active droplet generation with microfluidics: a review, Lab Chip 17 (2017) 34.
[26] N. Tottori, T. Hatsuzawa, T. Nisisako, Separation of main and satellite droplets in a deterministic lateral displacement microfluidic device, RSC Adv. 7 (2017) 35516.
[27] L.R. Huang, E.C. Cox, R.H. Austin, J.C. Sturm, Continuous particle separation through deterministic lateral displacement, Science 304 (2004) 987.
[28] A.A.S. Bhagat, S.S. Kuntaegowdanahalli, I. Papautsky, Continuous particle separation in spiral microchannels using dean flows and differential migration, Lab Chip 8 (2008) 1906.
[29] S. Dutz, M.E. Hayden, U.O. Häfeli, Fractionation of magnetic microspheres in a microfluidic spiral: interplay between magnetic and hydrodynamic forces, PLoS ONE 12 (2017) e0169919.
[30] S. Dutz, M.E. Hayden, A. Schaap, B. Stoeber, U.O. Häfeli, A microfluidic spiral for size-dependent fractionation of magnetic microspheres, J. Magn. Magn. Mater. 324 (2012) 3791.
[31] R. Zhou, C. Wang, Microfluidic separation of magnetic particles with soft magnetic microstructures, Microfluid. Nanofluid. 20 (2016) 48.
[32] Y.-C. Tan, V. Cristini, A.P. Lee, Monodispersed microfluidic droplet generation by shear focusing microfluidic device, Sens. Actuators B 114 (2006) 350.
[33] L. Derzsi, M. Kasprzyk, J.P. Plog, P. Garstecki, Flow focusing with viscoelastic liquids, Phys. Fluids 25 (2013) 092001.
[34] N.M. Kovalchuk, E. Nowak, M.J.H. Simmons, Effect of soluble surfactants on the kinetics of thinning of liquid bridges during drops formation and on size of satellite droplets, Langmuir 32 (2016) 5069.
[35] C.X. Zhao, E. Miller, J.J. Cooper-White, A.P.J. Middelberg, Effects of fluid–fluid interfacial elasticity on droplet formation in microfluidic devices, AIChE J. 57 (2011) 1669.
[36] T. Cubaud, T.G. Mason, Capillary threads and viscous droplets in square microchannels, Phys. Fluids 20 (2008) 053302.

[37] M. Bokharaei, T. Schneider, S. Dutz, R.C. Stone, O.T. Mefford, U.O. Häfeli, Production of monodispersed magnetic polymeric microspheres in a microfluidic chip and 3D simulation, Microfluid. Nanofluid. 20 (2016) 6.
[38] X. Liu, M.D. Kaminski, J.S. Riffle, H. Chen, M. Torno, M.R. Finck, L. Taylor, A.J. Rosengart, Preparation and characterization of biodegradable magnetic carriers by single emulsion-solvent evaporation, J. Magn. Magn. Mater. 311 (2007) 84.
[39] M.K. Mulligan, J.P. Rothstein, Scale-up and control of droplet production in coupled microfluidic flow-focusing geometries, Microfluid. Nanofluid. 13 (2012) 65.
[40] D. Conchouso, D. Castro, S.A. Khan, I.G. Foulds, Three-dimensional parallelization of microfluidic droplet generators for a litre per hour volume production of single emulsions, Lab Chip 14 (2014) 3011.
[41] E. Amstad, M. Chemama, M. Eggersdorfer, L.R. Arriaga, M.P. Brenner, D.A. Weitz, Robust scalable high throughput production of monodisperse drops, Lab Chip 16 (2016) 4163.
[42] L. Wu, X. Liu, Y. Zhao, Y. Chen, Role of local geometry on droplet formation in axisymmetric microfluidics, Chem. Eng. Sci. 163 (2017) 56.

# 13. Appendix III

**Publication 3: ACS Applied Materials & Interfaces**

---

Sticker, D.#, R. Geczy#, U.O. Häfeli, and J.P. Kutter*, *Thiol–Ene Based Polymers as Versatile Materials for Microfluidic Devices for Life Sciences Applications*, ACS Applied Materials & Interfaces, **2020**. 12, 10080-10095. #equal contribution

ACS APPLIED MATERIALS & INTERFACES

www.acsami.org Review

# Thiol–Ene Based Polymers as Versatile Materials for Microfluidic Devices for Life Sciences Applications

Drago Sticker,[‖] Reka Geczy,[‖] Urs O. Häfeli, and Jörg P. Kutter*

Cite This: *ACS Appl. Mater. Interfaces* 2020, 12, 10080–10095 Read Online





**ABSTRACT:** While there is a steady growth in the number of microfluidics applications, the search for an optimal material that delivers the diverse characteristics needed for the numerous tasks is still nowhere close to being settled. Often overlooked and still underrepresented, the thiol–ene family of polymer materials has an enormous potential for applications in organs-on-a-chip, droplet productions, microanalytics, and point of care testing. In this review, the main characteristics of the thiol–ene materials are given, and advantages and drawbacks with respect to their potential in microfluidic chip fabrication are critically assessed. Select applications, which exploit the versatility of the thiol–ene polymers, are presented and discussed. It is concluded that, in particular, the rapid prototyping possibility combined with the material's resulting mechanical strength, solvent resistance, and biocompatibility, as well as the inherently easy surface functionalization, are strong factors to make thiol–ene polymers strong contenders for promising future materials for many biological, clinical, and technical lab-on-a-chip applications.

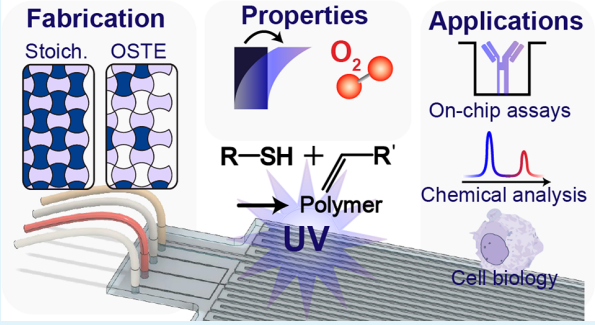


**KEYWORDS:** *thiol–ene chemistry, click chemistry, microfluidic chip materials, polymers, lab-on-a-chip*

## ■ INTRODUCTION

Choosing the right substrate material for the fabrication of a microfluidic device is a challenge as old as the field itself. Chemists have used glassware for hundreds of years as it fulfilled (and still does) all of the main requirements for the typical applications a chemist is faced with: optically clear for visual inspection, resistant to most commonly used chemicals, can be heated to several hundred degrees Celsius, and can be shaped in many different forms during manufacture. Similarly, cell biologists have adopted polystyrene as the *de facto* standard for their culture flasks, test tubes, and containers, because this material can be mass-produced and discarded after one use and is biocompatible, thus allowing for cells to be cultured directly on its native or slightly treated surface.

Ideally, the choice of material (and, in extension, the fabrication approach) for a microfluidic device should be determined by the needs of the application. In reality, however, fabrication options and materials choices for processing and structuring are limited in most research laboratories, dictating the applications that can be tackled. Alternatively, cumbersome (and often questionable) workarounds are implemented to somehow fit the available toolbox to the needs and requirements of the application.

The kind of equipment necessary to micromachine glass (or silicon) substrates is typically not readily available to many researchers who are interested in working with microfluidics devices or is quite expensive. When several groups introduced PDMS as a material for microfluidic chips in the mid to late 1990s[1−3] and Xia and Whitesides championed the use of "soft lithography" to fabricate channel networks in PDMS chips by a replica molding (or casting) process,[4,5] the field was opened up for basically anyone who always wanted to get started with microfluidic devices but lacked the access to sophisticated fabrication facilities or the funds to use them. Now, with inexpensive materials such as PDMS and the fairly straightforward way to produce chips from PDMS, the main costs are relegated to fabricating the master molds, which still (most often) need to be prepared using more advanced micromachining techniques. But, once this master mold is available, inexpensive copies can be cast or replica molded in PDMS. The introduction of PDMS to the lab-on-a-chip field thus led to a tangible surge in research groups developing microfluidic solutions, and in the ensuing "gold rush",

Received: December 5, 2019
Accepted: February 12, 2020
Published: February 12, 2020

shortcomings of this material were either ignored, dismissed, or somehow circumvented.

PDMS is extensively used for various applications, even though serious drawbacks are known.[6] This can only be attributed to the overall convenience of working with this material. Still, as the drawbacks of PDMS became harder to ignore, the quest for an "ideal" material for microfluidic devices picked up again and has done so steadily over the recent years. A list of desired properties for such a material encompasses, among others, being inexpensive, being easy to machine (e.g., by replica molding), allowing for fast prototyping, having at least some potential for mass production, presenting surfaces that can be easily chemically modified or functionalized, facilitating easy bonding, being transparent to at least the visible spectrum and with little or no autofluorescence, and being biocompatible (e.g., no leaching of monomers). A range of other polymers have been explored over the years, mainly poly(methyl methacrylate) (PMMA), polycarbonate (PC), and cyclic olefin (co)polymers (COC/COP), but they all fell short in at least one of the above-mentioned criteria, and researchers had to accept compromises again. In most cases, this can be related to the fact that these materials have not been "designed" with microfluidics in mind.

In their continued search for a "better" material, researchers had then begun to take note of the thiol−ene (TE) polymers—a family of polymers consisting of two monomers, each with at least two thiol or allyl (or ene) groups.[7,8] Polymerization with or without photoinitiator at the appropriate wavelengths yields a highly cross-linked thermoset polymer based on a radical induced polymerization mechanism involving a fast click chemistry reaction with close to 100% monomer conversion.[9] Fabrication of microfluidic devices from such materials is typically done by replica molding or double replica molding and allows very fast prototyping (especially when the molds are fabricated without invoking photolithographic methods) but can also be performed via direct photolithographic patterning (very similar to the photoresist SU-8, often used in microelectromechanical systems).[10] The TE type reactions have been known and studied for a number of years in various fields, such as for organic synthesis, surface modifications, optical components, and even drug delivery purposes.[11] Early examples go back to 2007,[12−14] where such materials were used, mostly in the form of the commercially available UV curing glue Norland Optical Adhesive (i.e., NOA-81), for the fabrication of microfluidics, already showcasing some of the advantages over other polymers, such as an improved tolerance to some organic solvents. The next push came around 2011, both using NOA-81,[15] but also more and more custom-made formulations,[16] and especially with the introduction of the so-called off-stoichiometric TEs (OSTE) by Carlborg et al., where the monomers are used in nonstoichiometric ratios.[17]

One interesting advantage of using nonstoichiometric ratios is that an excess of either thiol or allyl moieties remains available on the channel surfaces after fabrication and bonding. As both these functional groups lend themselves to click chemistry reactions, the OSTE materials offer straightforward possibilities to functionalize and alter the channel surfaces, e.g., either to change surface properties (charge, contact angle),[15] or to add molecules for biosensing,[18] enzymatic turnover,[19,20] or chromatographic retention,[21] to name just a few examples. This can also be done through photomasks,[22] thus achieving a high spatial control over which parts of the channel or chip are being modified. As will become clear throughout this review article, TE polymers are highly versatile materials, which are able to fulfill basically the entire list of desired properties for an ideal material mentioned above. At the same time, new developments (i.e., going from binary mixtures to ternary mixtures, which can include an epoxy monomer)[23,24] and a continued improved understanding of the physicochemical properties of these materials make them strong contenders for the ideal material for lab-on-a-chip and thus, in the long run, a serious option to replace materials such as glass, PDMS, polystyrene, and other polymers.

This review focuses on TE-based polymers used for the fabrication of microfluidic devices and highlights selected applications, where many characteristics of these materials are exploited favorably. The review does, however, not cover TE hydrogels or microfluidically produced TE materials, such as particles and filaments. While highly interesting and further emphasizing the large potential and versatility of this class of materials, it is beyond the scope of this review. It is instead our intention to provide an overview over the main characteristics of the TE materials and give a critical assessment of the advantages of these materials and their still remaining shortcomings, particularly with regard to their use for making microfluidic devices. With this, we hope to both continue to raise awareness for this material among the lab-on-a-chip community, provide pointers to researchers interested in picking up TEs for their fabrication needs and searching for replacements of the so far used materials, and show areas where still more input from material scientists, physical chemists, and engineers is needed to improve and tune the characteristics of the TEs further. To the best of our knowledge, this is the first review to discuss the TE polymers with respect to their potential in microfluidic chip fabrication and applications in the lab-on-a-chip field. Interestingly, earlier reviews discussing material options for microfluidic applications from 2013[25,26] do not even mention TE materials as serious contenders yet. However, the time is right to reconsider the true potential of this class of polymers, and the current review attempts to provide interested researchers with the necessary background and references to make an assessment of their own.

## ■ THIOL−ENE POLYMERS: BASICS, COMPOSITION, AND FABRICATION

The TE mechanism is a highly attractive reaction due to its simplicity of execution, mild reaction conditions, absence of offensive side products, orthogonality with other reactions and high yields (achieving nearly full polymerization). Hence, it is routinely classified as part of the click reaction concept. The concept of click chemistry was introduced by Sharpless in 2001 to define a set of simple, regioselective, robust, and high yielding reactions for synthetic chemistry.[27] Since then, the TE reaction, which has been known for a long time, has been experiencing a renaissance.[28] Besides the application in monomer synthesis and preparation of macromolecules, the TE reaction constitutes an efficient tool for surface modifications and in developing new materials. Since the latter two aspects of TE chemistry are highly relevant for microfluidic devices, the basics of the reaction, the material compositions, and the fabrication possibilities will be summarized in this chapter.

**Thiol−Ene Click Reaction.** The TE coupling is a reaction between a thiol and a nonactivated carbon−carbon double


https://dx.doi.org/10.1021/acsami.9b22050
ACS Appl. Mater. Interfaces 2020, 12, 10080−10095

bond (alkene) forming a thioether (Figure 1A). The reaction is initiated by the cleavage of the sulfur−hydrogen bond forming

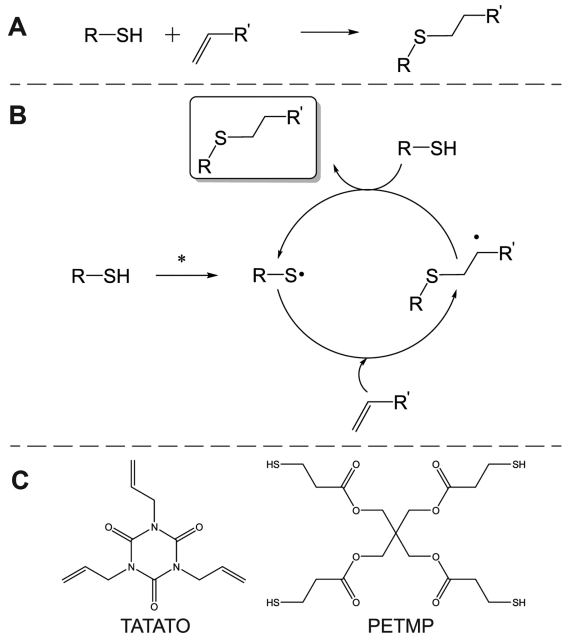


**Figure 1.** Thiol−ene click reaction and chemical structures. (A) Idealized reaction scheme of thiol−ene coupling. (B) Thiol−ene coupling showing the initiation, chain transfer, and propagation. Termination is not shown. In the case of catalyzed thiol−Michael addition the free electron on the radical is replaced by a negative charge. * indicates means of initiation using in-/direct photon deprotonation, thermal, redox, or enzymatic reaction (compare Figure 2). (C) Most commonly employed monomers for the synthesis of thiol−ene polymers in microfluidic applications. The trifunctional ene monomer has a rigid aromatic center (triazine) while the tetrafunctional thiol monomer has a flexible sugar center (pentaerythritol).

a thiyl radical, which can basically react with any nonsterically hindered "ene". The thiyl radical propagates via the alkene, forming the thioether, and generating an intermediate carbon centered radical, which then again abstracts the hydrogen from another thiol, at which point the cycle repeats (Figure 1B). During the polymerization cycle the same amount of thiols as alkenes are consumed and hence, ideally, no homopolymerization occurs (i.e., no ene-to-ene coupling).

In radical-mediated conversion, the thiols react with the double bonds following the usual mode (anti-Markovnikov mechanism).[9] This radical TE reaction is a step-growth polymerization process, which slowly builds up the cross-linked network, has a late gelation point, and results in a stress-free polymer. In contrast, thiols also react with electron poor alkenes via an anionic chain growth mechanism (nucleophilic addition), also known as thiol-Michael addition. This reaction is commonly initiated using base or nucleophile-based catalyst.[29] Both reaction mechanisms are very similar, but instead of radicals, anionic species are formed in the thiol-Michael reaction. Both reactions show a reduced sensitivity to oxygen inhibition, which practically implies that the fabrication/modifications can be carried out under atmospheric conditions in contrast to, e.g., methacrylate systems.[11,30] In this review, we mainly focus on, but are not strictly limited to, the free-radical TE reaction since it has been the most frequently employed polymerization method used for microdevice manufacturing.

A variety of different monomers with ene- and thiol-moieties are commercially available or can be synthesized (compare ref 9), but only a few of them are suitable for bulk polymerization. The main factors, which need to be considered when choosing monomers, are number of functional groups (higher branching increases cross-linking density), electron-deficiency of the ene-groups (the reactivity increases with increased electron density; with some exceptions[9]), molecular weight (with increasing molecular weight oxygen diffusion into the bulk material is decreased and hence inhibition of the polymerization by oxygen is decreased), and the three-dimensional structure of the monomer (for multifunctional monomers this is highly important to prevent steric hindrance). The combination of the four-functional thiol PETMP with the three-functional ene TATATO is most frequently used (see Figure 1C). This combination can be economically sourced, results in handleable/practical viscosity, and was shown to give a high polymerization degree as well as low polymerization shrinkage and stress.[16,17]

Apart from the chemical nature and structure of the monomers, the type of cross-linking initiation also determines the final material properties. The initiation of the TE reaction starts by the abstraction of the hydrogen from the thiol group.

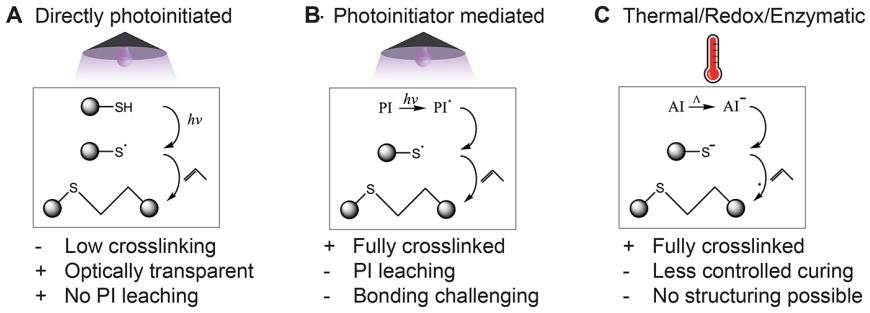


**Figure 2.** Cross-linking methods used for thiol−ene based microdevices. (A) UV-C light with a sufficiently high dose can directly deprotonate the thiol group and thus initiate the cross-linking reaction. (B) Typical photoinitiators (PI) absorb photons at a wavelength of 365 nm. After absorption, they get cleaved and a radical is generated (optionally several radicals), which then initiates the curing reaction. (C) Similarly, thermal initiators get cleaved at elevated temperatures; they produce a radical and kick-start the step-growth reaction. In case high temperatures cannot be tolerated, redox radical initiation systems can be applied. Enzymatic radical initiating systems have not been employed for microfluidic device fabrication (yet) but are nevertheless mentioned for the sake of completeness.


https://dx.doi.org/10.1021/acsami.9b22050
ACS Appl. Mater. Interfaces 2020, 12, 10080−10095

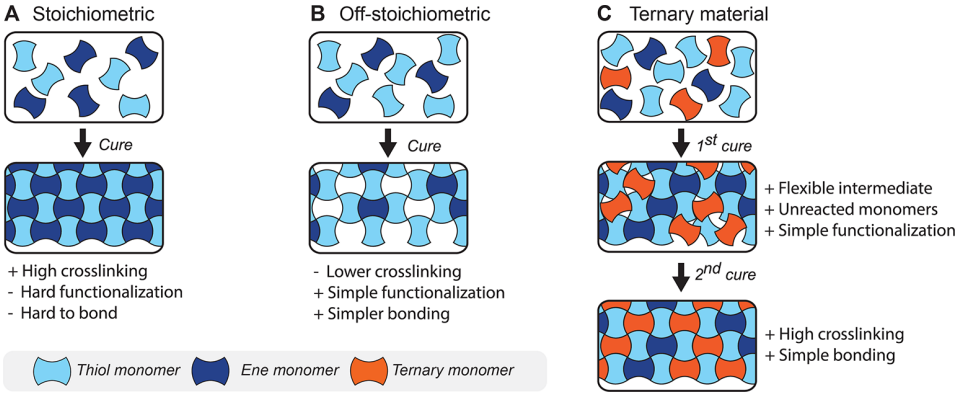


**Figure 3.** Concept of stoichiometric, off-stoichiometric, and ternary systems. Schematic illustration of (A) stoichiometric, (B) off-stoichiometric, and (C) ternary monomer systems prior to and after polymerization. The top row shows a mixture of monomers before polymerization while the bottom sketches represent the highly simplified final polymer structure.

This abstraction can be achieved via three general methods, which are summarized in Figure 2 together with the advantages and disadvantages in the context of microfluidic device fabrication. Cross-linking can be initiated either directly by UV-C light (wavelength at 254 nm),[31,32] indirectly by light-generated nucleophile radicals obtained from the cleavage of initiators,[33] or using thermal/redox/enzymatic radical initiating systems.[33−35]

Besides the option of carefully choosing monomers and combining them with appropriate initiators by the user, commercial products are available.[36,37]

**Off-Stoichiometric Mixtures and Ternary Systems.** Generally, when it comes to the preparation of a bulk polymeric network it is desirable to achieve the highest possible conversion of the functional groups to gain a fully polymerized material. Hence, in the case of TEs, the amounts of thiol- and ene-groups in the monomer mixture should ideally be balanced (stoichiometric), e.g., 4 mol TATATO to 3 mol PETMP (Figure 3A). However, if the amount of one type of functional groups is in excess, resulting in an off-stoichiometric mixture, the material properties will change (Figure 3B). Since during the radical TE reaction the same amounts of thiols and enes are consumed, any excess amount of a functional group is now present both in the bulk material as well as on the surface. In other words, the functional groups are not fully consumed and consequently the fewer cross-links in the network directly influence the stiffness and the glass transition temperature. By simply varying the monomer ratio the latter two parameters can be tuned which results in a glassy or rubbery polymer. Such off-stoichiometric compositions were, for example, used to tailor the polymerization and degradation behavior of hydrogels for biological applications.[55] In another publication, the thiol-to-acrylate ratio was altered for the purpose of surface modifications.[56] A similar approach was also used to nanostructure and surface modify TE substrates, and a detailed investigation of the photolithographical structuring of off-stoichiometric TE and thiol−acrylate systems was performed.[16,57]

Bowman's group added monothiols to a TE material to tailor the cross-linking density by terminating the radical reaction via the monofunctional compound.[12] With that approach, the authors showed that they could fabricate elastomeric membranes for pneumatically activated micropumps with a Young's modulus between 1 and 10.5 MPa.[12] In 2011, Carlborg et al. published a simplified approach, where the cross-linking degree was determined by the off-stoichiometric ratio without the addition of monofunctional compounds.[17] The authors named the resulting polymer "off-stoichiometric thiol−ene (OSTE)", and showed that the excess of functional groups remains unreacted in the network after photopolymerization and that the percentage of excess monomers directly determines the mechanical properties of the material (Youngs modulus from 250 to 1740 MPa and $T_g$ from 35 to 68 °C). Furthermore, it was shown that off-stoichiometric formulations provided unreacted thiol or ene groups on the surface, which can then be used for bonding or surface functionalization (Figure 3B). This feature alone sets these materials distinctly apart from most of the other polymer materials used for microfluidic devices. In a recent publication, Bowman's group showed how OSTE compositions in combination with thioester-moieties created a material, whose state of matter could be actively switched from solid to liquid using photoirradiation.[58]

Another approach for tailoring the polymer properties is to incorporate a third monomer to the precursor mixture (Figure 3C). These so-called ternary materials can be polymerized in one curing step, where the cross-linking reaction for all three monomers is initiated at the same time, or in a dual-cure procedure, where the two reactions are initiated separately. One-step curing has been used to fabricate very homogeneous networks using thiol-allyl ether-methacrylate systems,[59] or to achieve a high thermal stability (using a thiol−ene−ene ternary mixture).[60] Early studies were mostly focused on improving (meth)acrylate systems to tailor material properties (reduced shrinkage, mechanically uniform network, reduced oxygen inhibition) by incorporating thiol monomers.[23,61,62] Furthermore, the addition of epoxy monomers added another functional dimension to ternary TE polymers as the base catalyzed thiol-epoxy "click" reaction is a well-defined fusion process enabling simple postpolymerization modifications. As an example, Carioscia et al. incorporated bifunctional epoxy monomers to a TE mixture to improve the mechanical properties.[24] In this dual-cure system, the TE reaction was photoinitiated while the thiol-epoxy reaction was thermally initiated using an anionic catalyst (tris(dimethylaminomethyl)-phenol). The effects of monomer composition and curing order (first thiol−ene, then thiol−epoxy or vice versa) on polymerization kinetics and the mechanical properties have been studied by the authors. The highest conversion rate of functional groups was observed for the sequence where the


https://dx.doi.org/10.1021/acsami.9b22050
ACS Appl. Mater. Interfaces 2020, 12, 10080−10095

TEs were polymerized first and then the thiol−epoxy groups. However, the photopolymerization reaction also kick-started the second heat-initiated polymerization, and hence the timing of the two reactions could not be controlled separately.

Several groups have studied the thiol−ene/thiol−epoxy systems in more detail since they were introduced in 2007.[63−70] A major challenge during this development was to temporally separate the two curing stages, since normally the first exothermic TE reaction would kick-start the thermally initiated second thiol-epoxy reaction. This problem was resolved in van de Wijngaart's group using a new thiol−ene−epoxy system. They developed a three-component system called "OSTE+", where the "+"- symbol stands for the epoxy-functionalized monomer(s) (Figure 3C). This OSTE+ formulation enabled in particular to bond to untreated Si-wafers by simply spin-coating the polymer mixture onto the wafer, pressing wafers together, followed by thermal curing for 1 h at 90 °C.[49] Another advantage of the OSTE+ dual cure polymer is its applicability to the injection molding fabrication technique, which is the method of choice in industrial scale production.[44] In contrast to the "first-UV-then-thermal" curing process just discussed, another dual cure formulation was developed, where both the TE and the subsequent thiol-epoxy reactions were initiated by UV light, albeit at different wavelengths, and a successful delay of the second reaction was shown for up to 24 h.[66] Recently, the same researchers published a polymer system, where, after the first thiol-epoxy cure, the polymer could be stored for 2 months, and then the second TE reaction could be initiated to, in particular, facilitate bonding.[50] Although the employed chemistry was not fully disclosed, the authors showed—using FT-IR measurements—that after the first thermally initiated cure the epoxy peak completely disappeared, while the thiol peak decreased and the allyl peak stayed constant.

**Fabrication of Microfluidic Devices.** For a microfluidic device material to become widely accepted and utilized in research, it should fulfill certain criteria; that is, preparing structures should be simple and rapid, robust and straightforward bonding/assembly strategies should be available, handling the material should not be overly complicated, and simple surface modification protocols should exist. These crucial aspects to successfully manufacture usable devices (see also Table 1) will be discussed in the following section.

Manufacturing of microscale features using the liquid TE prepolymer can be accomplished through well-established methods of photolithography, replica molding, and reaction injection molding. For the photolithographical patterning, the thickness of the TE can be defined either by spin-coating, to achieve a thin polymer layer or by using spacers whereby the polymer is pressed between the substrate and the mask. A disadvantage of the spin-coating approach is that the TE, compared to other negative photoresists (e.g., SU-8), cannot be hardened prior to polymerization (this is often referred to as the soft-bake step when working with SU-8), and hence the mask must be aligned without any physical contact to the resin (proximity mode). This gives rise to diffraction when transferring the pattern and therefore limits the photolithographic resolution. However, this can be circumvented, when thicker layers (>100 $\mu$m) are desirable, by using spacers. In that case, a photomask is placed in direct contact with the prepolymer and a spacer in-between the (polymer) mask and the substrate defines the layer thickness.[12,16,38−41,51] Using the latter method, the best feature quality and an aspect ratio of up to 13 can be obtained using a minimal concentration of the photoinitiator and an initiator to inhibitor ratio of 1:1.[16] Interestingly, off-stoichiometric formulations improve the quality of photostructured features; the underlying reasons are elaborated in ref 42. Using photolithography, TE can thus be used to fabricate high aspect ratio microstructures on a master mold (as a cheaper alternative to SU-8) for, e.g., PDMS replica molding.[41,73,74]

**Table 1. Overview of Fabrication Methods Used in TE Device Manufacturing**

| Fabrication techniques | Methods | References |
|---|---|---|
| **Patterning** | Photolithography | 12, 16, 38−42 |
| | Casting (Replica molding) | 14, 17, 43 |
| | Injection molding | 44−47 |
| **Bonding** | Covalent bonding | 43, 48, 49 |
| | Adhesive bonding | 46, 47, 50 |
| **Surface modification** | Photolithographic grafting | 17, 51−53 |
| | Coatings | 53, 54 |
| | Bulk modification | 53, 54 |
| **Back-end processing** | Drilling, milling, dicing | 44 |
| | Cutting (scalpel, scissors, $CO_2$-laser[a]) | [b] |
| | Polishing/grinding | [b] |
| | Metallization | [b] |

[a]Attention: Hazardous gases may form. [b]These processes are often not described in more detail in the literature but have been employed during fabrication.

Replica molding with TE materials has to be performed in a mold, which is UV-transparent (at least from one side) to enable photocuring. Traditionally, molds have been fabricated using PDMS, but molds from aluminum and SU-8/silicon wafers covered with a UV-transparent sheet are also applicable. Since TEs are resins, the mold needs to be coated with an antiadhesion layer such as Teflon/PTFE to prevent TE adhesion to the master.[17] However, it is important to keep in mind that this antiadhesive layer may be transferred to the TE surface and thus may change its surface properties.

Another fabrication possibility for TE devices is reaction injection molding. This technique is very similar to replica molding; however, the prepolymer is injected into a structured cavity rather then poured into a mold. The big difference to conventional injection molding is the fact that one side of the mold has to be transparent when using photocurable TE systems. It was reported that reaction injection molding of OSTE+ using glass-covered aluminum masters is advantageous compared to PMMA molds due to the higher heat conductance of the metal which improves removal of excess heat during the exothermic TE reaction.[44] The reduced temperature gradient delays and slows down the second thiol-epoxy reaction and hence improves the demolding step while still supporting the subsequent bonding of the polymer. Still, a further modified version of injection molding can prove advantageous when bonding to challenging materials is required. In the literature, injection molding was reported using a PDMS mold, which is directly attached to the substrate where the TE is intended to be bonded to, and the TE prepolymer is injected into the cavity provided by the mold and the substrate.[45−47] Since the liquid TE monomers fill out any small roughness on the surface, and even fill pores in membranes, the resulting mechanical interlocking provides a strong adhesion.


https://dx.doi.org/10.1021/acsami.9b22050
ACS Appl. Mater. Interfaces 2020, 12, 10080−10095

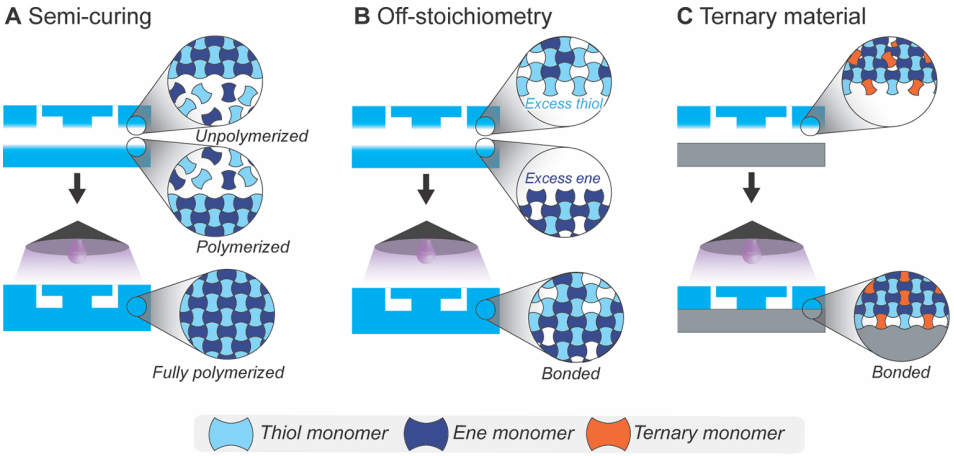


**Figure 4.** Bonding strategies using different formulations of thiol–ene polymers. The top row shows two separate layers after (a first) curing, and the inlays show a magnification of the interface. The bottom row represents the final device after complete curing. (A) The most frequently employed bonding method is semicuring where a thin unpolymerized layer enables subsequent bonding. (B) With the off-stoichiometric method two different stoichiometric mixtures enable the robust bonding approach. (C) Ternary materials are often used to facilitate bonding to nonthiol–ene materials, therefore the gray substrate represents a nonspecified material.

**Table 2. Bonding Possibilities of TE Based Polymers to Selected Non-TE Materials[a]**

| | Glass or Silicon | PDMS | Aluminum | Gold | PMMA | Teflon |
|---|---|---|---|---|---|---|
| **TE** | Plasma/photolith. | MPTMS[c] | | Photolith. | | |
| **OSTE** | MPTMS, Isocyanate | MPTMS[c] | | Directly[b] | | |
| **OSTE+** | Plasma | APTES[d], MPTMS[c] | APTES, MPTMS | Directly | APTES | Cemented film[46] |
| **NOA 81** | Plasma/photolith.[71] | MPTMS[c] | | | | Teflon AF[72] |

[a]Surface treatments are indicated. [b]Only thiol-excess OSTE. [c]MPTMS = mercaptopropyltrimethoxysilane. [d]APTES = aminopropyltriethoxysilane.

Besides the standard molding techniques, TE can also be processed using other fabrication techniques, such as (soft) imprint lithography,[72,75] even in a roll-to-plate mass production format. The latter was applied to produce structured TE sheets with a speed of up to 19 m $min^{-1}$, fabricating channels with a maximal depth of 90 $\mu$m and an aspect ratio of 2:1.[76] Due to the disadvantageously low viscosity of the TE resin for this fabrication approach, the prepolymer was rheologically modified either by using silica particle fillers or by precuring of thiol-terminated oligomers, showing again the large operational flexibility offered by this class of materials.

A final interesting and increasingly popular fabrication approach, namely 3D printing, has also embraced TE materials, albeit rarely in the context of microfluidic device fabrication. TEs are uniquely applicable to digital light processing or stereolithography, due to high refractive indices, low oxygen inhibition, and little shrinkage upon polymerization.[77] Shafagh et al. have shown electron beam structured nanoscale features, allowing for the creation of complex designs out of OSTE materials.[78] However, achieving the necessary size features for microfluidic devices over a sufficiently large footprint is still challenging and time-consuming.

It is important to stress that a major advantage of TE materials is the much simpler bonding compared to other materials. Challenges to realize appropriate bonding are often the "Achilles heel" for many materials. Covalent bonding of two separately prepared TE parts is straightforward, without the need for any surface activation or treatment. The three basic bonding concepts for TE materials are shown in Figure 4. The most frequently applied technique is semicuring, where a minimal UV-dose is used to polymerize the bulk from the top (i.e., directly facing the light source), leaving a thin superficial layer on the far side unreacted (Figure 4A). This superficial layer is primarily a result of oxygen inhibition (therefore, the mold material should generally be gas permeable, e.g., PDMS)[9,75] and the fact that the polymer cures from the illuminated (near) side to the far side, like a traveling wave.[79,80] Exploiting these two phenomena enables the production of two semicured parts, which are then manually pressed together and subsequently photocured to generate a covalently bonded device. This technique is mainly used for the fabrication of NOA-based devices[75] or photoinitiator-free formulations.[43] Based on the authors' experience, the bonding of photoinitiator-containing TE systems (PETMP/TATATO, Figure 1C) is more challenging since the polymerization proceeds very fast and hence the two parts must be aligned and pressed together within seconds after the initial cure, to result in successful bonding. A solution to this limitation is shown in Figure 4B, where two OSTE parts, one with excess thiol and the other with excess ene, can readily be bonded in the presence of a photoinitiator.[17] Although this strategy enables simple device bonding, it must be stressed that the two layers possess different mechanical properties and that resulting buried structures have varying surface properties. This is likely the main reason why OSTE materials have not found wider applicability yet.[81]

Unique, in terms of bonding properties and fabrication possibilities, is the previously discussed class of dual-cure ternary materials (see Figure 3C). Ternary materials, which are sequentially cured in two steps, are highly interesting for applications, where, in a first process, the polymer is shaped into the desired form while it still maintains its elastic and, not least, its adhesive properties (Figure 4C). In this state, the


https://dx.doi.org/10.1021/acsami.9b22050
ACS Appl. Mater. Interfaces 2020, 12, 10080−10095

material can be further processed (e.g., demolded, cut in shape, surface treated), and stored for later use (or shipped to a customer) without initiating the second reaction. At a later stage, the polymer can then be transferred onto a substrate, where bonding is initiated by the second curing step. An example is the OSTE+ material, where surface epoxy-groups facilitate the covalent bonding to a variety of materials (compare Table 2). Due to the remaining conformability after the first UV-curing step, the material additionally facilitates mechanical interlocking and hence increases bonding strength. In cases where TEs cannot directly bond to a material, surface treatment must be applied, e.g., when bonding to PDMS, where surface silanization allows for bonding.[82]

In summary, changes in the TE composition, whether through changes in the monomers, their ratios or the addition of initiators, allow for versatile cross-linking approaches to suit most microfluidic applications and fabrication goals. The previous sections highlighted key TE-based materials and fabrication approaches; still, the possibilities are near limitless given the vast choice of formulation possibilities.

## ■ PROPERTIES OF THIOL−ENE POLYMERS

A great variety of monomers can be used when preparing TE polymers, and the resulting final material properties are consequently very diverse as well. In this chapter, we will summarize the properties of the most common TE compositions and commercial formulations, which have already been used in the context of microfluidic fabrication. Aspects, which are important during the material selection process, including the mechanical properties (elastic moduli and $T_g$), optical properties, solvent and oxygen permeability, wetting properties, and biocompatibility, will be critically assessed.

**Mechanical Properties.** With a wide range of both in-house synthesized and commercially available monomers, along with entire formulations ready to be used, the mechanical properties of TE polymers can be easily tailored to fit the needs of the application. The following section attempts to summarize the various ways in which the elasticity and glass transition temperature of TEs can be modulated. A summary of the reported moduli and $T_g$ are shown in Table 3.

TEs with elastomeric properties with low Young's modulus (0.1−10 MPa) can be realized by choosing appropriate monomers, resulting in a hybrid "OSTE-PDMS" material composed of vinyl and thiol terminated polydimethylsiloxanes. Its applicability was shown for pneumatically actuated microvalves as mentioned previously.[17,83] Similarly, varying the number of functional groups of the thiol monomer (di-, tri-, or tetrathiol) in combination with a divinyl "ene" monomer has been shown to produce materials with 1−10 MPa moduli for the implementation of microvalves.[12]

As opposed to changes to the monomer composition, rather large variations in elasticity can be achieved using off-stoichiometric formulations. For example, varying the allyl to thiol ratios, the elastic modulus ranges from 0.1 to 800 MPa, such that increasing the thiol monomer concentration results in lower moduli and decreased $T_g$ values.[83] It has been postulated that this is due to the lower cross-linking density that results from the limiting number of functional groups;[17] moreover, the thiol-monomer has longer side chains as opposed to the more rigid allyl monomer, where the increased bond rotation contributes to the material's flexibility. An increase in the storage modulus can also be achieved by the addition of ternary components into the formulation, such as epoxy monomers;[63,66] however, conflicting data have been shown, where increasing epoxy content lowers the stiffness of the material.[67] Similarly, moduli can also be varied through the addition of composite solids, such as carbon nanotubes,[88] or aluminum oxide nanoparticles.[89] The addition of 0.75 wt % carbon nanotubes resulted in a 3-fold increase in the storage modulus of NOA-83H, from 970 to 2850 MPa, or 5.7 wt % aluminum oxide nanoparticles nearly doubled the storage modulus of the thiol−acrylate system. These solids are thought to reinforce the TE network, resulting in a stiffer material.

**Table 3. Mechanical Properties of Selected TE Polymers**

| Material | Glass transition temperature ($T_g$, °C) | Young (E) or Storage (E′) Modulus (MPa) | Reference |
|---|---|---|---|
| **PDMS** | −135 | 0.5−3 (E) | 17, 84, 85 |
| **PETMP + diallyl-PDMS** | n.a. | 0.2−0.7 (E) | 83 |
| **Thiol-PDMS + vinyl-PDMS** | −36 | 0.1−0.3 (E) | 17, 83 |
| **PETMP + diallyl** | n.a. | 10.5 (E) | 12 |
| **Ostemer 324 Flex** | n.a. | 28 (E) | Manufacturer |
| **Ostemer 322** | 69−80 | 1000 (E), 2300 (E′) | Manufacturer,44 |
| **NOA-81** | 35−75 | 850−1400 (E) | 17, 86 |
| **Trithiol + TATATO** | 68−74 | 100−1740 (E, varied molar ratio) | 17, 83 |
| **PETMP + TATATO + BADGE** | 71−77 | 1900 (E′) | 44 |
| **PETMP + TATATO (1:1)** | 51−74 | 1100−1400 (E), 1600−2300 (E′) | 66, 67, 86, 87 |
| **PETMP + TATATO heat treated** | 117 | 2500 (E′) | 87 |

In addition to the polymer formulation, heat, curing wavelength, and postproduction heat treatment can affect the mechanical properties. For example, by varying the temperature during UV curing of NOA-81, it is possible to control the mechanical properties of the final material.[79] In this contribution, the authors show that by increasing the temperature during the curing process from 23 to 100 °C, the modulus increases 7-fold, from 30 to 190 MPa. In a thiol−ene/acrylate system with an added photoinitiator, shorter wavelength light during curing (254 nm as opposed to the "standard" 365 nm) has been shown to produce polymers with significantly higher storage modulus, and up to 20 °C higher glass transition temperatures.[90] High intensity 254 nm light carries sufficient energy to break the S−H bond; therefore, in combination with a photoinitiator in the system, the resulting polymer is likely more cross-linked, resulting in a stiffer material. Lastly, the glass transition temperature significantly increases following a postpolymerization heat treatment. It was shown that 60 h, 200 °C heat treatment results in an increase of $T_g$ from 64 to 117 °C for PETMP and TATATO, though a much smaller gain in the storage modulus.[87] Such high glass transition temperatures may be critical for high temperature applications, e.g., to implement on-chip PCR.

Overall, the mechanical properties of TE materials can be drastically altered through the chemical nature of the monomers as well as the monomer ratios; moreover, they


https://dx.doi.org/10.1021/acsami.9b22050
ACS Appl. Mater. Interfaces 2020, 12, 10080−10095

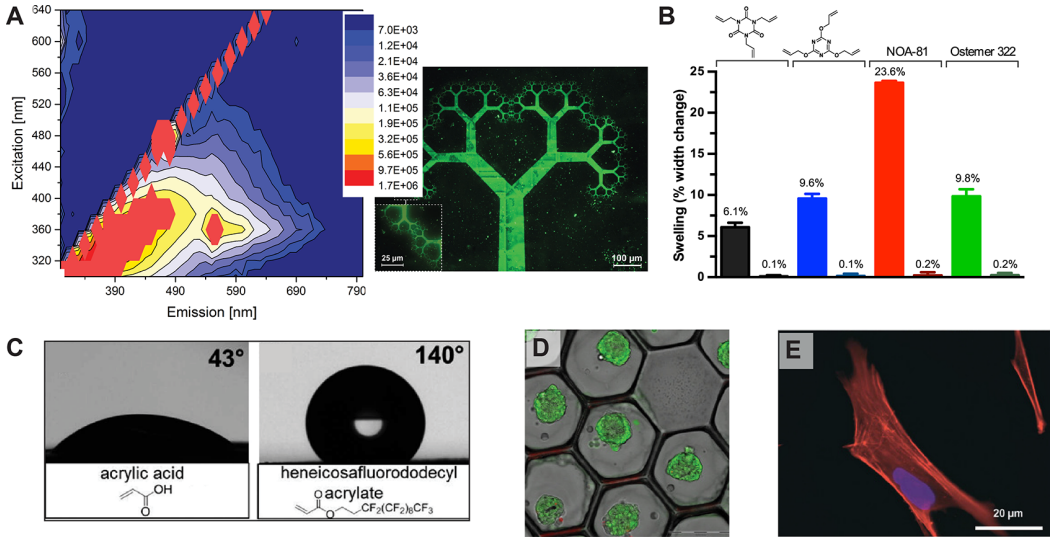


**Figure 5.** Selected examples of thiol−ene materials properties. (A) Autofluorescence scan of OSTEmer 322 recorded with a plate reader[46] and fluorescently labeled ($\lambda_{ex}$ 488 nm) nanopatterned OSTE structure of a tree shape with branches as small as 100 nm.[78] (B) Extensive heat-treatment significantly improves the compatibility of several thiol−ene formulations with chloroform. Data shows the swelling of samples before and after heat-treatment.[87] (C) Contact angle measurements of Thiol-OSTE with postfunctionalization using acrylic acid or heneicosafluorododecyl acrylate.[83] (D) Biocompatibility of TE-based materials investigated in terms of cell culture viability. Live−dead staining of spheroids in a microwell made from thiol−ene.[98] (E) Primary stem cells grown on TE substrates coated with gelatin and stained actin cytoskeleton (red) and nucleus (blue).[46] (A, B, E) Reprinted from refs[46,87] with permission of The Royal Society of Chemistry. (D) Reprinted from ref 98 with permission from Elsevier.

can be further modulated by heat treatment and by changing the wavelength of the UV light used for curing.

**Optical Properties.** For optical applications, the microfluidic material should be transparent in the region of interest. The gold-standard polymers for optical applications are cyclic olefin copolymers (COC) and PMMA, given their low absorption both in the visible and near-UV range.[44] TEs exhibit high optical transparency in the visible spectrum;[18] however, UV transmittance varies with composition. Certain TEs can compete with the near-UV transmittance of COCs and PMMA. For example, PETMP/TATATO show good transmittance in the UV-A region above 325 nm,[18] whereas Ostemer 322 and OSTE+ show substantial absorption below 380 and 420 nm, respectively,[44] while still transparent in the visible region.

For certain applications, the refractive index of the liquid inside the microfluidic channel should match the refractive index of the material, eliminating imaging artifacts near the edge of the channel.[94] To realize optical elements such as lenses or waveguides, on the other hand, a high refractive index is more advantageous. TEs generally have a relatively high refractive index, with NOAs ranging from 1.52 to 1.56,[14,95] Ostemer 322 at 1.58, and PETMP/TATATO around 1.56 for all stochiometric ratios.[18] For this reason, thiol−ene−epoxy[96] and NOA-89[97] have been successfully used to prepare microoptical elements.

For fluorescence-based applications, the autofluorescence and light scattering of the material is important to consider. For TEs, an important contribution to autofluorescence stems from the addition of a photoinitiator, and therefore this should be avoided for high sensitivity detection applications.[52] An excitation/emission scan of Ostemer 322 is shown in Figure 5A, where the strong emission seen in the UV-A excitation wavelength range ($\lambda_{ex}$) was concluded to be autofluorescence.[46] However, the authors might have misinterpreted these results, as the emission profile follows the increasing excitation wavelength, which is consistent with Stokes−Raman inelastic scattering. The single emission maxima at $\lambda_{ex}$ 360 nm and $\lambda_{ex}$ 540 nm are, however, consistent with autofluorescence. Therefore, Ostemer 322 may exhibit strong scattering properties along with local fluorescent centers. Additionally, the authors compare the emission of Ostemer 322 with glass, COCs, and polystyrene, where the presumed Raman scattering of Ostemer 322 results in significantly higher emission in the short wavelength region of the visible spectrum. This notwithstanding, the authors showed excellent cell visualization using a range of fluorescent dyes in chips prepared with Ostemer 322. In contrast to Ostemers, NOA's were specifically developed for optical applications, and while NOA-81 does contain photoinitiator, it has been reported to have four times lower levels of autofluorescence than PDMS;[75] however, the scattering properties of the material are undocumented. Nonetheless, with high optical clarity in the visible spectrum, TEs are appropriate for fluorescence-based applications such as cell staining or as shown in Figure 5A, for visualization purposes using Alexa Fluor 488.[78,98] It has to be kept in mind that if the material is heat treated to increase solvent compatibility or decrease the oxygen depletion effect (see further below), it takes on a first yellowish and then brownish hue, significantly altering the optical properties.[87]

**Solvent Compatibility.** A pertinent property of microfluidic materials is their compatibility with the chemical environment they are exposed to. This could include extreme pH values, but in particular also the use of organic solvents. TEs are generally regarded to be significantly more solvent resistant than other polymer materials, such as PDMS, PMMA, and COCs. Furthermore, with the possibility of replica molding, as opposed to hot embossing for COCs and PTFE, TEs are attractive polymers for organic solvent-based applications such as in analytical and synthetic chemistry. A


https://dx.doi.org/10.1021/acsami.9b22050
ACS Appl. Mater. Interfaces 2020, 12, 10080−10095

short list of frequently used solvents is given in Table 4, where TEs (both NOA-81 and in-house mixtures), PDMS, and COCs are compared with respect to swelling in those solvents.

**Table 4. TE Swelling, in Comparison to PDMS and COCs[a]**

| | Thiol−ene | | | | |
|---|---|---|---|---|---|
| | NOA-81[93] | PETMP + TTT[87] | PETMP + TTT Heat treated[87] | PDMS[91] | COC[92] |
| | $S^a$ (%) | $S^b$ (%) | $S^b$ (%) | $S^a$ (%) | $S^c$ (%) |
| $H_2O$ | 1 | 0.5 | 0 | 0 | <3 |
| EtOH | 0 | 0 | 0 | 4 | <3 |
| Isopropyl alcohol | 0 | 0.5 | 0 | 7 | <3 |
| Hexane | 0 | 0 | 0 | 35 | >8 |
| Toluene | 2 | 0.5 | 0 | 31 | >8 |
| THF | 16 | 5 | 0 | 38 | >8 |
| DMF | n.a. | 7.5 | 0 | 2 | <3 |
| Dichloromethane | 27 | 25* | 13* | 22 | >8 |
| Acetone | 12 | 6 | 0.5 | 6 | <3 |
| Acetonitrile | 11 | 12 | 3 | 1 | <3 |
| Chloroform | 34 | 20 | 0 | 39 | >8 |

[a] $S^a$ is percent swelling in 2 mm polymer squares after 24 h immersion, $S^b$ is percent swelling in 500 $\mu$m wide channels after 24 h solvent immersion. $S^c$ is the percent weight increase over the course of 8 weeks. *swelling after 4 h.

Interestingly, recent findings show that heat treatment of TEs, well beyond their glass-transition temperature, results in significantly improved solvent resistant properties.[87] In Figure 5B, the effect of heat treatment on chloroform compatibility is shown for four different TE formulations. TE solvent resistance, including solvent-induced delamination, was also investigated in other published articles;[53,71,99] however, a direct comparison of the data is difficult due to the various methodologies used in these investigations to determine the effect of solvents on the materials. It is important to keep in mind that the type of monomers and the stoichiometry used plays a crucial role in the solvent compatibility of the material.[83] Both aspects are connected to the relationship between $T_g$ and the void volume of the material, such that softer, more elastic networks of polymers are more susceptible to solvent permeation and swelling induced deformation. Moreover, as the storage modulus of the material is correlated with the cross-linking density, the expected solvent resistance can often be gauged from the degree of cross-linking. Consequently, the concentration of photoinitiator in the mixture plays an important role in the solvent compatibility properties as it determines the resulting cross-linking density of the material.

The addition of filler materials has also been shown to modify solvent resistance. For example, for NOA 83H mixed with carbon nanotubes (CNTs), toluene-induced swelling could be reduced from 18.3% to 1.6%. For acetone, a more moderate reduction occurred from 9.9% to 4.6%.[88] However, the addition of CNTs renders TEs nontransparent.

Similar to the previously investigated properties, the solvent compatibility of TE largely depends on the monomer composition. Generally speaking, however, the TE family of polymers are inherently more solvent resistant than many common polymers. Additional treatments and modifications, such as higher photoinitiator content, temperature treatment, or additives can greatly increase solvent compatibility further, making it an ideal polymer for solvent-based applications.

**Wetting Properties.** With the high surface area to volume ratio in microfluidics, the surface properties need to be tightly controlled. Wettability of a material plays a critical role in determining flow properties, as well as for applications such as droplet microfluidics, while assays involving large molecules depend on reduced nonspecific adsorption. For example, biomolecules tend to adsorb onto surfaces primarily through hydrophobic interactions, which can be mitigated by increasing the hydrophilicity of the surfaces.[103,104]

TEs are mildly hydrophilic polymers with a water contact angle (WCA) between 60° and 80°[14,15,51,53,72,105] depending on the stoichiometric ratio of the monomers[17,106,107] and the curing duration.[106] Classical approaches to increase hydrophilicity toward glasslike contact angles include oxygen plasma[14,53,87,106] and UV/ozone[105] treatments, yielding surface energy modifications, which are stable for several days.

As mentioned previously, a particular advantage of off-stoichiometric TEs is the ability to retain free allyl or thiol surface groups for photografting of various molecules. Covalent click-modification of the surface is more desirable when compared to more transient adsorption-based approaches (Figure 5C). Various hydrophilic surface modifiers have been employed, including PEG derivates (WCA 35−52°[17,83]), acrylic acid (WCA 43°),[83] hydroxylethyl methacrylate (WCA 25−43°),[51,108] and allyl malonic acid (WCA 25°).[81] Similarly, hydrophobic modifiers include fluorinated acrylates (WCA 102°−140°)[51,83,107] and PDMS derivatives (WCA 77−97°).[17] Selective masking of the TE bulk material during photografting allows for the realization of dual-wetting properties, for example for double emulsion droplet microfluidics.[102]

As surface modifications may be cumbersome to implement and prone to heterogeneity or local defects, bulk modification of the microfluidic device is another approach to change wetting properties by directly incorporating functional monomers into the prepolymer mixture. Examples from the literature describe a hydrophobic modifier premixed into NOA 81[53] and an innovative approach, where both hydrophilic and hydrophobic monomers were incorporated into the prepolymer and simultaneously patterned by self-assembly of the monomers onto a hydrophilic/hydrophobic patterned master mold.[54]

The aforementioned examples of surface modifications again highlight the versatility of off-stoichiometric TEs thanks to their inherent ability to be click-modified resulting in readily prepared customized surfaces.

**Permeability.** Given the broad range of possible compositions of TE-based polymers, permeability to gas or liquids varies depending on the formulation.[109] Generally speaking, for commonly used TEs (such as NOA-81, PETMP/TATATO, and OSTE+), oxygen, water-vapor, and molecular permeation are limited or very low. For example, PETMP/TATATO and OSTE+ exhibit slight water absorption (1.5−2.7%) while the flexible OSTE+, with similar mechanical properties to PDMS, has a 90% lower water vapor permeability than PDMS.[66,110] In terms of gas permeability, PETMP/TATATO exhibits an order of magnitude lower oxygen permeability when compared to polyethylene terephthalate (PET).[109] The combination of OSTE and PDMS, however, shows high gas permeability and a stronger adsorption of small molecules, mainly due to the presence of the PDMS backbone.


https://dx.doi.org/10.1021/acsami.9b22050
ACS Appl. Mater. Interfaces 2020, 12, 10080−10095

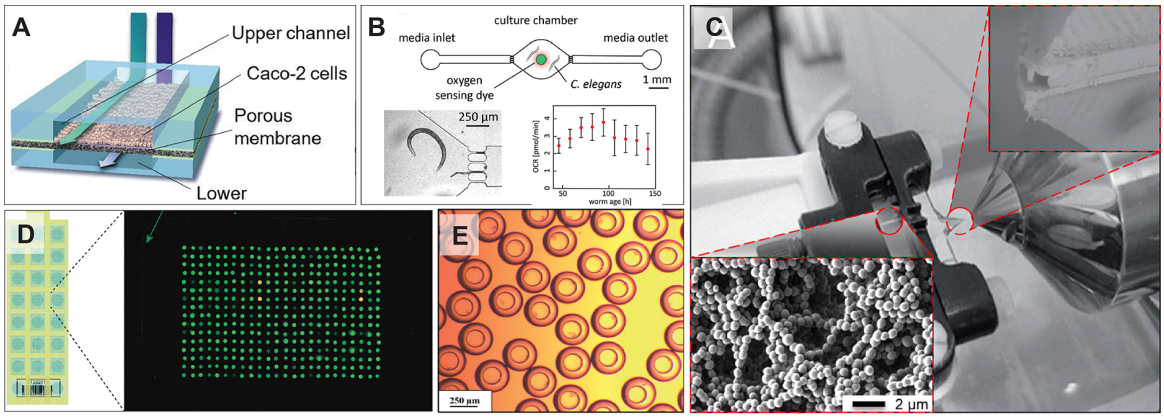


**Figure 6.** Examples of TE based microfluidic devices. (A) Intestine-barrier model using CaCo-2 cells on a porous membrane-integrated TE device. Adapted from ref 100. (B) Flow chamber for *C. elegans* culture and oxygen consumption rate measurements. Adapted from ref 101. (C) Analytical device fully made of TE featuring an emulsion-templated porous structure for solid phase extraction (bottom left inlay) and a 3D-tapered emitter for electrospray ionization (top-right inlay) coupled to mass spectrometry. Adapted from ref 21. (D) Microfluidic TE gasket for immunoassay readout showing 384 printed protein spots in one well.[50] (E) Optical microscopy image of water in PDMS in water double emulsion showing the narrow size distributions of the overall capsule size and its inner phase diameter.[102] (B, C) Adapted from ref 101 with permission from The Royal Society of Chemistry. (A, D, E) Reprinted from refs 21, 50, 102 with permission from The Royal Society of Chemistry.

However, it is important to keep the correlation between $T_g$ (relating to the free-volume of the polymer) and permeability/diffusivity in mind. Kwisnek et al. show a strong correlation between $T_g$ and oxygen permeability and diffusivity for various TEs.[109] For elastomeric TEs with $T_g$ values below room temperature, as $T_g$ increases, both the free volume and oxygen diffusivity are reduced. For densely cross-linked, glassy TEs, increasing $T_g$ results in increased free-volume and oxygen diffusivity, albeit still exhibiting overall low permeability and diffusivity. Therefore, based on the glass transition temperature, the expected permeability of the TE polymer can be estimated.

**Oxygen Uptake.** TE polymers can take up oxygen from the environment, which is a unique characteristic among plastics and was just recently described in more detail.[111] Since the cured TE polymer is a poly sulfur network, consisting of thioether-linkages, each sulfur atom in the polymer chain can react with up to two additional oxygens. As a consequence, any fluid containing dissolved oxygen, which is in contact with OSTE+, will be depleted of oxygen. In a microfluidic channel made from this particular TE material, the oxygen concentration dropped from 20% to close to the detection limit within a few minutes. Interestingly, the oxygen depletion rate can be tuned depending on a postpolymerization heat-treatment of the OSTE+, varying with duration and temperature level of the treatment. This rather exotic material property has direct implications for the compatibility of this material with biological systems.

**Biocompatibility.** The application of microfluidics to study cell cultures or create complex in vitro models, e.g., organ-on-chips, is growing rapidly, and as such TEs are of interest for these applications as well. In this context, biocompatibility refers to the ability of growing cell cultures in TE devices without altering the specific cell functions. Several studies have been investigating this issue, but so far no conclusive results could be drawn. For example, the cell viability assessed using a metabolic activity assay showed no significant difference for cells cultivated together with pieces of TE (PETMP/TATATO) or without them.[100] In experiments where cells were grown directly on OSTE+ substrates, viability slightly increased, while cells which were grown in the presence of TE extractions (water that was previously incubated with TE polymer samples) showed a decrease in viability in a concentration dependent manner.[112,113] In another study, cells were grown in microwells made of NOA 63, showing good biocompatibility (Figure 5D).[114] Conversely, in another study, leaching monomers were identified as a potential source of cytotoxicity, although preincubation of OSTE+ in water mitigated any negative cell responses.[113] Additional investigations of cell morphology and stem cell differentiation suggest biocompatibility of OSTE+ (Figure 5E).[46] Notably, thiol-excess OSTE yields a lower viability compared to allyl-excess, while plasma treatment of the thiol-excess OSTE increases cell viability.[115,116]

According to ISO 10993-5, TE-based materials can most likely be classified as biocompatible;[113] however, the oxygen depletion property mentioned further above can seriously impact cell function in a closed compartment. Therefore, the material should be heat treated prior to use to reduce this effect, in case it is not desired.[111]

The challenge to draw general conclusions on the biocompatibility of TE stems largely from the fact that the monomer composition determines this property. However, several previously mentioned formulations were tested and no cytotoxic effects or other unexpected variation in cell responses were reported, as outlined above. If other formulations than the ones already described are used, in particular together with special additives (initiators, inhibitors, plasticizers etc.), additional tests for biocompatibility are highly recommended.

## ■ EXAMPLES OF TE-BASED MICROFLUIDIC DEVICES

As was described in detail above, TE polymers show a number of interesting properties and fabrication possibilities that should make them preferred materials for many microfluidic applications, or, at least, a highly promising alternative worthy of consideration. Indeed, these polymers have already been applied in various research fields ranging from analytical chemistry to organ-on-a-chip. However, since their more widespread use is only just starting and many efforts so far have been on the material characterization and fabrication side,


https://dx.doi.org/10.1021/acsami.9b22050
ACS Appl. Mater. Interfaces 2020, 12, 10080−10095

there is only a limited set of published papers available that highlight how TE polymers can make a difference for specific applications. In this section, we will present select examples from within three application areas, and assess the specific role of TE polymers. In a related recently published review article a broad overview over microscale applications of click chemistry in general is given.[117] This should provide further inspiration to implement some of these chemistries also in the context of TE-based microfluidic systems.

**Cell Culture and Biological Applications.** Microfluidics approaches were introduced to life science applications to increase the degree of automation, allow a high throughput of samples, mimic more closely *in vivo* conditions (e.g., shear forces as they occur in blood vessels), and integrate real-time sensors.

One area where TE polymers were applied is the preparation of microarrays for the culturing and high-throughput screening of cells[114] and breast cancer spheroids,[98] respectively. In both cases, these microarrays were fabricated from commercial NOA 63[114] or NOA 81[98] by imprint lithography using a PDMS stamp. For cellular spheroids production, a simple coating procedure was advantageous to prevent cellular attachment to the microchamber and form the desired spheres.

In another work, a two-chamber microsystem with an integrated membrane was used to mimic the intestinal barrier function, where all parts (other than the membrane) were fabricated using TE (Figure 6A).[100] The microdevice enabled transport studies across a Caco-2 cell layer while optical and functional monitoring of barrier integrity was performed in real-time in eight parallel chambers. TEs are highly desirable for drug transport studies compared to PDMS due to the negligible absorption of small molecules inside the polymer. Besides culturing cells and bacteria, also the multicellular organism *C. elegans* has been grown in OSTE+ highlighting the versatility for biological applications.[101] The very low oxygen permeability of TEs allowed real-time monitoring of the oxygen consumption solely due to the respiration of the organisms, neglecting the influx of oxygen molecules through the substrate material (Figure 6B).

OSTE is an attractive option for applications that require rigid microfluidic channels. This property was used for the fabrication of a microfluidic array of pinch-points, to mechanically lyse cells.[118] OSTE materials do not expand under pressure, thus maintaining a high energy dissipation rate. As a result, 85% of tumor cells pumped through the system were lysed, while similar soft PDMS devices only provide an efficiency of 40%. In related work, an approach to increase the mechanical stiffness of PDMS by applying thin coatings of TE was described.[119] Coated PDMS micropillars showed 70% less deformation compared to the noncoated ones.

In another application, an elastic membrane was integrated into an OSTE+ device to realize a mechanically actuated wound healing or migration assay.[82] The functional groups on the OSTE+ surface enabled covalent bonding of the elastic membrane while the OSTE+ rigidity ensured no deformation of the device during the actuation of the membrane by pressurized air.

Due to their biocompatibility, optical transparency, avoidance of absorption of small molecules, and overall favorable and tunable mechanical properties, TE polymers show excellent prospects for cell-based applications, awaiting their full potential to be explored.

**Analytical Microdevices.** The very first microfluidic devices were developed for applications in analytical chemistry, namely flow-injection analysis, chromatography, and electrophoresis.[120] Initially, these devices were glass and/or silicon based, but due to the demand for rapid prototyping and single-use devices, polymers are nowadays increasingly favored to prepare analytical microdevices. TE polymers have already been shown to be ideally suited for analytical applications due to their good solvent compatibility and straightforward surface modification possibilities. For example, TE was used for the fabrication of separation channels for electrophoretic separations of small molecules and peptides.[43,99,106] On top of the simple fabrication technique, TE facilitates physical (by oxygen plasma)[106] and chemical (by neutral polyacrylate coating)[52] surface modifications to vary surface charges and, hence, electro-osmotic flow (EOF) mobilities. Stable EOFs, and consequently reproducible migration times (<0.9% RSD), were reported.[99]

While analytical separations have been successful using TEs, detection can pose a challenge. In particular, TE's limited optical transmission in the near-UV range increases the limit of detection by 10-fold compared to Borofloat glass (i.e., the detection is less sensitive).[106] Therefore, a different approach to optical detection was facilitated by the integration of TE-based waveguides on-chip. The first example was a ternary system (thiol−ene−methacrylate), which inherently generates a refractive index gradient perpendicular to the edges of the waveguide and thus greatly reduces optical losses due to edge scattering.[121] In a related article, off-stoichiometric TE waveguides were used for a classical bioanalytical biotin−streptavidin assay; however, the linear detection range was shown to be very narrow (0−5 $\mu$M streptavidin).[18]

To increase detection sensitivity (and circumvent any issues and challenges with optical detection), emitters for electrospray ionization mass spectrometry (ESI-MS) were developed using replica molding of TE.[21,99,122] Initially, the emitter taper was made in 2D, but for robust and long-term spray stabilities sharp emitter apexes are desired, and an improved version with a three-dimensional tapered geometry was developed (Figure 6C).[21] These 3D emitters lasted for more than a month before mechanical deterioration and showed good spray stabilities for at least 3 h, providing a relative standard deviation of 8% for the baseline over 15 min. Notably, when using off-stoichiometric mixtures to fabricate these chips and emitters, leaching monomers were visible in the background spectrum, and thus, the chips had to be thoroughly rinsed prior to application to remove the remaining monomers.

Upstream of the emitter, an important sample preparation technique, namely solid phase extraction (SPE), was implemented on the same chip.[21] To realize the retention functionality, undecanethiol (C11) was immobilized on a TE emulsion template monolith (compare Figure 6C bottom inlay). Using monoliths allows for an increased surface area to volume ratio for C11 modification and resulted in a column capacity of 14 $\mu$g m$^{-2}$ for anthracene as test compound. However, the nonfunctionalized monolith already showed significant retention in its native state, and the achieved recovery for another test compound, progesterone, was only around 40−50%, leaving room for improvement. One challenge here appears to be how to increase the surface density of thiol or ene groups available for surface functionalization.


https://dx.doi.org/10.1021/acsami.9b22050
ACS Appl. Mater. Interfaces 2020, 12, 10080−10095

Emulsion-templated TE-beads filling the entire lumen of a channel (aka "porous monoliths") are ideally suited for the immobilization of enzymes due to the high surface-area to volume ratio. In a protein analytical workflow it is often preferred that enzymes are immobilized and therefore do not interfere with any downstream processes and also can be reused. Microfluidic solutions for in-line immobilized enzymatic reactors (IMERs) furthermore allow the immobilization of rare and/or expensive enzymes since only a small amount is needed to cover the internal surface. Two commonly used proteases, pepsin and trypsin, as well as galactose oxidase and a deglycosilating enzyme, PNGase F, were successfully immobilized via the TE click chemistry and an ascorbic acid linker.[19,20,123] In a recent publication, a small TE monolith segment was used as a highly efficient mixer for fast labeling experiments during the sample preparation step for a hydrogen−deuterium exchange (HDX) workflow.[104] Similar to monoliths, micropillar arrays were made with OSTE, where abundant surface thiols were functionalized with gold nanoparticles and those in turn coated with a protease.[124] Replica molding was facilitated without the use of photoinitiators and gave excellent control over the number of free surface thiols allowing for variable hydrolysis rates. In these examples, TE devices in conjunction with beads or pillars yielded robust enzyme reactor systems for proteomics research.

Instead of micropillars, an elegant way of producing microarrays of molecules is to microprint them with the help of a photochemical printer.[50,125] Protein microarrays have been generated on epoxy coated glass slides, to which a special room temperature bonding thiol−ene−epoxy material was formulated to create a leak-tight seal between the microarray and a flow chamber (Figure 6D).[50] Using this TE-based gasket, biofunctionalized microarrays were simply combined with microfluidic chambers as the bonding is initiated at room temperature and hence no denaturation of the temperature sensitive proteins could occur. Combining such a gasket material with the microprinting system, many other bioassay investigations will become possible, for example, potentially even *in vitro* for cells interacting with different compounds. Such systems might turn into very efficient tools for biologists.

Other sample preparation techniques, such as liquid−liquid extraction and electromembrane extraction, benefit from the good solvent compatibility of TEs as well as the simple and versatile fabrication possibilities.[47,126] In the case of electromembrane extraction, reaction injection molding using TE enabled the integration of porous polypropylene membranes, which is challenging to achieve with other polymers.[47]

In general, TE's inherently good solvent compatibility is a big advantage in many analytical chemistry applications where it is often necessary to employ organic solvents. Moreover, the high degree of polymerization results in very low amounts of leachable monomers which prevents sample contamination.

**Flow-Focusing Devices.** The preparation of small droplets of an inner phase solvent not miscible with an outer phase solvent often requires large (10−100×) flow rate differences between the two phases, producing high back pressures that can easily lead to delamination and leaks. TE polymers provide high bonding strengths and mechanical stiffness, solvent compatibility, as well as the ease of surface modification to suit both water-in-oil and oil-in-water droplet generation. Combined, TEs are ideally suited for flow-focusing devices.[87,102,127] Figure 6E shows the achievable narrow size distributions of inner containers and the encapsulating outer spheres obtained by a double emulsion approach performed on a TE chip.[102] This contribution exemplifies the versatility of TE for selective surface modifications needed for double emulsion droplet generation. In related work, researchers looked at how the deformability of PDMS (adversely) affects the efficiency of inertial focusing and, along with that, the resulting particle size distribution.[127] The main reason for obtaining a wider size distribution was the changing cross sectional geometry of the channels, which was directly related to material deformability. In a recent work, a TE flow focusing device was shown to produce chloroform-based PLGA particles at 1 $\mu$m diameters.[128] The monodisperse chloroform droplets were produced at high flow rates generating extreme backpressures, where the TE chip maintained structural integrity, highlighting both the bonding strength, mechanical stiffness, and solvent compatibility of the material. With these core strengths of TE materials, there is a huge potential for designing and building robust flow focusing devices from TEs.

## ■ SUMMARY AND PERSPECTIVES

It is probably not entirely far-fetched to claim that most microfluidic devices to date have been manufactured using a less than optimal material and that developers of lab-on-a-chip applications have—more often than not—had to deal with frustrating shortcomings of one or the other material, leading to hampered performances or cumbersome workarounds. Most of these issues stem from the fact that so far no material was "invented" or tailored specifically to the needs of microfluidic fabrication and application, but almost always had been materials that were "off the shelf" or "used by others before".

It was the intention of this review to make a case for the TE polymer family of materials and to provide the readers with sufficient background and information to allow their own assessment of whether this material has the potential to be a valid and promising alternative to materials used so far. We tried to argue that, because of the chemical principles involved and the large variety of possible monomer combinations, this material family is extremely versatile and poised to be applicable to almost all challenges encountered in the wider field of lab-on-a-chip. Flexibility and ease of fabrication are immediate advantages, but more long-term benefits, such as the implementation of "green chemistry" protocols and sustainable production, should not be underestimated either.

TE- (and, in general, click-chemistry)-type materials have been known and studied for quite some time already, but still many "secrets" and characteristics of these materials remain less than fully understood and yet to be exploited properly. While this fuzzy parameter space is a main reason for the overall versatility of the material, it also, somewhat understandably, delays its further acceptance in the community, who—given the choice—would probably prefer a fully explored, matured, and hence almost immutable material. Thus, this review has mainly focused on collecting a wealth of material properties and mapping out numerous ways to tailor these materials for specific fabrication and applications needs, whereas the number of published examples of TEs being used for lab-on-a-chip is still limited. While these very promising materials still have shortcomings (most of them have been mentioned in the review), they also certainly have the potential to overcome most, if not all, of these limitations given the versatility that is inherent in the underlying chemical approach to designing, fabricating, and tuning TE materials.


https://dx.doi.org/10.1021/acsami.9b22050
ACS Appl. Mater. Interfaces 2020, 12, 10080−10095

It is unlikely that there ever will be a "standard" material for microfluidic devices (as, for example, fused silica is for capillaries), but TE materials are very strong contenders to replace many "less than perfect" materials in today's designs and products or, at least, become a powerful addition to the toolbox of microfluidic designers, to be used in connection with other materials, such as the still ubiquitous glass and PDMS.

## ■ AUTHOR INFORMATION


### Corresponding Author

**Jörg P. Kutter** − *Department of Pharmacy, Faculty of Health and Medical Sciences, University of Copenhagen, 2100 Copenhagen, Denmark;* orcid.org/0000-0003-1065-1985; Email: jorg.kutter@sund.ku.dk

### Authors

**Drago Sticker** − *Department of Pharmacy, Faculty of Health and Medical Sciences, University of Copenhagen, 2100 Copenhagen, Denmark;* orcid.org/0000-0001-7688-6977

**Reka Geczy** − *Department of Pharmacy, Faculty of Health and Medical Sciences, University of Copenhagen, 2100 Copenhagen, Denmark; Faculty of Pharmaceutical Sciences, University of British Columbia, Vancouver, British Columbia V6T 1Z3, Canada;* orcid.org/0000-0002-9901-110X

**Urs O. Häfeli** − *Department of Pharmacy, Faculty of Health and Medical Sciences, University of Copenhagen, 2100 Copenhagen, Denmark; Faculty of Pharmaceutical Sciences, University of British Columbia, Vancouver, British Columbia V6T 1Z3, Canada;* orcid.org/0000-0003-0671-4509

Complete contact information is available at: https://pubs.acs.org/10.1021/acsami.9b22050


### Author Contributions

[‖]The manuscript was written through contributions of all authors. All authors have given approval to the final version of the manuscript. D.S. and R.G. contributed equally.


### Funding

Lundbeck Foundation grant number 2014-4176.


### Notes

The authors declare no competing financial interest.

## ■ ACKNOWLEDGMENTS

U.O.H. acknowledges support by the Lundbeck Foundation, Denmark (grant number 2014-4176, the UBC-SUND Lundbeck Foundation professorship).

## ■ REFERENCES


(1) Effenhauser, C. S.; Bruin, G. J. M.; Paulus, A.; Ehrat, M. Integrated Capillary Electrophoresis on Flexible Silicone Microdevices: Analysis of DNA Restriction Fragments and Detection of Single DNA Molecules on Microchips. *Anal. Chem.* **1997**, *69*, 3451−3457.

(2) Delamarche, E.; Schmid, H.; Michel, B.; Biebuyck, H. Stability of Molded Polydimethylsiloxane Microstructures. *Adv. Mater.* **1997**, *9*, 741−746.

(3) Xia, Y.; Kim, E.; Whitesides, G. M. Micromolding of Polymers in Capillaries: Applications in Microfabrication. *Chem. Mater.* **1996**, *8*, 1558−1567.

(4) Xia, Y.; Whitesides, G. M. Soft Lithography. *Annu. Rev. Mater. Sci.* **1998**, *28*, 153−184.

(5) Xia, Y.; Whitesides, G. M. Soft Lithography. *Angew. Chem., Int. Ed.* **1998**, *37*, 550−575.

(6) Berthier, E.; Young, E. W. K.; Beebe, D. Engineers Are from PDMS-Land, Biologists Are from Polystyrenia. *Lab Chip* **2012**, *12*, 1224−1237.

(7) Türünç, O.; Meier, M. A. R. The Thiol-Ene (Click) Reaction for the Synthesis of Plant Oil Derived Polymers. *Eur. J. Lipid Sci. Technol.* **2013**, *115*, 41−54.

(8) Machado, T. O.; Sayer, C.; Araujo, P. H. H. Thiol-Ene Polymerisation: A Promising Technique to Obtain Novel Biomaterials. *Eur. Polym. J.* **2017**, *86*, 200−215.

(9) Hoyle, C. E.; Lee, T. Y.; Roper, T. Thiol−Enes: Chemistry of the Past with Promise for the Future. *J. Polym. Sci., Part A: Polym. Chem.* **2004**, *42*, 5301−5338.

(10) Lorenz, H.; Despont, M.; Fahrni, N.; LaBianca, N.; Renaud, P.; Vettiger, P. SU-8: A Low-Cost Negative Resist for Mems. *J. Micromech. Microeng.* **1997**, *7*, 121−124.

(11) Hoyle, C. E.; Bowman, C. N. Thiol−Ene Click Chemistry. *Angew. Chem., Int. Ed.* **2010**, *49*, 1540−1573.

(12) Good, B. T.; Reddy, S.; Davis, R. H.; Bowman, C. N. Tailorable Low Modulus, Reversibly Deformable Elastomeric Thiol-Ene Materials for Microfluidic Applications. *Sens. Actuators, B* **2007**, *120*, 473−480.

(13) Kim, S. H.; Yang, Y.; Kim, M.; Nam, S.-W.; Lee, K.-M.; Lee, N. Y.; Kim, Y. S.; Park, S. Simple Route to Hydrophilic Microfluidic Chip Fabrication Using an Ultraviolet (UV)-Cured Polymer. *Adv. Funct. Mater.* **2007**, *17*, 3493−3498.

(14) Hung, L.-H.; Lin, R.; Lee, A. P. Rapid Microfabrication of Solvent-Resistant Biocompatible Microfluidic Devices. *Lab Chip* **2008**, *8*, 983−987.

(15) Silvestrini, S.; Ferraro, D.; Toth, T.; Pierno, M.; Carofiglio, T.; Mistura, G.; Maggini, M. Tailoring the Wetting Properties of Thiolene Microfluidic Materials. *Lab Chip* **2012**, *12*, 4041−4043.

(16) Ashley, J. F.; Cramer, N. B.; Davis, R. H.; Bowman, C. N. Soft-Lithography Fabrication of Microfluidic Features Using Thiol-Ene Formulations. *Lab Chip* **2011**, *11*, 2772−2778.

(17) Carlborg, C. F.; Haraldsson, T.; Oberg, K.; Malkoch, M.; van der Wijngaart, W. Beyond PDMS: Off-Stoichiometry Thiol-Ene (Oste) Based Soft Lithography for Rapid Prototyping of Microfluidic Devices. *Lab Chip* **2011**, *11*, 3136−3147.

(18) Feidenhans'l, N. A.; Lafleur, J. P.; Jensen, T. G.; Kutter, J. P. Surface Functionalized Thiol-Ene Waveguides for Fluorescence Biosensing in Microfluidic Devices. *Electrophoresis* **2014**, *35*, 282−288.

(19) Lafleur, J. P.; Senkbeil, S.; Novotny, J.; Nys, G.; Bogelund, N.; Rand, K. D.; Foret, F.; Kutter, J. P. Rapid and Simple Preparation of Thiol-Ene Emulsion-Templated Monoliths and Their Application as Enzymatic Microreactors. *Lab Chip* **2015**, *15*, 2162−2172.

(20) Jonsson, A.; Svejdal, R. R.; Bogelund, N.; Nguyen, T.; Flindt, H.; Kutter, J. P.; Rand, K. D.; Lafleur, J. P. Thiol-Ene Monolithic Pepsin Microreactor with a 3D-Printed Interface for Efficient Uplc-Ms Peptide Mapping Analyses. *Anal. Chem.* **2017**, *89*, 4573−4580.

(21) Jönsson, A.; Lafleur, J. P.; Sticker, D.; Kutter, J. P. An All Thiol−Ene Microchip for Solid Phase Extraction Featuring an in Situ Polymerized Monolith and Integrated 3D Replica-Molded Emitter for Direct Electrospray Mass Spectrometry. *Anal. Methods* **2018**, *10*, 2854−2862.

(22) Lafleur, J. P.; Kwapiszewski, R.; Jensen, T. G.; Kutter, J. P. Rapid Photochemical Surface Patterning of Proteins in Thiol-Ene Based Microfluidic Devices. *Analyst* **2013**, *138*, 845−849.

(23) Senyurt, A. F.; Wei, H.; Hoyle, C. E.; Piland, S. G.; Gould, T. E. Ternary Thiol−Ene/Acrylate Photopolymers: Effect of Acrylate Structure on Mechanical Properties. *Macromolecules* **2007**, *40*, 4901−4909.

(24) Carioscia, J. A.; Stansbury, J. W.; Bowman, C. N. Evaluation and Control of Thiol-Ene/Thiol-Epoxy Hybrid Networks. *Polymer* **2007**, *48*, 1526−1532.

(25) Ren, K.; Zhou, J.; Wu, H. Materials for Microfluidic Chip Fabrication. *Acc. Chem. Res.* **2013**, *46*, 2396.

(26) Nge, P. N.; Rogers, C. I.; Woolley, A. T. Advances in Microfluidic Materials, Functions, Integration, and Applications. *Chem. Rev.* **2013**, *113*, 2550−2583.
(27) Kolb, H. C.; Finn, M. G.; Sharpless, K. B. Click Chemistry: Diverse Chemical Function from a Few Good Reactions. *Angew. Chem., Int. Ed.* **2001**, *40*, 2004−2021.
(28) Lowe, A. B. Thiol-Ene "Click" Reactions and Recent Applications in Polymer and Materials Synthesis: A First Update. *Polym. Chem.* **2014**, *5*, 4820−4870.
(29) Nair, D. P.; Podgórski, M.; Chatani, S.; Gong, T.; Xi, W.; Fenoli, C. R.; Bowman, C. N. The Thiol-Michael Addition Click Reaction: A Powerful and Widely Used Tool in Materials Chemistry. *Chem. Mater.* **2014**, *26*, 724−744.
(30) O'Brien, A. K.; Cramer, N. B.; Bowman, C. N. Oxygen Inhibition in Thiol−Acrylate Photopolymerizations. *J. Polym. Sci., Part A: Polym. Chem.* **2006**, *44*, 2007−2014.
(31) Cramer, N. B.; Scott, J. P.; Bowman, C. N. Photopolymerizations of Thiol−Ene Polymers without Photoinitiators. *Macromolecules* **2002**, *35*, 5361−5365.
(32) Cramer, N. B.; Reddy, S. K.; Cole, M.; Hoyle, C.; Bowman, C. N. Initiation and Kinetics of Thiol−Ene Photopolymerizations without Photoinitiators. *J. Polym. Sci., Part A: Polym. Chem.* **2004**, *42*, 5817−5826.
(33) Cook, W. D.; Chen, F.; Pattison, D. W.; Hopson, P.; Beaujon, M. Thermal Polymerization of Thiol−Ene Network-Forming Systems. *Polym. Int.* **2007**, *56*, 1572−1579.
(34) Cole, M. A.; Jankousky, K. C.; Bowman, C. N. Redox Initiation of Bulk Thiol-Ene Polymerizations. *Polym. Chem.* **2013**, *4*, 1167−1175.
(35) Zavada, S. R.; McHardy, N. R.; Scott, T. F. Oxygen-Mediated Enzymatic Polymerization of Thiol-Ene Hydrogels. *J. Mater. Chem. B* **2014**, *2*, 2598−2605.
(36) Mercene Labs AB, OSTEMERs. http://www.ostemers.com.
(37) Norland Products Inc., Norland Adhesives. www.norlandprod.com (accessed 2019-02-21).
(38) Kasprzak, S. E.; Wester, B. A.; Raj, T.; Allen, M.; Gall, K. Photopatterning of Thiol-Ene-Acrylate Copolymers. *J. Microelectromech. Syst.* **2013**, *22*, 339−348.
(39) Lee, N. Y.; Lim, J. R.; Lee, M. J.; Kim, J. B.; Jo, S. J.; Baik, H. K.; Kim, Y. S. Hydrophilic Composite Elastomeric Mold for High-Resolution Soft Lithography. *Langmuir* **2006**, *22*, 9018−9022.
(40) Corgier, B. P.; Juncker, D. Polymeric Microfabricated Electrochemical Nanoprobe with Addressable Electrodes. *Sens. Actuators, B* **2011**, *157*, 691−696.
(41) Martínez-Crespiera, S.; Ionescu, E.; Schlosser, M.; Flittner, K.; Mistura, G.; Riedel, R.; Schlaak, H. F. Fabrication of Silicon Oxycarbide-Based Microcomponents Via Photolithographic and Soft Lithography Approaches. *Sens. Actuators, A* **2011**, *169*, 242−249.
(42) Hillmering, M.; Pardon, G.; Vastesson, A.; Supekar, O.; Carlborg, C. F.; Brandner, B. D.; van der Wijngaart, W.; Haraldsson, T. Off-Stoichiometry Improves the Photostructuring of Thiol−Enes through Diffusion-Induced Monomer Depletion. *Microsyst. Nanoeng.* **2016**, *2*, 15043.
(43) Sikanen, T. M.; Lafleur, J. P.; Moilanen, M. E.; Zhuang, G.; Jensen, T. G.; Kutter, J. P. Fabrication and Bonding of Thiol-Ene-Based Microfluidic Devices. *J. Micromech. Microeng.* **2013**, *23*, 037002
(44) Sandström, N.; Shafagh, R. Z.; Vastesson, A.; Carlborg, C. F.; van der Wijngaart, W.; Haraldsson, T. Reaction Injection Molding and Direct Covalent Bonding of OSTE+ Polymer Microfluidic Devices. *J. Micromech. Microeng.* **2015**, *25*, 075002.
(45) Morel, M.; Galas, J.-C.; Dahan, M.; Studer, V. Concentration Landscape Generators for Shear Free Dynamic Chemical Stimulation. *Lab Chip* **2012**, *12*, 1340−1346.
(46) Sticker, D.; Rothbauer, M.; Lechner, S.; Hehenberger, M. T.; Ertl, P. Multi-Layered, Membrane-Integrated Microfluidics Based on Replica Molding of a Thiol-Ene Epoxy Thermoset for Organ-on-a-Chip Applications. *Lab Chip* **2015**, *15*, 4542−4554.
(47) Hansen, F. A.; Sticker, D.; Kutter, J. P.; Petersen, N. J.; Pedersen-Bjergaard, S. Nanoliter-Scale Electromembrane Extraction and Enrichment in a Microfluidic Chip. *Anal. Chem.* **2018**, *90*, 9322−9329.
(48) Saharil, F.; Carlborg, C. F.; Haraldsson, T.; van der Wijngaart, W. Biocompatible "Click" Wafer Bonding for Microfluidic Devices. *Lab Chip* **2012**, *12*, 3032−3035.
(49) Forsberg, F.; Saharil, F.; Haraldsson, T.; Roxhed, N.; Stemme, G.; van der Wijngaart, W.; Niklaus, F. A Comparative Study of the Bonding Energy in Adhesive Wafer Bonding. *J. Micromech. Microeng.* **2013**, *23*, 7.
(50) Zhou, X. C.; Sjoberg, R.; Druet, A.; Schwenk, J. M.; van der Wijngaart, W.; Haraldsson, T.; Carlborg, C. F. Thiol-Ene-Epoxy Thermoset for Low-Temperature Bonding to Biofunctionalized Microarray Surfaces. *Lab Chip* **2017**, *17*, 3672−3681.
(51) Pardon, G.; Saharil, F.; Karlsson, J. M.; Supekar, O.; Carlborg, C. F.; van der Wijngaart, W.; Haraldsson, T. Rapid Mold-Free Manufacturing of Microfluidic Devices with Robust and Spatially Directed Surface Modifications. *Microfluid. Nanofluid.* **2014**, *17*, 773−779.
(52) Mesbah, K.; Mai, T. D.; Jensen, T. G.; Sola, L.; Chiari, M.; Kutter, J. P.; Taverna, M. A Neutral Polyacrylate Copolymer Coating for Surface Modification of Thiol-Ene Microchannels for Improved Performance of Protein Separation by Microchip Electrophoresis. *Microchim. Acta* **2016**, *183*, 2111−2121.
(53) Wägli, P.; Homsy, A.; de Rooij, N. F. Norland Optical Adhesive (NOA81) Microchannels with Adjustable Wetting Behavior and High Chemical Resistance against a Range of Mid-Infrared-Transparent Organic Solvents. *Sens. Actuators, B* **2011**, *156*, 994−1001.
(54) Pardon, G.; Haraldsson, T.; van der Wijngaart, W. Simultaneous Replication of Hydrophilic and Superhydrophobic Micropatterns through Area-Selective Monomers Self-Assembly. *Adv. Mater. Interfaces* **2016**, *3*, 1600404.
(55) Rydholm, A. E.; Bowman, C. N.; Anseth, K. S. Degradable Thiol-Acrylate Photopolymers: Polymerization and Degradation Behavior of an in Situ Forming Biomaterial. *Biomaterials* **2005**, *26*, 4495−4506.
(56) Khire, V. S.; Lee, T. Y.; Bowman, C. N. Surface Modification Using Thiol−Acrylate Conjugate Addition Reactions. *Macromolecules* **2007**, *40*, 5669−5677.
(57) Khire, V. S.; Yi, Y.; Clark, N. A.; Bowman, C. N. Formation and Surface Modification of Nanopatterned Thiol-Ene Substrates Using Step and Flash Imprint Lithography. *Adv. Mater.* **2008**, *20*, 3308−3313.
(58) Worrell, B. T.; McBride, M. K.; Lyon, G. B.; Cox, L. M.; Wang, C.; Mavila, S.; Lim, C.-H.; Coley, H. M.; Musgrave, C. B.; Ding, Y.; Bowman, C. N. Bistable and Photoswitchable States of Matter. *Nat. Commun.* **2018**, *9*, 2804.
(59) Lee, T. Y.; Roper, T. M.; Guymon, C. A.; Jonsson, E. S.; Hoyle, C. E. Copolymerization Mechanism of Photoinitiator Free Thiol—Vinyl Acrylate Systems. *Film Formation, ACS* **2006**, *941*, 17−28.
(60) Fan, S.; Boey, F. Y. C.; Abadie, M. J. M. The Application of Thiol-Ene Reaction on Preparing UV Curable Bismaleimide-Containing Liquid Formulations. *Eur. Polym. J.* **2008**, *44*, 2123−2129.
(61) Lee, T. Y.; Smith, Z.; Reddy, S. K.; Cramer, N. B.; Bowman, C. N. Thiol−Allyl Ether−Methacrylate Ternary Systems. Polymerization Mechanism. *Macromolecules* **2007**, *40*, 1466−1472.
(62) Kasprzak, S. E.; Martin, B.; Raj, T.; Gall, K. Synthesis and Thermomechanical Behavior of (Qua)Ternary Thiol-Ene(/Acrylate) Copolymers. *Polymer* **2009**, *50*, 5549−5558.
(63) Sangermano, M.; Cerrone, M.; Colucci, G.; Roppolo, I.; Acosta, R. O. Preparation and Characterization of Hybrid Thiol-Ene/Epoxy UV−Thermal Dual-Cured Systems. *Polym. Int.* **2010**, *59*, 1046−1051.
(64) Flores, M.; Tomuta, A. M.; Fernández-Francos, X.; Ramis, X.; Sangermano, M.; Serra, A. A New Two-Stage Curing System: Thiol-Ene/Epoxy Homopolymerization Using an Allyl Terminated Hyperbranched Polyester as Reactive Modifier. *Polymer* **2013**, *54*, 5473−5481.
(65) Jian, Y.; He, Y.; Sun, Y.; Yang, H.; Yang, W.; Nie, J. Thiol−Epoxy/Thiol−Acrylate Hybrid Materials Synthesized by Photopolymerization. *J. Mater. Chem. C* **2013**, *1*, 4481−4489.


https://dx.doi.org/10.1021/acsami.9b22050
ACS Appl. Mater. Interfaces 2020, 12, 10080−10095

(66) Carlborg, C. F.; Vastesson, A.; Liu, Y.; van der Wijngaart, W.; Johansson, M.; Haraldsson, T. Functional Off-Stoichiometry Thiol-Ene-Epoxy Thermosets Featuring Temporally Controlled Curing Stages Via an UV/UV Dual Cure Process. *J. Polym. Sci., Part A: Polym. Chem.* **2014**, *52*, 2604−2615.
(67) Guzmán, D.; Ramis, X.; Fernandez-Francos, X.; Serra, A. Preparation of Click Thiol-Ene/Thiol-Epoxy Thermosets by Controlled Photo/Thermal Dual Curing Sequence. *RSC Adv.* **2015**, *5*, 101623−101633.
(68) Acebo, C.; Fernandez-Francos, X.; Ramis, X.; Serra, A. Multifunctional Allyl-Terminated Hyperbranched Poly(Ethyleneimine) as Component of New Thiol-Ene/Thiol-Epoxy Materials. *React. Funct. Polym.* **2016**, *99*, 17−25.
(69) Guzmán, D.; Ramis, X.; Fernández-Francos, X.; De la Flor, S.; Serra, A. New Bio-Based Materials Obtained by Thiol-Ene/Thiol-Epoxy Dual Curing Click Procedures from Eugenol Derivates. *Eur. Polym. J.* **2017**, *93*, 530−544.
(70) Mishra, V.; Desai, J.; Patel, K. I. High-Performance Waterborne UV-Curable Polyurethane Dispersion Based on Thiol-Acrylate/Thiol-Epoxy Hybrid Networks. *J. Coat. Technol. Res.* **2017**, *14*, 1069−1081.
(71) Cygan, Z. T.; Cabral, J. T.; Beers, K. L.; Amis, E. J. Microfluidic Platform for the Generation of Organic-Phase Microreactors. *Langmuir* **2005**, *21*, 3629−3634.
(72) Gu, H.; Duits, M. H. G.; Mugele, F. A Hybrid Microfluidic Chip with Electrowetting Functionality Using Ultraviolet (UV)-Curable Polymer. *Lab Chip* **2010**, *10*, 1550−1556.
(73) Brigo, L.; Carofiglio, T.; Fregonese, C.; Meneguzzi, F.; Mistura, G.; Natali, M.; Tonellato, U. An Optical Sensor for pH Supported onto Tentagel Resin Beads. *Sens. Actuators, B* **2008**, *130*, 477−482.
(74) Tesfai, J. T.; Perry, R. N.; Jablonski, E. L. Water-in-Oil Emulsion Separation within a Milli-Fluidic Device. *J. Colloid Interface Sci.* **2011**, *354*, 895−899.
(75) Bartolo, D.; Degre, G.; Nghe, P.; Studer, V. Microfluidic Stickers. *Lab Chip* **2008**, *8*, 274−279.
(76) Senkbeil, S.; Aho, J.; Yde, L.; Lindvold, L. R.; Stensborg, J. F.; Rantanen, J.; Lafleur, J. P.; Kutter, J. P. Roll-to-Plate Fabrication of Microfluidic Devices with Rheology-Modified Thiol-Ene Resins. *J. Micromech. Microeng.* **2016**, *26*, 9.
(77) Chen, L.; Wu, Q.; Wei, G.; Liu, R.; Li, Z. Highly Stable Thiol−Ene Systems: From Their Structure−Property Relationship to DLP 3D Printing. *J. Mater. Chem. C* **2018**, *6*, 11561−11568.
(78) Shafagh, R. Z.; Vastesson, A.; Guo, W. J.; van der Wijngaart, W.; Haraldsson, T. E-Beam Nanostructuring and Direct Click Biofunctionalization of Thiol-Ene Resist. *ACS Nano* **2018**, *12*, 9940−9946.
(79) Vitale, A.; Hennessy, M. G.; Matar, O. K.; Cabral, J. T. Interfacial Profile and Propagation of Frontal Photopolymerization Waves. *Macromolecules* **2015**, *48*, 198−205.
(80) Cabral, J. T.; Hudson, S. D.; Harrison, C.; Douglas, J. F. Frontal Photopolymerization for Microfluidic Applications. *Langmuir* **2004**, *20*, 10020−10029.
(81) Hoffmann, C.; Pinelo, M.; Woodley, J. M.; Daugaard, A. E. Development of a Thiol-Ene Based Screening Platform for Enzyme Immobilization Demonstrated Using Horseradish Peroxidase. *Biotechnol. Prog.* **2017**, *33*, 1267−1277.
(82) Sticker, D.; Lechner, S.; Jungreuthrnayer, C.; Zanghellini, J.; Ertl, P. Microfluidic Migration and Wound Healing Assay Based on Mechanically Induced Injuries of Defined and Highly Reproducible Areas. *Anal. Chem.* **2017**, *89*, 2326−2333.
(83) Mongkhontreerat, S.; Oberg, K.; Erixon, L.; Lowenhielm, P.; Hult, A.; Malkoch, M. UV Initiated Thiol-Ene Chemistry: A Facile and Modular Synthetic Methodology for the Construction of Functional 3D Networks with Tunable Properties. *J. Mater. Chem. A* **2013**, *1*, 13732−13737.
(84) Johnston, I. D.; McCluskey, D. K.; Tan, C. K. L.; Tracey, M. C. Mechanical Characterization of Bulk Sylgard 184 for Microfluidics and Microengineering. *J. Micromech. Microeng.* **2014**, *24*, 035017.
(85) Qin, D.; Xia, Y.; Whitesides, G. M. Soft Lithography for Micro- and Nanoscale Patterning. *Nat. Protoc.* **2010**, *5*, 491.
(86) Mays, R. L.; Pourhossein, P.; Savithri, D.; Genzer, J.; Chiechi, R. C.; Dickey, M. D. Thiol-Containing Polymeric Embedding Materials for Nanoskiving. *J. Mater. Chem. C* **2013**, *1*, 121−130.
(87) Geczy, R.; Sticker, D.; Bovet, N.; Häfeli, U. O.; Kutter, J. P. Chloroform Compatible, Thiol-Ene Based Replica Molded Micro Chemical Devices as an Alternative to Glass Microfluidic Chips. *Lab Chip* **2019**, *19*, 798
(88) Prichard, T. D.; Singh, S. S.; Chawla, N.; Vogt, B. D. Flocculated Carbon Nanotube Composites for Solvent Resistant Soft Templated Microfeatures. *Polymer* **2013**, *54*, 1130−1135.
(89) Lee, D. G.; An, S. Y.; Um, M. S.; Choi, W. J.; Noh, S. M.; Jung, H. W.; Oh, J. K. Photo-Induced Thiol-Ene Crosslinked Polymethacrylate Networks Reinforced with Al2O3 Nanoparticles. *Polymer* **2016**, *101*, 119−126.
(90) Do, D.-H.; Ecker, M.; Voit, W. E. Characterization of a Thiol-Ene/Acrylate-Based Polymer for Neuroprosthetic Implants. *ACS Omega* **2017**, *2*, 4604−4611.
(91) Lee, J. N.; Park, C.; Whitesides, G. M. Solvent Compatibility of Poly(Dimethylsiloxane)-Based Microfluidic Devices. *Anal. Chem.* **2003**, *75*, 6544−6554.
(92) Biron, M. Chapter 4 - Detailed Accounts of Thermoplastic Resins. In *Thermoplastics and Thermoplastic Composites*, 3rd ed.; Biron, M., Ed.; William Andrew Publishing: 2018; pp 252−253.
(93) Sheppard, G.; Oseki, T.; Baba, A.; Patton, D.; Kaneko, F.; Mao, L.; Locklin, J. Thiolene-Based Microfluidic Flow Cells for Surface Plasmon Resonance Imaging. *Biomicrofluidics* **2011**, *5*, 26501.
(94) Kim, D. N. H.; Kim, K. T.; Kim, C.; Teitell, M. A.; Zangle, T. A. Soft Lithography Fabrication of Index-Matched Microfluidic Devices for Reducing Artifacts in Fluorescence and Quantitative Phase Imaging. *Microfluid. Nanofluid.* **2018**, *22*, 2.
(95) Huby, N.; Pluchon, D.; Coulon, N.; Belloul, M.; Moreac, A.; Gaviot, E.; Panizza, P.; Bêche, B. Design of Organic 3D Microresonators with Microfluidics Coupled to Thin-Film Processes for Photonic Applications. *Opt. Commun.* **2010**, *283*, 2451−2456.
(96) Siudzinska, A.; Miszczuk, A.; Marczak, J.; Komorowska, K. Fluorescent Sensing with Fresnel Microlenses for Optofluidic Systems. *Opt. Eng.* **2017**, *56*, 8.
(97) Chen, C.-T.; Tsai, T.-W. Multilayer Polymer Light Guides Integrated with Refractive Microlenses and Liquid by Micromolding and Inkjet Printing. *Sens. Actuators, A* **2016**, *244*, 252−260.
(98) Markovitz-Bishitz, Y.; Tauber, Y.; Afrimzon, E.; Zurgil, N.; Sobolev, M.; Shafran, Y.; Deutsch, A.; Howitz, S.; Deutsch, M. A Polymer Microstructure Array for the Formation, Culturing, and High Throughput Drug Screening of Breast Cancer Spheroids. *Biomaterials* **2010**, *31*, 8436−8444.
(99) Tähkä, S. M.; Bonabi, A.; Jokinen, V. P.; Sikanen, T. M. Aqueous and Non-Aqueous Microchip Electrophoresis with on-Chip Electrospray Ionization Mass Spectrometry on Replica-Molded Thiol-Ene Microfluidic Devices. *J. Chromatogr. A* **2017**, *1496*, 150−156.
(100) Tan, H.-Y.; Trier, S.; Rahbek, U. L.; Dufva, M.; Kutter, J. P.; Andresen, T. L. A Multi-Chamber Microfluidic Intestinal Barrier Model Using Caco-2 Cells for Drug Transport Studies. *PLoS One* **2018**, *13*, e0197101.
(101) Krenger, R.; Cornaglia, M.; Lehnert, T.; Gijs, M. A. M. Microfluidic System for Caenorhabditis Elegans Culture and Oxygen Consumption Rate Measurements. *Lab Chip* **2020**, *20*, 126
(102) Mazurek, P.; Daugaard, A. E.; Skolimowski, M.; Hvilsted, S.; Skov, A. L. Preparing Mono-Dispersed Liquid Core PDMS Microcapsules from Thiol-Ene-Epoxy-Tailored Flow-Focusing Microfluidic Devices. *RSC Adv.* **2015**, *5*, 15379−15386.
(103) Li, D. *Encyclopedia of Microfluidics and Nanofluidics*; Springer Science & Business Media: 2008.
(104) Svejdal, R. R.; Dickinson, E. R.; Sticker, D.; Kutter, J. P.; Rand, K. D. Thiol-Ene Microfluidic Chip for Performing Hydrogen/Deuterium Exchange of Proteins at Subsecond Time Scales. *Anal. Chem.* **2019**, *91*, 1309−1317.
(105) Levache, B.; Azioune, A.; Bourrel, M.; Studer, V.; Bartolo, D. Engineering the Surface Properties of Microfluidic Stickers. *Lab Chip* **2012**, *12*, 3028−3031.

(106) Tähkä, S. M.; Bonabi, A.; Nordberg, M.-E.; Kanerva, M.; Jokinen, V. P.; Sikanen, T. M. Thiol-Ene Microfluidic Devices for Microchip Electrophoresis: Effects of Curing Conditions and Monomer Composition on Surface Properties. *J. Chromatogr. A* **2015**, *1426*, 233−240.

(107) Çakmakçi, E.; Yuce-Dursun, B.; Demir, S. Maleic Anhydride Functionalization of Oste Based Coatings Via Thiol-Ene "Click" Reaction for the Covalent Immobilization of Xylanase. *React. Funct. Polym.* **2017**, *111*, 38−43.

(108) Hansson, J.; Yasuga, H.; Haraldsson, T.; van der Wijngaart, W. Synthetic Microfluidic Paper: High Surface Area and High Porosity Polymer Micropillar Arrays. *Lab Chip* **2016**, *16*, 298−304.

(109) Kwisnek, L.; Nazarenko, S.; Hoyle, C. E. Oxygen Transport Properties of Thiol−Ene Networks. *Macromolecules* **2009**, *42*, 7031−7041.

(110) Hansson, J.; Karlsson, J. M.; Carlborg, C. F.; Wijngaart, W. v. d.; Haraldsson, T. In *Low Gas Permeable and Non-Absorbent Rubbery Oste+ for Pneumatic Microvalves*, 2014 IEEE 27th International Conference on Micro Electro Mechanical Systems (MEMS), 26−30 January 2014; pp 987−990.

(111) Sticker, D.; Rothbauer, M.; Ehgartner, J.; Steininger, C.; Liske, O.; Liska, R.; Neuhaus, W.; Mayr, T.; Haraldsson, T.; Kutter, J. P.; Ertl, P. Oxygen Management at the Microscale: A Functional Biochip Material with Long-Lasting and Tunable Oxygen Scavenging Properties for Cell Culture Applications. *ACS Appl. Mater. Interfaces* **2019**, *11*, 9730

(112) Li, R.; Lv, X.; Hasan, M.; Xu, J.; Xu, Y.; Zhang, X.; Qin, K.; Wang, J.; Zhou, D.; Deng, Y. A Rapidly Fabricated Microfluidic Chip for Cell Culture. *J. Chromatogr. Sci.* **2016**, *54*, 523−530.

(113) Ejserholm, F.; Stegmayr, J.; Bauer, P.; Johansson, F.; Wallman, L.; Bengtsson, M.; Oredsson, S. Biocompatibility of a Polymer Based on Off-Stoichiometry Thiol-Enes + Epoxy (OSTE+) for Neural Implants. *Biomater. Res.* **2015**, *19*, 1−10.

(114) Zurgil, N.; Afrimzon, E.; Deutsch, A.; Namer, Y.; Shafran, Y.; Sobolev, M.; Tauber, Y.; Ravid-Hermesh, O.; Deutsch, M. Polymer Live-Cell Array for Real-Time Kinetic Imaging of Immune Cells. *Biomaterials* **2010**, *31*, 5022−5029.

(115) Chen, T. F.; Siow, K. S.; Ng, P. Y.; Majlis, B. Y. Enhancing the Biocompatibility of the Polyurethane Methacrylate and Off-Stoichiometry Thiol-Ene Polymers by Argon and Nitrogen Plasma Treatment. *Mater. Sci. Eng., C* **2017**, *79*, 613−621.

(116) Liu, W.; Li, Y.; Ding, X. Cell Adhesion Pattern Created by OSTE Polymers. *Biofabrication* **2017**, *9*, 025006

(117) Hong, T.; Liu, W.; Li, M.; Chen, C. Click Chemistry at the Microscale. *Analyst* **2019**, *144*, 1492

(118) Burke, J. M.; Pandit, K. R.; Goertz, J. P.; White, I. M. Fabrication of Rigid Microstructures with Thiol-Ene-Based Soft Lithography for Continuous-Flow Cell Lysis. *Biomicrofluidics* **2014**, *8*, 056503.

(119) Madadi, H.; Mohammadi, M.; Casals-Terre, J.; Lopez, R. C. A Novel Fabrication Technique to Minimize Poly(Dimethylsiloxane)-Microchannels Deformation under High-Pressure Operation. *Electrophoresis* **2013**, *34*, 3126−3132.

(120) Manz, A.; Graber, N.; Widmer, H. M. Miniaturized Total Chemical Analysis Systems: A Novel Concept for Chemical Sensing. *Sens. Actuators, B* **1990**, *1*, 244−248.

(121) Baylor, M. E.; Cerjan, B. W.; Pfiefer, C. R.; Boyne, R. W.; Couch, C. L.; Cramer, N. B.; Bowman, C. N.; McLeod, R. R. Monolithic Integration of Optical Waveguide and Fluidic Channel Structures in a Thiol-Ene/Methacrylate Photopolymer. *Opt. Mater. Express* **2012**, *2*, 1548−1555.

(122) Lipponen, K.; Tahka, S.; Sikanen, T.; Jokinen, V.; Tatikonda, A.; Franssila, S.; Kostiainen, R.; Kotiaho, T. Thiol-Ene Micropillar Array Electrospray Ionization Platform for Zeptomole Level Bioanalysis. *Analyst* **2017**, *142*, 2552−2557.

(123) Bataille, J.; Viodé, A.; Pereiro, I.; Lafleur, J. P.; Varenne, F.; Descroix, S.; Becher, F.; Kutter, J. P.; Roesch, C.; Poüs, C.; Taverna, M.; Pallandre, A.; Smadja, C.; Le Potier, I. On-a-Chip Tryptic Digestion of Transthyretin: A Step toward an Integrated Microfluidic System for the Follow-up of Familial Transthyretin Amyloidosis. *Analyst* **2018**, *143*, 1077−1086.

(124) Tahka, S.; Sarfraz, J.; Urvas, L.; Provenzani, R.; Wiedmer, S. K.; Peltonen, J.; Jokinen, V.; Sikanen, T. Immobilization of Proteolytic Enzymes on Replica-Molded Thiol-Ene Micropillar Reactors Via Thiol-Gold Interaction. *Anal. Bioanal. Chem.* **2019**, *411*, 2339−2349.

(125) Valles, D. J.; Naeem, Y.; Rozenfeld, A. Y.; Aldasooky; Rawan, W.; Wong, A. M.; Carbonell, C.; Mootoo, D. R.; Braunschweig, A. B. Multivalent Binding of Concanavalin a on Variable-Density Mannoside Microarrays. *Faraday Discuss.* **2019**, *219*, 77−89.

(126) Goyal, S.; Desai, A. V.; Lewis, R. W.; Ranganathan, D. R.; Li, H. R.; Zeng, D. X.; Reichert, D. E.; Kenis, P. J. A. Thiolene and SIFEL-Based Microfluidic Platforms for Liquid-Liquid Extraction. *Sens. Actuators, B* **2014**, *190*, 634−644.

(127) Sollier, E.; Murray, C.; Maoddi, P.; Di Carlo, D. Rapid Prototyping Polymers for Microfluidic Devices and High Pressure Injections. *Lab Chip* **2011**, *11*, 3752−3765.

(128) Geczy, R.; Agnoletti, M.; Hansen, M. F.; Kutter, J. P.; Saatchi, K.; Häfeli, U. O. Microfluidic Approaches for the Production of Monodisperse, Superparamagnetic Microspheres in the Low Micrometer Size Range. *J. Magn. Magn. Mater.* **2019**, *471*, 286−293.



https://dx.doi.org/10.1021/acsami.9b22050
*ACS Appl. Mater. Interfaces* 2020, 12, 10080−10095

GRADUATE SCHOOL OF HEALTH AND MEDICAL SCIENCES
UNIVERSITY OF COPENHAGEN

# PHD-THESIS
# DECLARATION OF CO-AUTHORSHIP

*The declaration is for PhD students and must be completed for each conjointly authored article. Please note that if a manuscript or published paper has ten or less co-authors, all co-authors must sign the declaration of co-authorship. If it has more than ten co-authors, declarations of co-authorship from the corresponding author(s), the senior author and the principal supervisor (if relevant) are a minimum requirement.*

| **1. Declaration by** | |
|---|---|
| Name of PhD student | Reka Geczy |
| E-mail | reka.geczy@sund.ku.dk |
| Name of principal supervisor | Urs O. Häfeli |
| Title of the PhD thesis | Design and Fabrication of Solvent Compatible Polymer Microfluidic Chips and its application to Particle Production and Drug Delivery |

| **2. The declaration applies to the following article** | |
|---|---|
| Title of article | Chloroform compatible, thiol-ene based replica molded micro chemical devices as an alternative to glass microfluidic chips |
| **Article status** | |
| Published ☒<br>Date: 22 Jan 2019 | Accepted for publication ☐<br>Date: |
| Manuscript submitted ☐<br>Date: | Manuscript not submitted ☐ |
| If the article is published or accepted for publication, please state the name of journal, year, volume, page and DOI (if you have the information). | Lab on a Chip, 2019,19, 798-806<br>DOI: 10.1039/c8lc01260a |

| **3. The PhD student's contribution to the article** ***(please use the scale A-F as benchmark)***<br>Benchmark scale of the PhD-student's contribution to the article<br>**A**. Has essentially done all the work (> 90 %) **B**. Has done most of the work (60-90 %) **C**. Has contributed considerably (30-60 %) **D.** Has contributed (10-30 %) **E.** No or little contribution (<10 %) **F.** Not relevant | **A, B, C, D, E, F** |
|---|---|
| 1. Formulation/identification of the scientific problem | A |
| 2. Development of the key methods | B |
| 3. Planning of the experiments and methodology design and development | B |
| 4. Conducting the experimental work/clinical studies/data collection/obtaining access to data | B |
| 5. Conducting the analysis of data | B |
| 6. Interpretation of the results | B |
| 7. Writing of the first draft of the manuscript | A |
| 8. Finalisation of the manuscript and submission | A |
| Provide a short description of the PhD student´s specific contribution to the article.[i]<br>PhD student identified the problem and planned/conducted ~75% of the experiments. Student wrote the first draft, submitted the paper and wrote the initial review comments. | |

*Latest update of the declaration: December 2018*

| 4. Material from another thesis / dissertation[ii] | |
|---|---|
| Does the article contain work which has also formed part of another thesis, e.g. master's thesis, PhD thesis or doctoral dissertation (the PhD student's or another person's)? | Yes: ☐ No: ☒ |
| If yes, please state name of the author and title of thesis / dissertation. | |
| If the article is part of another author's academic degree, please describe the PhD student's and the author s contributions to the article so that the individual contributions are clearly distinguishable from one another. | |

| 5. Signatures of the co-authors[iii] | | | | |
|---|---|---|---|---|
| | Date | Name | Title | Signature |
| 1. | 11/3/2020 | Reka Geczy | PhD student | |
| 2. | 12/3/2020 | Drago Sticker | PhD, Scientist | |
| 3. | | Nikolas Bovet | PhD, Senior Researcher | |
| 4. | 11/3/2020 | Urs O. Häfeli | PhD, Professor | |
| 5. | 11-3-2020 | Jörg P. Kutter | PhD, Professor | |
| 6. | | | | |
| 7. | | | | |
| 8. | | | | |
| 9. | | | | |
| 10. | | | | |

| 6. Signature of the principal supervisor |
|---|
| I solemnly declare that the information provided in this declaration is accurate to the best of my knowledge.<br>Date: 11-March-20<br>Principal supervisor: |

| 7. Signature of the PhD student |
|---|
| I solemnly declare that the information provided in this declaration is accurate to the best of my knowledge.<br>Date: 11/3/2020<br>PhD student: |

Please learn more about responsible conduct of research on the Faculty of Health and Medical Sciences' website.

GRADUATE SCHOOL OF HEALTH AND MEDICAL SCIENCES
UNIVERSITY OF COPENHAGEN

# PHD-THESIS
# DECLARATION OF CO-AUTHORSHIP

*The declaration is for PhD students and must be completed for each conjointly authored article. Please note that if a manuscript or published paper has ten or less co-authors, all co-authors must sign the declaration of co-authorship. If it has more than ten co-authors, declarations of co-authorship from the corresponding author(s), the senior author and the principal supervisor (if relevant) are a minimum requirement.*

| **1. Declaration by** | |
|---|---|
| Name of PhD student | Reka Geczy |
| E-mail | reka.geczy@sund.ku.dk |
| Name of principal supervisor | Urs O. Häfeli |
| Title of the PhD thesis | Design and Fabrication of Solvent Compatible Polymer Microfluidic Chips and its application to Particle Production and Drug Delivery |

| **2. The declaration applies to the following article** | |
|---|---|
| Title of article | Microfluidic approaches for the production of monodisperse, superparamagnetic microspheres in the low micrometer size range |
| **Article status** | |
| Published ☒<br>Date: 25 Sept 2018 | Accepted for publication ☐<br>Date: |
| Manuscript submitted ☐<br>Date: | Manuscript not submitted ☐ |
| If the article is published or accepted for publication, please state the name of journal, year, volume, page and DOI (if you have the information). | Journal of Magnetism and Magnetic Materials, 2019, 471, 286–293<br>https://doi.org/10.1016/j.jmmm.2018.09.091 |

| **3. The PhD student's contribution to the article** ***(please use the scale A-F as benchmark)***<br>Benchmark scale of the PhD-student's contribution to the article<br>**A**. Has essentially done all the work (> 90 %) **B**. Has done most of the work (60-90 %) **C**. Has contributed considerably (30-60 %) **D.** Has contributed (10-30 %) **E.** No or little contribution (<10 %) **F.** Not relevant | **A, B, C, D, E, F** |
|---|---|
| 1. Formulation/identification of the scientific problem | C |
| 2. Development of the key methods | B |
| 3. Planning of the experiments and methodology design and development | A |
| 4. Conducting the experimental work/clinical studies/data collection/obtaining access to data | B |
| 5. Conducting the analysis of data | B |
| 6. Interpretation of the results | A |
| 7. Writing of the first draft of the manuscript | A |
| 8. Finalisation of the manuscript and submission | A |
| Provide a short description of the PhD student´s specific contribution to the article.[i]<br>PhD student has planned and performed the vast majority of experiments, wrote the first draft, submitted the paper, and responded to review comments. | |

*Latest update of the declaration: December 2018*

| 4. Material from another thesis / dissertation[ii] | |
|---|---|
| Does the article contain work which has also formed part of another thesis, e.g. master's thesis, PhD thesis or doctoral dissertation (the PhD student's or another person's)? | Yes: ☐ No: ☒ |
| If yes, please state name of the author and title of thesis / dissertation. | |
| If the article is part of another author's academic degree, please describe the PhD student´s and the author´s contributions to the article so that the individual contributions are clearly distinguishable from one another. | |

**5. Signatures of the co-authors[iii]**

| | Date | Name | Title | Signature |
|---|---|---|---|---|
| 1. | 11/3/2020 | Reka Geczy | PhD student | |
| 2. | 11/3/2020 | Monica Agnoletti | PhD student | |
| 3. | 12/3/2020 | Katayoun Saatchi | PhD, Research associate | |
| 4. | 11-Mar-20 | Jörg P. Kutter | PhD, Professor | |
| 5. | 12-Mar 2020 | Mikkel F. Hansen | PhD, Professor | |
| 6. | | Urs O. Häfeli | PhD, Professor | |
| 7. | | | | |
| 8. | | | | |
| 9. | | | | |
| 10. | | | | |

**6. Signature of the principal supervisor**

I solemnly declare that the information provided in this declaration is accurate to the best of my knowledge.
Date: 12/3/2020
Principal supervisor:

**7. Signature of the PhD student**

I solemnly declare that the information provided in this declaration is accurate to the best of my knowledge.
Date: 11/3/2020
PhD student: Reka Geczy

Please learn more about responsible conduct of research on the Faculty of Health and Medical Sciences' website.